Advanced Processing and Manufacturing Technologies for Structural and Multifunctional Materials II

Advanced Processing and Manufacturing Technologies for Structural and Multifunctional Materials II

A Collection of Papers Presented at the 32nd International Conference on Advanced Ceramics and Composites January 27–February 1, 2008 Daytona Beach, Florida

Editors

Tatsuki Ohji

Mrityunjay Singh

Volume Editors

Tatsuki Ohji

Andrew Wereszczak

WILEY

A John Wiley & Sons, Inc., Publication

Published by John Wiley & Sons, Inc., Hoboken, New Jersey.
Published simultaneously in Canada.

Library of Congress Cataloging-in-Publication Data is available.

ISBN 978-0-470-34499-6

Printed in the United States of America.

10 9 8 7 6 5 4 3 2 1

Contents

Preface ix

Introduction xi

Development and Characterization of the Bonding and Integration Technologies Needed for Fabricating Silicon Carbide Based Injector Components 1
Michael C. Halbig and Mrityunjay Singh

Bonding and Integration of C-C Composite to Cu-Clad-Molybdenum for Thermal Management Applications 15
R. Asthana and M. Singh

Polymer Impregnation and Pyrolysis Process Combined with Powder Space Holder Technique (PSH-PIP) 27
Masaki Kotani, Aline Zimmer, Satoru Matsuzaki, and Kazuaki Nishiyabu

Oxidation Behavior of C/C-SiC Composites in Open Atmosphere 33
V.K. Srivastava and Shraddha Singh

Processing Method for Interpenetrating Network Metal-Ceramic Composites with a Non-Linear Compositional Gradient 43
M. Neukam and M. Willert-Porada

3-D Simulation of Self-Propagating High-Temperature Synthesis of Solid Oxide Fuel Cell Cathode Materials 53
Sidney Lin and Jiri Selig

Influence of Green Part Microstructure and Sintering Atmosphere on the Formation of Porous Silicon Nitride Ceramics with Yb-Silicate Matrix 63
M. Knoll and M. Willert-Porada

R-SiC for Novel Gel-Cast Cross Flow Filter 73
J. Homa, S. Zellhofer, A. Liersch, and J. Stampfl

Reaction Bonded SiC Processed with Two Different Types of Carbon Precursors 87
Cristiane Evelise Ribeiro da Silva, Célio A. Costa, and Maria Cecília de Sousa Nóbrega

Evidence of Uniform Microstructure in Microwave Sintered Yttria Stabilized Zirconia (YSZ) by Impedance Analysis 95
Kanchan Lata Singh, Ajay Kumar, Anirudh P. Singh, and S.S. Sekhon

Modeling of Field Assisted Sintering Technology (FAST) and Its Application to Electro-Conductive Systems 109
K. Vanmeensel, S.H. Huang, A. Laptev, J. Vleugels, and O. Van der Biest

Polydimethylsiloxane Derived Ceramics: Influence of Pyrolysis Temperature on Ceramic Phases 123
Marilia Sérgio da Silva Beltrão, Marysilvia Ferreira, and Célio A. Costa

Freeform Fabrication of Alumina Dental-Crown Models by Using Stereolithography 131
Masahito Ishikawa, Soshu Kirihara, Yoshinari Miyamoto, and Taiji Sohmura

Silicon Nitride Rapid Decomposition for Formation of Nanosized Powders for Shaping Microdevices 139
Dariusz Kata and Jerzy Lis

The Relation between Peierls and Mott-Hubbard Transition in VO_2 by Tunneling Spectroscopy 147
Changman Kim, Tomoya Ohno, Takashi Tamura, Yasushi Oikawa, Jae-Soo Shin, and Hajime Ozaki

Localization of Terahertz Waves in Photonic Fractal Arrays of Alumina Fabricated by Micro-Stereolithography 155
T. Hibino, S. Kirihara, and Y. Miyamoto

Anisotropic Varistor via Magnetic Texturing 163
Yoshiaki Kinemuchi, Kumi Okanoue, Hisashi Kaga, Juan P. Wiff, Satoshi Tanaka, Keizo Uematsu, and Koji Watari

Faradayic Process for Electrophoretic Deposition of Thermal Barrier Coatings 169
Joseph Kell, Heather McCrabb, and Binod Kumar

Indium Tin Oxide Ceramic Rotary Sputtering Targets for Transparent Conductive Film Preparation 179
Eugene Medvedovski, Christopher J. Szepesi, Olga Yankov, and Maryam K. Olsson

The Effect of Doping with Titania and Calcium Titanate on the Microstructure and Electrical Properties of the Giant Dielectric Constant Ceramic $CaCu_3Ti_4O_{12}$ 185
Barry A. Bender, Ed Gorzkowski, and Ming-Jen Pan

Synthesis and Characterization of Electrodeposited Nickel Nanowires 195
Valeska da Rocha Caffarena, Alberto Passos Guimarães, Magali Silveira Pinho, Elizandra Martins Silva, Jefferson Leixas Capitaneo, and Marilia Sergio da Silva Beltrão

Crystallization of Titania Films in Aqueous Solutions and Their Dye Adsorption Properties 203
Yoshitake Masuda, Tatsuo Kimura, Xiulan Hu, Xiangju Meng, Kazumi Kato, and Tatsuki Ohji

Micro Scale Measurement of Thermal Effusivity/Conductivity of SiC by Thermal Microscope 215
Ikuko Yamada, Shoichi Kume, Koji Watari, Kimihito Hatori, and Genzo Matsui

Author Index 223

Preface

The Second International Symposium on Advanced Processing and Manufacturing Technologies for Structural and Multifunctional Materials and Systems (APMT) was held during the 32nd International Cocoa Beach Conference on Advanced Ceramics and Composites, in Daytona Beach, FL, January 27-February 1, 2008. The aim of this international symposium was to discuss global advances in the research and development of advanced processing and manufacturing technologies for a wide variety of non-oxide and oxide based structural ceramics, particulate and fiber reinforced composites, and multifunctional materials. This year's symposium also honored Professor Yoshinari Miyamoto, Osaka University, Japan, for his long term and outstanding contributions to processing and manufacturing science and technologies. A total of 67 papers, including invited talks, oral presentations and posters, were presented from 10 countries (USA, Japan, Germany, Australia, Ireland, Belgium, Brazil, Canada, France, Korea, India, Poland, and Slovenia). The speakers represented universities, industry and research laboratories.

This issue contains 23 invited and contributed papers, all peer reviewed according to the American Ceramic Society Review Process. The latest developments in processing and manufacturing technologies are covered, including smart processing, advanced composite manufacturing, novel forming and sintering technologies, microwave-processing, polymer-based processing and film deposition technologies. These papers discuss the most important aspects necessary for understanding and further development of processing and manufacturing of ceramic materials and systems.

The editors wish to extend their gratitude and appreciation to all the authors for their cooperation and contributions, to all the participants and session chairs for their time and efforts, and to all the reviewers for their valuable comments and suggestions. Financial support from Ube Industries, Ltd., Japan, as well as the Engineering Ceramic Division and The American Ceramic Society is gratefully acknowledged. Thanks are due to the staff of the meetings and publication departments of The American Ceramic Society for their invaluable assistance.

We hope that this issue will serve as a useful reference for the researchers and technologists working in the field of interested in processing and manufacturing of ceramic materials and systems.

Tatsuki Ohji
Advanced Manufacturing Research Institute
AIST, Nagoya, Japan

Mrityunjay Singh
Ohio Aerospace Institute
Cleveland, OH, USA

Introduction

Organized by the Engineering Ceramics Division (ECD) in conjunction with the Basic Science Division (BSD) of The American Ceramic Society (ACerS), the 32nd International Conference on Advanced Ceramics and Composites (ICACC) was held on January 27 to February 1, 2008, in Daytona Beach, Florida. 2008 was the second year that the meeting venue changed from Cocoa Beach, where ICACC was originated in January 1977 and was fostered to establish a meeting that is today the most preeminent international conference on advanced ceramics and composites

The 32nd ICACC hosted 1,247 attendees from 40 countries and 724 presentations on topics ranging from ceramic nanomaterials to structural reliability of ceramic components, demonstrating the linkage between materials science developments at the atomic level and macro level structural applications. The conference was organized into the following symposia and focused sessions:

Symposium 1	Mechanical Behavior and Structural Design of Monolithic and Composite Ceramics
Symposium 2	Advanced Ceramic Coatings for Structural, Environmental, and Functional Applications
Symposium 3	5th International Symposium on Solid Oxide Fuel Cells (SOFC): Materials, Science, and Technology
Symposium 4	Ceramic Armor
Symposium 5	Next Generation Bioceramics
Symposium 6	2nd International Symposium on Thermoelectric Materials for Power Conversion Applications
Symposium 7	2nd International Symposium on Nanostructured Materials and Nanotechnology: Development and Applications
Symposium 8	Advanced Processing & Manufacturing Technologies for Structural & Multifunctional Materials and Systems (APMT): An International Symposium in Honor of Prof. Yoshinari Miyamoto
Symposium 9	Porous Ceramics: Novel Developments and Applications

Symposium 10	Basic Science of Multifunctional Ceramics
Symposium 11	Science of Ceramic Interfaces: An International Symposium Memorializing Dr. Rowland M. Cannon
Focused Session 1	Geopolymers
Focused Session 2	Materials for Solid State Lighting

Peer reviewed papers were divided into nine issues of the 2008 Ceramic Engineering & Science Proceedings (CESP); Volume 29, Issues 2-10, as outlined below:

- Mechanical Properties and Processing of Ceramic Binary, Ternary and Composite Systems, Vol. 29, Is 2 (includes papers from symposium 1)
- Corrosion, Wear, Fatigue, and Reliability of Ceramics, Vol. 29, Is 3 (includes papers from symposium 1)
- Advanced Ceramic Coatings and Interfaces III, Vol. 29, Is 4 (includes papers from symposium 2)
- Advances in Solid Oxide Fuel Cells IV, Vol. 29, Is 5 (includes papers from symposium 3)
- Advances in Ceramic Armor IV, Vol. 29, Is 6 (includes papers from symposium 4)
- Advances in Bioceramics and Porous Ceramics, Vol. 29, Is 7 (includes papers from symposia 5 and 9)
- Nanostructured Materials and Nanotechnology II, Vol. 29, Is 8 (includes papers from symposium 7)
- Advanced Processing and Manufacturing Technologies for Structural and Multifunctional Materials II, Vol. 29, Is 9 (includes papers from symposium 8)
- Developments in Strategic Materials, Vol. 29, Is 10 (includes papers from symposia 6, 10, and 11, and focused sessions 1 and 2)

The organization of the Daytona Beach meeting and the publication of these proceedings were possible thanks to the professional staff of ACerS and the tireless dedication of many ECD and BSD members. We would especially like to express our sincere thanks to the symposia organizers, session chairs, presenters and conference attendees, for their efforts and enthusiastic participation in the vibrant and cutting-edge conference.

ACerS and the ECD invite you to attend the 33rd International Conference on Advanced Ceramics and Composites (http://www.ceramics.org/daytona2009) January 18–23, 2009 in Daytona Beach, Florida.

TATSUKI OHJI and ANDREW A. WERESZCZAK, Volume Editors
July 2008

Advanced Processing and Manufacturing Technologies for Structural and Multifunctional Materials II
Edited by Tatsuki Ohji and Mrityunjay Singh

DEVELOPMENT AND CHARACTERIZATION OF THE BONDING AND INTEGRATION TECHNOLOGIES NEEDED FOR FABRICATING SILICON CARBIDE BASED INJECTOR COMPONENTS

Michael C. Halbig
Army Research Laboratory, NASA Glenn Research Center
Cleveland, OH, USA

Mrityunjay Singh
Ohio Aerospace Institute, NASA Glenn Research Center
Cleveland, OH, USA

ABSTRACT

Advanced ceramic bonding and integration technologies play a critical role in the fabrication and application of silicon carbide based components for a number of aerospace and ground based applications. One such application is a lean direct injector for a turbine engine to achieve low NOx emissions. Ceramic to ceramic diffusion bonding and ceramic to metal brazing technologies are being developed for this injector application. For the diffusion bonding technology, titanium interlayers (coatings and foils) were used to aid in the joining of silicon carbide (SiC) substrates. The influence of such variables as surface finish, interlayer thickness, and processing time were investigated. Electron microprobe analysis was used to identify the reaction formed phases. In the diffusion bonds, an intermediate phase, $Ti_5Si_3C_x$, formed that is thermally incompatible in its thermal expansion and caused thermal stresses and cracking during the processing cool-down. Thinner interlayers of pure titanium and/or longer processing times resulted in an optimized microstructure. Tensile tests on the joined materials resulted in strengths of 13-28 MPa depending on the SiC substrate material. Non-destructive evaluation using ultrasonic immersion showed well formed bonds. For the joining technology of brazing Kovar fuel tubes to silicon carbide, preliminary development of the joining approach has begun. Various technical issues and requirements for the injector application are addressed.

INTRODUCTION

Silicon carbide ceramics are a very promising material for use in high-temperature, structural applications. The beneficial properties include high creep resistance, corrosion resistance, and high temperature strength and stability over long durations. One such application is for a ceramic injector in jet engines that enables more efficient fuel combustion and lower emissions during sub-sonic and super-sonic cruise. The ceramic lean-direct injector which is to be fabricated from SiC laminates is illustrated in Figure 1. Each laminate section contains its own distinct hole pattern for channeling the fuel and combustion air separately. When the laminates are stacked in order, fluid circuits for the fuel and combustion air are formed. At the exiting surface, the fuel and combustion air mix to provide efficient combustion with low emissions and low NOx.

The diffusion bonding of SiC laminates and the brazing of Kovar tubes to SiC are enabling technologies for developing the injector. The diffusion bonding allows for the fabrication of a multilayered component with complex internal passages. The brazing technology allows the injector component to be integrated into the surrounding engine system through the adjoining fuel system. Requirements of the SiC laminate bonding technology include the ability to join relatively large, flat geometries (i.e. 10.16 cm diameter discs), leak free operation, and chemical and mechanical stability for long durations at operation conditions. Technical challenges in developing the diffusion bonding

and brazing approaches include chemical incompatibility and the formation of residual stresses during the cool-down after processing. The residual stresses are due to thermal expansion mismatches between the two joined materials and/or the bonding interlayers. The proper selection of joining interlayers and processing conditions can help alleviate these challenges.

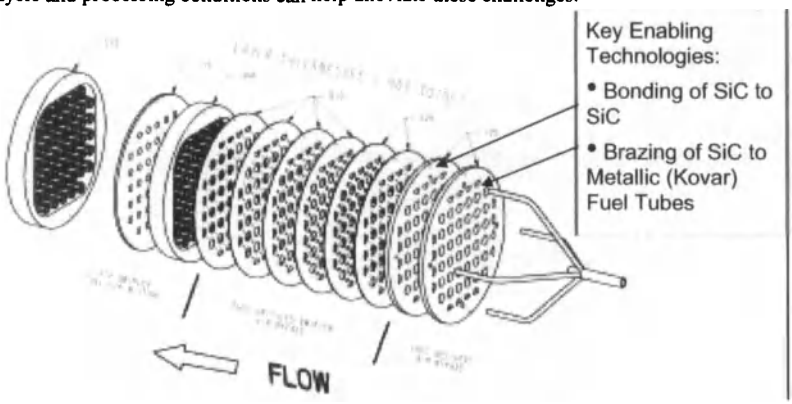

Figure 1. Illustration of the lean-direct injector design (LDI)[1].

The use of titanium interlayers was selected as the bonding aid for joining SiC substrates. The titanium interlayer can be utilized in several different forms such as foils and coatings. In previous studies[2,3], Ti alloys (Ti-6Al-4V) and physically vapor deposited (PVD) pure Ti coatings were investigated as interlayers for bonding SiC. The resulting diffusion bonds were uniform, had high strengths, and were leak free. The diffusion bonds were well adhered to the SiC substrate with no delaminations observed between the SiC layers. However, microcracks were observed in all bonds formed from using the alloyed Ti foil interlayer. Microcracks still formed despite efforts to alleviate cracking by varying the SiC substrate type (i.e. alpha-SiC and chemically vapor deposited SiC) and by varying processing conditions (i.e. applied pressure, temperature, and cooling rate). The microcracks may have been due to a single factor or a combination of factors. However, the primary factors appear to be the formation of the $Ti_5Si_3C_x$ phase and high concentrations of alpha and beta Ti alloy phases. The titanium silicide (Ti_5Si_3) phase is anisotropic in its thermal expansion[4,5]. The coefficient of thermal expansion (CTE) in the a-direction is 6.11 ppm/K and in the c-direction it is 16.62 ppm/K which gives a ratio of CTE(c)/CTE(a) equal to 2.72. Other researchers have reported the anisotropy to give a ratio as high as 4.39 [6]. The formation of alpha and beta Ti alloy phases is also believed to be a contributor to cracking. The central core of the diffusion bonds had concentrated alpha and beta Ti alloy phases. The alpha phase has an anisotropic thermal expansion which is 20 % greater along the c-axis[7]. Also, the beta phase has a thermal expansion that is 6 x higher in the temperature range of 600-1000°C (5.8x10-5/°C) compared the thermal expansion below 600°C (9.2x10-6/°C)[8]. These anisotropy and CTE mismatches could cause the microcracking due to thermal stresses forming during the cool down step after hot pressing. Due to the formation of complex diffusion bonds that consisted of several reaction formed phases and due to the formation of microcracks, the alloyed Ti foil was not considered for further investigation.

In the study of diffusion bonds formed with the PVD Ti coating as the interlayer, mixed results were obtained depending on the interlayer thickness. Diffusion bonds with Ti interlayer thicknesses of 10 and 20 microns were fabricated. Uniform and well adhered diffusion bonds were formed and no

debonding was observed. However, microcracking occurred in the diffusion bond formed with the thicker 20 micron interlayer due to the formation of the Ti_5Si_3 phase.

In the current study, processing optimization and diffusion bond characterization were the primary focus. Pure Ti interlayers (PVD coatings and foils) were down selected as the preferred interlayer. The results discussed in the previous paragraph will be presented in this paper to serve as an introduction to the characterization and processing optimization that was conducted. Additional joint fabrication was conducted using pure Ti foils in different thicknesses and at different processing times in an effort to better understand the formation of the reaction formed phases in the diffusion bond and the conditions which contributed to crack and void formation. Further characterization was conducted through non-destructive evaluation (NDE), strength tests, optical microscopy, scanning electron microscopy (SEM), and electron microprobe analysis.

EXPERIMENTAL

Silicon carbide was diffusion bonded to silicon carbide with the aid of Ti interlayers. The silicon carbide material was fabricated by Rohm & Haas through the method of chemical vapor deposition (CVD). Pure Ti was used as the interlayer. For the preliminary study (discussed in the introduction), physically vapor deposited (PVD) Ti coatings with a thickness of 10 microns were applied to the SiC substrates. In one case, coated and uncoated substrates were matched to provide a 10 micron interlayer. In another case, two coated substrates were matched to provide a 20 micron interlayer. Processing of the diffusion bonds was carried out in a hot press with an environmental chamber. The paired substrates were processed at the following conditions: 1250°C, vacuum, 31 MPa applied pressure, and a 2 hr hold, followed by a cooling rate of 2 °C per minute. The joints were analyzed using a JEOL JXA-8200 Superprobe electron microprobe to provide scanning electron microscopy and EDS analysis to identify the quality of the bonds and to identify the reaction formed phases.

In order to obtain samples for NDE and strength tests, two sets of 2.54 cm diameter discs were also bonded at the above conditions. A 10 micron thick PVD coating had been applied to the inner 1.66 cm diameter of the one of the matching discs. The two paired sets of discs had different surface finishes. In one case, the matching discs were highly polished and had a black, mirror like finish. In the other case, the matching discs were unpolished so that they had a dull, non-reflective, grey finish. The sets of discs are shown in Figure 2. Before the discs were bonded, the surfaces and applied coatings were evaluated under an optical microscope. After bonding, these sets of joined discs were non-destructively evaluated using the methods of pulsed thermography and ultrasonic immersion. Finally, the discs were fracture tested to determine the strength of the bonds. The fracture surfaces were analyzed under an optical microscope.

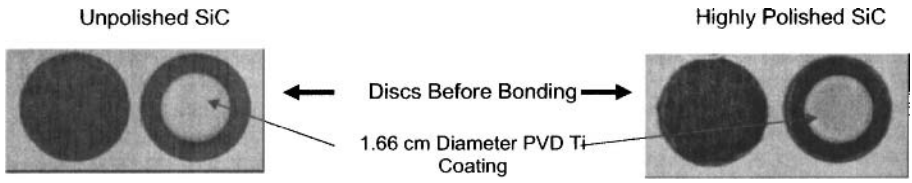

Figure 2. Photos of the coated and uncoated sets of SiC discs before bonding. The less polished discs are on the left and the more polished discs are on the right.

In another study, the effects of processing time and Ti interlayer thickness were investigated. The Ti foils were obtained from Goodfellow Corporation. The foils were placed between the SiC substrates and processing was carried out at the same conditions as above except the hold times were varied. The foil thicknesses and processing times that were investigated were 10 micron at 2 hours, 20 microns at 1, 2, and 4 hours, and 50 microns at 1, 2, 4, 8, and 16 hours. Polished cross sections of the diffusion bonds were prepared for analysis under an optical microscope. In the future, analysis with scanning electron microscopy (SEM) and electron dispersive x-ray spectrometry (EDS) will be conducted.

For a final study, a final pair of substrates (Hexoloy SiC) were bonded with a Ti foil interlayer that had a hole pattern cut out of it to simulate debonded areas. The purpose was to determine the size limitations for detecting flaws and debonds using NDE. The joined substrates were analyzed with the NDE method of ultrasonic immersion.

RESULTS AND DISCUSSION

Polished cross-sections of the diffusion bonds that were formed with the PVD Ti interlayers with thicknesses of 20 microns and 10 microns are shown in Figures 3 and 4 respectively. In both cases, the reaction formed diffusion bonds are well adhered to the SiC substrates. However microcracks were observed in the diffusion bond formed with the thicker 20 micron PVD Ti interlayer. The corresponding microprobe analysis of the reaction formed phases is given in Table I. The presence of the phase, $Ti_5Si_3C_x$ (Phase C in Figure 3 and Table I), is observed which was also one of the phases believed to contribute to microcracking when the Ti-6Al-4V alloy foil was used as an interlayer[2,3]. The $Ti_5Si_3C_x$ phase was suggested by Naka *et al.*[9] to be an intermediate phase that will not be present when the phase reactions have gone to completion. Therefore, in our approach for forming stable fully reacted diffusion bonds, the $Ti_5Si_3C_x$ phase can be avoided in the final diffusion bond by either using a Ti interlayer that is thinner than 20 microns or by processing for longer durations. This appears to be the case as seen in the bond formed from the thinner 10 micron PVD Ti interlayer. The micrograph in Figure 4 shows a well formed diffusion bond. Two phases are present as seen from the microprobe analysis in Table II. The absence of microcracking is because the detrimental phase of Ti_5Si_3 was not present. The use of a thinner interlayer while maintaining the same processing time resulted in a stable diffusion bond with no intermediate phases. The source of the dark pores in the bond still has to be determined. It may be due to the formation of more dense phases during the diffusion bonding process. The presence of the pores may not have a significant effect on the mechanical and leakage properties of the bond, since the pores are very small and isolated. Future tests and analysis will determine if the small, isolated pores have an effect on leakage through the bonds.

The two sets of discs that were bonded were analyzed by NDE followed by strength tests. The two sets of discs that were bonded had different surface finishes as shown in Figure 2. Greater detail of the discs and coatings is shown in Figure 5. The highly polished substrate has a more dense surface which allowed for a more dense PVD coating to be applied. For the less polished substrate, the applied coating is less dense. The transition between the coated and uncoated sections on this substrate was difficult to distinguish due to the rough surface. The first NDE approach that was investigated was pulsed thermography (alternately referred to as flash thermography). A description of the pulsed thermography method is illustrated in Figure 6. Since the coating was only applied to the inner 1.66 cm diameter of the 2.54 cm diameter discs, it would be expected that NDE would detect a bonded inner diameter and a non-bonded outer ring. However, pulsed thermography was not able to clearly detect these bonded and non-bonded areas as shown in the NDE results in Figure 7. The general region where bonding was presumed to have occurred was detected; however, the image was not very sharp. The results regarding the bonding quality are inconclusive due to high surface reflectivity.

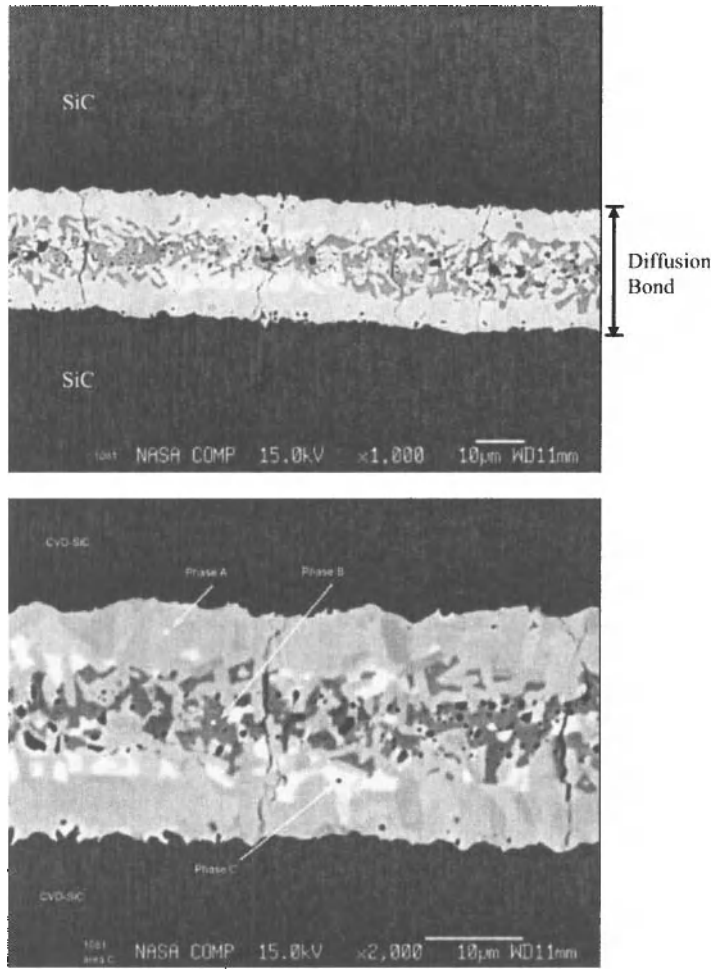

Figure 3. Diffusion bond when a 20 micron thick PVD Ti coating was used as the interlayer between the Rohm & Haas SiC substrates. The top is at a magnification of x1000 and the bottom micrograph is at a magnification of x2000. Microcracks and the presence of three phases are observed.

Table I. Microprobe analysis of the atomic ratios for the reaction formed phases in the diffusion bond as shown in Figure 3 (*atomic ratios are an average from five locations for each phase*).

Phase	Al	Fe	Ti	Si	C	Cr	Total
Phase A	0.011	0.001	56.426	17.792	25.757	0.014	100.000
Phase B	0.007	0.005	35.794	62.621	1.570	0.003	100.000
Phase C	0.027	0.153	58.767	33.891	7.140	0.023	100.000

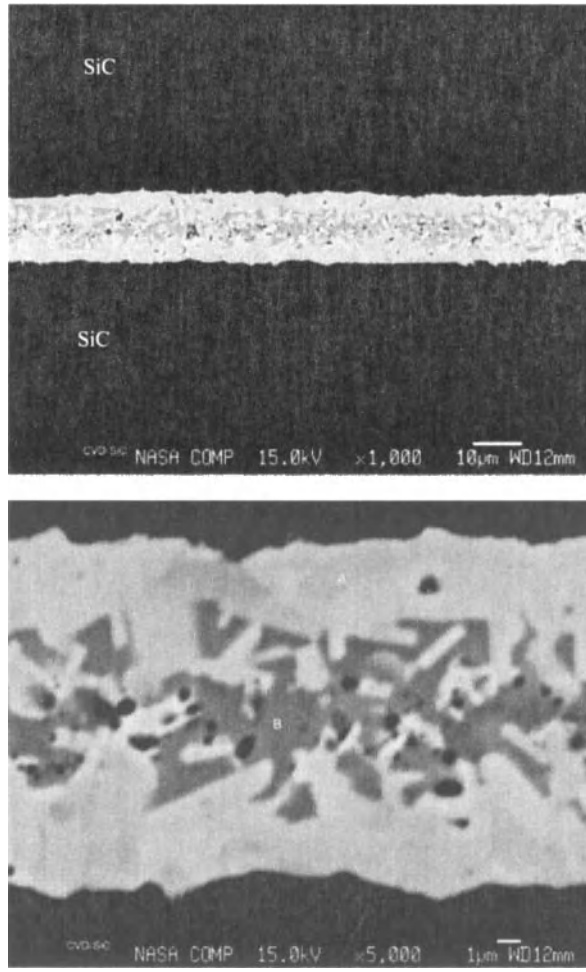

Figure 4. Diffusion bond when a 10 micron thick PVD Ti coating was used as the interlayer between the Rohm & Haas SiC substrates. The top is at a magnification of x1000 and the bottom micrograph is at a magnification of x5000. No microcracks and the presence of three phases are observed.

Table II. Microprobe analysis of the atomic ratios for the reaction formed phases in the diffusion bond as shown in Figure 4 (*atomic ratios are an average from five locations for each phase*).

Phase	C	Si	Ti	Al	Cr	Total
SiC	45.890	54.096	0.011	0.000	0.004	100.000
Phase A	24.686	18.690	56.621	-	0.003	100.000
Phase B	3.028	61.217	35.752	-	0.003	100.000

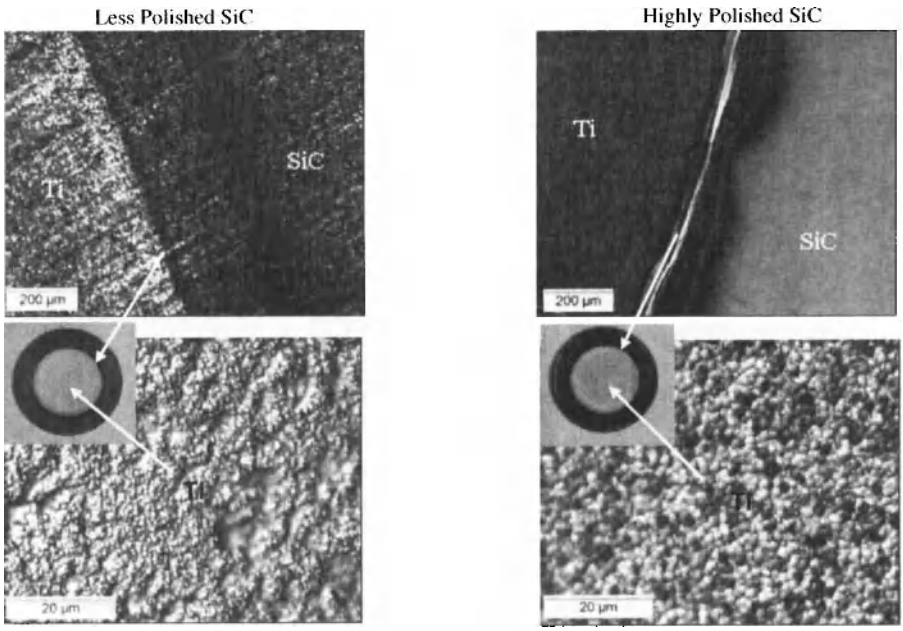

Figure 5. Optical views of the SiC substrate and PVD Ti coatings for the less polished (left) and the more polished SiC (right). Macroviews of the discs are shown for reference.

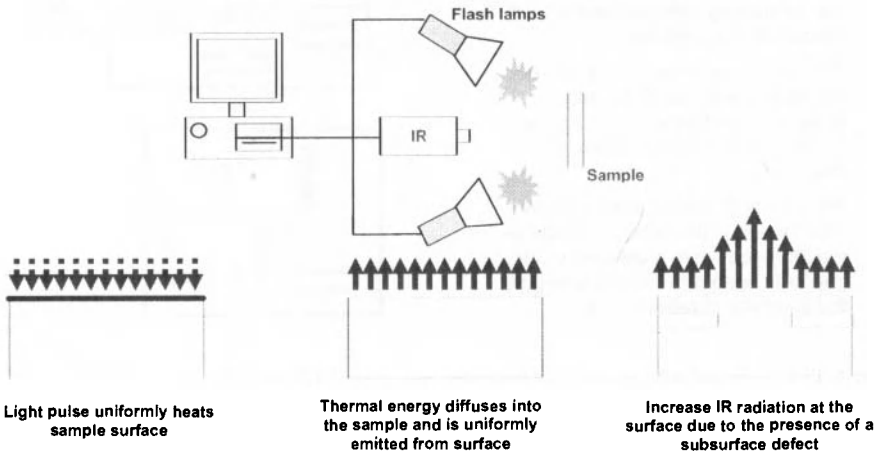

Figure 6. Illustration and description of the flash thermography NDE method.

Figure 7. Results from pulsed thermography for the less polished pair of joined substrates (left) and for the more polished pair (right).

The second method of NDE that was investigated was ultrasonic immersion. This method is illustrated and described in Figure 8. Ultrasonic immersion gave much better NDE results, as seen in Fig. 9, compared to using pulsed thermography. The inner diameter of the bonded surface and the outer ring of a non-bonded area are very clearly visible. The ultrasonic immersion results for the more polished set of substrates resulted in a sharper image than for the less polished set of substrates which appear as slightly blurred. The results suggest that the more polished substrates gave a more dense and higher quality bond.

- A high frequency ultrasonic pulse (U) enters specimen.
- Some of the signal is reflected back at the bond interface (R) while the remaining energy is transmitted (T) and eventually reflected at the back surface of the sample.
- The amount of energy reflected at the interface depends on the acoustic impedance (z) mismatch between the materials at the interface.
- Well bonded, similar materials will result in very little or no reflection at the interface while a disbond or air gap will cause more of the energy at the interface to reflect back.

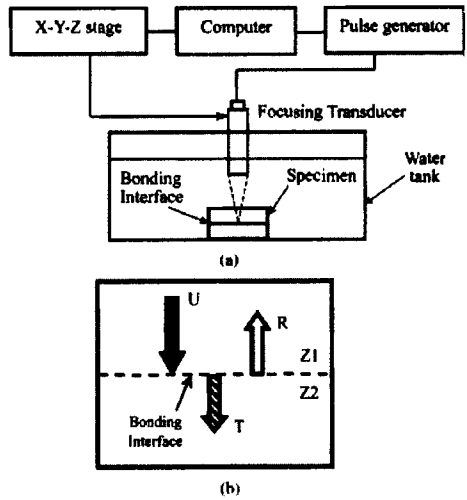

Figure 8. Illustration and description of the ultrasonic immersion NDE method.

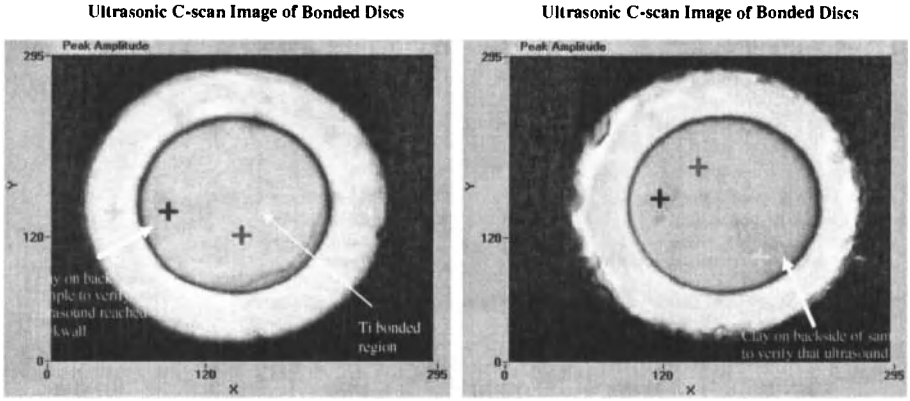

Figure 9. Results from ultrasonic immersion for the less polished pair of joined substrates (left) and for the more polished pair (right).

After completion of the NDE analysis on the two sets of joined discs, they were tensile tested and analyzed under an optical microscope. An illustration of the samples under stress is shown in Figure 10 along with the configuration for additional square samples that were previously tested. The stress versus strain curves are shown in Figure 11 for the joined discs. The less polished set of joined discs had a strength of 13.4 MPa and the more polished set had a strength of 15.0 MPa. This was lower than previous strength test of two sets of joined square SiC substrates with dimensions of 2.54 cm x 2.54 cm. The joined square substrates had strengths of greater than 23.6 MPa and 28.4 MPa. Failures occurred in the adhesives used to attach the test fixtures to the substrates. Despite the discrepancy in strengths from the two sample configurations, the strengths are much higher than those required for the application which is 3.45-6.89 MPa. The stress versus strain curves for the discs in Figure 11 show that the more polished discs had a slightly higher strength. Although the limited testing may not be able to identify a true trend in strength, the higher strength for the more polished samples could be due to such effects as stronger bonds due to the smoother finish and more dense coating or due to the more polished SiC material having fewer surface flaws. Optical micrographs of the fracture surfaces are shown in Figure 12. For the less polished set of joined discs, failure was in the SiC substrate rather than the bond. The bond was pulled out intact from the failing SiC substrate. For the more polished set of joined discs, failure was primarily in the SiC as failure started in one substrate crossed through the bond region and continued in the other SiC substrate.

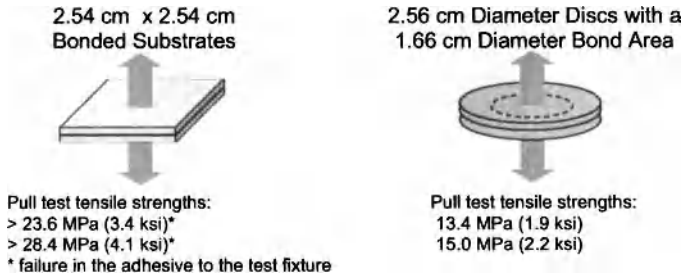

Figure 10. Illustration of the tensile tested samples and the resulting strengths.

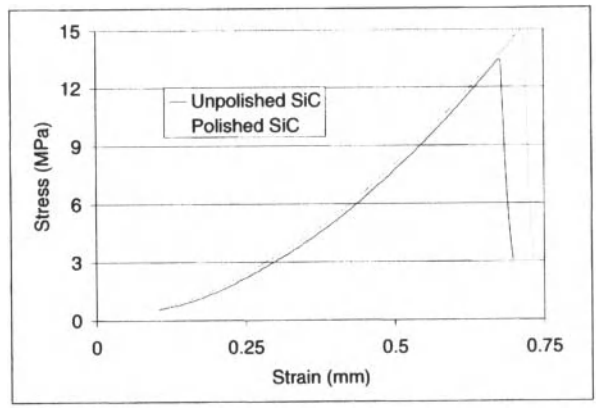

Figure 11. Stress versus strain curves for the two sets of joined discs.

The limitations of flaw identification with ultrasonic immersion were investigated through the analysis of joined Hexaloy SiC substrates that had simulated flaws and disbonds. The Ti foil interlayer had cut out shapes as shown in Figure 13a. The shapes were of circles, triangles, and squares. The widths/diameters of the shapes were 0.51 cm, 1.27 cm, 2.54 cm, and 3.81 cm. During processing of the bond, SiC bonding will only occur in regions where there is Ti. The general pattern of the flaws was distinguishable in the ultrasonic immersion results as seen in figure 13b. The simulated flaw areas appear as nonbonded regions. However, the resolution was much lower than for the bonded CVD discs that had a reduced bond area. The lower resolution is believed to be primarily due to the use of Hexaloy SiC which had three factors that could hinder good results in ultrasonic immersion. These factors are: thicker SiC substrates of 0.25" compared to the 60 mill thick CVD SiC, a lower density of 3.1 g/cm^3 vs. 3.21 g/cm^3 for the CVD SiC, and higher porosity (2-3% closed porosity) vs. no porosity for the CVD SiC.

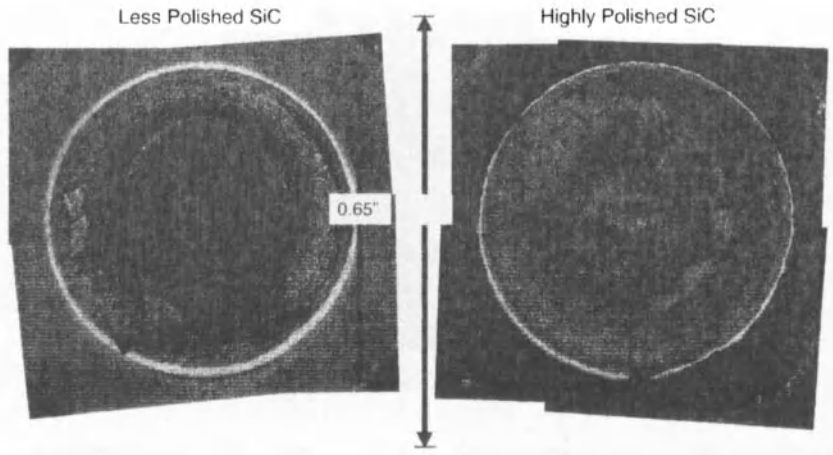

Figure 12. Optical micrographs of the failed surfaces in the tensile tested discs. Failure on the less polished set of discs is shown on the left and the failure for the more polished set of discs is on the right.

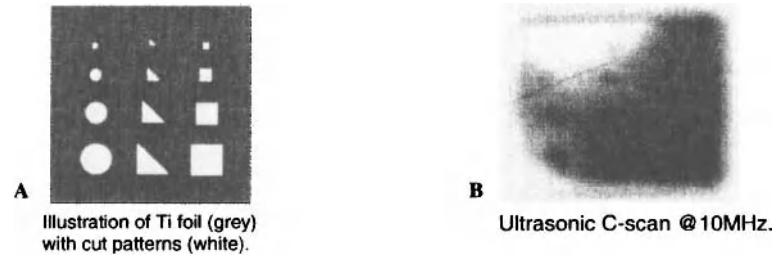

Figure 13a and 13b. Ultrasonic immersion of the bonded Hexaloy SiC with simulated flaws. An illustration of the Ti foil with cutout sections is shown in figure a. The resulting C-scan image from ultrasonic immersion is shown in figure b.

The diffusion bonds that were obtained from variations Ti interlayer thickness and diffusion bond processing times are shown in Figure 14 – 16. Figure 14 shows similar results for the diffusion bond formed from the 10 micron Ti foil at 2 hr as compared to one formed from the 10 micron PVD Ti coating at 2 hr (Figure 4). No microcracking was observed. For the 20 micron interlayer, an intermediate phase was observed in the core of the diffusion bond in the bond formed during the 2 hr hold. However the intermediate phase was not seen in the bond processed for 4 hr. For the bonds formed with the thick 50 micron Ti foil, microcracking, porosity, and the intermediate phase are observed as the processing time increased up to 16 hr. Future analysis with an SEM will further evaluate the diffusion bonds obtained in this study.

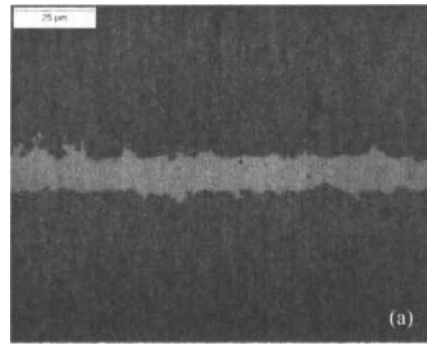

Figure 14. Optical micrograph of the SiC substrates joined with a 10 micron interlayer for 2 hr.

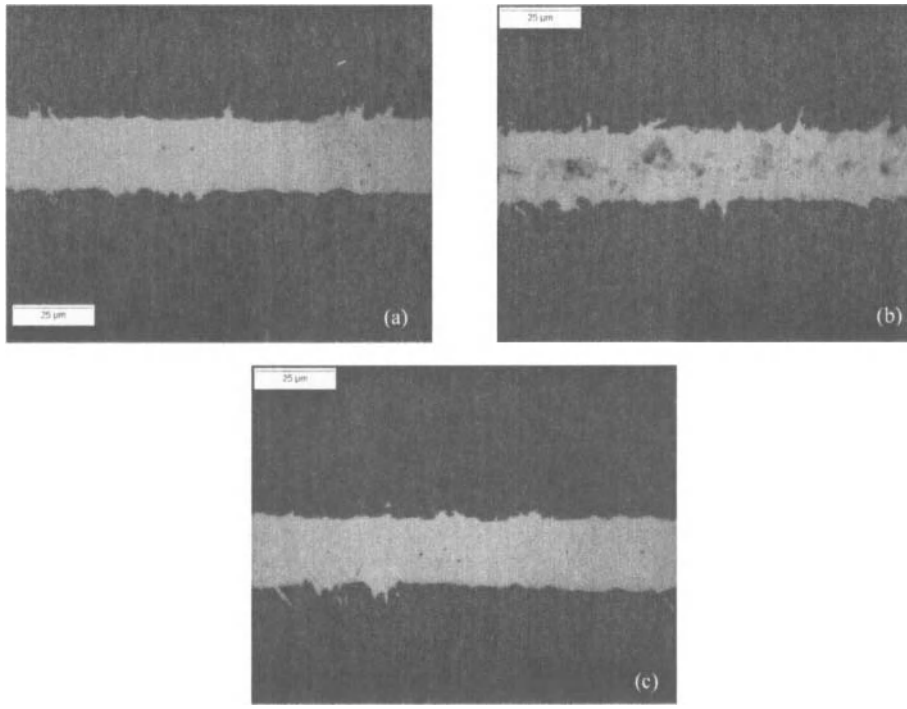

Figure 15. Optical micrographs of the SiC substrates joined with a 20 micron interlayer for 1 hr (a), a 20 micron interlayer for 2 hr (b), and a 20 micron interlayer for 4 hr (c).

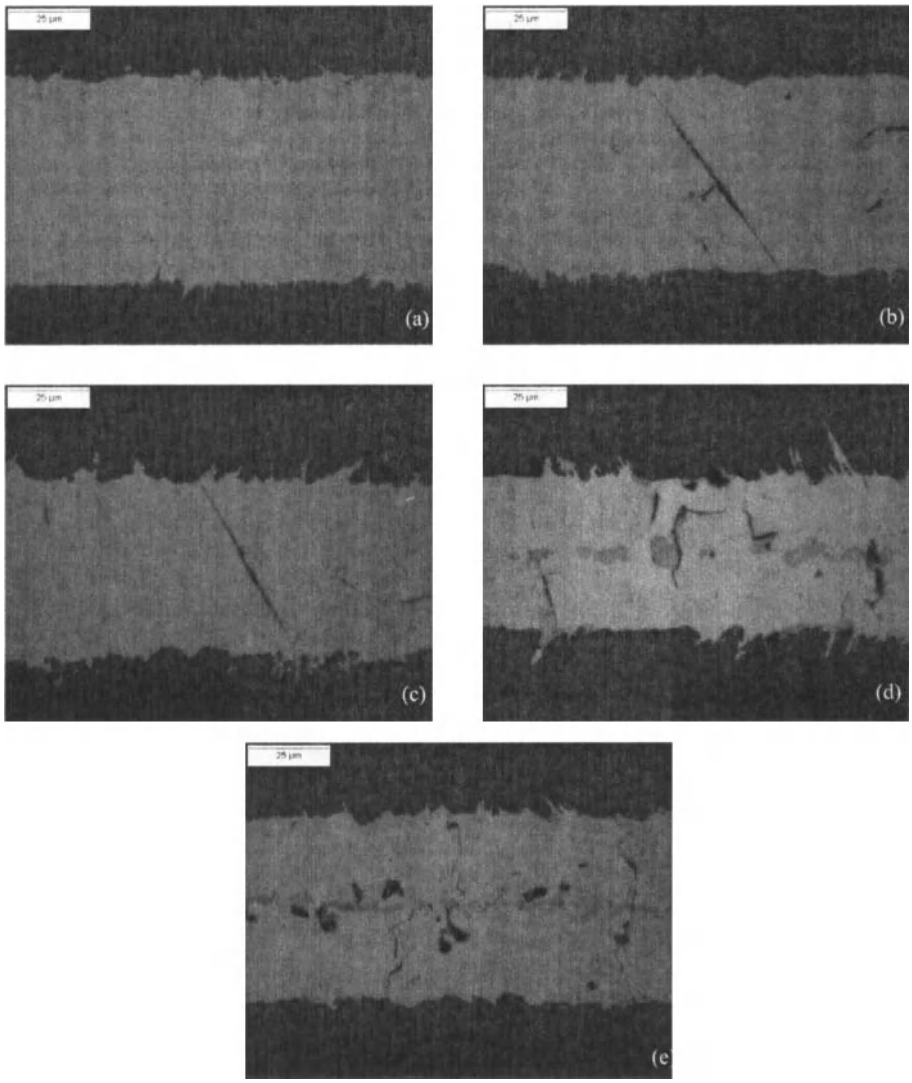

Figure 16. Optical micrographs of the SiC substrates joined with a 50 micron interlayer for 1 hr (a), a 50 micron interlayer for 2 hr (b), a 50 micron interlayer for 4 hr (c), a 50 micron interlayer for 8 hr (d), and a 50 micron interlayer for 16 hr (e).

CONCLUSIONS

A diffusion bonding approach that is well suited for fabricating a low emission ceramic injector was developed and characterized. Pure Ti interlayers were used to join SiC substrates. The resulting diffusion bonds were well adhered to the SiC substrates, with no delaminations. Microcracking was observed in some diffusion bonds due to the formation of $Ti_5Si_3C_x$ which is highly anisotropic in its thermal expansion. It was shown that microcracking could be avoided by preventing the formation of the intermediate phase of $Ti_5Si_3C_x$. The use of thin interlayers and longer processing times resulted in uniform, crack free bonds. The NDE method of ultrasonic immersion proved to be a very good method for analyzing the bond quality and for detecting small flaws and debonded areas. A polished surface finish was shown to have a positive effect on bond quality and strength compared to a more dull finish. The optimization of the processing of the diffusion bond and the resulting properties suggest that diffusion bonding is a good processing approach for fabricating complex shaped components.

ACKNOWLEDGEMENTS

This effort was supported by the NASA Glenn Research Center under the Subsonics Fixed Wing Project. The authors would like to thank James Smith for conducting microprobe analysis and Dr. Robert Okojie of NASA GRC for applying PVD Ti coatings. The authors would also like to thank Richard E. Martin and Laura M. Cosgriff of Cleveland State University for conducting NDE.

REFERENCES

1. R. Tacina, C. Wey, P. Laing, and A. Mansour, "A Low Lean Direct Injection, Multipoint Integrated Module Combustor Concept for Advanced Aircraft Gas Turbines," NASA/TM-2002-211347, April 2002.

2. M. C. Halbig, M. Singh, T. P. Shpargel, J. D. Kiser, "Diffusion Bonding of Silicon Carbide Ceramics Using Titanium Interlayers," Proceedings of the 30th International Conference & Exposition on Advanced Ceramics & Composites, Cocoa Beach, FL, Jan. 22-27, 2006.

3. M. C. Halbig, M. Singh, T. P. Shpargel, J. D. Kiser, "Diffusion Bonding of Silicon Carbide for MEMS- LDI Applications," Proceedings of the 31st International Conference & Exposition on Advanced Ceramics & Composites, Daytona Beach, FL, Jan. 21-26, 2007.

4. J. H. Schneibel, C. J. Rawn, E. A. Payzant, and C. L. Fu, "Controlling the Thermal Expansion Anisotropy of Mo_5Si_3 and Ti_5Si_3 Silicides," *Intermetallics*, **12**, 845-850 (2004).

5. J. H. Schneibel and C. J. Rawn, "Thermal Expansion Anisotropy of Ternary Silicides Based on Ti_5Si_3," *Acta Materialia*, **52**, 3843-3848 (2004).

6. L. Zhang and J. Wu, "Thermal Expansion and Elastic Moduli of the Silicide Based Intermetallic Alloys $Ti_5Si_3(X)$ and Nb_5Si_3," *Scripta Materiallia*, **38**, 2, 307-313 (1998).

7. R. Boyer, G. Welsch, E.W. Colling, Material Properties Handbook: Titanium Alloys, ASM International, Materials Park, OH, 1994, p.p. 516.

8. J. W. Elmer, T. A . Palmer, S. S. Babu, E. D. Specht, " In Situ Observations of Lattice Expansion and Transformation Rates of α and β Phases in Ti-6Al-4V," *Materials Science and Engineering A*, **391**, 2005, pp. 104-113.

9. M. Naka, J. C. Feng, and J. C. Schuster, "Phase Reaction and Diffusion Path of the SiC/Ti System," *Metallurgical and Materials Transactions A*, **24A**, 1385-1390, (1997).

Advanced Processing and Manufacturing Technologies
for Structural and Multifunctional Materials II
Edited by Tatsuki Ohji and Mrityunjay Singh

BONDING AND INTEGRATION OF C-C COMPOSITE TO Cu-CLAD-MOLYBDENUM FOR THERMAL MANAGEMENT APPLICATIONS

R. Asthana[1] and M. Singh[2]

[1]Department of Engineering and Technology
University of Wisconsin-Stout, Menomonie, WI 54751

[2]Ohio Aerospace Institute, MS 106-5, Ceramics Branch
NASA Glenn Research Center, Cleveland, OH 44135

ABSTRACT

Carbon fiber-reinforced carbon matrix composites were brazed to copper-clad molybdenum using two active Ag-Cu braze alloys, Cusil-ABA and Ticusil. The SEM and EDS examination of the brazed joints revealed good bonding and preferential precipitation of Ti at the composite/braze interface. Some tendency toward de-lamination was observed within resin-derived C-C composite due to its low inter-laminar shear strength. The inter-fiber channels between carbon fibers in the 3-D C-C composites were infiltrated with the molten braze. The Knoop hardness (HK) distribution across the joints was reproducible and revealed sharp hardness gradients at the Cu-clad-Mo/braze interface. Higher hardness was observed in Ticusil (~85-250 HK) than in Cusil-ABA (~50-150 HK), possibly due to the higher Ti content of Ticusil (4.5% Ti) than Cusil-ABA (1.75% Ti). Steady-state heat conduction calculations show that the joined assembly may have 22% lower thermal resistance compared to C-C composite of the same dimensions. This suggests that C-C/Cu-clad-Mo joints may be promising for thermal management applications.

INTRODUCTION

Carbon-carbon (C-C) composites are used in a number of advanced applications such as nose cone and leading edges of the space shuttle, rocket nozzles, exit cones, heat shield, and aircraft braking systems [1]. In addition to thermo-structural applications, C-C composites containing high-conductivity carbon fibers have also been used in thermal management applications since they provide excellent heat dissipation and low expansion properties. For example, the axial thermal conductivity (K) values of high-modulus (HM) and ultra-high modulus (UHM) carbon fibers are ~120-300 W/m.K and ~500-1100 W/m.K, respectively [1]. The conductivity of C-C composites is, however, anisotropic and varies considerably; for example, for 2D and 3D composites, $K_{C\text{-}C}$ = 60 and 190 W/m-K perpendicular and parallel to the carbon cloth at 500K [1]. The coefficient of thermal expansion (CTE) of C-C composites is quite low (~$2.0\text{-}4.0\times10^{-6}$/K over 20-2500°C [1]), indicating considerable thermal stability of C-C composite structures in elevated-temperature applications.

Thermal management applications typically require materials possessing high thermal conductivity and low CTE. Currently, a number of thermal management applications utilize copper-clad-molybdenum because of its high conductivity (~214 W/m.K at 25% Cu [2]) and relatively low CTE (~$7.5\text{x}10^{-6}$/K [2]). To realize the high conductivity and low expansion benefits in heat sink components, graphite [3] and more recently, C-C composites [4] have been joined to copper-clad-molybdenum. Acting in combination at a joint, Cu-clad Mo and C-C composite can provide excellent heat dissipation capability at reduced weight compared to the heavier Cu-clad Mo acting in isolation. In addition, a moderate difference in the CTE of C-C and Cu-clad Mo, and the high ductility provided

by copper cladding on Mo shall be beneficial for accommodating residual stresses during temperature excursions.

In a recent study [4], we had brazed resin-derived C-C composites containing T300 C fibers to Cu-clad-Mo using four active brazes: Cu-ABA, Ticuni, Ticusil and Cusin-1 ABA. In the present work, we report the brazing and joint characterization of 3D C-C composites with resin+CVI carbon matrices to Cu-clad-Mo using two Ti-containing Ag-Cu active braze alloys (Ticusil and Cusil-ABA). These alloys have thermal conductivity either higher than or comparable to the conductivity of braze alloys used in [4]. For example, the thermal conductivity of Cusil-ABA (180 W/m.K) is better than that of Cu-ABA (38 W/m.K) and Cusin-1 ABA (170 W/m.K) used in our earlier work. In addition, the ductility of Cusil-ABA (42%) is better than the ductility of Cusin-1 ABA (22%) and comparable to Cu-ABA (42%).

In the present study, C-C composites were vacuum brazed to Cu-clad-Mo using Cusil-ABA (1.75% Ti) and Ticusil (4.5% Ti). Copper as a cladding on Mo and as an alloying additive in braze is expected to promote the wetting and metallurgical bonding. A limited number of runs were made with 2-D resin-derived C-C composites to generate comparative base-line data on joining response. The brazed joints were characterized using optical microscopy, field emission scanning electron microscopy (FESEM), energy dispersive spectrometry (EDS), and by microhardness measurements.

EXPERIMENTAL PROCEDURE

The 3-D carbon-carbon composites were obtained from Goodrich Corp., Santa Fe, CA. The composite substrates were sectioned along two orthogonal directions to expose fiber plies with different fiber arrangements; thus, two sets of composite samples were used for joining: those with oriented fibers at the exposed C-C surface and those with random (non-oriented) fibers at the exposed surface. Some joints were made of 2-D C-C composites with T-300 fibers in a resin-derived matrix, which were obtained from Carbon-Carbon Advanced Technology (C-CAT Composites) Inc., Fort Worth, TX. Copper-clad Molybdenum (Cu-Mo-Cu) plates from H.C. Starck, Inc., Newton, MA, were used as the metal substrate. The Cu-to-Mo-to-Cu layer thickness ratio was 13%-74%-13%. The material combines the high conductivity of Cu with the CTE of Mo; the CTE of the material is tailored by changing the clad ratio of Cu-Mo-Cu. The commercial brazes, Cusil-ABA and Ticusil, were in powder form and obtained from Morgan Advanced Ceramics, Hayward, CA. The compositions, liquidus and solidus temperatures, and selected physical and mechanical properties of the braze alloys are given in Table I.

The composite panels and Cu-clad Mo plates were sliced into 2.54 cm x 1.25 cm x 0.25 cm pieces. All materials were ultrasonically cleaned in acetone for 15 min. prior to brazing. The braze powders were mixed with glycerin to create a thick paste with dough-like consistency, and applied manually to the C-C surface using a spatula. The Cu-clad-Mo plate was laid over the braze layer and a

Table 1. Composition and Selected Properties of Brazes used

Braze (composition, %)	T_L, °C	T_S, °C	E, GPa	YS, MPa	UTS, MPa	CTE, $\times 10^{-6}$ C^{-1}	% El.	K, W/m.K
Cusil-ABA® (63Ag-35.3Cu-1.75Ti)	815	780	83	271	346	18.5	42	180
Ticusil® (68.8Ag-26.7Cu-4.5Ti)	900	780	85	292	339	18.5	28	219

E: Young's modulus, YS: yield strength, UTS: tensile strength, CTE: coefficient of thermal expansion, %El: percent elongation, K: thermal conductivity. Cusil-ABA® and Ticusil® are active braze alloys from Morgan Advanced Ceramics, Hayward, CA.

load of 0.30-0.4 N was applied to the assembly. The assembly was placed in a vacuum furnace with the composite on top and Cu-clad-Mo at the bottom. The samples were heated to the brazing temperature (15-20 °C above the braze liquidus) under vacuum (~10^{-6} torr), isothermally held for 5 min. at the brazing temperature, then slowly cooled (~5°C per min.) to 400°C followed by furnace cooling to room temperature.

The brazed joints were mounted in epoxy, ground and polished, and examined using optical microscopy, and Field Emission Scanning Electron Microscopy (FESEM) (model: Hitachi 4700) coupled with energy dispersive x-ray spectroscopy (EDS). Microhardness scans were made with a Knoop indenter across the joint interfaces on a Struers Duramin-A300 machine under a load of 200 g and loading time of 10 s. To check the reproducibility of the hardness profiles, 4 to 6 hardness scans were made across each joint.

RESULTS AND DISCUSSION

The microstructures of the composite/braze interface and braze/Cu-clad-Mo interface in Cu clad Mo/C-C composite joints are shown in Fig. 1. Both Cusil-ABA and Ticusil have infiltrated the inter-

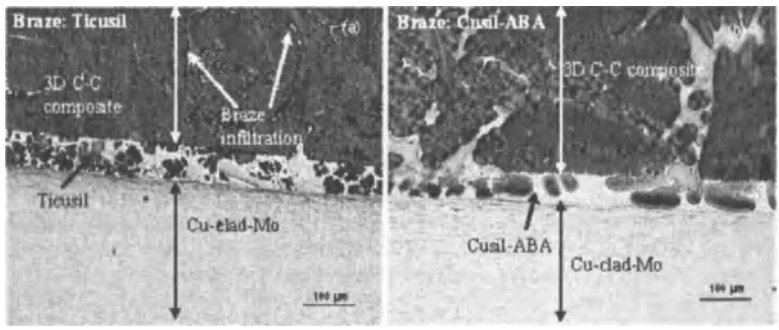

Fig. 1 A 3-D C-C composite joined to Cu-clad-Mo using (a) Ticusil and (b) Cusil-ABA. Large-scale infiltration of inter-fiber channels by molten brazes, and dissolution of Cu cladding have occurred.

fiber regions in the 3-D C-C composite to several hundred micrometer distance in just 5 min. of contact. There was no effect of fiber ply orientation at the mating surface on the extent of infiltration. The reaction of carbon with Ti in the braze forms the wettable compound titanium carbide [5] which facilitates self-infiltration. The large infiltration distance achieved is significant because the carbide forming reactions did not choke the metal flow or limit the extent of braze infiltration. The TiC reaction layer that forms via the reaction Ti + C → TiC is known to be discontinuous with a non-homogenous structure [6]; this permits extensive infiltration of porous carbon. Our observations of extensive infiltration of Ti-bearing Ag-Cu braze alloys in the C-C composites are consistent with the sessile-drop wettability test results [7] on Cu-Ti/carbon system. It was reported in [7] that the sessile drop volume continuously decreased due to the reactive infiltration of open porosity in graphite; in fact, sessile drops of high Ti content (e.g., Cu-28Ti) rapidly and completely disappeared into the graphite substrate.

Joint Microstructure and Composition

Figures 2 through 6 show the SEM views of the joint microstructure of C-C composite with Cu-clad-Mo. All joints display intimate physical contact, and the joints and the braze matrix are free of

common structural imperfections. The orientation of the carbon fiber ply at the joint interface had no influence either on the infiltration distance or the microstructure of the joint.

The EDS elemental compositions at the composite/braze and braze/Cu-clad-Mo interfaces are shown in Tables 2 through 9. Only relative atomic percentages among the alloying elements are provided. There is minimal diffusion of Ag, Mo and Ti in the composite matrix. The braze matrix exhibits a two-phase eutectic structure with Ag-rich light-grey areas (point 3, Fig. 2) and Cu-rich dark areas (point 4, Fig. 2). In the Ag-Cu-Ti system, intermetallics such as AgTi, Ti_2Cu_3, and $TiCu_2$ may also form. A higher titanium concentration is observed at the composite/braze interface (e.g., point 2 in Fig. 2b & 3b) than in the nearby regions of the joints. The preferential segregation of Ti at the composite/braze interface is due to the high chemical affinity of Ti toward C, which promotes the formation of the TiC and possibly also wettable sub-stoichiometric carbides such as $TiC_{0.95}$, $TiC_{0.91}$.

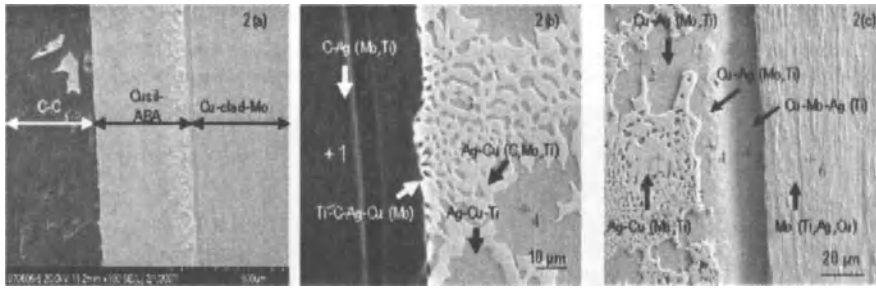

Fig. 2. A 3-D C-C (oriented fibers) composite/Cusil ABA/Cu-clad-Mo joint showing (a) overall view of the joint, (b) C-C/Cusil-ABA interface, and (c) Cusil-ABA/Cu-clad-Mo interface. The EDS analyses for points marked in (b) and (c) are given in Tables 2 and 3, respectively.

Table 2. Relative Atomic Percentages of Elements (Fig. 2b)

Location	C	Ti	Cu	Mo	Ag
Point 1	96.468	0.693	0.000	0.723	2.116
Point 2	35.131	49.912	5.203	0.941	8.813
Point 3	0.675	0.328	3.881	0.281	94.835
Point 4	0.000	2.437	89.469	0.000	8.094

Table 3. Relative Atomic Percentages of Elements (Fig. 2c)

Location	Ti	Cu	Mo	Ag
Point 1	0.339	3.838	0.250	95.573
Point 2	0.801	87.267	1.159	10.773
Point 3	10.733	12.685	1.354	75.228
Point 4	1.346	86.443	1.361	10.850
Point 5	0.826	96.051	2.077	1.046
Point 6	1.155	0.515	97.672	0.658

$TiC_{0.80}$, $TiC_{0.70}$, $TiC_{0.60}$ and $TiC_{0.48}$. The Gibb's free energy change for TiC formation via Ti+C→ TiC at a brazing temperature of 850° C is -171.18 kJ, which strongly favors TiC formation. Phase diagram considerations show that at the brazing temperature used, the Ag-Cu-Ti alloy forms a Ti-impoverished liquid phase and a Ti-rich liquid phase. It is conceivable that the Ti-rich liquid reacts with the carbon to form the carbides. Besides forming carbides, Ti could react with minute amounts of residual oxygen in the furnace atmosphere (or in the surface scale on C-clad-Mo) leading to oxy-carbides and oxides such as the wettability-enhancing, metal-like compound TiO, which is known to form an interfacial layer on carbon in the Cu-Ti-O system.

The Cusil-ABA/Cu-clad-Mo interface (Fig. 3c) displays evidence of good wetting and somewhat diffuse interface character. The light-grey (Ag-rich) and dark (Cu-rich) eutectic micro-constituents are distributed within the braze region. The Cu cladding at the braze/Cu-clad-Mo interface appears to be intact because the joining temperature (830°C) is below the melting point of Cu (1086°C); this is further confirmed by a lack of any conceivable microstructural signature of solidification in the clad layer. Some chemical dissolution has probably occurred at the Cu-cladding/braze interface. Small amounts of Ag and Cu from braze are detected within the C-C composite region (point 1, Fig. 3b) but no measurable quantity of Mo is noted. The C-C/Cusil-ABA interface is rich in titanium and the Ti concentration decreases rather systematically with increasing distance from the interface (9.2 atom%, 4.2 atom% and 1.8 atom% at points 2, 4 and 5, respectively, in Fig. 3b). In C-C/Cu-clad-Mo joints made using Ticusil (Fig. 4), a small amount of Cu is detected within the composite region (points 5 and 6, Fig. 4b). The normal two-phase eutectic structure with a characteristic acicular morphology (Fig. 4b & c) is observed within the braze region. Some carbon has dissolved in the molten braze, possibly because of the higher brazing temperature (915°C) of Ticusil which led to C diffusion in the eutectic micro-constituents (points 1 and 2, Fig. 4b). In addition, carbon is detected within the Cu-clad-Mo region (points 3-6, Fig. 4c). Finally, as stated in a preceding paragraph, oxygen (from the copper oxide scale on Cu-clad-Mo) could also be playing a role. Upon contact with the molten braze, the scale will dissociate and dissolve, yielding an oxygen-rich braze layer. As a result, besides carbides, oxides such as TiO and TiO_2 may also form at the C-C/metal joint because stable oxides of Ti can form at very low oxygen partial pressures.

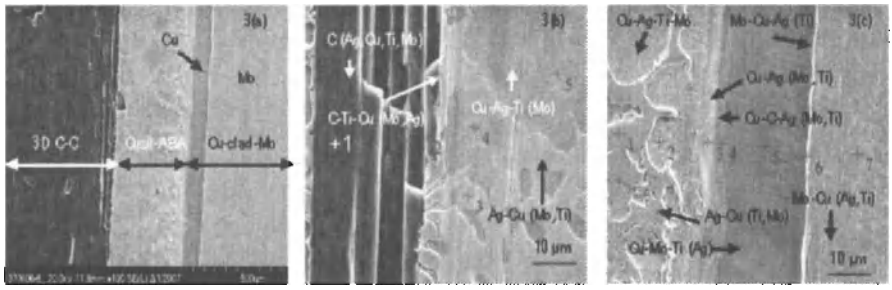

Fig. 3 A 3-D C-C (non-oriented fibers) composite/Cusil-ABA/Cu-clad-Mo joint showing (a) overall view of the joint, (b) C-C/Cusil-ABA interface, and (c) Cusil-ABA/Cu-clad-Mo interface. The EDS analyses for points marked in (b) and (c) are given in Tables 4 and 5, respectively.

Table 4. Relative Atomic Percentages of Elements (Fig. 3(b))

Location	C	Ti	Cu	Mo	Ag
Point 1	93.479	0.722	2.144	0.616	3.039
Point 2	85.396	9.160	3.100	0.805	1.538
Point 3	0.000	0.566	3.909	0.532	94.994
Point 4	0.000	4.161	87.138	0.261	8.441
Point 5	0.000	1.755	88.985	0.000	9.260

Table 5. Relative Atomic Percentages of Elements (Fig. 3(c))

Location	Ti	Cu	Mo	Ag
Point 1	1.000	4.661	0.275	94.063
Point 2	4.702	86.588	1.833	6.878
Point 3	1.557	94.313	1.937	2.192
Point 4	0.252	91.198	0.554	1.271
Point 5	1.312	96.747	1.790	0.151
Point 6	0.624	7.868	88.846	2.662
Point 7	0.439	1.177	97.438	0.946

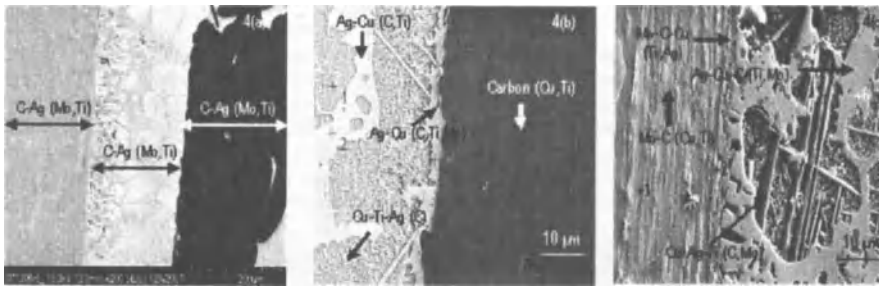

Fig. 4 A 3-D C-C (non-oriented fibers) composite/Ticusil/Cu-clad-Mo joint showing (a) overall view of the joint, (b) C-C/Ticusil interface, and (c) Ticusil/Cu-clad-Mo interface. The EDS analyses for points marked in (b) and (c) are given in Tables 6 and 7, respectively.

Table 6. Relative Atomic Percentages of Elements (Fig. 4b)

Location	C	Ti	Cu	Mo	Ag
Point 1	5.345	8.090	81.097	0.314	5.154
Point 2	2.097	0.228	4.540	0.508	92.627
Point 3	0.000	10.084	75.623	0.236	14.057
Point 4	1.852	0.368	3.776	0.382	93.623
Point 5	98.060	0.264	1.183	0.231	0.262
Point 6	26.237	54.484	16.697	0.553	2.030

Table 7. Relative Atomic Percentages of Elements (Fig. 4c)

Location	C	Ti	Cu	Mo	Ag
Point 1	7.679	0.178	0.446	91.603	0.094
Point 2	14.986	0.227	4.036	80.515	0.235
Point 3	4.616	10.537	65.709	0.379	18.760
Point 4	5.039	42.850	50.659	0.398	1.054
Point 5	3.482	10.474	52.933	0.310	32.801
Point 6	2.330	0.167	1.981	0.212	95.310

Figure 5 shows joint interfaces between resin-derived C-C composite (C-CAT Composites) and Cu-clad-Mo made using Ticusil. Microstructurally sound joints have formed but there is some cracking within the C-C composite (Fig. 5a) presumably due to the low inter-laminar shear strength of C-C composites. Ag- and Cu-rich phases have formed in the braze matrix with the Ag-rich phase preferentially precipitating onto both C-C surface (point 2, Fig. 5b) and Cu-clad-Mo surface (point 2, Fig. 6c). A small amount of Cu is detected within the composite (point 4, Fig. 5b).

In summary, whereas extensive chemical interactions did not occur and observable interfacial reaction layers did not form at the C-C/CuAgTi interfaces, limited redistribution of alloying elements appears to have occurred. Large titanium concentrations occur at the C-C/braze interface, indicating favorable surface modification due presumably to a carbide-forming reaction that promoted bonding.

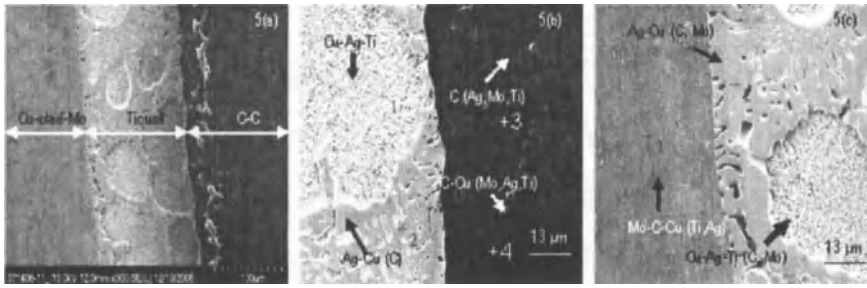

Fig. 5 A C-C (resin-derived) composite/Ticusil/Cu-clad-Mo joint showing (a) overall view of the joint, (b) C-C/Ticusil interface, and (c) Ticusil/Cu-clad-Mo interface. The EDS analyses for points marked in (b) and (c) are given in Tables 8 and 9, respectively.

Table 8. Relative Atomic Percentages of Elements (Fig. 5(b))

Location	C	Ti	Cu	Mo	Ag
Point 1	0.799	6.603	77.559	0.422	14.617
Point 2	2.198	0.495	9.874	0.460	86.973
Point 3	99.472	0.112	0.000	0.198	0.218
Point 4	78.303	0.527	18.766	1.136	1.268

Table 9. Relative Atomic Percentages of Elements (Fig. 5(c))

Location	C	Ti	Cu	Mo	Ag
Point 1	7.464	0.363	3.304	88.645	0.223
Point 2	1.171	0.264	8.930	0.498	89.138
Point 3	2.027	8.504	73.068	0.365	16.036
Point 4	0.000	0.058	6.198	0.657	93.087

Microhardness

Knoop microhardness (HK) profiles across the joints made using Cusil-ABA and Ticusil are shown in Fig. 6. Fiber ply orientation did not affect the HK distribution either within the Cu-clad Mo region or within the braze. There was no effect of the composite type (CVI *vs* resin-derived) on the HK values within the braze region. The hardness of the Mo substrate is ~200-330 HK and the hardness of braze depends on braze type; Ticusil (Fig. 6a, b & d) exhibits a higher hardness (~85-200 HK) than Cusil-ABA (~50-150 HK). This is consistent with the somewhat greater Ti-induced hardening expected in Ticusil (4.5%Ti) than in Cusil-ABA (1.75%Ti), and with the somewhat larger residual stresses expected with Ticusil because of its higher liquidus temperature (T_L ~ 920°C) than with Cusil-ABA (T_L ~ 815°C). Additionally, residual stresses due to CTE mismatch also possibly influenced hardness values.

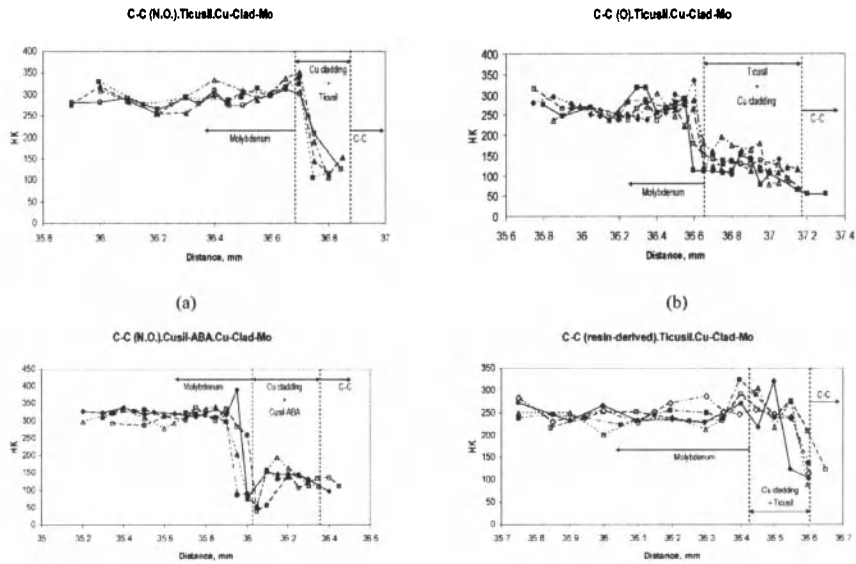

Fig. 6. Knoop hardness (HK) distribution across joints: (a) & (b) C-C/Ticusil/Cu-clad-Mo joint with (a) non-oriented C fibers at the mating surface and (b) oriented C fibers at the mating surface; (c) C-C/Cusil-ABA/Cu-clad-Mo joint with non-oriented fibers at the mating surface, and (d) resin-derived C-C composite/Ticusil/Cu-clad-Mo joint.

Residual Stress at the Joint

Upon cooling the brazed joint, large residual stresses arising from CTE mismatch may lower the fracture strength. For the C-C/Cu-clad-Mo joints, the CTE (α) of Cu-clad Mo is ~5.7×10^{-6}/K and the CTE of C-C composites is ~$2.0\text{-}4.0\times10^{-6}$/K over 20-2500°C. The CTE mismatch ($\Delta\alpha$) between C-C and Cu-clad Mo is, therefore, moderate, and the thermoelastic stresses may possibly be accommodated without leading to joint failure. However, the CTE of the metallic braze alloys used in our study is very large (18.5×10^{-6}/K, Table 1) which shall give rise to large elastic thermal strain, $\Delta\alpha\Delta T$ ($\Delta\alpha$: CTE mismatch, ΔT: temperature interval). It is, therefore, important to consider the simultaneous effect of braze plasticity and CTE mismatch between the three materials.

A model due to Eager and coworkers [8,9] analyzes residual stress relief by metal interlayers taking into account the CTE mismatch and interlayer plasticity. Their models permit estimation of the strain energy in the ceramic for well-bonded ceramic-metal joints. For a small CTE mismatch between the ceramic (C) and the metal substrate (M), but with a large CTE mismatch between the ductile interlayer (I) and the base materials, which is true of our joints, the elastic strain energy, U_{eC}, in the non-metallic substrate is approximated to a good accuracy by [9]

$$U_{eC} = \frac{\sigma^2_{YI}.\Phi.r^3}{E_C}(0.26\Pi_I + 0.54) \qquad .....[1]$$

where

$$\Phi = 1 - \left(\frac{\alpha_M - \alpha_I}{\alpha_C - \alpha_I}\right)^m \qquad .....[2]$$

and

$$\Pi_I = \frac{(\alpha_M - \alpha_C)\Delta T E_I}{\sigma_{YI}} \qquad .....[3]$$

Here, σ_{YI} is the yield strength of the interlayer, r is the radial distance from the center of the joint, E_C and E_I are the elastic modulus of the ceramic and the interlayer, respectively, ΔT is the temperature change, and α is the CTE of the subscripted phases (M, C, and I). The exponent m=1 for $\alpha_I > (\alpha_M + \alpha_C)/2$, and m=—1 for $\alpha_I < (\alpha_M + \alpha_C)/2$.

The parameters Π_I and Φ in the above equations are dimensionless quantities. The parameter Π_I is the ratio of the thermal residual strain at the interface to the yield strain of the braze interlayer; the smaller Π_I is, the larger the portion of the interface that remains elastic. The parameter Φ specifies the relative difference in CTE's between the ceramic (C), braze interlayer (I), and metal substrate (M), and it quantifies the uniformity and symmetry of the residual stress distribution in the interlayer [9]. As Φ approaches zero, the stress distribution in the interlayer becomes more symmetric, which in turn, causes a larger volume of the braze to deform plastically and lower the strain energy in the ceramic, thus reducing the probability of failure from residual stresses.

The strain energy in the C-C/ Ticusil/Cu-clad-Mo joints was computed using the following data: $\alpha_M = 5.7\times10^{-6}$/K, $\alpha_I = 18.5\times10^{-6}$/K (Table 1), $\alpha_C = 3\times10^{-6}$/K (average CTE for C-C composite) [http://www.composites-by-design.com/carbon-carbon.htm], m = 1 for C-C/Ticusil/Cu-clad-Mo joint, E_C = 70 GPa, E_I = 85 GPa (Table 1), ΔT = 887°C, and σ_{YI} = 292 MPa (Table 1). These values yield $U_{eC} = 152.98\times10^3.r^3$ where r is the radial distance in meters. The configuration analyzed by Eager et al [9] is a cylindrical disc-shaped joint whereas out joints are rectangular in cross-section (2.54 cm × 1.25 cm). For calculation purpose, we take an effective radius to be the minimum distance to the edge of our samples (0.625 cm). This yields the elastic strain energy in the composite as 37.4 mJ, which is of the same order as the U_{eC} (~ 18-74 mJ) of a number of ceramic-metal joints analyzed by Eager et al

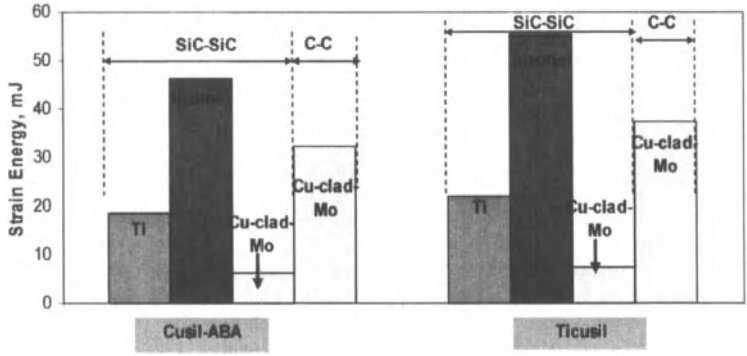

Fig. 7. Estimates of strain energy in some composite-to-metal joints based on a model due to Eager and coworkers [9].

[8,9]. Figure 7 shows the calculated values of the strain energy for some composite-to-metal joints for Cusil-ABA and Ticusil braze alloys based on Eager et al's model [9]. Less strain energy develops in Cusil-ABA joints than in Ticusil joints, and lower strain energy is obtained in SiC-SiC/Cu-clad-Mo joints than in C-C/Cu-clad-Mo joints. Considering the fact that the model strictly applies to a cylindrical joint configuration and monolithic ceramics rather than anisotropic materials such as C-C composites, and the fact that chemical interactions and solute segregation will irrevocably and unpredictably modulate the joint properties, the calculated strain energy values are considered to be reasonable. The relatively large amount of porosity in our C-C composites that was impregnated by the ductile braze during joint fabrication shall possibly provide some strain relief.

Thermal Conduction in Brazed Joints

Because C-C/Cu-clad-Mo joints are being proposed for thermal management applications, considerations of heat transport via thermal conduction are important. For 1-D steady-state heat conduction, the joined materials form a series thermal circuit with an effective thermal resistance, $R_{eff} = \Sigma(\Delta x_i/K_i)$, where Δx_i and K_i are the thickness and thermal conductivity, respectively, of the i^{th} layer. For our joints, $\Delta x_{C\text{-}C} = \Delta x_{Cu\text{-}Mo} = 0.25\times10^{-2}$ m, $\Delta x_{Ticusil} \sim 100\times10^{-6}$ m, $K_{Cu\text{-}Mo} = 214$ W/m-K [2], and $K_{Ticusil} = 219$ W/m-K (Table 1). For C-C composites, even though $K_{C\text{-}C}$ is anisotropic and variable, we take an average as 125 W/m-K for 2D and 3D composites. The effective thermal resistance of our joint assembly is obtained as 31.7×10^{-6} m^2.K/W. This value should be compared to the thermal resistance of a C-C block of the same total thickness (5.1×10^{-3} m) as the joined materials; the thermal resistance of the C-C block is 40.8×10^{-6} m^2.K/W, which is 22% higher than the resistance of the joined assembly. Thus, C-C/Cu-clad-Mo joints have better thermal conduction property than just the monolithic C-C composite. The only concern would be that the gains in conductivity shall be achieved at 39% penalty on the weight of the assembly; this shall not, however, be a concern in stationary parts. The Rule-of-Mixtures (ROM) density (ρ) of our joint assembly is ~5,878 $kg.m^{-3}$ compared to 9,700 $kg.m^{-3}$ for Cu-clad-Mo alone ($\rho_{C\text{-}C}$ = 1,900 $kg.m^{-3}$) (ignoring the thin braze interlayer does not introduce any sensible error in the density calculations).

The above considerations illustrate the potential benefits of joining C-C to Cu-clad-Mo to create thermal management systems. Even with the lower conductivity Cusil-ABA interlayer ($K_{Cusil\text{-}}$

$_{ABA}$ = 180 W/m-K) between C-C and Cu-clad-Mo, calculations analogous to the preceding case show that there will be less than 1% difference with respect to the above projections for Ticusil because of the minute thickness of the braze interlayer. There is, therefore, considerable flexibility in selecting brazes to satisfy criteria such as ductility and wetting characteristics without impairing the thermal conductivity of the joined materials.

CONCLUSIONS

Brazed joints of carbon-carbon composites to copper-clad molybdenum using two Ti-containing active braze alloys (Cusil-ABA and Ticusil) led to large-scale braze penetration of the inter-fiber spaces in the porous CVI C-C composites, good interfacial bonding, and some segregation of Ti at the composite/braze interface. The distribution of microhardness across the joints was reproducible and led to sharp gradients at the Cu-clad-Mo/braze interface. The sound composite joints produced and the projected benefits of reduced thermal stress and thermal resistance, suggest that C-C composite/Cu-clad-Mo joints may be considered for potential thermal management applications.

ACKNOWLEDGEMENT: Technical assistance of T.P. Shpargel is thankfully acknowledged. R. Asthana gratefully acknowledges the research support received from the NASA Glenn Research Center, Cleveland, OH.

REFERENCES

[1]R. Taylor, Carbon Matrix Composites, in: *Comprehensive Composite Materials*, Elsevier Science Ltd., Boston, **4**, 387-426 (2000).
[2]C.A. Harper, *Electronic Materials and Processes Handbook*, McGraw-Hill, 2003.
[3]S.A. McKeown, R.D. LeVasseur, 'High performance heat sink for surface mount applications', CH 3030-4/91/0000-0153, IEEE, 153-157 (1991).
[4]M. Singh, R. Asthana, and T.P. Shpargel, Brazing of C-C Composites to Cu-clad Mo for Thermal Management Applications, *Mater. Sci. Eng. A.* **452-453**, 699-704 (2007).
[5]N. Eustathopoulos, M.G. Nicholas, and B. Drevet, *Wettability at High Temperatures*, Pergamon, Boston, 281-282 (1999).
[6]N. Sobczak, J. Sobczak, M. Ksiazek, W. Radziwill and J. Morgiel, in *Proc. 2nd Int. Conf. on High-Temp. Capillarity*, Eustathopoulos and Sobczak (eds.), Foundry Research Institute (Krakow), 97-98 (1997).
[7]N. Sobczak, J. Sobczak, P. Rohatgi, M. Ksiazek, W. Radziwill and J. Morgiel, in *Proc. Int. Conf. High-Temperature Capillarity*, 1997, Krakow (Poland), eds. N. Eustathopoulos and N. Sobczak, Foundry Research Inst., 145-151 (1997).
[8]J. -W. Park, P. F. Mendez and T. W. Eagar, Strain Energy Distribution in Ceramic-to-Metal Joints, *Acta Mater.*, **50(5)**, 883-899 (2002).
[9]J. -W. Park, P. F. Mendez and T.W. Eagar, Strain Energy Release in Ceramic-to-Metal Joints by Ductile Metal Interlayers, *Scripta Mater.*, **53(7)**, 857-861 (2005).

Advanced Processing and Manufacturing Technologies for Structural and Multifunctional Materials II
Edited by Tatsuki Ohji and Mrityunjay Singh

POLYMER IMPREGNATION AND PYROLYSIS PROCESS COMBINED WITH POWDER SPACE HOLDER TECHNIQUE (PSH-PIP)

Masaki KOTANI
Japan Aerospace Exploration Agency (JAXA)
6-13-1 Osawa, Mitaka, Tokyo 181-0015, Japan

Aline ZIMMER
University of Stuttgart
Pfaffenwaldring 31, 70569 Stuttgart, Germany

Satoru MATSUZAKI
Taisei Kogyo Co. Ltd.
26-1 Ikeda-kita, Neyagawa, Osaka 572-0073, Japan

Kazuaki NISHIYABU
Osaka Prefectural College of Technology
26-12 Saiwai, Neyagawa, Osaka 572-8572, Japan

ABSTRACT

As a promising approach to improve the matrix microstructure of SiC fiber reinforced SiC matrix composite, a new polymer impregnation and pyrolysis process which is combined with powder space holder technique has been developed. PSH was employed for making porous structure in a matrix at the first PIP processing. It potentially contributes to efficient gas purge and uniform shrinkage during the polymer pyrolysis and is capable of being densified by the subsequent processing. Under the condition which had been found the best for matrix producing the monolith beforehand, unidirectional SiC/SiC composites were successfully fabricated. By comparing them with a composite obtained by the conventional PIP, the matrix of improved uniformity with smaller amount of process defects was certainly formed by PSH-PIP. The composites of the improved matrix exhibited higher mechanical properties such as tensile strengths and fracture toughness.

INTRODUCTION

SiC fiber reinforced SiC matrix (SiC/SiC) composite material is one of the most hopeful candidates for high-temperature structural material used in mid-high heat load air-frame structures such as the leading edge of a main wing or the rudder face of a reusable space transportation system and used in various engine components such as thruster nozzles, combustor liners or turbine brisks[1].

In terms of matrix forming techniques, chemical vapor infiltration (CVI) is used in France[2] in many cases and the molten Si impregnation (MI) is often used in the US[3] and Germany[4]. While the polymer impregnation and pyrolysis (PIP) has been commonly applied in Japan[5]. PIP is a very attractive manufacturing method technically and in cost because it has many similarities in techniques and facilities used for CFRP. It is advantageous to be launched with relatively small financial impact, to be applied for large/complex shaped component production and to control matrix microstructure in a wide range. However, when a precursor polymer impregnated in a fiber preform is pyrolyzed, gas evolution and shrinkage inevitably occur and many process defects were consequently generated. In case that a polymer or its slurry is pyrolyzed by itself, many critical cracks are initiated and fail into pieces. This big issue of the PIP has not been sufficiently solved yet and has to be cleared for wide industrial application.

In this research, a new hybrid process, PSH-PIP, in which the PIP was combined with the powder

space holder technique (PSH), was proposed to solve the above problems of the PIP. PSH method has been originally developed as the metallurgical technique to make a porous metal material by mixing space holding particle into metal powder and removing it during sintering[6]. The best condition for slurry preparation to make a polymer-derived porous monolith has already been acquired by a systematic investigation[7]. The composite production by the PSH-PIP consists of the two stages: 1) a porous matrix formation by mixing space holding particles into a precursor polymer at the first PIP processing and 2) the matrix densification by the subsequent multiple PIP processing. The main advantage to be expected is that the out gassing and uniform thermal shrinkage are enhanced in the porous microstructure, which contributes to reducing process defects, and that the pores were then well densified to be a solid matrix. For process details, see the Reference[7].

In order to verify the applicability of the PSH-PIP to composite fabrication and the effects of the process on the microstructure and mechanical properties of a composite, unidirectional composites were fabricated by using the PSH-PIP and also by using the conventional PIP for comparison. The composites were comparatively evaluated by microstructure observations and various mechanical tests. Consequently, it was confirmed that the composites fabricated by using the PSH-PIP had less amount of process defects and showed higher tensile strengths in both the fiber direction and the direction perpendicular to the fiber direction and fracture toughness.

EXPERIMENTALS

Tyranno ZMI fiber (Ube Industry, Ltd., Japan) was used as the reinforcement. As the SiC precursor polymer, allylhydridopolycarbosilane (AHPCS) (SMP-10, Starfire Systems Inc., USA) was used because of its high ceramic yield and SiC purity. As the space holding particle, i.e. the material that forms pores in the PSH process, polymethylmethacrylate (PMMA) particles of average particle diameter of 10 μm (Chemisnow MX-100, Soken Chemical & Engineering Co., Ltd., Japan) was used. The SiC powder of average particle diameter of 0.27 μm (Beta random ultra fine, IBIDEN Co., Ltd., Japan) was used as the filler material in the conventional PIP process.

The composites were fabricated in the following steps: (1) Wound the fiber bundle uniformly on the carbon fixture to make a fibrous preform, (2) Formed an interfacial layer on the fibers' surface by the CVI method, (3) Prepared the polymeric precursor slurry by mixing the contents, (4) Immersed the preform in the slurry to make a prepreg, (5) Cut, stacked and then bagged the prepreg, (6) Cured the prepreg at higher than 100 °C with vacuuming to make a green body, (7) Pyrolyzed the green body at 1000 °C in argon atmosphere to obtain a porous-matrix composite, then (8) Densified the composite by repeating the subsequent impregnation and pyrolysis with only the precursor polymer six times, and finally the flat composite plate was obtained.

The interfacial layer consisted of inner C layer and outer SiC layer. For the PSH-PIP composites, two types of thickness of 100 nm and 300 nm were prepared for examining the interaction of matrix microstructure with interface property and its effect on the mechanical characteristics of a composite. The thickness of SiC layer was consistently set to 100 nm for all the composites. Based on the previous detailed studies[7,8], the preparation conditions of the polymeric slurries were determined such that the PMMA particle of 10 μm and the SiC particle of sub-micron size were mixed to the AHPCS at the ratio of 64 wt.% and 30 wt.% respectively. The slurry for the PSH-PIP was controlled for fluidity by adding a hexane solvent at the appropriate rate whereas the slurry for the conventional PIP consisted of only the polymer and the filler. The polymer operations such as mixing and impregnation were all conducted in the atmosphere. The prepreg sheet-stacked body was pressured by an atmosphere during the curing, and consequently some amount of slurry was squeezed out of the bag. The curing and pyrolysis were carried out in the same condition for all composites. The sizes and fiber volume fractions of the composites were about 160 mm square and 22~24 % respectively.

The composite plates were machined into the specimen shapes and were subjected to various evaluations. Cross-sectional observation was performed for the composite specimens after first and final PIP processing using SEM. For the mechanical properties, tensile test in the fiber direction and the vertical direction of the fiber, compressive test in the fiber direction, fracture toughness test (SENB) and bending test were conducted. In all the tests, at least five specimens were prepared for each composite. The specimens tested were subjected to fractography using optical microscope and SEM. For the specimens of the compressive test, micro X-ray CT was carried out. The push-out test for the fiber/matrix interface shear strength and the hardness test for the matrix were performed using a nano-indentation system with a Berkovich-shape indenter at the loading rate of 2000 mgf/s. For the push-out test, the indenter with flat bottom was utilized. For the hardness test, maximum load was set to 100 gf.

RESULTS AND DISCUSSION

Figure 1 is the cross-sectional SEM micrographs of the composites fabricated by the PSH-PIP. The micrographs (a) and (b) show an inter-fiber (intra-bundle) microstructure after the first and the final subsequent PIP processing respectively. In the micrograph (a), spherical pores were fully formed all over the region, similarly to the case of a monolith[7]. This confirmed that the space holding particles in the slurry could be well impregnated into the inter-fiber area under the presently-adopted technique and they could work to make the porous structure. In the micrograph (b), highly-densified inter-fiber matrix with a small amount of defect was found. It could be considered that many of the initially-formed pores were continuously distributed and be ready to be impregnated and densified by the subsequent PIP processing.

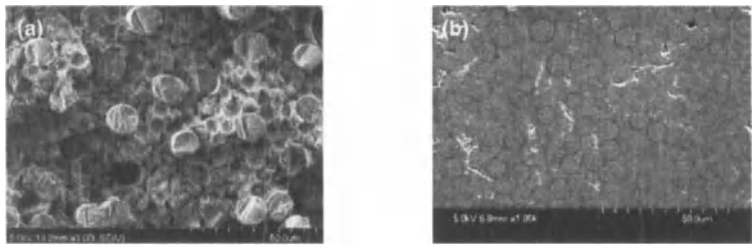

Figure 1. SEM micrographs of the PSH-PIP composites
after (a) the first and (b) the final subsequent PIP processing.

Figure 2 is the cross-sectional SEM micrographs of the composites fabricated by (a) the conventional PIP and (b) the PSH-PIP. They exhibit the distribution of relatively large pores corresponding to the inter-bundle pores especially. In the micrograph (a), many pores of the diameter up to several 100μm are distributed all over the area. In the micrograph (b), those are significantly reduced in size and number. Although the morphological characteristic of a composite's matrix depends on many process factors, the predominant reason for the remarkable reduction of large pore in the PSH-PIP composite was considered to be the efficient out gassing and uniform thermal shrinkage as expected.

According to the above results, it was confirmed that the PSH-PIP process can reduce process defect by making a porous structure even in an inter-fiber area which promotes gas purge and uniform shrinkage and is able to be densified in a subsequent processing.

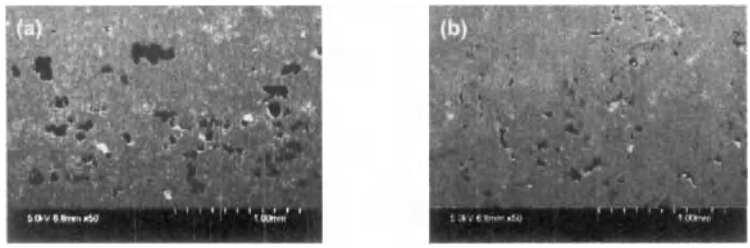

Figure 2. SEM micrographs of the composites
fabricated by (a) the conventional PIP and (b) the PHS-PIP.

Figure 3 exhibits the results of the tensile test in the vertical direction of the fiber. The results of the PSH-PIP composites of 100 nm and 300 nm of interfacial layer thickness and the PIP composite of 300 nm thickness are presented. Because the characteristic of a matrix stands out in the vertical direction, the matrix strengths could be compared here. The PSH-PIP composites showed more than twice strength of the conventional PIP one. On the other hand, noticeable effect of the interface thickness was not found between the PSH-PIP composites, taking the magnitudes of the variations among the speciments into consideration. Therefore, main factor for the strengths should be the distribution of large pore and the strengthening of a matrix by the PSH-PIP could be successfully achieved.

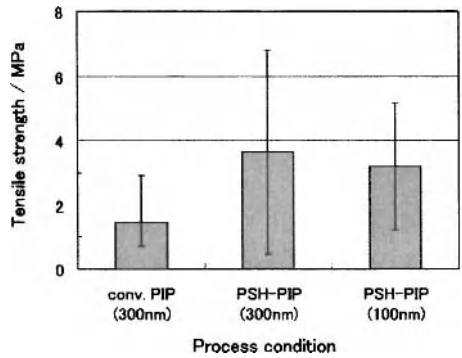

Figure 3. The results of the tensile test in the vertical direction of the fiber.

Figure 4 presents the results of the tensile test in the fiber direction. The PSH-PIP composites showed higher strengths than the PIP composite by about 10 %. The PSH-PIP composites with the interfacial layer thicknesses of 100 nm and 300 nm showed almost the same strength. On the whole, the tensile strengths in the fiber direction were mainly dependent on the matrices. Possible reason of these results is that the unified and densified matrix to a certain extent by the PSH-PIP could serve to make a stress on the fibers more averaged, which contributed to lowering those breakdown probability.

and to transfer a load which a broken fiber had originally sustained before breaking to adjacent intact fibers more efficiently. In addition, the possibility that a fiber/matrix sliding capability can be enhanced in the PSH-PIP-derived matrix even with a thin interfacial layer was implied. These issues are much important and will be further investigated.

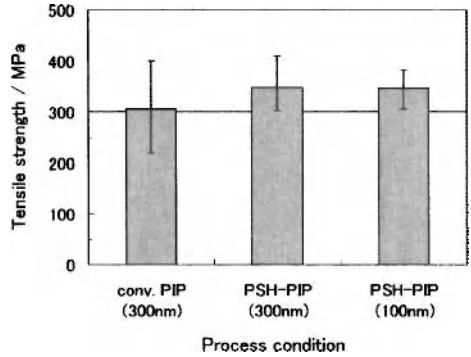

Figure 4. The results of the tensile test in the fiber direction.

SUMMARY

To enhance the mechanical properties of a SiC/SiC composite by improving a matrix microstructure, a new hybrid process, PSH-PIP, was proposed and the followings have been demonstrated:

i) The PSH-PIP process could be well applied to make a ceramic matrix composite under an appropriate condition of slurry preparation, impregnation and forming.
ii) It could much reduce the amount of process defects, compared to the conventional PIP.
iii) The improvement of a matrix microstructure by the PSH-PIP significantly contributed to improving the representative mechanical properties of a composite.

ACKNOWLEDGEMENT

This work has been carried out as a part of R&D activity of Space Open Lab. program operated by Japan Aerospace Exploration Agency (JAXA).

REFERENCES

1. F. Christin, High temperature ceramic matrix composites., Weinhein (FRG): Wiley VCH, 731-743 (2001).
2. R. Naslain, Design, Preparation and Properties of Non-oxide CMCs for Application in Engines and Nuclear Reactors: An Overview, Comp. Sci. Tec., **64**, 155-170 (2004).
3. J. A. DiCarlo, H.-K. Yun, G. N. Morscher and R. T. Bhatt, SiC/SiC Composites for 1200 °C and Above, NASA TM-2004-213048.
4. W. Krenkel and F. Berndt, C/C-SiC Composites for Space Applications and Advanced Friction Systems, Mater. Sci. Eng., **A 412**, 177-181 (2005).
5. T. Ishikawa, Overview for Ceramics in Aerospace Field in the 21st Century: Particulary Composites, Ceramics, **36**, 1, 27-31 (2001). (in Japanese)

6. K. Nishiyabu, S. Matsuzaki and S. Tanaka, Dimensional accuracy of micro-porous metal injection and extrusion molded components produced by powder space holder method, J. Japan Soc. Powder and Powder Metallurgy, **53**, 9, 776-781 (2006). (in Japanese).
7. K. Nishiyabu, S. Matsuzaki and M. Kotani, Development of Silicon Carbide Heat-resistant Composites with Micro-porous Structure, Proc. Sixteenth Int. Conf. Comp. Mater., WeHA1-04 in CD-ROM, 2007.
8. M. Kotani, T. Inoue, A. Kohyama, Y. Katoh and K. Okamura, Effect of SiC Particle Dispersion on Microstructure and Mechanical Properties of Polymer-Derived SiC/SiC Composite, Mater. Sc. Eng., **A357**, 376-385 (2003).

Advanced Processing and Manufacturing Technologies for Structural and Multifunctional Materials II
Edited by Tatsuki Ohji and Mrityunjay Singh

OXIDATION BEHAVIOR OF C/C-SiC COMPOSITES IN OPEN ATMOSPHERE

V. K. Srivastava* and Shraddha Singh
*Professor in Production Engineering
Department of Mechanical Engineering
Institute of Technology
Banaras Hindu University, Varanasi – 221005, INDIA
E-mail: vk_sa@yahoo.co.in and vijays.sa55@gmail.com

ABSTRACT

C/C and C/C-SiC composites plates were directly exposed with the flame of oxyacetylene gas welding to see the effect of temperature (>1000^{O}C) in open atmosphere. Duration of exposure time was increased to measure the weight loss and ultimate performance of composites. Weight loss, maximum tensile stress and compressive stress tests were performed to find the behavior of C/C-SiC composites after the exposure of oxyacetylene gas flame in open atmosphere. The amount of the heat transferred to the base material depends upon the distance, the torch is held from the materials. The results show that the weight loss increases with increase of exposure time. Which clearly indicates that the excess amount of carbon is oxidized with the oxygen to form the carbon mono-oxide. The matrix materials undergo pyrolysis reactions within short periods which generate volatiles and leave behind a porous skeleton of carbon fibres. Therefore, ultimate performance of C/C and C/C-SiC composites was reduced with increase of exposure times. However, 2D C/C composites give lower values than the C/C-SiC composites.

1. INTRODUCTION

Carbon-carbon composites are a family of advanced composite materials. They are the most advanced form of carbon and consist of a fibre based on carbon precursors embedded in a carbon matrix. This unique composition gives them such properties as low density, high thermal conductivity and shock resistance, low thermal expansion and high modulus. Carbon-carbon is mostly used in aerospace applications, mainly for aircraft disk brakes, rocket re-entry nose tips and for parts of rocket nozzles [1].

C/C-SiC composites are promising materials for use in high temperature structural applications. This material offers high strength to density ratios.

Carbon fibre reinforced carbon matrix composites retain specific strength, specific toughness and any other mechanical properties at higher temperature in an inert atmosphere or in vacuum. From this view point, they are expected as only material for the structures of aerospace applications and microgas turbine used as higher than 1500^{0}C. However, C/C composites have serious disadvantage such as oxidation in high temperature in air. They are degraded at temperatures as low as about 500^{0}C and oxidation protection system have been developed [2].

In view of the above information, the present work was developed to obtain the effect of oxidation on the performance of C/C-SiC composite due to gas flame exposure in open atmosphere. The Scanning Electron Microscopy (SEM) method was used to obtain the morphological change due to oxidation. Tensile and Compressive behavior were compared, which are expected to provide

valuable information for tailoring the mechanical properties to achieve the desired performance of the material.

2. EXPERIMENTAL PROCEDURE

The C/C-SiC composites used in this experiment were processed by Liquid Silicon Infiltration (LSI) process. This process consists of three steps, (i) A carbon fibre reinforced plastic is produced. (ii) This green composite is pyrolysed. In this step, the shrinkage of the polymeric matrix is hindered by the fibres, which lead to the development of a regular crack pattern. (iii) The C/C perform is infiltrated with liquid silicon that reacts to SiC, yielding a dense material with C/C segment separated from each other by SiC. The LSI process leads to damage tolerate ceramic material that has a significantly lower component fabrication time and therefore reduced component costs compared with other ceramic matrix composites (CMC) manufacturing processes. C/C- SiC are tough ceramics when the fibre matrix bonding is properly optimized usually through a thin layer of an interfacial material refereed to as the interphase.

The 2D C/C-SiC composite plates were cut from the bulk with dimension (1cm×1cm). The specimens were cleaned ultrasonically to remove any incompact particle and dried. The samples were weighted by electronic balance without any exposure and the surface of C/C-SiC composite was oxidized at temperature about 700^0C with the gas flame of Oxy- Acetylene torch. The distance was tried to maintain 10 mm in between the nozzle of gas and surface (Fig.1). C/C-SiC composites were oxidized with the variation of the time such as 5 min, 10 min, 15 min and 20 minutes and then they were weighted again. The cumulative weight change of samples was reported as a function of oxidation time.

The morphology of each specimen was quite different on microscopic scale due to conditioning of specimen and loads.

The tension and compression tests were generally performed on flat specimens. The most commonly used specimen geometries are the dog-bone specimen and straight-sided specimen with end tabs. A uniaxial load is applied through the ends. The ASTM standard test method for tensile properties of fibre–resin composites has the designation D3039-76. It recommends that the specimens with fibres parallel to the loading direction should be 12.7 mm wide and mode with 6–8 plies. Length of the test section should be 153 mm. The tensile and compressive tests were performed on the universal testing machine and results were analyzed to calculate the tensile strength of C/C-SiC composite samples only because C/C samples were very poor strength after the oxidation. Finally, morphology of fractured samples was observed by scanning electron microscope (SEM) method. The deformation of fibres, matrix and distribution of Si, SiC were quite different on microscopic scale due to conditioning of specimen and load, which images are discussed in details.

3. RESULT & DISCUSSION

3.1. Effect of oxidation

The weight of unexposed and exposed samples was measured by electronic balance to see effect of high temperature oxidation in open atmosphere. The results show that the weight loss increases with increase of exposure time as shown in Fig. 2. Due to carbon degradation the weight loss of C/C-SiC composite decreased by about 0.125 gm during the oxidation process. The carbon matrix reacts with oxygen and forms the carbon-mono-oxide, which debonded and delamination the carbon fibre from

the matrix. It's clearly indicates that the composite surface texture was fully oxidized with the oxidation effect, which creates more microcracks due to degradation of carbon and matrix/fibre interface. The oxidized surfaces are appeared in the form of grey colour.

During the oxidation thermal expansion coefficient of SiC ceramic was largely higher than that of C/C composite, which induced the formation of cracks. The cracking was caused by thermal stresses due to the coefficient of expansion mismatch between the carbon fibres and the SiC matrix. Which also results in through the wall porosity in the composite.

3.2.Tensile and compressive test

For determining the difference in tensile strength and compressive strength of exposed and unexposed samples as well as the difference between C/C-SiC and C/C composites, tensile and compressive tests have been conducted. The effect of oxidation on C/C-SiC is clearly mentioned by the tensile test that was visualized by the following Figs.3-7.

When material is exposed to oxy-acetylene gas torch it could degrade because of oxidation. Oxygen could attack the fibres especially in the vicinity of cracks or porosity.

A chemical reaction could also occur in the matrix if non-reacted Si from the infiltration process is available. The lower viscosity of the SiO_2 at high temperatures could result in a shelf healing of micro cracks. Because of the oxidation of the carbon a loss of mass of about 20% could be seen. The tensile test was performed on the exposed and unexposed samples of C/C-SiC and also on the C/C composite.

3.3.SEM test:

The microstructure indicates severe reaction between carbon fibre and molten silicon. In the present study, both type of samples oxidized as well as unoxidized shows the microstructure of unexposed C/C-SiC composite, which indicates that the number and height of peaks become reduced. This reduction in number and height of peaks is due to the morphological change in the sample. After oxidation carbon degraded in the form of carbon-di-oxide and carbon-mono-oxide ($C+O_2 \rightarrow CO_2\uparrow$, $2C+O_2 \rightarrow 2CO\uparrow$) and Si reduce in the form of silicon oxide ($Si+O_2 \rightarrow SiO_2$).

Due to the loss of carbon and silicon particle from the sample, the morphological characters were changed and hence the reduction in number and height of peak obtained.

Thermal conductivity is a key property in many applications of C/C-SiC composites. Generally these are relatively good conductors of heat but their conductivity depends upon the crystallinity of their constituents. And due to change in the proportion of oxygen, carbon and silicon, the conductivity becomes also changed.

Also, morphological observation in Figs. 8-11 appears that the fracture surface of oxidised and unoxidised C/C-SiC composite was under different loading conditions. The SEM at higher magnification observed the fractured and unfractured samples of C/C-SiC and C/C composite. The deformation of fibres, matrix and the distribution of constituent particle were quite different on microscopic scale due to the fracture.

4. CONCLUSION

Based on the experimental observation, the results clearly indicate that weight of C/C-SiC composite is damaged severally at about 2.3%, when oxidised in open atmosphere by the flame of oxy-acetylene gas. The reduction in tensile and compressive strength of oxidised and unoxidised samples indicates that the strength of both composites are affected by the delamination, debonding, pyrolysis of matrix and formation of CO, CO_2 and SiO_2. Therefore, maximum tensile and elastic modulus of ceramic composites decreased with the oxidation time in open atmosphere by oxyacetylene gas flame.

ACKNOWLEDGEMENTS

The authors wish to express sincere thanks to the Air Force Office of Scientific Research-Asian Office of Aerospace Research and Development, Tokyo, Japan for their financial support. This work also supported by the Department of Mechanical Engineering, Department of Metallurgical Engineering, Institute of Technology and Solid State lab., Department of Physics, Banaras Hindu University, Varanasi, India.

REFERENCES

1. Windhorst T., Blount G., Carbon-carbon composites: a summary of recent developments and applications, Material & Design, Vol. 18, No. 1, pp. 11-15, 1997
2. McKee, D.W., Oxidation behavior and protection of carbon/carbon composites, carbon, Vol. 25, No. 4, pp. 551-557, 1987
3. Heinmann D, Bill J, Aldinger F, Schanz P, Gern FH, Krenkel W, Kochendorfer R. Development of oxidation protected carbon/carbon. Z Flugwiss Weitraum, 19: 180-8, 1995

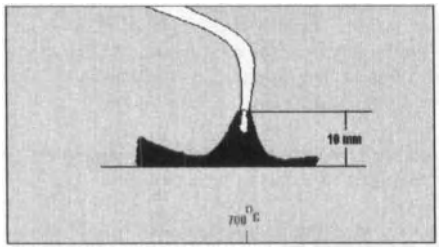

Fig. 1. Flame compressed with surface of C/C-SiC composites.

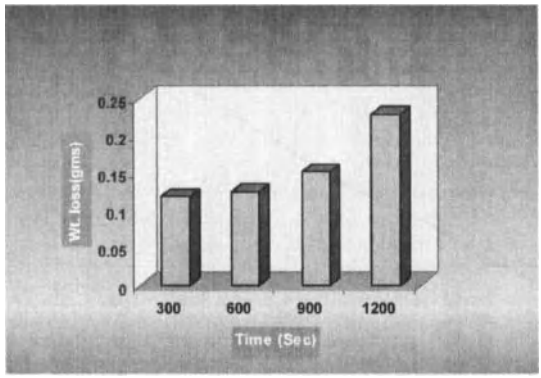

Fig. 2. Variation of weight loss with the variation of time.

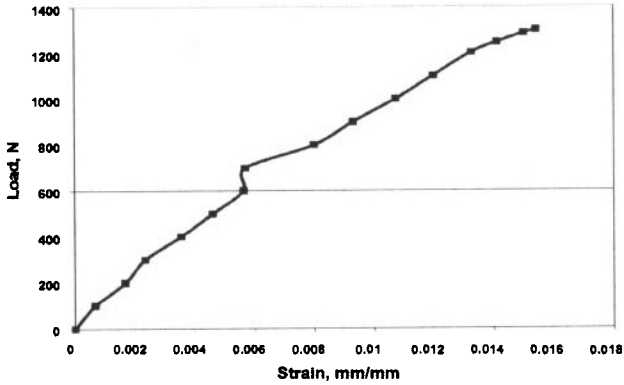

Fig. 3. Tensile test of C/C-SiC (without exposure)

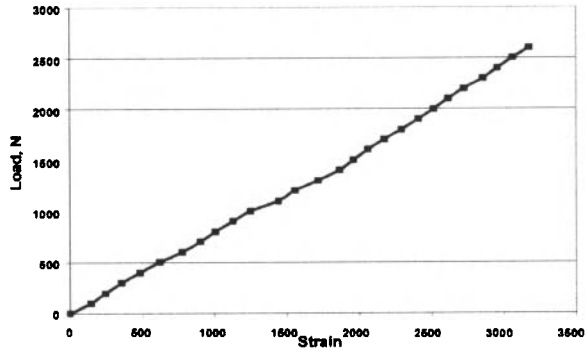

Fig. 4. Tensile test of C/C-SiC (exposed)

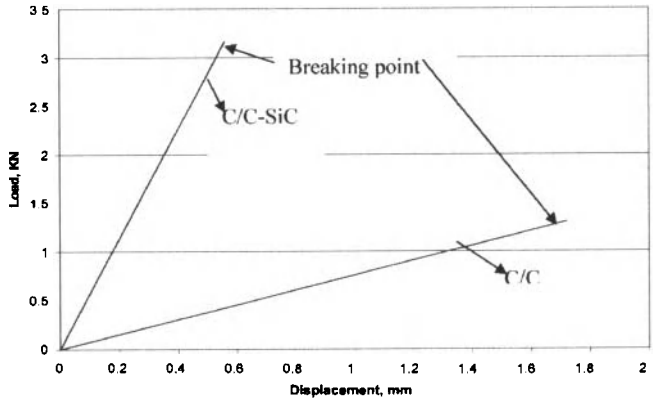

Fig. 5. Variation of load with displacement of oxidized composites under tension.

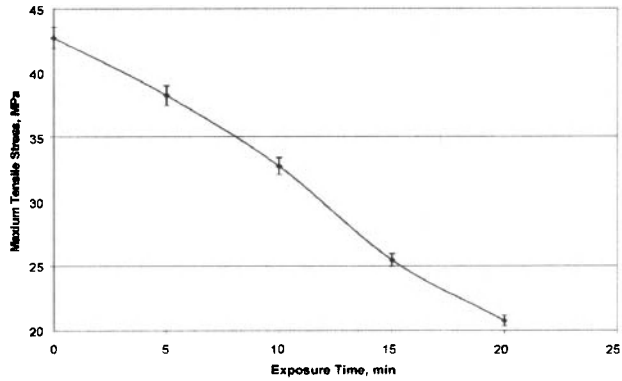

Fig. 6. Degradation of maximum tensile stress with increase of exposure time of gas flame on C/C composite

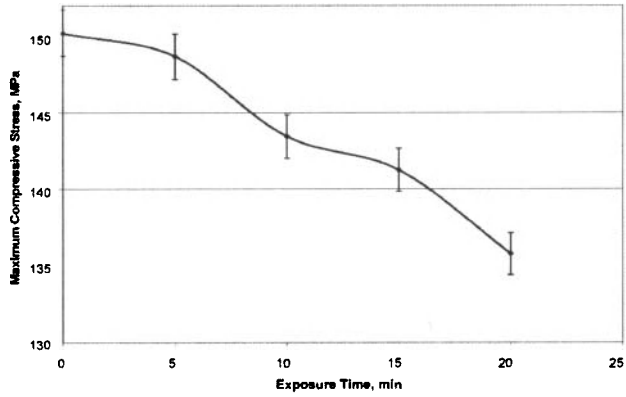

Fig. 7. Degradation of maximum compressive stress with increase of exposure time of gas flame on C/C-SiC

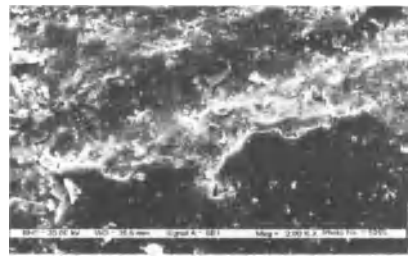

Fig. 8. SEM of C/C/SiC composites without fracture

Fig.9. SEM of fractured sample of C/C-SiC composites.

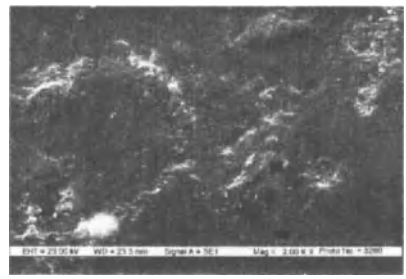

Fig. 10. C/C Composites without fracture.

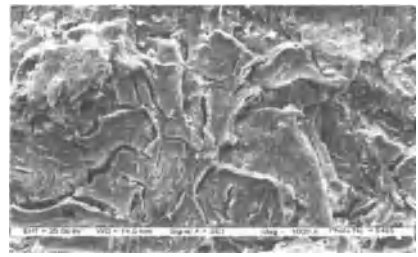

Fig. 11. Fractured sample of C/C composites.

Advanced Processing and Manufacturing Technologies for Structural and Multifunctional Materials II
Edited by Tatsuki Ohji and Mrityunjay Singh

PROCESSING METHOD FOR INTERPENETRATING NETWORK METAL-CERAMIC COMPOSITES WITH A NON-LINEAR COMPOSITIONAL GRADIENT

M. Neukam, M. Willert-Porada
Chair of Materials Processing
Faculty of Applied Natural Sciences, University of Bayreuth
D-95447 Bayreuth, Germany

ABSTRACT

A new method for processing large flat compositionally graded metal-ceramic parts with connected interpenetrating metal and ceramic network is described. Based on powder metallurgical methods, a metal foam is obtained by slip casting of metal powder slurries on a polyurethane foam, and used as preform to achieve a metallic interpenetration within the composite. The porous metallic preform is infiltrated with a ceramic slip and co-sintered. The composites contain Ni-Cr-alloy, or the P/M superalloy Saratherm 2 and Nimonic 90 as metallic part and pure 8Y-ZrO_2 or zirconia mixed with $ZrSiO_4$, as ceramic part. Sintering behaviour, microstructure development and phase composition were characterised by dilatometer measurements, X-ray diffraction, light and scanning electron microscopy and energy dispersive X-ray analysis, for different variants of the process. Composites of nominal same composition sintered without the metal foam preform show no metallic interpenetration.

INTRODUCTION

Metal-ceramic composites with an interpenetrating metallic network within the ceramic phase are expected to show superior mechanical and thermo-mechanical properties, as far as the metallic phase is very homogeneously distributed and constrained as thin film between the ceramic grains. A metal-ceramic compositional gradient will add multi-functionality into such a material, abbreviated as IPN-FGM.

Various processing methods for the fabrication of metal-ceramic composites have been reported for metal matrix composites (MMC) and ceramic matrix composites (CMC), which utilise metallic melts either for infiltration of a ceramic preform or for oxide dispersion strengthened cast alloys[1,2]. With this technique interpenetrating metal-ceramic composites are obtained, but incomplete infiltration due to poor wettability of the ceramic and a low interfacial bonding as well as limitations due to high melting temperature of most refractory or superalloy metals are some of the major drawbacks of the existing technology.

For FGMs a huge variety of processes is known to generate a gradient[3]. Besides casting also powder metallurgy routes can be applied, e.g., pressing of layered powder mixtures[4], sequential slip casting[5] or tape casting[6]. Opposite to the "discontinuous" FGMs obtained by such methods, sedimentation techniques have the potential for formation of a continuous compositional gradient in a FGM[7,8]. The drawback of such processing routes is the lack of an interpenetrating metal-ceramic network. Therefore poor mechanical properties and limited corrosion resistance is observed[9].

Within a systematic investigation a new material and processing concept has been tested: a metal foam with sufficient sintering activity is utilised as preform for ceramic and metal-

ceramic slip casting, followed by co-sintering of the powder green part. The key problems to be solved are:

- Preparation of an extremely porous metal foam with thin struts
- Development of stable slips with high solid content
- Development of a drying and sintering process

As the ceramic material 8 mol% Y_2O_3-stabilised zirconia (8Y-FSZ) was chosen. It shows excellent thermal barrier properties, anti-corrosion and wear resistance and is a good solid electrolyte, e.g. for fuel cell applications. Zircon ($ZrSiO_4$) was used as an additive. It reduces the thermal conductivity, relaxes the residual stresses in the ceramic zone and increases the oxidation resistance[10]. Nickel-base alloys have been chosen as the metallic material, because of their high corrosion and oxidation resistance, and high strength at high temperatures. They are used at high temperatures in harsh environments, for example in gas turbines.

EXPERIMENTAL PROCEDURE

The following commercially available powders have been used as raw materials: (1) 8 mol% Y_2O_3-doped fully stabilized zirconia (8Y-TZS, 99.9 %, Tosoh Corp., Japan) with specific surface area 7±2 m^2/g and average particle size d_{50}=0.54 µm; (2) Zircon ($ZrSiO_4$, 99%, Auer-Remy, Germany), specific surface area 2.3 m^2/g and average particle size d_{50}=4.02 µm as ceramic materials; (3) Nickel-Chromium alloy (NiCr8020, 99 %, H.C. Starck, Germany); (4) Nickel-base superalloy (Nimonic 90, UltraFine Powder Tech., USA); (5) Nickel-base superalloy (Saratherm 2, Saar Hartmetall und Werkzeuge GmbH, Germany). The compositions and properties of these materials are listed in Table I.

Table I. Composition and properties of metallic materials

Alloy	Composition (wt-%)						density	T(solidus)	T(liquidus)	T(γ'-solvus)	d_{90} [µm]	atomization
	Ni	Cr	Co	Al	Ti	Mo	[g/cm³]	[°C]	[°C]	[°C]		
NiCr8020	80	20					8.32	1419	1421	-----	<45 µm	water
Nimonic 90	Bal.	20.4	18.4	1.7	2.6		8.12	1320	1387	1014	<22 µm	argon
Saratherm 2	Bal.	15	18	4	3.5	5	7.95	1315	1351	1154	<100 µm	argon

Aqueous metallic slips with 70 wt% solids content were produced, using distilled water as the solvent and 4 wt% of a hydrocolloidal stabilizer (PRODUKT KM 2000, Zschimmer&Schwarz, Germany). Ceramic and mixed metal-ceramic slips with 75 wt% solids content were produced, using distilled water as a solvent and an anionic polyelectrolyte (Dolapix CE64, Zschimmer&Schwarz, Germany) as a dispersant. The ceramic slips were first mixed and de-agglomerated in a planetary ball mill for 1 h and then aged in a tumble mixer. The different slips produced are listed in Table II.

Table II. Compositions of the different ceramic and mixed slips

Slip ID	Component 1 (Vol%)	Component 2 (Vol%)	Component 3 (Vol%)	Dispersant (wt%)
S1	TZ-8YS (100)	-	-	-
S2	TZ-8YS (74)	$ZrSiO_4$ (26)	-	0.25
S3	TZ-8YS (60)	-	Ni-base alloy (40)	-
S4	TZ-8YS (44.4)	$ZrSiO_4$ (15.6)	Ni-base alloy (40)	-

The experimental flow sheet is shown in Figure 1. As a template for the processing of the metal foam commercially available polyurethane foams (Poret soft filter foam, EMW

Filtertechnik, Germany) with 45 pores per inch (PPI 45) and a thickness of 10 mm were used. The polymer foam was first infiltrated with an epoxy resin (Epofix, Struers GmbH, Germany) to provide a good adhesion of the metallic slip and after hardening a good stability of the foam. After infiltration with the metallic slip, the foams are rolled (space between cylinders: 3 mm) to remove the excessive slip. The removal of the polymer is performed in a quartz tube furnace (HST 12/400, Carbolite, Germany) under Ar/H_2 atmosphere, to avoid oxidation of the metal. A heating rate of 0.5 K/min. up to 500°C was applied followed by 1 hour dwell time and further heating up to 1000°C at a heating rate of 5 K/min.

For the vacuum slip casting, the metal foam was placed on a glass frit, pore class P16 (pore size 10-16 µm, ROBU, Germany) with a filter paper in between, pore size 2.5 µm (Grade 42, Whatman, Germany), to provide a good removal of the sample after slip casting. The vacuum is applied with a water jet pump to soak the water through the frit. For comparison, also samples without metal foam were slip cast using slip S3 and S4.

After drying in ambient air, the samples were sintered in an alumina tube furnace (Thermal Technology GmbH, Germany) for 1 hour at 1300°C in Ar/H_2 atmosphere with a heating rate of 5 K/min. The samples were placed in an insulating casket made from aluminosilicate fibers board. Composite samples have a diameter of around 30 mm and a thickness of 5-8 mm.

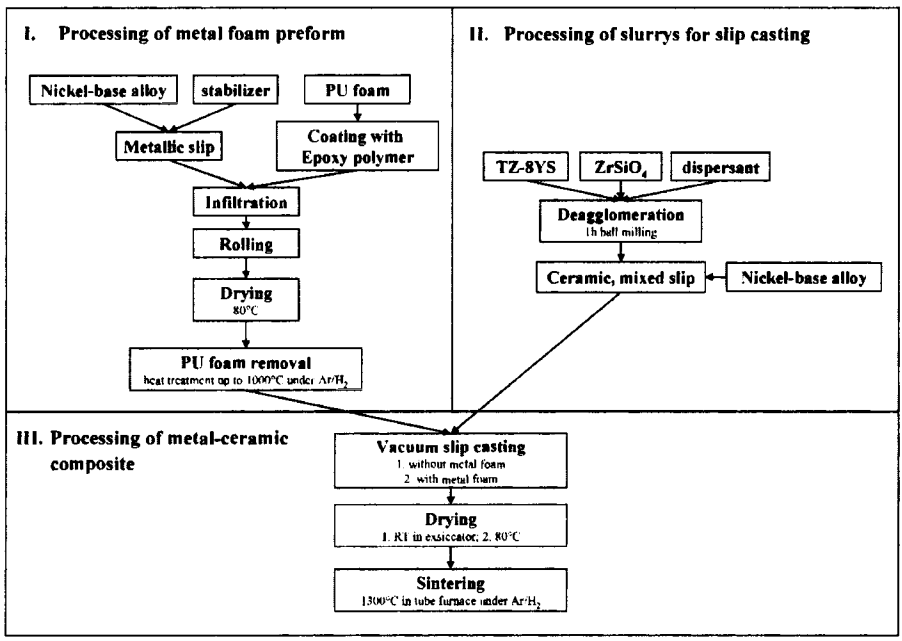

Figure 1. Schematic diagram of experimental procedure

Powder density was measured by He-pycnometry (AccuPyk 1330, Micromeritics, Germany). Zeta potential measurements (DT-1200, Quantachrome, Germany) and Electrokinetic Sonic Analysis (ESA, MBS 8000, Matec Applied Sciences, USA) were used to characterize the ceramic slips and evaluate the amount of dispersant needed. For characterization of the material scanning electron microscopy (SEM, JSM-840, JEOL, Germany), light stereomicroscopy (SZX-ZB12, Olympus, Germany) and optical microscopy (BX60MF3, Olympus, Germany) were applied to cross sections of polished samples. X-ray diffractometry (XRD, Philips X'Pert PW3040) and energy dispersive X-ray analysis (EDX) in a scanning electron microscope (SEM) were used for measuring the phase composition and elemental distribution of the composites; dilatometer measurements (DIL 402 E/7, Netzsch, Germany) were performed to detect the different thermal expansion and sintering shrinkage of the compounds. To characterize the removal of the polymer and the reactions during sintering, thermogravimetry (TG) and differential scanning calorimetry (DSC) measurements (STA 449 C Jupiter, Netzsch, Germany) were applied.

RESULTS AND DISCUSSION

Metal Foams

As shown in Figure 2, highly porous metal foams with 100-200 μm strut thickness are obtained after removal of the polymer template. "Geometric" porosity of about 90-95 % is achieved. But according to the results of TGA measurements, after heating up to 900°C in Ar/5vol%H_2, 4.67 wt% carbon residues is trapped in the foam. As shown in the SEM images in Figure 2b, this carbon is sintered together with the metal powder and can participate in reactions with the other materials added upon subsequent processing.

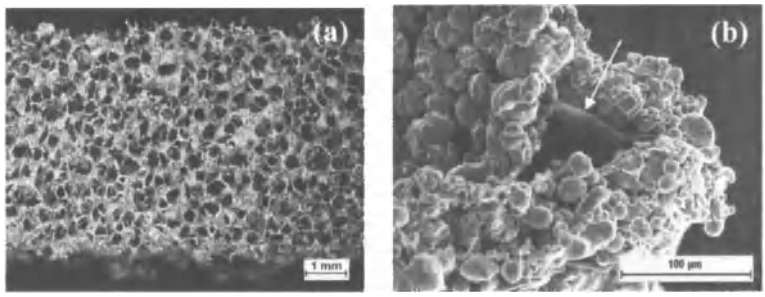

Figure 2. (a) Light stereomicroscope image of NiCr8020 foam; (b) SEM image of foam strut, arrow points to residual carbon

Slip characterization

Ceramic TZ-8YS and $ZrSiO_4$ slips have an initial pH value of around 5.5-6. The zeta potential at this pH region without dispersant is positive for the TZ-8YS slip and negative for the $ZrSiO_4$ slip, as shown in Figure 3a. In order to achieve a stable dispersion of the mixed slip S2, an anionic dispersant is used to adjust the surface charge of TZ-8YS to negative values. The sufficient amount of 0.25 wt% is determined by ESA measurements as shown in Figure 3b. In case of metal-ceramic slips S3 and S4 addition of 0.25 wt% of Dolapix CE64 is detrimental and causes rapid sedimentation. Without dispersant, the slips are more stable

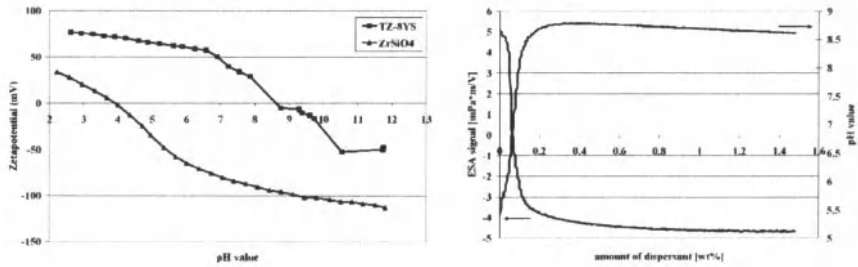

(a) (b)

Figure 3. (a) Zeta-potential of TZ-8YS and ZrSiO4 with pH variation, (b) ESA signal of TZ-8YS with dispersant variation

Sintered composites without porous metal preform

As shown in Table III. a large specific density difference exists between the metallic components and the ceramic ones. Therefore sedimentation of the metal powder is expected to occur during vacuum slip casting of mixed slurries, without a metal foam as porous preform. With the right casting speed, a gradient between metal and ceramic content is formed.

The sample shown in Figure 4 is made from a mixed slip with TZ-8YS and NiCr8020 (S3). The large metal particles are concentrated at the lower surface of the sample. in the upper region there is a high amount of ceramic content. The Ni-Cr-particles are dispersed in the zirconia matrix throughout the compositional gradient. Upon sintering bending of the sample occurs, due to differential shrinkage between metal and ceramic. The dilatometer measurements shown in Figure 5, reveal that upon heating up to 1300 °C the NiCr8020 phase exhibits no shrinkage but thermal expansion.

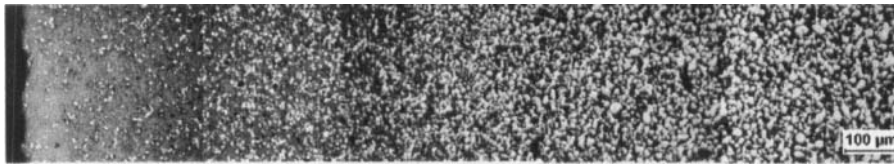

Figure 4. Optical microscopy image of sintered sample with S3 slip, light phase: NiCr8020, dark phase: TZ-8YS, left side: upper surface

Table III. Density of starting materials determined with He-pycnometry

Material	average density [g/cm^3]
TZ-8YS	6.19
$ZrSiO_4$	4.71
NiCr8020	8.32
Nimonic 90	8.12
Saratherm 2	7.95

Sintered composites with porous metal preform

Composites obtained from slip casting a ceramic or metal-ceramic composite slurry into a metal foam preform do not show bending but exhibit cracks during drying. These cracks are prone to growth during sintering. Addition of 26 vol% $ZrSiO_4$ in the ceramic phase reduces the sintering shrinkage of the zirconia-ceramic but does not prevent crack growth, as visible from Figure 5. A compositional gradient is formed, with a ceramic enriched region on top of the part. This region has the largest shrinkage upon co-sintering.

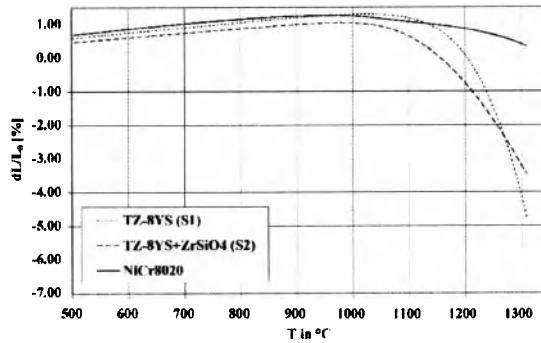

Figure 5. Dilatometer measurements under Argon of pressed samples

The carbon content in the metallic foam reacts with Cr-metal in the alloy to form a liquid phase. Due to sintering stresses some of the liquid phase is "squeezed out". The liquid phase remaining in the composite solidifies to yield a eutectic structure, as shown in Figure 6b.

XRD measurements and EDX analysis shown in Figure 7 and Figure 8 confirm, that the second phase in addition to the NiCr8020-alloy is chromium carbide, mainly Cr_7C_3. The melting point of the metal foam is reduced to 1250°C, as shown by the DSC curve in Figure 9. This is consistent to the results of Bondar et al.[11] who investigated the system Cr-Ni-C. The foams made from nickel-base superalloy powders and the polyurethane template show a similar behavior as NiCr8020.

The formation of a carbide-metal eutectic facilitates densification upon co-sintering, with the struts well connected with the ceramic, as shown in Figure 7. Besides some cracks resulting from drying, the foam struts have a good bonding to the zirconia matrix. Furthermore, the large interpenetrating metallic network is retained, as visible from the light stereomicroscopy image in Figure 6a.

This is the major difference in connectivity when compared to parts sintered from a metal-ceramic slip, e.g., S3, only. In the FGM obtained without a metal foam preform the metal particles are dispersed in the ceramic matrix, throughout the compositional gradient. Only within the almost 100% metal powder region, and only in case of NiCr8020 powder sintering necks are formed, but for the Ni-base superalloys no neck formation could be observed due to the low sintering activity and the oxide layers formed on the particle surfaces. The low sintering activity is not only caused by the coarseness of the metal powders but also by oxide layers. Nimonic 90 forms a Cr_2O_3 oxide layer and Saratherm 2 forms a Al_2O_3 oxide layer on the surface because of

the high amount of aluminum in the alloy. as shown in Table I. In the ceramic phase some porosity is still present due to the relatively low sintering temperature of 1300°C for zirconia.

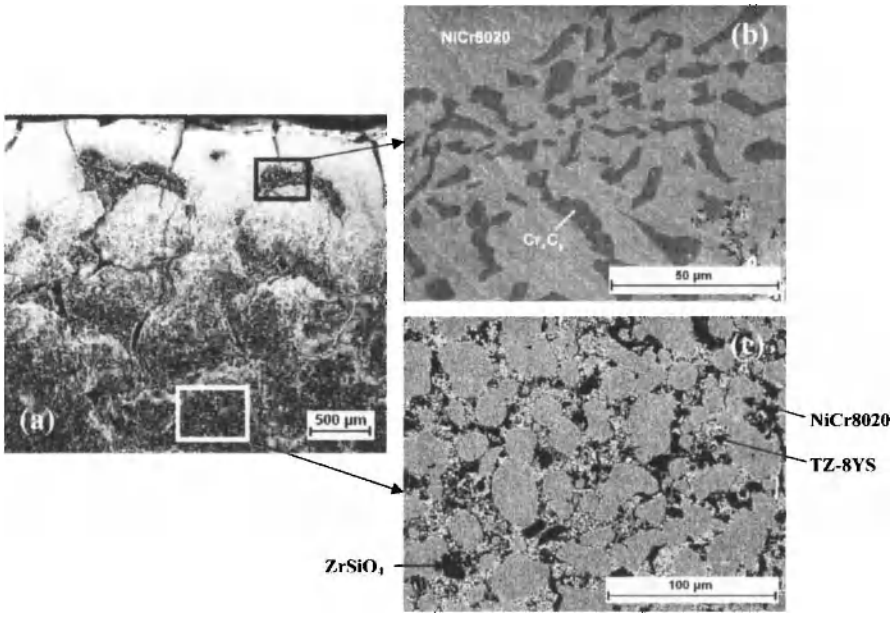

Figure 6. (a) Light stereomicroscopy image of sintered S4 sample with foam (16x), light phase: TZ-8YS+$ZrSiO_4$, dark phase: NiCr8020; (b) SEM image of foam microstructure (1000x); (c) backscattered SEM image of composite between foam struts (500x)

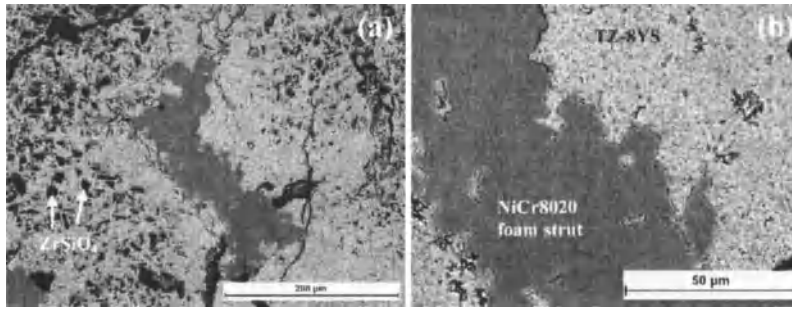

Figure 7. SEM images of sintered S2 sample with foam: (a) 250x; (b) 1000x

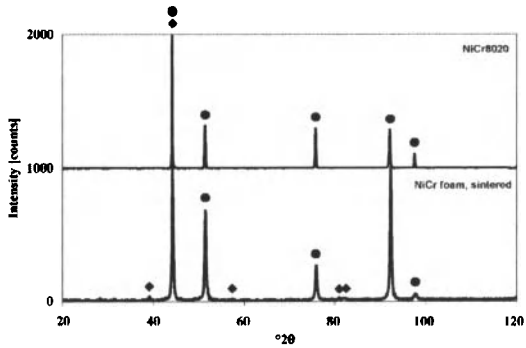

Figure 8. XRD measurements: ●: NiCr8020 (γ-phase), ◆ : Cr_7C_3

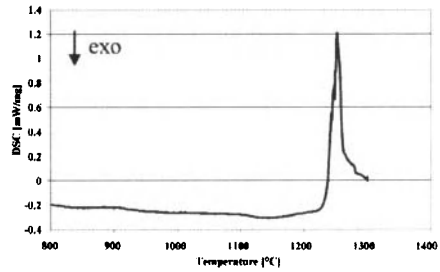

Figure 9. DSC curve for NiCr8020 foam after heat treatment (1000°C)

CONCLUSION

A new processing concept for fabrication of fully interconnected multiple phase metal-ceramic composites based on vacuum slip casting of ceramic and metal ceramic slips into metal foams was tested.

Using polyurethane foams as template, > 90% open porosity metal foams were successfully synthesized from NiCr8020, Nimonic 90 and Saratherm 2 powders. By adjusting the zeta potentials stable water based ceramic and metal-ceramic slips with ~75wt% solid content were obtained and infiltrated into the porous metal foam, serving as preform. Due to sedimentation a compositional gradient with high ceramic content in the top part and high metal content at the bottom part of the samples is formed. Upon co-sintering the compositional gradient as well as the interpenetrating metal-network is preserved, although significant shrinkage and densification occur.

FGM-parts can also be obtained by vacuum slip casting and sedimentation without using metallic foam as preform. However, in such parts no interpenetrating metal network is developed, rather a dispersion of metal particles in a ceramic matrix.

Problems still to be solved arise from carbon impurities in the metal foam. Eutectic Cr-carbide-Cr melt is formed, which facilitates co-sintering of the IPN-FGM but restricts the sintering temperature to <1300°C and also lowers the thermal stability of the IPN-FGM. Future work will concentrate on reactive additives to consume the eutectic melt upon sintering.

Drying cracks are another problem; they grow further upon co-sintering. A careful adjustment of the green density in the ceramic rich zone of the IPN-FGM should help to overcome this problem.

ACKNOWLEDGEMENTS

The financial support of German Science Foundation within the graduate school 1229 is gratefully acknowledged. Collaboration on dilatometer measurements and slip characterization measurements at the Chair of Ceramic Materials Engineering (Prof. Krenkel) was very helpful in this work.

REFERENCES

[1]A. Mattern, B. Huchler, D. Staudenecker, R. Oberacker, A. Nagel, and M.J. Hoffmann, Preparation of interpenetrating ceramic-metal composites, *Journal of the European Ceramic Society: Engineering Ceramics 2003*, **24**(12), 3399-408 (2004).

[2]F.F. Lange, B.V. Velamakanni, and A.G. Evans, Method for Processing Metal-Reinforced Ceramic Composites, *Journal of the American Ceramic Society*, **73**(2), 388-93 (1990).

[3]B. Kieback, A. Neubrand, and H. Riedel, Processing techniques for functionally graded materials, *Materials Science and Engineering A: Papers from the German Priority Program (Functionally Graded Materials)*, **362**(1-2), 81-106 (2003).

[4]M. Willert-Porada and R. Borchert, An Oxidation Resistant Metal-Ceramic Functional Gradient Material: Material Concept and Processing Requirements, *Materials Science Forum*, **308-311**, 422-27 (1999).

[5]R. Moreno, A.J. Sanchez-Herencia, and J.S. Moya, Functionally gradient materials by sequential slip casting: alumina-yttria tetragonal zirconia, *Ceramic transactions*, **34**, 149-56 (1993).

[6]J.-G. Yeo, Y.-G. Jung, and S.-C. Choi, Design and microstructure of ZrO_2/SUS316 functionally graded materials by tape casting, *Materials Letters*, **37**(6), 304-11 (1998).

[7]Y.-G. Jung, C.-G. Ha, J.-H. Shin, S.-K. Hur, and U. Paik, Fabrication of functionally graded ZrO_2/NiCrAlY composites by plasma activated sintering using tape casting and it's thermal barrier property, *Materials Science and Engineering A*, **323**(1-2), 110-18 (2002).

[8]S. Lopez-Esteban, J.F. Bartolome, C. Pecharroman, and J.S. Moya, Zirconia/stainless-steel continuous functionally graded material, *Journal of the European Ceramic Society*, **22**(16), 2799-804 (2002).

[9]R. Borchert, Verfahrensentwicklung zur Herstellung metallisch-keramischer Gradientenwerkstoffe durch Mikrowellensintern, in *Fachbereich Chemietechnik*. 1997, Dortmund: Dortmund.

[10]R. Borchert and M. Willert-Porada, Metal-Ceramic Gradient Material Product made from a Metal-Ceramic Gradient Material and Process for Producing a Metal-Ceramic Gradient Material, *Siemens Aktiengesellschaft, Munich*, US patent 6,322,897 **B1** (2001).

[11]A. Bondar, V. Maslyuk, T. Velikanova, and A. Grytsiv, Phase equilibria in the Cr-Ni-C system and their use for developing physicochemical principles for design of hard alloys based on chromium carbide, *Powder Metallurgy and Metal Ceramics*, **36**(5), 242-52 (1997).

Advanced Processing and Manufacturing Technologies for Structural and Multifunctional Materials II
Edited by Tatsuki Ohji and Mrityunjay Singh

3-D SIMULATION OF SELF-PROPAGATING HIGH-TEMPERATURE SYNTHESIS OF SOLID OXIDE FUEL CELL CATHODE MATERIALS

Sidney Lin and Jiri Selig
Chemical Engineering Department
Lamar University
Beaumont, TX 77710
U.S.A.

ABSTRACT

Finite element analysis was used to model the Self-propagating High-temperature Synthesis (SHS) of $La_{1-x}Sr_xMnO_3$ when a solid oxidizer is used. The contributions to heat loss from the reaction pellet surface to surroundings by radiation and convection were calculated and compared. Temperature distributions and inside the reaction pellet during the syntheses of $La_{1-x}Sr_xMnO_3$ of various Sr doping levels, and ambient oxygen flow rate were calculated. A 3-D calculation was performed and the calculated results were compared with those calculated from a 2-D model.

INTRODUCTION

Fuel cells generate electrical power via chemical reactions between fuels and oxygen (air). Because there is no mechanical moving device in a fuel cell, a higher efficiency can be achieved compared to an internal combustion power generator.

A Solid Oxide Fuel Cells (SOFC) consists of ceramic cathode (e.g. Sr doped $LaMnO_3$), anode (e.g. Ni/YSZ), and electrolyte (e.g. YSZ) and operates at a temperature around or below 700 °C. The high quality waste heat generated by SOFC's can be used for regeneration. Therefore, SOFC systems generate electrical power at a higher efficiency than other types of fuel cells.

The high cost of cathode materials has been identified as one of the bottle necks in Solid Oxide Fuel Cell commercialization by U.S. DOE's Solid-State Energy Conversion Alliance (SECA) consortium because it costs more than 40% of the total cost in SOFC production. The current market price of cathode materials is US$700-1,000/kg. Self-propagating High-temperature Synthesis (SHS) process utilizes highly exothermic reaction to produce high quality cathode powders [1, 2] at a cost less than US$100/kg. A stable combustion front movement and uniform temperature distribution during the synthesis is needed to produce high quality cathode materials. In order to improve and control the SHS of cathode materials production, a mathematical model using the finite element analysis was developed in our lab. to study the 3-dimensional temperature history during the SHS process.

SHS of Sr doped $LaMnO_3$ oxides have been successfully synthesized in our lab. In our syntheses, gaseous oxygen and a solid oxidizer ($NaClO_4$) have both been used as the oxidizer to produce high quality $La_{1-x}Sr_xMnO_3$ (x = 0-0.8) as shown in reaction (1) and reaction (2) separately.

$$\frac{1-x}{2}La_2O_3 + x\,SrO_2 + Mn + \frac{3-x}{4}O_2 \rightarrow La_{1-x}Sr_xMnO_3 \qquad (1)$$

$$\frac{1-x}{2}La_2O_3 + x\,SrO_2 + Mn + \frac{3-x}{8}NaClO_4 \rightarrow La_{1-x}Sr_xMnO_3 + \frac{3-x}{8}NaCl\uparrow \qquad (2)$$

Although the adiabatic temperature of the reaction (2) is lower than that of the reaction (1) due to the endothermic $NaClO_4$ decomposition, it has a better intimate contact between the oxidizer and

other solid reactant powders and less oxygen diffusion resistance into the center of reactant pellet. Therefore, a faster reaction rate and a higher combustion temperature are observed (Figure 1). In many experiments, the measured combustion temperature of reaction (2) reached or slightly exceeded the measurement limit of our thermocouples (R type thermocouples, with maximum operating temperature of 1450 °C). In order to understanding and control of these SHS reaction systems, a finite element analysis model was developed to predict the temperature distribution and temperature history during the SHS reactions.

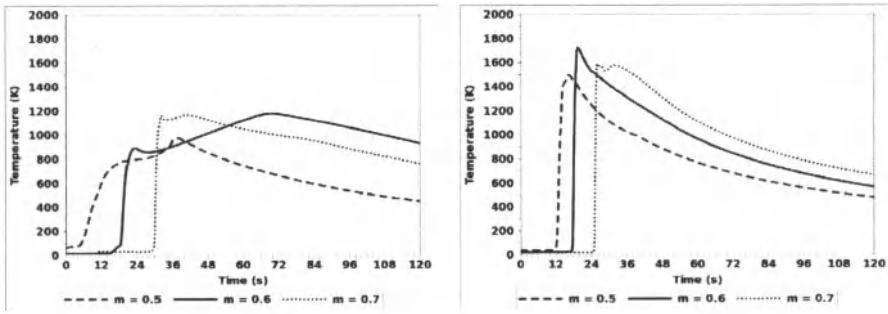

(a) (b)

Figure 1. Experimental temperature histories of SHS of $La_{0.6}Sr_{0.4}MnO_3$ at various fuel ratios.

(a) 0.3 La_2O_3 + 0.4 SrO_2 + m Mn + (1-m) MnO_2 + (m-0.35)O_2 $\rightarrow$ $La_{0.6}Sr_{0.4}MnO_3$.

(b) 0.3 La_2O_3 + 0.4 SrO_2 + m Mn + (1- m) MnO_2 + (0.5m-0.175) $NaClO_4$

$\rightarrow$ $La_{0.6}Sr_{0.4}MnO_3$ + (0.5-0.175) NaCl.

METHODOLOGY

Mathematical Model

Reaction (2) which uses $NaClO_4$ as a solid oxidizer is studied in this model. The theoretical adiabatic heat temperatures of SHS reactions are calculated by equation (3):

$$\sum_i \left(\int_{298}^{T_{ad}} n_i c_{p_i} dT \right) = -\Delta H_r^0 \tag{3}$$

where C_p is the specific heat of product, n_i is stoichiometric coefficient of component i, and ΔH_r^0 is standard heat of reaction.

Different heat transfer mechanisms are considered in the model. The convection heat loss from the pellet surface to the surrounding oxygen, conduction heat transfer inside the pellet and from the pellet to an underneath sample holder are characterized by equation (4).

$$-\mathbf{n} \cdot \left(k_1 \nabla T_1 + \rho_1 C_{p1} T_1 \mathbf{u}_1 - k_2 \nabla T_2 \right) = q_0 \tag{4}$$

where the subscript 1 represents the gas phase surrounding the reaction pellet and subscript 2 represents the reaction pellet, k is the thermal conductivity, ρ is the density of the pellet, $\mathbf{u}_1$ is the oxygen velocity vector, and q_n is the inward heat flux.

Radiation heat loss from the pellet surface is calculated using the Stefan-Boltzmann equation,

$$q_{rad} = -\varepsilon\sigma\left(T_2^4 - 293^4\right) \tag{5}$$

where ε is the emissivity and σ is the Stefan-Boltzmann constant. In our current calculation, a maximum radiation heat loss is considered by assuming $\varepsilon=1$.

In some cases, oxygen is not flowing into the reactor and the natural convection heat loss from the pellet surface to the surroundings is calculated using equation (6).

$$q_0 = -h(T_f - T_\infty) \tag{6}$$

where T_f is the film temperature, T_∞ is the surrounding temperature, and h is the average convection heat transfer coefficient at T_f and is estimated by the Nusselt number (Nu), Rayleigh number (Ra), and Plandtl number (Pr) as shown in equations (7)-(9)[3].

$$Nu = 0.68 + \frac{0.670\,Ra^{1/4}}{[1 + (0.492/\mathrm{Pr})^{9/16}]^{4/9}} \tag{7}$$

$$Ra = \frac{g(T - T_\infty)L^3}{Tv^2}\mathrm{Pr} \tag{8}$$

$$h = \frac{Nu}{L}k \tag{9}$$

where g is the gravitational acceleration, L is the specific length, and v is the viscosity of air.

The specific length in this case was the length of one section of pellet (0.25 mm). From equations (7)-(9) and using a film temperature of 800 K, an average heat transfer coefficient of 200 W/(m^2 K) is used in our calculation.

Forced convection was implemented by specifying velocity field. In this presented model, the velocity of air is 3 m/s in the axial direction of reaction pellet.

Physical Properties

Reaction heat and other thermodynamic data, such as thermal conductivity are calculated based on experimental data [4,5] and properties from handbooks [6,7]. Physical properties used in the model, such as thermal conductivity (k), specific heat capcity (c_p), and heat of reaction (ΔH) are functions of temperature. However, due to the lack of temperature dependent data of some proprties, constant thermal conductivity, density and specific heat of product are used in this model. Most specific heats are included as a function of temperature. All physical properties of surrounding atmosphere are

specified as functions of temperature. The constant physical properties used in this model are listed in Table I.

Table I. Physical Properties used in the Model for SHS of $La_{1-x}Sr_xMnO_3$.

x	Heat of Reaction[8] (kJ/mol)	Adiabatic Temperature (K)	Heat Capacity $C_{p\text{-}prod}$ (J/mol K)	Density[9,10] ρ_{prod} (kg/m^3)	Thermal Conductivity k_{prod} (W/m s)	Thermal Conductivity $k_{reactant}$ (W/m s)
0.0	-480	2327	236	6600	2	20
0.2	-527	2565	233	5600	2	20
0.4	-530	2614	229	5600	2	20
0.6	-538	2687	225	5600	2	20
0.8	-547	2772	221	5600	2	20

Geometry and Mesh

The model geometry is a 1 cm long and 1 cm diameter pellet surrounded by oxygen as shown in Figure 2. The pellet is divided into 0.25 mm thick subsections. Each of these subsections is meshed into small rectangular subsection. Since average velocity of propagation is used the movement of the reaction through the pellet can be approximated as consecutive burning of small sections. The thickness (0.25 mm) is used as a good balance between the accuracy of the results and computational time. The size of the section does not make large difference for a 2-D model, but for a 3-D model the computational time increases significantly with decreasing section size. Bellow the pellet is a subdomain representing a pellet holder. The three dimensional model is constructed in a similar fashion, with the same dimensions as the 2D model. Final mesh for 2D model consists of 7,200 elements and 29,211 degrees of freedom.

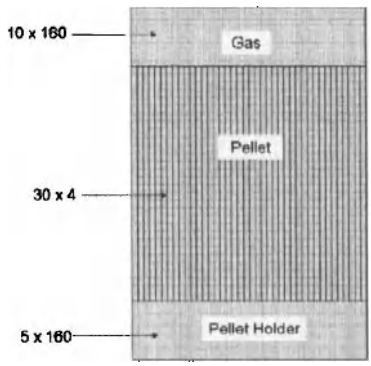

Figure 2. The geometry and mesh used in the model.

RESULTS AND DISCUSSION

Heat loss from the reaction pellet during the SHS process takes place by both radiation and convection transfers. Figure 3 shows the temperature profile at the pellet top surface when different heat transfer modes are considered separately. With no heat loss, temperature on the surface (at x = 5 mm) reaches 2,500K and the temperature keeps at about the same temperature for a while after the reaction. As the radiation heat loss is taken into account, the maximum temperature decreases to 2,454 K. When the natural convection heat loss is added, a smaller temperature decrease (approximately 25 K) presents. If oxygen or air flows around the pellet, a large temperature drop (75 K) is caused by forced convection. And the total decrease in temperature is about 150 K. It is clear that radiation and forced convection are dominant heat losses. Final maximum temperature, including radiative and convective heat losses is 2,350, which is in a good agreement with reported experimental data[4]

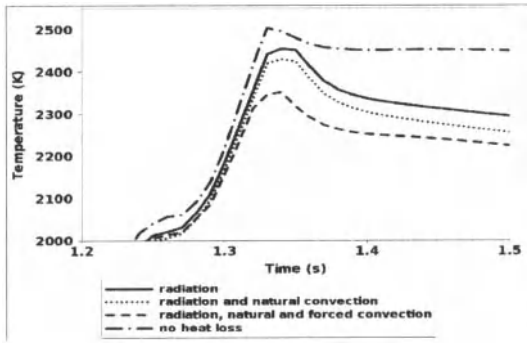

Figure 3. Temperature distribution when different heat transfer mechanisms are considered during SHS of $La_{0.6}Sr_{0.4}MnO_3$.

The reaction heat increases when a higher amount of Sr is doped as shown in Table I. Figure 4 shows calculated top surface temperature histories at different Sr doping levels (value of x). It is apparent that with an increasing doping level, the combustion temperature increases. However, it is surprising to see the temperature does not increase at the same speed even though a constant combustion front movement velocity (3.92 m/s) is used in our model. The maximum temperature is reached sooner at a higher value of x. This may be caused by a higher conductive heat transfer at a higher temperature and also by the increased exothermicity of the reaction system at higher dopant concentrations.

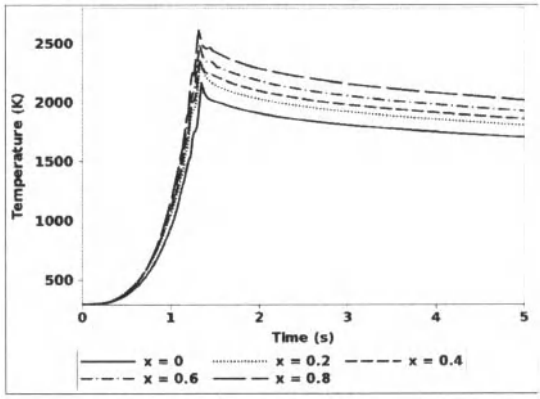

Figure 4. Surface temperature histories for SHS of various $La_{1-x}Sr_xMnO_3$ (x = 0-0.8).

Forced convection plays important role in temperature profile on the pellet surface during the SHS process (Figure 5). As described above, forced convection substantially reduces surface temperature and this cooling effect changes as surrounding gas flow changes. Our model shows that the temperature during combustion is reduced more significant when gas velocity is opposite to the direction of reaction propagation (counter-flow) than when the gas velocity is in the direction of reaction propagation (co-current flow).

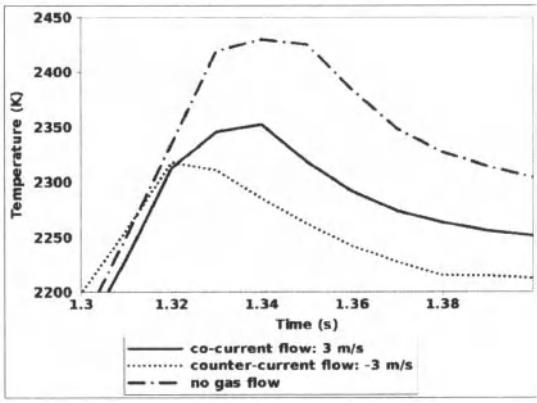

Figure 5. Impact of the gas velocity on the surface temperature profile during the SHS of $La_{0.6}Sr_{0.4}MnO_3$.

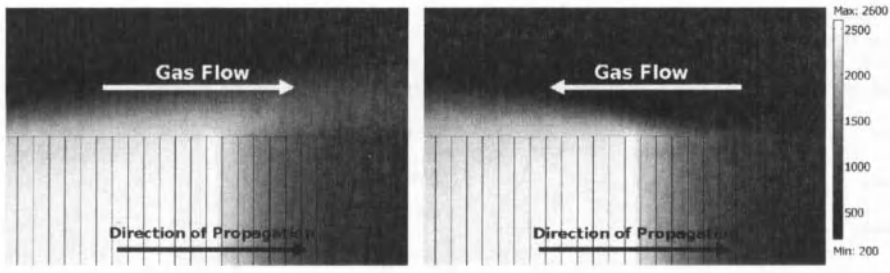

Figure 6. Effect of gas flow on temperature profile inside the reaction pellet (Reaction is propagating from left to right).

For the co-current flow case, initially cool gas is heated up by reacted (but still very hot) pellet and by the heat from the reaction. The gas flows over the cool unreacted pellet and preheats the unreacted pellet and results in a higher surface temperature. When the gas flow counter currently to the reaction unreacted pellet is not preheated nor does temperature of gas increase. This unheated gas cools the reaction front more effectively and reduces the surface temperature during reaction. Gas is heated by the reaction and is less effective in cooling the already reacted pellet. Effect of gas direction on temperature profile inside the pellet is presented in Figure 6.

A 3-D model is developed using the similar approach with the same boundary condition. The pellet considered is also 1 cm long and 1 cm in diameter. Geometry of 3-D model is in figure 7.

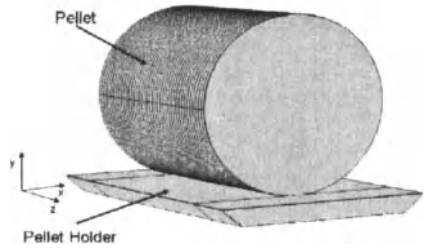

Figure 7. Geometry of 3-D model

Main motivation for the three dimensional model is to examine if it provides similar results from 2-D model. Figure 8 shows the temperature profiles of SHS of $La_{0.6}Sr_{0.4}MnO_3$ on the top pellet surface at different times. The sharp temperature decrease to room temperature at t = 0.1 and 1 s indicates the position of reaction front. These profiles follow the same trend as predicted by the 2-D model, but the temperatures are lower by about 200 K. The decrease in temperature could be

attributed to the increased heat loss that comes with the addition of extra dimension and heat loss is not limited to only the top surface and pellet sides but to the whole surface. These results show that it is possible to get approximate temperature profile using much simpler, and hardware efficient 2-D model, but is also shows that 3-D model might be necessary to get more accurate results.

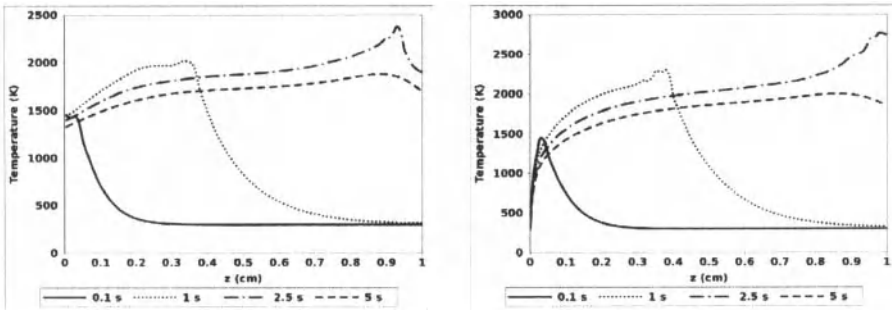

(a) (b)

Figure 8. Surface temperature profile for SHS of $La_{0.6}Sr_{0.4}MnO_3$ calculated by (a) 3-D model and (b) 2-D model.

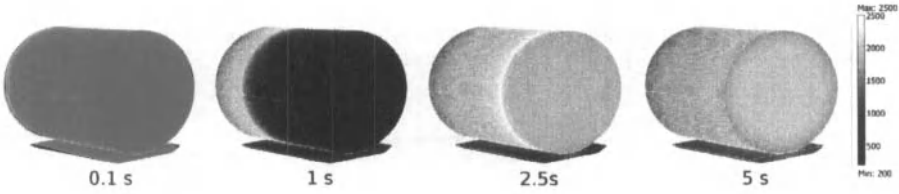

Figure 9. The calculated 3_D temperature distribution of SHS of $La_{0.6}Sr_{0.4}MnO_3$ at different times.

Figure 9 shows the calculated results of 3-D temperature distribution when radiation and natural convection are considered. From this figure it can be seen clearly that the temperature at the center is higher than the surface. This can be deduced from figure corresponding to t=5s, where the center is white and the surface is darker (i.e. has lower temperature). Also, it was observed that conduction heat loss between the pellet and sample holder significantly reduces the temperature near the bottom of the pellet.

CONCLUSIONS

A mathematical model based on finite element analysis has been developed to study the temperature profile and history during the SHS of $La_{1-x}Sr_xMnO_3$. Our model can be used to predict the maximum combustion temperature and the time and position it occurs. Maximum temperature of 2350 K and 2150 K was reached during modeling for 2-D and 3-D model, respectively. These results are in agreement with published experimental data. From the result we can conclude that the surrounding gas flow rate and direction has decisive impact on the temperature distribution. Our results

show that convective heat loss is the dominant heat loss affecting the temperature distribution. The 3-D temperature distribution during the SHS process was calculated and compared with the results calculated from a 2-D model. It was observed that maximum reaction temperature for 3-D model is on average 200 K lower than the maximum temperature of 2-D model.

ACKNOWLEDGEMENTS

The authors wish to thank the financial support from Texas Air Research Center, Texas Hazardous Waste Research Center and Lamar University Research Enhancement Grant.

REFERENCES

1. Ming, Q., M. Nersesyan, K. Ross, J. T. Richardson and D. Luss," Reaction Steps and Microstruture Formation during SHS of $La_{0.8}Sr_{0.2}CrO_3$", Comb. Sci. & Tech., **128**, 279 (1997).
2. Ming, Q., J., M.D. Nersesyan, S. Lin, J.T. Richardson, D. Luss, Chemical Rate processes Involved in SHS of $La_{0.9}Sr_{0.1}CrO_3$, Int. J. Of SHS, **7(4)**, 447 (1998).
3. Holman, J.P., "Heat Transfer" (9th Edition) McGraw Hill Publishing, 2002 (ISBN 0-07-240655-0).
4. Kuznetsov, Maxim V., Ivan Parkin, Daren J. Caruana, Yuri G. Morozov, "Combustion Synthesis of Alkaline-Earth Substituted Lanthanum Manganites ", J. of Mater. Chem., **14**, 1377 (2004).
5. Jacob, K. T., M. Attaluri, "Refinement of Thermodynamic Data for $LaMnO_3$"; J. of Meter. Chem., **13**, 934 (2003).
6. Yaws, Carl L., "Chemical Properties Handbook", McGraw-Hill Inc, New York, NY (1999), ISBN: 0070734011.
7. Barin, Ihsan, "Thermochemical Data of Pure Substances", VCH, New York, NY (1993), ISBN: 1560817178.
8. Rormark L., Svein Stolen, Kjell Wiik, and Tor Grande, "Enthalpies of Formation of $La_{1-x}A_xMnO_{3+\delta}$ (A=Ca and Sr) Measured by High-Temperature Solution Calorimetry", Journal of Solid State Chemistry 163, 186-193 (2002).
9. Huang, Q.J., Y. Cheng, X.J. Liu, X.D. Xu and S.Y. Zhang, "Study of the Elastic Constants in a $La_{0.6}Sr_{0.4}MnO_3$ Film by Means of Laser-Generated Ultrasonic Wave Method", Ultrasonics, 44(1), 1223-27 (2006).
10. Miha'ly, L., D. Talbayev, L. F. Kis, and J. Zhou, "Field-frequency mapping of the electron spin resonance in the paramagnetic and antiferromagnetic states of LaMnO3", Physical Review B 69, 024414 (2004).

Advanced Processing and Manufacturing Technologies
for Structural and Multifunctional Materials II
Edited by Tatsuki Ohji and Mrityunjay Singh

INFLUENCE OF GREEN PART MICROSTRUCTURE AND SINTERING ATMOSPHERE ON THE FORMATION OF POROUS SILICON NITRIDE CERAMICS WITH YB-SILICATE MATRIX

M. Knoll, M. Willert-Porada
Chair of Materials Processing
Faculty of Applied Natural Sciences, University of Bayreuth
D-95447 Bayreuth, Germany

ABSTRACT

This paper summarizes results of a study on grain boundary phase distribution and surface layer composition in porous silicon nitride ceramics with Yb-silicate utilized as liquid phase forming additive, upon sintering at ambient pressure in a silicon nitride powder bed. The lowest amount of Yb_2SiO_5-additive sufficient to achieve complete transformation of α-Si_3N_4 to β-Si_3N_4 is 3.2 mol%, corresponding to 10wt%. The pure silicate is superior as additive when compared with oxide-silicate mixtures. The soaking temperature is identified as the major factor influencing the shrinkage and weight loss, while the extension of a compositional gradient of the additive within the sintered part and the composition of the surface near layers is significantly affected by the composition of the sintering atmosphere during heat up. When argon gas is used during heating up and replaced by nitrogen upon soaking the surface of the sintered ceramic is free of Yb_2SiO_5, whereas in N_2-atmosphere a silicate-rich coating is found as surface layer of the porous silicon nitride ceramic.

INTRODUCTION

Porous silicon nitride ceramics have been studied as promising candidates for high temperature applications, e.g., for gas filters, catalyst supports and metal-ceramic thermal engineering components, because of their outstanding mechanical properties at both room temperature and high temperatures. These properties include high strength, high fracture toughness, excellent resistance to thermo chemical corrosion, and excellent thermal shock resistance[1]. Superior properties of porous Si_3N_4 can only be achieved by formation of an anisotropic microstructure in which rod-like β-silicon nitride grains display a high degree of directionality [2-9] and only a small amount of a creep resistant grain boundary phase is present. Such a refractory grain boundary phase is formed when a rare earth oxide forming high temperature stable silicates, like e.g., ytterbia, Yb_2O_3 is used [10-14].

For dense Si_3N_4-ceramics sintered with ytterbia good oxidation resistance[10] and high temperature strenght[12] are reported. The sintering behavior, development of microstructure and its effect on mechanical properties using ytterbia as sintering additive for dense high temperature structural silicon nitride ceramics has been thoroughly investigated[9, 15-19], but no such information has been reported about porous silicon nitride ceramics.

In such ceramics, a competition between densification and growth of large β-Si_3N_4-grains should take place: very large grains could also grow by an evaporation-condensation process and not only by crystallization from a supersaturated melt. Whereas the later process occurs upon liquid phase sintering of dense ceramics, the former could be very important to obtain porous ceramics with a low amount of refractory grain boundary phase. Therefore the amount, composition and spatial distribution of the Yb-containing additive have to be carefully controlled.

Because the numerous reactions between Yb_2O_3 with Si_3N_4 as well as with SiO_2 yield a grain boundary phase with a very complex composition, in this work ytterbium silicate Yb_2SiO_5 is investigated as additive for pressureless sintering of α-Si_3N_4 powder, replacing the commonly used sintering additive ytterbia and enabling a better control of the grain boundary phase composition. Different sintering atmosphere conditions - pure nitrogen versus Ar-N_2 in certain temperature regimes - are investigated in

order to distinguish between solid state reaction contributing to the grain boundary phase formation and final distribution in the ceramic part as compared to gas-liquid or gas-solid phase reactions, contributing to the grain growth and porosity formation.

EXPERIMENTAL PROCEDURE

Commercially available silicon nitride powder (H.C.Starck Grade M11 "higher purity") with 92.8% α-Si_3N_4 content, BET surface area 13.8 m^2/g and the average particle size 0.6 μm was used as starting material. The sintering additive Yb_2SiO_5 was synthesized from ytterbia (Yb_2O_3, Chempur, 99.9%) and silica (SiO_2, Chempur, 99.99%) by solid state reaction. The Yb_2O_3-SiO_2 powder mixture in the molar ratio of one, according to the phase diagram[20], was homogenized by milling in a planetary mill for 2 h, using acetone as wetting agent and silicon nitride grinding beaker and balls. The dried mixture was charged into a zirconia crucible and heat treated in air (Nabertherm HT 08/17 High Temperature furnace) at 1200°C, 1400°C and 1600°C for 20 h at each temperature. Between each sintering step the material was crushed in a mortar followed by grinding in a planetary mill for 1h. The progress of the solid state reaction was analyzed by X-ray diffractometry (XRD, Philips X'Pert PW3040). Finally the obtained ytterbium silicate was milled again and the grain size fraction < 32 μm was used as sintering additive.

The mixtures of powders adjusted by weight to Si_3N_4 / 10 wt% Yb_2SiO_5 were dispersed in acetone and homogenized in a planetary mill for 4 h. The solvent was removed by evaporation. The dried soft agglomerated powders were crushed and screened through a 125 μm sieve. Cylindrical samples of 10 g weight encapsulated and sealed in rubber bags were compacted by cold isostatic pressing at 40 MPa.

Additionally, three powder batches were prepared by replacing a part of the ytterbium silicate phase by the ytterbium oxide phase in different molar ratios (Yb_2O_3:Yb_2SiO_5 = 1:1, 1:2 and 2:1) retaining the additive amount of 3.2 mol% Yb-ions, as shown in Table I. The starting oxygen content of the Si_3N_4 powder (1.48 %) was taken into account, assuming a thin SiO_2 layer on the silicon nitride particles.

Table I. Composition of silicon nitride samples

Sample ID	Composition	x (Si_3N_4) [mol%]	x (Yb_2O_3) [mol%]	x (Yb_2SiO_5) [mol%]	x (SiO_2) [mol%]	w (Si_3N_4) [wt%]	w (Yb_2O_3) [wt%]	w (Yb_2SiO_5) [wt%]	w (SiO_2) [wt%]	c(Yb) [at%]
10wYbs	10 wt% Yb_2SiO_5	90.74	0	3.20	6.06	87.50	0	10.00	2.50	0.94
9-1-1	Yb_2O_3:Yb_2SiO_5 = 1:1	90.74	1.60	1.60	6.06	88.08	4.37	5.03	2.52	0.95
9-1-2	Yb_2O_3:Yb_2SiO_5 = 1:2	90.74	1.07	2.14	6.06	87.89	2.90	6.70	2.51	0.95
9-2-1	Yb_2O_3:Yb_2SiO_5 = 2:1	90.74	2.14	1.07	6.06	88.28	5.84	3.36	2.52	0.95

The samples were placed in a silicon nitride powder bed (H.C. Starck, grade M11) in an alumina fiber insulation casket (KVS 174/400, Rath). Sintering was performed at ambient pressure in a high temperature horizontal tube furnace (type T.H., Thermal Technology, Degussit® Al23 alumina tube) at three different temperatures, 1700°C, 1725°C and 1750°C, respectively, with heating and cooling rates of 5 K min^{-1} and a dwell time of 180 minutes. The first set of experiments has been carried out under nitrogen atmosphere during the complete sintering schedule; the second set was conducted using argon during heating-up and nitrogen during dwell time and cooling. The exchange of sintering atmosphere from argon to nitrogen was achieved by repeated evacuation of the tube down to 300 mbar and refilling it with nitrogen three times at the beginning of each dwell time.

Weight loss and shrinkage behavior were recorded by measuring weight and size changes. XRD measurements of the crystalline grain boundary phases developed in the core region and in the surface near region were performed on the cross section of polished samples (SiC, 4000 mesh).

Microstructure characterization on the polished cross sections was performed by scanning electron microscopy and EDX (SEM, JEOL, JSM-840), using secondary electrons and backscattered imaging (BSE), to characterize additive distribution in the green state and in the heat treated samples. Mercury porosimetry was used to investigate the changes in pore size distribution of the sintered samples. The bulk density was measured via the Archimedes method using water as immersion liquid.

RESULTS AND DISCUSSION

Additive Synthesis

Because the used additive Yb_2SiO_5 was not commercially available the silicate was synthesized stepwise by solid state reaction at different temperatures.

$$Yb_2O_3 + SiO_2 \rightleftharpoons Yb_2SiO_5 \qquad (1)$$

The adjustment of additive distribution in the silicon nitride green parts with 10 wt% Yb_2SiO_5 was investigated depending upon the milling time.

As visible in Figure 1, the results of BSE-imaging show, that the higher the milling time the smaller the agglomerate size and the more homogeneous the distribution of the additive in the green part. Large spots indicate the presence of coarse grains or agglomerates of the additive.

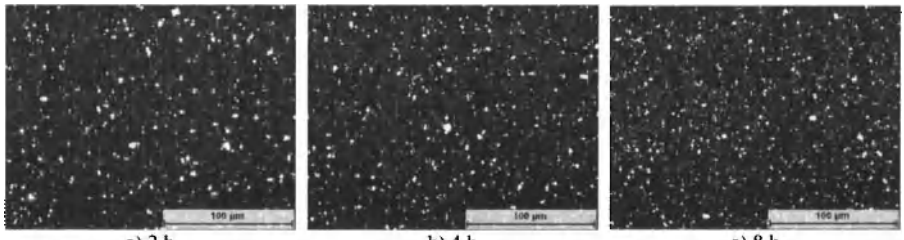

a) 2 h b) 4 h c) 8 h

Figure 1. Backscattered electron images of green compacts of Yb_2SiO_5 containing Si_3N_4-samples after a) 2 hours, b) 4 hours and c) 8 hours milling time in planetary mill. The light spots are the additive grains or agglomerates distributed in the green compacts (black)

However, after 8 hours of ball milling there are still larger Yb_2SiO_5 crystallites present in the green compact. They were removed by sieving; only the fraction below 32 µm was utilized for sintering experiments.

The reduction of specific surface area of the starting Si_3N_4-powder upon addition of 10wt% of the Yb-silicate is significant, as shown in Table II.

Table II. Comparison of surface area after different milling time

		BET surface [m^2/g]	d_{50} [µm]
Si_3N_4-M11(hP)		13.69	0.6
10 wt% Yb_2SiO_5	2h milling time	11.11	1.8 (Yb_2SiO_5)
	4h milling time	11.69	
	8h milling time	11.84	

The drop in surface area in comparison to the starting powder is due to the coarse grain size of the synthesized additive Yb_2SiO_5, apparent from the median grain size values in Table II. With prolonged milling time there is no significant increase in surface area; therefore most probably milling only reduces the agglomerate size, not the primary particle size of the silicate. However, a longer milling

time has an effect on the weight loss during sintering. After sintering at 1700°C for 3h in nitrogen weight losses of 2.7%, 3.2% and 3.9% for 2h, 4h and 8h milling time, respectively, are observed, whereas the shrinkage rate remains constant at 20 %.

Porous Sintered Silicon Nitride

The microstructure of the heat treated samples is shown in Figure 2. In all sintered samples a complete α to β transformation of silicon nitride was achieved, as confirmed by X-ray diffraction measurements. A network of β-Si_3N_4 grains with high aspect ratio has developed during sintering, embedded in an ytterbium rich grain boundary phase as indicated by the BSE signal. Upon increase in soaking temperature from 1700°C to 1750°C the amount of grain boundary phase is significantly increased and a larger fraction of the β-Si_3N_4 grains is covered by it.

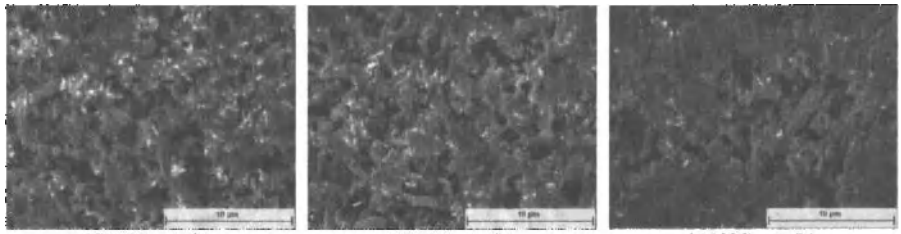

1700°C - Ar/N_2 1725°C - Ar/N_2 1750°C - Ar/N_2

Figure 2. Microstructure in the bulk region of Si_3N_4-10 wt% Yb_2SiO_5 ceramics sintered at different temperatures in argon atmosphere during heat up (BSE images)

The composition of the starting Yb-additive has a strong influence on the microstructure upon sintering, as shown in Figure 3. Samples with nominally the same molar amount of Yb-ions in the additive but mixed from Yb_2SiO_5 and Yb_2O_3 show a very inhomogeneous distribution of the additive phase as compared to pure Yb_2SiO_5. The Yb-containing phase is accumulated into dendrite-like areas, which are almost dense. In the remaining areas porous, almost Yb-free Si_3N_4 is found.

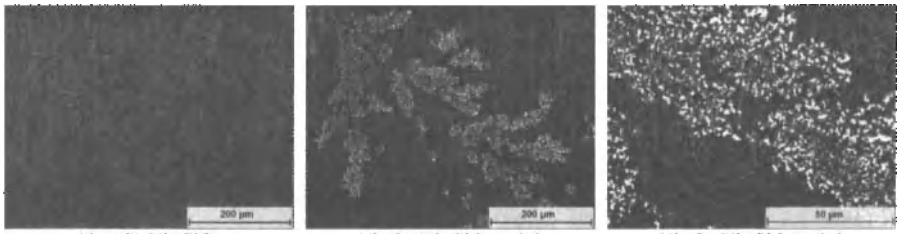

10 wt% Yb_2SiO_5 Yb_2O_3:Yb_2SiO_5 = 1:1 Yb_2O_3:Yb_2SiO_5 = 1:1

Figure 3. BSE images of bulk region of different samples sintered at 1750°C under nitrogen atmosphere showing inhomogeneous distribution of ytterbium in dendrite like, Yb-rich and porous, Yb-free areas.

For any type of structural application of sintered silicon nitride at elevated temperatures such inhomogeneous. Yb-rich areas inside the bulk of the material have to be avoided.

In the surface near region, such an Yb-rich phase could be useful as dense coating, which could protect the bulk porous ceramic from corrosion.
Such a graded distribution of the Yb-containing phase is observed for samples containing only Yb_2SiO_5 as additive. Whereas a homogeneous, Yb-depleted grain boundary phase distribution is found in the bulk of the sample, as shown in Figure 2 and 3, an Yb-rich phase is accumulated in the outer region of the sample, which was in contact with the Si_3N_4 powder bed, as shown in Figure 4.
This Yb-rich phase has an extension of some hundred micrometers, as shown in Figure 4 by the backscattered electron images of the cross section of the samples.

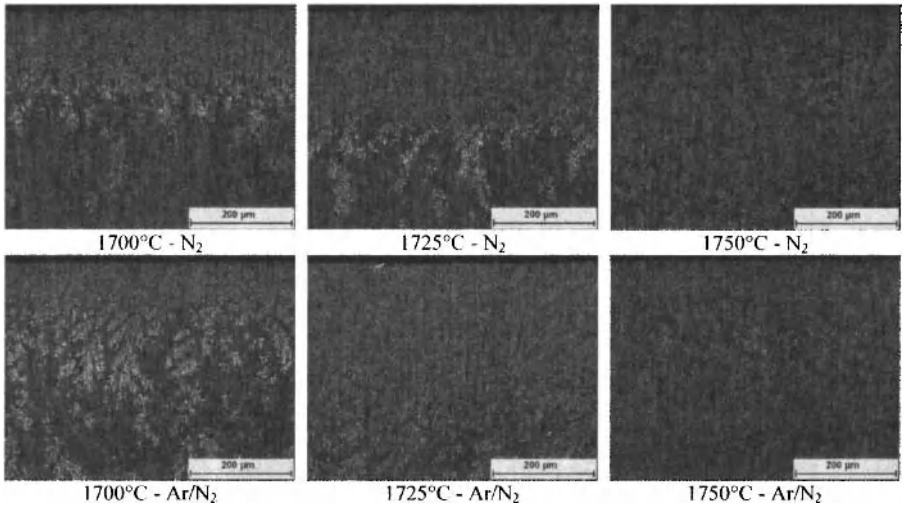

Figure 4. BSE images of the sample cross section near the surface in 10 wt% Yb_2SiO_5 containing Si_3N_4 samples sintered at 1700°C, 1725°C and 1750°C in different atmospheres during heating up

As visible from the upper images in Figure 4, the size of the outer ytterbium rich scale is growing with increased sintering temperature. The composition of this scale is affected by changing the atmosphere during the heating up from argon to nitrogen gas. A darker boundary zone represents Yb-depletion of the scale, seen for samples heated in argon prior to soaking in nitrogen. With increased soaking temperature the Yb-depleted zone becomes broader, reaching a depth of about 200 µm after 180 minutes soaking at 1750°C.

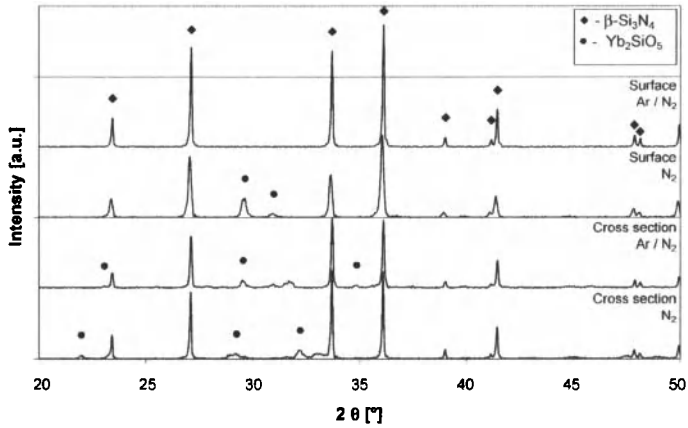

Figure 5. XRD diffraction pattern of the 10 wt% Yb_2SiO_5 samples sintered at 1750°C for 3h, heated up in different atmosphere, comparison of cross section with surface composition

On principle, the depletion of Yb can be caused by loss of Yb into the surrounding Si_3N_4-powder bed or by preferential dissolution of the Yb-additive into the bulk, if solid state reactions would take place only. The phase composition of the samples sintered with exchange of atmosphere is significantly different as compared to the material sintered in nitrogen only, as revealed from XRD-measurements. In Figure 5 the bulk composition and the surface composition of Si_3N_4-10wt%Yb_2SiO_5 is shown for two different sintering atmospheres. Whereas there are no significant differences in crystalline phases developed in the bulk of the silicon nitride samples, there is a difference when comparing the surface composition. The Yb-depletion of the surface region already detected by BSE-SEM is confirmed by XRD: this sample has no crystalline Yb_2SiO_5 in the surface.
Therefore enrichment of the bulk of Si_3N_4 with Yb-silicate upon sintering with atmosphere exchange from Ar to N_2 is quite unlikely. But the strong temperature dependence of the scale formation can also indicate a contribution of material transport due to evaporation. The effect of evaporation and condensation mechanisms during sintering with increased temperature and different atmosphere can be analyzed by comparison of weight losses and densification, as shown in Table III and Figure 6.
As known from liquid phase sintering of silicon nitride ceramics in protective powder beds there is an increase of weight loss with increasing sintering temperature.[21]

Table III. Weight loss [%] of samples during sintering

Temperature	1700°C		1725°C		1750°C	
Atmosphere	Nitrogen	Argon / N_2	Nitrogen	Argon / N_2	Nitrogen	Argon / N_2
10wYbs	3.2	3.9	3.6	4.4	4.6	6.1
9-1-1	2.4	3.5	3.6	4.2	4.7	5.7
9-1-2	3.1	4.2	4.3	5.0	5.3	6.4
9-2-1	3.2	4.0	4.3	4.8	5.2	6.3

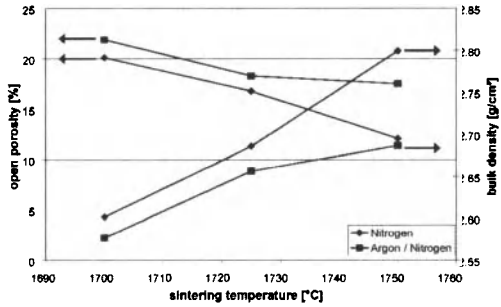

Figure 6. Open porosity and bulk density for Si_3N_4-10 wt% Yb_2SiO_5 sintered under different atmospheres during heat up

With increasing sintering temperature the open porosity decreases and the bulk density increases. Use of argon upon heat up causes a higher porosity in the sintered material. Therefrom some evidence is given, that Yb-containing volatile phases are released to the surrounding. Because the Yb-content is different between samples sintered in mixed atmosphere condition as compared to N_2, the small difference in open porosity is accompanied by a large difference in bulk density, with the Ar/N_2-samples showing a lower specific density and a slightly higher open porosity, as visible in Figure 6. But because of Yb-loss the large decrease in bulk density does not correspond with the rather small increase in open porosity.

The increased open porosity of samples sintered under mixed atmosphere condition is also confirmed by porosity measurement results, as shown in Figure 7. The mixed atmosphere sintered samples develop approximately 10% more open porosity as compared to the N_2-sintered ones, particularly at the highest soaking temperature.

In terms of pore size distribution all sintered materials are very similar, showing a monomodal pore size distribution, with an average pore size of 0.5 µm as compared to <0,1 µm in the green sample, which were compacted by CIP to 60% theoretical density. The large pore size corresponds well with the size of the elongated β-Si_3N_4-grains, which form the porous network, as visible in Figure 3.The total open porosity is decreasing with increasing sintering temperature.

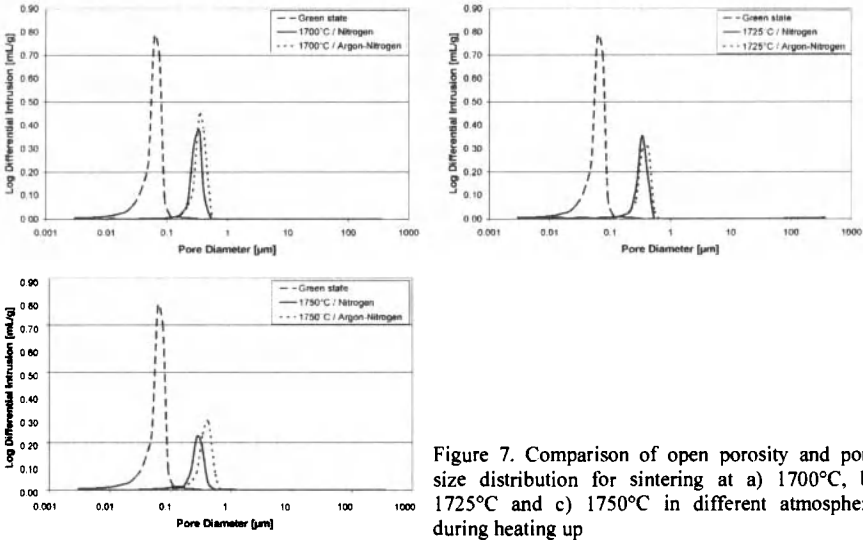

Figure 7. Comparison of open porosity and pore size distribution for sintering at a) 1700°C, b) 1725°C and c) 1750°C in different atmosphere during heating up

CONCLUSIONS

It has been demonstrated that ytterbium silicate Yb_2SiO_5 is a better additive for the fabrication of porous silicon nitride ceramics as Yb-oxide or mixtures of the Yb-oxide and Yb-silicate, in terms of homogeneity of microstructure and Yb-content in the bulk of the ceramic.

A complete α to β -Si_3N_4 transformation is achieved with 3.2mol% additive content, corresponding to 10wt%. A gradient of Yb-containing phase is obtained, with increasing Yb-content in the surface near region and low Yb-content in the bulk of the ceramic. The extension of this graded composition can be modified by the composition of the sintering atmosphere while a Si_3N_4-powder bed is applied to adjust the silicon and nitrogen activity in the surface near region of the samples. When argon is used during heat up and nitrogen during soaking an Yb-silicate free surface near region is obtained. Beneath this region an Yb-rich, dense zone is developed, which can seal the porous ceramic against further weight loss by evaporation of volatile oxynitrides.

The presented work shows the potential for production of porous silicon nitride ceramics containing refractory grain boundary phases and having a "naturally grown" coating build up from volatile Yb-compounds during sintering.

Future work will investigate whether the growth mechanism of the elongated β-Si_3N_4 grains occurs by super-saturation and crystallization from a liquid phase or whether some contribution of gas phase reactions is present.

ACKNOWLEDGEMENTS

The financial support of German Science Foundation within the Graduate School 1229 is gratefully acknowledged.

REFERENCES

[1]Riley, F.L., Silicon Nitride and Related Materials, *J. Am. Ceram. Soc.*, **83**(2), 245-265 (2000).
[2]Shigegaki, Y., et al., Strain Tolerant Porous Silicon Nitride, *J. Am. Ceram. Soc.*, **80**(2), 495-498 (1997).
[3]Kondo, N., et al., Fabrication and Mechanical Properties of Porous Anisotropic Silicon Nitride with Lutetia Additive, *J. Cer. Soc. Japan*, **112**(6), 316-320 (2004).
[4]Kawai, C. and A. Yamakawa, Effect of Porosity and Microstructure on the Strength of Si_3N_4: Designed Microstructure for High Strength, High Thermal Shock Resistance, and Facile Machining, *J. Am. Ceram. Soc.*, **80**(10), 2705-2708 (1997).
[5]Inagaki, Y., T. Ohji, and S. Kanzaki, Fracture Energy of an Aligned Porous Silicon Nitride, *J. Am. Ceram. Soc.*, **83**(7), 1807-1809 (2000).
[6]Kondo, N., et al., Fabrication of porous anisotropic silicon nitride by using partial sinter-forging technique, *Mat. Sci. Eng. A*, **335**(1-2), 26-31 (2002).
[7]Yang, J.-F., Z.-Y. Deng, and T. Ohji, Fabrication and characterisation of porous silicon nitride ceramics using Yb_2O_3 as sintering additive, *J. Europ. Ceram. Soc.*, **23**(2), 371-378 (2003).
[8]Inagaki, Y., N. Kondo, and T. Ohji, High performance porous silicon nitrides, *J. Europ. Ceram. Soc.*, **22**(14-15), 2489-2494 (2002).
[9]Kondo, N., et al., High-temperature mechanical properties of sinter-forged silicon nitride with ytterbia additive, *J. Europ. Ceram. Soc.*, **23**(5), 809-815 (2003).
[10]Cinibulk, M.K. and G. Thomas, Oxidation behaviour of rare-earth disilicate-silicon nitride ceramics, *J. Am. Ceram. Soc.*, **75**(8), 2044-2049 (1992).
[11]Cinibulk, M.K. and G. Thomas, Fabrication and secondary-phase crystallization of rare-earth disilicate-silicon nitride ceramics, *J. Am. Ceram. Soc.*, **75**(8), 2037-2043 (1992).
[12]Cinibulk, M.K. and G. Thomas, Strength and Creep Behavior of Rare-Earth Disilicate-Silicon Nitride Ceramics, *J. Am. Ceram. Soc.*, **75**(8), 2050-2055 (1992).
[13]Hong, Z.L., et al., The effect of additives on sintering behavior and strength retention in silicon nitride with RE-disilicate, *J. Europ. Ceram. Soc.*, **22**(4), 527-534 (2002).
[14]Nishimura, T., et al., Improving Heat Resistance of Silicon Nitride Ceramics with Rare-Earth Silicon Oxynitride, *J. Cer. Soc. Japan*, **114**(11), 880-887 (2006).
[15]Park, H. and H.-E. Kim, Microstructural Evolution and mechanical properties of Si_3N_4 with Yb_2O_3 as a sintering additive, *J. Am. Ceram. Soc.*, **80**(3), 750-756 (1997).
[16]Liu, Y., et al., Secondary crystalline phases and mechanical properties of heat-treated Si_3N_4, *Material Science and Engineering*, **A363**, 93-98 (2003).
[17]Herrmann, H., et al. High temperature properties of silicon nitride materials with rare-earth additives. in International Symposium on Ceramic Materials and Components for Engines. 1994, 211-214, Shanghai: World Scientific.
[18]Lo, W.-T., et al., The effects of ytterbium oxide on the microstructure and R-curve behaviors of silicon nitride, *Materials Chemistry and Physics*, **73**, 123-128 (2002).
[19]Jinhui, D., L. Jianbao, and C. Yongjun, The phase transformation behavior of Si_3N_4 with single Re_2O_3 (Re = Ce, Nd, Sm, Eu, Gd, Dy, Er, Yb) additive, *Materials Chemistry and Physics*, **80**, 356-359 (2003).
[20]Toropov, N.A. and I.A. Bondar, Silicate of rare earth elements. VI. Phase diagrams for the binary systems Sm_2O_3-SiO_2 and Yb_2O_3-SiO_2 and a comparison of them with silicates of other rare earth elements, *Uch. Zap. Kazan. Gos. Univ.*, **8**, 1372-1379 (1961).
[21]Lee, S.-H., et al., Effects of powder bed conditions on the liquid-phase sintering of Si_3N_4, *J. Mater. Res.*, **17**(2), 465-472 (2001).

Advanced Processing and Manufacturing Technologies
for Structural and Multifunctional Materials II
Edited by Tatsuki Ohji and Mrityunjay Singh

R-SiC FOR NOVEL GEL-CAST CROSS FLOW FILTER

J. Homa, S. Zellhofer, A. Liersch, J. Stampfl
Vienna University of Technology
Vienna, Austria

ABSTRACT

Currently most of the ceramic Diesel Particulate Filters (DPFs) are produced in a honeycomb shape by extrusion. Alternate plugging of the channels on the front and back side forces the gas to flow through the walls and inorganic ashes are accumulated in the filter. Cross flow filters can avoid this accumulation by introducing a removable ash-chamber. This paper describes the production process of cross flow DPFs made of recrystallized silicon carbide (RSiC) by gelcasting in combination with different wax mold fabrication techniques. Since a low viscosity slurry is crucial for a complete filling of the mold, the effects of different SiC powders on the slurry rheology have been examined. The sinter mechanism of RSiC is briefly described and the influence of different parameters is explained. The material was as well examined with respect to its mechanical and thermal properties. It is shown that both the flexural strength and the thermal conductivity are strongly dependent on the average pore diameter.

INTRODUCTION

Particulate filters are necessary to reduce the emission of particulate matter of diesel engines, because these emissions are restricted by the European Union, USA and other countries due to a potential health risk. Diesel particulate filters (DPF) invented in the early 1980 are still mainly extruded in a honeycomb shape and made of porous ceramics[1]. There are as well other materials and other types of filters available, but porous wall flow filter made of recrystallized silicon carbide (RSiC) or cordierite are mostly in use for a high efficiency diesel particulate filtration[2]. A scheme of a honeycomb shaped DPF with porous walls is depicted in Figure 1. The exhaust gas enters the filter through the inlet channels, which are plugged at the rear side, is filtered through the porous walls and the purified gas leaves the filter through the outlet channels, which are plugged at the front side. After a certain amount of particulate matter has been filtered, the particles have to be burnt off. Different regeneration mechanisms and strategies can be applied[3]. Since only organic material can be burnt off, the inorganic ashes, which steam from motor wear and fuel additives, are accumulated in the filter and reduces the effective filter volume gradually from the rear side and finally causes a complete breakdown of the filter[4].

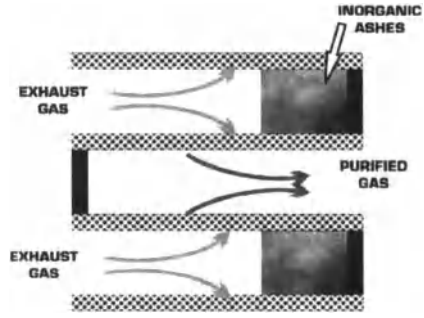

Figure 1. Scheme of a honeycomb DPF.

MATERIAL SELECTION FOR DPFS

Ceramics are very good materials for DPF applications due to their high thermal stability and corrosion resistance. Filter materials are exposed to temperatures from –30°C to 900°C (or locally even more) and during regeneration temperature gradients up to 500°C/cm occur. Naturally the melting point of the material should be higher than the maximum temperatures during regeneration. A low coefficient of thermal expansion (CTE) is favorable to minimize the thermal stresses, which emerge due to temperature gradients. Temperature gradients are minimized when using materials with high thermal conductivity. A low heat capacity of the material is on the one hand good, because the filter does not need so much energy for heating up to trigger the regeneration and therefore diminish the fuel consumption. On the other hand a material with high heat capacity can absorb the heat which is generated during regeneration which helps to avoid hot spots[1]. Additionally to good thermal properties the material should have a high filtration efficiency with a low pressure drop. Filtration efficiency is measured in terms of the mass or number of particles removed from the gas flow, which is mainly determined by the porosity, average pore diameter, pore size distribution and pore connectivity. Highly porous materials are very good in terms of low pressure drop but high porosity compromises high strength, which is important for the canning of the filter and to withstand the vibrations during the application in a vehicle. A low elastic modulus corresponds with low stresses at given strains. Due to the fact that many material parameters are important for the selection of the material, no perfect material exists, but has to be matched with the regeneration strategy, application and costs[1]. SiC has been the main filter material for DPFs but other material like cordierite, aluminum titanate and mullite are emerging[5]. In Table 1 the most important thermal and mechanical properties of different porous DPF materials are depicted.

Table 1. Mechanical and thermal properties of porous DPF candidate materials[1, 6, 7, 8]

Material	CTE (10^{-6}/°C)	Young's modulus (GPa)	Strength (MPa)	Thermal conductivity @ 500°C (W/m K)	Melting Temperature (°C)	Heat Capacity @ 500°C (J/g °C)
Cordierite	0,6	11	8	1	1460	1,11
Mullite	5,3	30	30	2	1810	1,15
Aluminum Titante	1	1,45	1,47	1	1600	1,06
α-bond SiC	4,5	49	53	20	2400	1,12

RECRISTALLIZED SILICON CARBIDE FOR DPFS

Silicon Carbide is the most common material for DPF applications, although it has a high CTE, which leads to cracks during regeneration. This problem can be handled by either using split-type DPF, where small filter segments are put together with a cement or by increasing the bulk density of the whole filter, which increases the thermal mass to adsorb the heat, but this will in succession increase the fuel consumption due to a higher pressure drop and due to a higher need of heat to initiate the regeneration [4,9]. Another major drawback of SiC is the expensive raw material and the expensive post processing. The sintering has to be conducted in an inert atmosphere and temperatures up to 2200°C need to be reached. But due to the high sintering temperature (which is actually a sublimation temperature), SiC would hardly react with compounds in the exhaust gas and it can be used up to high temperatures. A main advantage of SiC is its high thermal conductivity which is approximately one order of magnitude higher than comparable DPF materials. The heat produced during regeneration can be diffused more easily and hot spots, which generates high temperature gradients can be avoided. Furthermore the sintered material has a high mechanical strength which is favorable for canning and a good resistance to vibration in the vehicle.

CROSS FLOW FILTER

As mentioned above the prevailing design of wall flow DPFs is the extruded honeycomb shape with alternate plugged channels. The plugging of the inlet channels leads to a clogging of the filter with inorganic ashes and finally to a breakdown of the filter[4]. To handle this problem a cross flow filter was designed (see Patent WO 2005/033477 A1[10]), where the outlet channels are orthogonal to the inlet channels and the inorganic ashes are collected in an ash-chamber, which can be removed. As shown in Figure 2 the exhaust gas enters the filter opposite to the ash-chamber and after filtration through the porous walls exits orthogonal to the inlet channels.

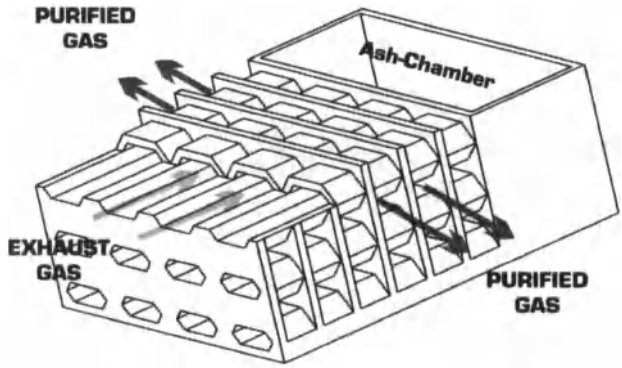

Figure 2. Scheme of a cross flow DPF.

Since the cross flow structure cannot be produced by extrusion other fabrication techniques have to be applied. Generative fabrication techniques are capable of producing such designs, but are not useful for a larger scale production. Another approach is the lamination of wavy ceramic foils, but due to the fact that cement is used to bond the layers, they tend to delaminate during thermal stresses because the cement and the foils have different coefficients of thermal expansion[11]. Cross flow structures can also be gelcast with hard tools, but since the design of the cross flow filter in Figure 2 has internal undercuts, the tool cannot be removed without destroying the parts[12]. But by the combination of gelcasting and a lost mold made of wax every design can be produced[13]. Gelcasting is a slurry based forming technique, where a low viscosity slurry, consisting of ceramic or metallic powder, a solvent, dispersant and two organic monomers, is poured into a mold and polymerized in situ. The polymerization is triggered by a free radical initiator and a catalyst and thereby forming a firm polymer-solvent gel matrix which immobilizes the particles in the desired shape of the mold. After drying the parts may be machined then they are debinded and sintered[14,15]. The wax mold can either be produced by a generative fabrication process, e.g. Soldidscape wax-printer, or by stacking two different sort wax layers to form the mould. These wax layers can be produced by either milling or injection molding. Since the costs for design alterations and the lead time for milling and injection molding is rather high the generative approach with the Solidscape wax-printer is very useful for the evaluation of the design but it is very slow. Injection molding should be chosen if the design is fixed and if a high amount of molds is necessary. In Table 2 the lead time and build speed of the different fabrication techniques is summarized (for further details see [11]).

Table 2. Lead time and build speed for different building strategies

Build Strategy	Lead Time	Build Speed
Solidscape wax-printer	1 h	1 – 10 cm^3/h
Milling	3 – 5 days	20- 200 cm^3/h
Injection Molding	4 -6 weeks	10 000 to 100 000 cm^3/h

Figure 3 shows a concept model of a cross flow DPF with a constant wall thickness of 0,5 mm and the hexagonal inlet channels have a cross section of 3,8 mm^2. This model was cast into an RP-mold made with the Solidscape wax-printer and has a total volume of 25 x 36 x 65 mm^3. Larger models cannot be build that way because larger parts (50 x 50 mm^2 base) with fine structure tend to break and curl due to thermal stresses and the build times become inhibitively high.

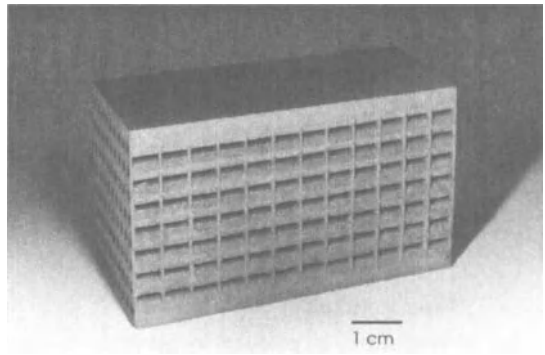

Figure 3. Cross flow DPF model made with a Solidscape wax-printer mold.

For the production of larger prototypes milling of wax layers is the more appropriate technique because hardly any tool cost occur but it is still too slow for a larger scale production. The filter shown in Figure 4 was cast into a mold, which was produced by stacking two different kind of wax layers, which where milled by a CNC-machine. The DPF has a total volume of 90 x 90 x 40 mm^3, an inlet cross section of 32 mm^2 and a wall thickness of 1 mm.

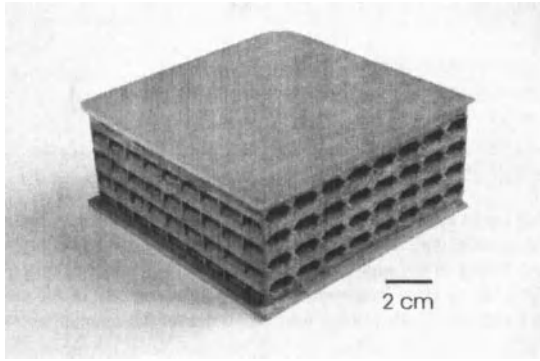

Figure 4. Cross flow DPF model made by stacking milled wax layers to a mold.

Two above mentioned fabrication techniques are only suitable for concept and design models, because of the attainable dimensions and wall thickness, respectively. The wax layers have to be injection molded for the production of filters with a higher volume and a small wall thickness at the same time. This fabrication technique should be suitable for a production on a larger scale. Figure 5 shows a filter which was cast in a mold, where the layers have been injection molded with a constant wall thickness of 0,45 mm, a filtration area of 0,36 m^2/l and the cell density of 14 cpsi (single count).

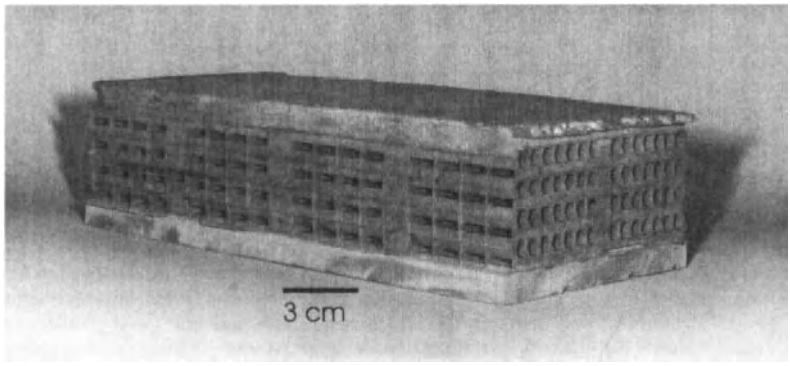

Figure 5. Cross flow DPF made by stacking injection molded wax layers to a mold.

SLURRY PREPARATION

As mentioned above a gelcasting slurry was used for filling the molds. Compared to slip casting non porous molds can be used and the material properties are more homogenous through the whole body and there is no limitation on the complexity of the parts. The gelcasting slurry consists of the following components shown in Table 3:

Table 3. Components of the slurry

Amount	Material
5 g	gel forming monomer (Methacrylamide)
15 g	cross linking monomer (N,N' – Methylenebisacrylamide)
50 g	deionised water
0,5 g	dispersant (Tetramethylammonium hydroxide)
200 g	SiC (mixture of fine and coarse grain)

After ball milling for at least 12 h all agglomerates have been broken and the components are perfectly mixed. The thinner the wall thickness of the resulting filter, the less viscous the slurry has to be to achieve a complete filling of the mold. In Figure 6 the typical shear thinning behavior of an SiC slurry over a wide range of shear rates is shown. But since the shear rate of the slurry during filling is approximately between 1 and 100 1/s this range was examined for the comparison of different slurries.

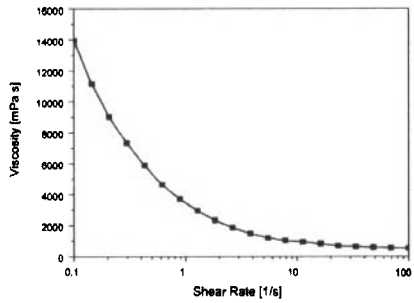

Figure 6. Viscosity of the SiC-slurry in dependence of the shear rate.

A high viscosity slurry is detrimental for filling a mold with very narrow sluts (down to 0,3 mm) therefore a rheology study was conducted for the determination of the slurry with minimum viscosity. Since the volumetric filling level must reach a certain level to avoid cracking and to ensure a good sintering, the powders were altered. The fabrication of porous silicon carbide materials requires a bimodal powder distribution and therefore the size of the coarse and fine grain powders can be adjusted. Figure 7 shows the viscosity of different coarse grain powders in the gelcasting slurry with the same fine powder. The viscosity of the slurry decreases with increasing mean grain size diameter. It has to be noted that the choice of the coarse powder is not only dependent on the rheological properties of the slurry, but also on the desired mean pore diameter of the sintered filter material.

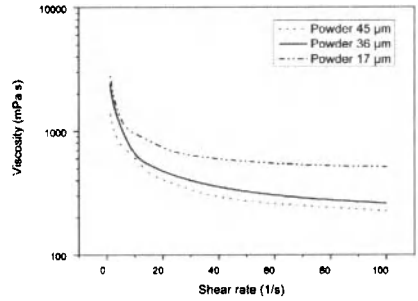

Figure 7. Viscosity of slurry with different coarse grain powders.

Figure 8 shows the effect on the viscosity when the fine fraction is altered. The viscosity decreases with decreasing mean particle size, which is favorable because finer powders have a higher sintering activity and therefore sintering can be conducted at lower temperatures. Disadvantageous is the increasing price of the powder with decreasing particle size.

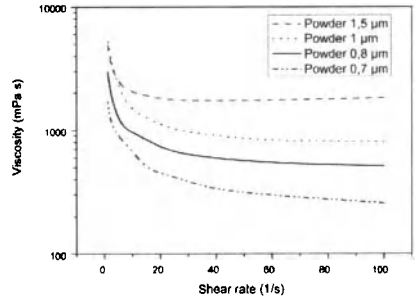

Figure 8. Viscosity of slurry with different fine grain powders.

SINTERING OF RSIC

The dominating sinter mechanism for recrystallized silicon carbide (RSiC), which consist as mentioned above of a bimodal distributed powder is a gas-phase sintering mechanism, where the fine grain powder undergoes an evaporation - condensation-mechanism. The vapor pressure of the fine grains is higher than that of the coarse grain and the fine grain vanishes at the expanse of the coarse grain. This consolidation – evaporation-process, where no shrinkage occur, will not be finished as long as there are still some fine grain particles. The evaporating fine particles condensate on the neck between the coarse particles and fuse them together. Since this is a non-shrinkage mechanism no densification of the body occurs and this results in an inherent open porosity of the material[16,17]. This sinter mechanism can be suppressed in the presence of only a small amount of elemental carbon, which is used in the solid sintered SiC (SSiC). Hence all organic binder has to be removed prior to sintering

to ensure the predominance of the gas-phase sintering mechanism. Therefore the burnout characteristics have been studied by thermal gravimetrical analysis (TGA) of the polymerized binder alone and of the gelcast sample in air and nitrogen. The removal of the binder in the gelcasted sample is actually an uncritical processing step compared to powder injection the molding. The very low binder content (5 to 10 wt%) and the previous drying of the specimen lead to hardly any cracks during debinding. Figure 9b and Figure 9c show the burnout characteristics in nitrogen and air of the green part and of the polymerized binder alone, respectively. It can be seen from both figures that there is in either cases a residue left, which is mainly elemental carbon, if debinded in nitrogen, whereas hardly any residue is left in air. If the burnout is conducted in air SiC can oxidize to SiO_2 at elevated temperatures. Figure 9a shows the weight gain of the fine grain SiC particles during oxidation in air. Some SiO_2 is generated even under 600 °C, where the debinding usually takes place, but this is not so crucial as the elimination of the elemental carbon.

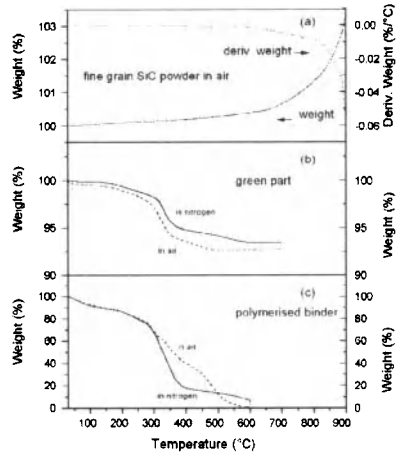

Figure 9. TGA analysis.

Not only the elimination of the elemental carbon is crucial for a gas phase sintering of RSiC, but as well the grain size of both the fine and coarse particles. As with any other ceramic material the sinter activity of the fine powder fraction, which seems to be exclusively responsible for this sinter mechanism, rises with decreasing grain size. But the size of the coarse grain does also have a significant influence on the sintering behavior of the material. Originally the contact points of the coarse grains where favored as the first sinks for the consolidation, because of their concave character, but it is assumed that special lattice defects act as first sinks for this mechanism[16]. Following the original theory would result in a higher sinter activity if the coarse grain fraction would have bigger particles. Two specimen are shown in Figure 10, which were sintered at the same temperature and with the same fine powder fraction. On the left side all fine particles have vanished and the coarse particles, which have a diameter of 17 μm, have been rounded and are connected by a neck. The 70 μm big coarse particles on the right picture have still sharp edges and the fine powder fraction has not evaporated and consolidated yet. So the particle size of both the fine and the coarse powders are crucial for the RSiC sinter mechanism.

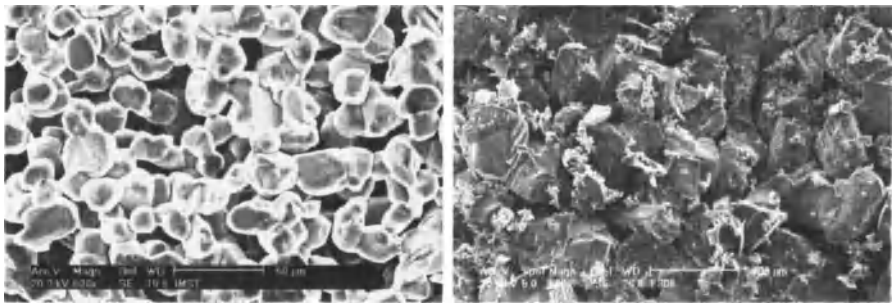

Figure 10. Completely sintered specimen with 17 µm coarse particle size (left) and partially sintered specimen with 70 µm coarse particle size (right).

Specimen with bigger coarse grain sized can be completely sintered at higher temperatures or with a more sinter active fine grain powder. The specimen in Figure 11 has the same coarse particle size as the one on the right side of Figure 10 but a smaller fine grain, which is completely vanished. The coarse grains are rounded but there is no neck formation and hence hardly any bonding between the grains.

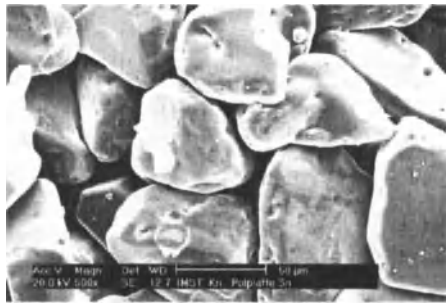

Figure 11. Completely sintered specimen with 70 µm coarse particle size but with hardly any neck formation.

MATERIAL PROPERTIES

For the evaluation of the material different mechanical and thermal properties of the material were determined. The Weibull modulus of sintered RSiC specimen with a coarse grain size of 17 µm was determined by 3-point bending test with a span width of 20 mm. The specimen (3 x 4 x >25 mm³) were tested as fired without chamfering the edges. The samples had a porosity of 39 % with an average pore radius of 4,6 µm. From Figure 12 a Weibull modulus of 10 was calculated by evaluating 30 samples.

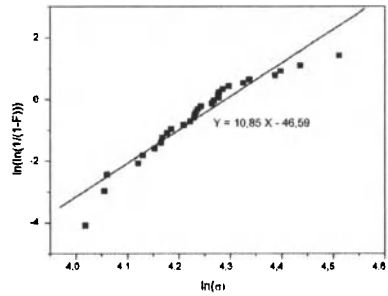

Figure 12. Weibull modulus of sintered RSiC.

The thermal shock resistance of the material was tested through water quenching and following 3 point bending test. The specimen were heated up with 1000 °C/h to the required temperatures and then quenched in water with 20 °C. As shown in Figure 13 the strength of the material does not decrease up to 400 °C temperature difference. At 600 °C temperature difference the strength deceases from about 70 ± 7 MPa to 54 ± 20 MPa, but no significant further decrease was detected up 1000 °C temperature difference.

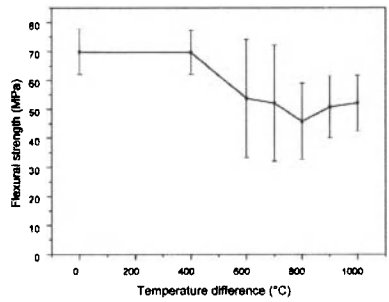

Figure 13. Influence of water quenching on the flexural strength of sintered RSiC specimen.

The strength of the material is furthermore dependent on the average pore radius which is shown in Figure 14. The flexural strength of the sintered specimen, which is indicated on the top of the picture, with a average pore radius of 4,6 µm is 60 ± 5,2 MPa and the one of the specimen with 9 µm average pore radius is only 4,8 MPa. The coarse grain size of the specimen is 17 µm and 35 µm, respectively. It should be further noted, that the pore size distribution is very narrow as shown in Figure 14 at the bottom and that the porosity of the two specimen is approximately the same with about 38 %. It should be noted that the pore size distribution of both specimen is very narrow, which is favorable for a low pressure drop in a DPF application.

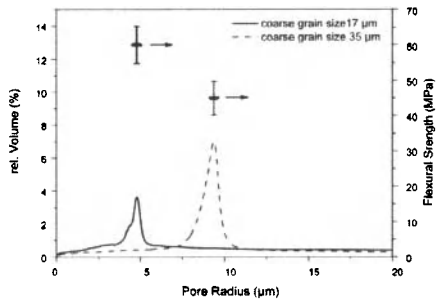

Figure 14. Pore size distribution and flexural strength of sintered RSiC specimen with coarse grain particle size of 17 µm and 35 µm, respectively.

The heat capacity of the material, which was measured by laser-flash calorimetry, is shown in Figure 15. There is no significant difference between the specimen with a coarse grain powder of 17 µm and 35 µm, respectively. The heat capacity of the material increases from 780 J/kg K at 100 °C to 1400 J/kg K at 900 °C.

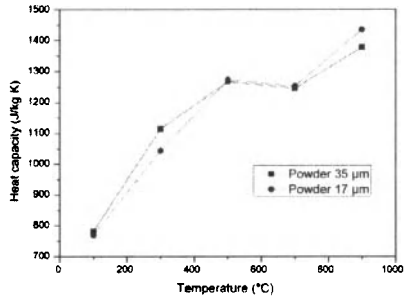

Figure 15. Heat capacity of sintered RSiC specimen with coarse grain particle size of 17 µm and 35 µm, respectively.

The thermal conductivity is dependent on the average pore radius of the material. As shown in Figure 16 there is a significant difference between the specimen with an average pore radius of 17 µm and 35 µm. The specimen with the smaller pore radius has a higher thermal conductivity of 36 W/m K at 100 °C and of 16 W/m K at 900 °C. The other specimen has a thermal conductivity of 20 W/m K at 100 °C and of 9 W/m K at 900 °C. It should also be noted that the relative difference of the thermal conductivity of the two specimen remains constant over the whole temperature range.

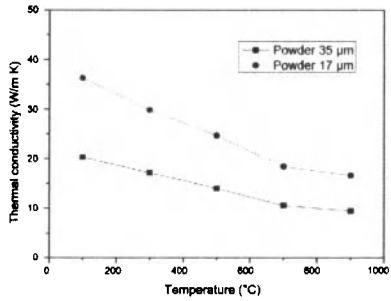

Figure 16. Thermal conductivity of sintered RSiC specimen with coarse grain particle size of 17 µm and 35 µm, respectively.

CONCLUSION

Cross flow filters with internal undercuts can only be produced by the combination of wax molds and gelcasting. Different mold fabrication techniques have been evaluated with respect to achievable wall thickness, size and building speed. RSiC was chosen for the production of the gelcasted cross flow filters and the material properties were analyzed. It could be shown that both the flexural strength and the thermal conductivity is significantly dependent on the average pore radius at the same porosity. The achieved flexural strength is higher than known from literature and the Weibull modulus is 10. Furthermore the sinter mechanism of RSiC has been described and it could be shown that the sinter mechanism is not only dependent on the fine powder fraction, but also on the coarse fraction.

ACKNOWLEDGEMENTS

Financial support by the Austrian Research Promotion Agency (FFG) under the project "Rapid Prototyping zellularer Keramiken" (Project-number: 810064) and Clean Air Technology is kindly acknowledged. The milling of the wax layers by the Fachhochschule Wiener Neustadt (University of Applied Science Wiener Neustadt) and the Institut für Fertigungstechnik (Vienna University of Technology) is kindly acknowledged. We also thank Prof. Bauer from the Institute of Solid State Physics (Vienna University of Technology) for conducting the laser-flash calorimetry measurements.

REFERENCES

[1] Cutler, Willard A., (2004), "Overview of Ceramic Material for Diesel Particulate Filter Applications", Ceramic Engineering and Science Proceedings, Vol. 25, No. 3, pp 421-430.

[2] Adler, Joerg, (2005),"Ceramic diesel particulate filters", International Journal of Applied Ceramic Technology, Vol. 2, No. 6, pp. 429-439.

[3] Khair, M. K., (2003), "A Review of Diesel Particulate Filter Technologies", SAE Paper 2003-01-2303.

[4] Shimato, K., Komori, T., Salvat, O., Ohno, K., Taoka, N., Ninomiya, T. and Santae, H., (2000), "Characterization of SiC-DPF for Passenger Car", SAE Paper 2000-01-0185.

[5] Johnson, T. V., (2007), "Diesel Emission Control in Review", SAE Paper 2007-01-0233.

[6] Pyzik, A. J. and Li, C. G., (2005), "New design of a ceramic filter for diesel emission control applications", International Journal of Applied Ceramic Technology, Vol. 2, No. 6, pp. 440-451.

[7] Bogner, T., Heibel, A.K., Rose, D., Cutler, W.A., Tennet, D.L., (2005), "Evaluation of New Diesel ParticulateFilters Based on Stabilized Aluminium Titanate", MTZ Motortechnische Zeitschrift, Vol. 66, No. 9.
[8] Schäfer-Sindlinger, A. and Vogt, C.D., (2003), " Filtermaterialien für die additivgestützte und katalytische Dieselpartikelreduktion", MTZ Motortechnische Zeitschrift, Vol. 64, No. 3.
[9] Young, D. M., Warren, C. J. and Gadkaree, K. P., Johanessen, L., (2002), "Silicon Carbide for Diesel Particulate Filter Applications: Material Development and Thermal Design", SAE Paper 2002-01-0324.
[10] Hoffschmied, B., Fend, T., Miebach, R., (2005), "Particulate Filter for an Internal Combustion Engine", PCT/EP2004/010177, WO 2005/033477 A1.
[11] Homa J., Zellhofer S. and Stampfl J., (2007) „Novel Fabrication Technique for Ceramic Filters", Proceedings of 10. International Conference and Exhibition of the European Ceramic Society 2007, in print.
[12] Vaubert, V., Stinton, D. P., Barra, C. and Limaye, S., (2001) "Appendix A: Design and Initial Development of Monolithic Cross-Flow Ceramic hot-gas Filters" in Vaubert, V., Armstrong, B., Janney, M., Walls, C., Stinton, D., Barra, C., Nagesvaran, R. and Limaye S., (2001) "Design and Development of a Ceramic hot-gas filter for Fossil Energy", CRADA Final Report, C/ORNL 97-0476, viewed 2 August 2007, < http://www.ornl.gov/~webworks/cppr/y2001/rpt/110061.pdf>.
[13] Stampfl, J., Liu, H., Nam, S., Sakamoto, K., Tsuru, H., Kang, S., Cooper, A. G., Nickel, A., Prinz, F. B., (2002), "Rapid Prototyping and Manufacturing by gelcasting of metallic and ceramic slurries", Materials Science and Engineering A, Vol. 334, No. 1-2, pp. 187-192.
[14] Janney, M. A., Omatete, O. O., (1991), "Method for molding ceramic powders using a water-based gel casting", US Patent 5,028,362.
[15] Janney, M. A., Omatete, O. O., Walls, C. A., Nunn, S. D. Ogle, R. J., Westmoreland, G.,(1998), "Development of low-toxicity gelcasting systems", Journal of the American Ceramic Society, Vol. 81, No. 3, pp 581-591.
[16] Kriegesmann, J. and Jodlauk J., (2002) „Characterizing the Consolidation of Bimodally Distributed Fine-Grained Silicon Carbide Powders", CFI Ceramic Forum International, Vol. 79, No. 12, pp. E37-E44.
[17] Kriegesmann, J., (2004), "Microstructure Control During Consolidation of Fine Grained Recrystallized Silicon Carbide", Key Engineering Materials, Vols. 264-268, No. III, Euro Ceramics VIII, pp 2199-2202.

Advanced Processing and Manufacturing Technologies for Structural and Multifunctional Materials II
Edited by Tatsuki Ohji and Mrityunjay Singh

REACTION BONDED SIC PROCESSED WITH TWO DIFFERENT TYPES OF CARBON PRECURSORS

Cristiane Evelise Ribeiro da Silva, M.Sc, Chemical Engineer
Federal of University Rio de Janeiro– Technology Center – PEMM/COPPE/UFRJ
Rio de Janeiro/RJ – BRAZIL

Célio A. Costa, Ph.D
Federal University of Rio de Janeiro – Technology Center – PEMM/COPPE/UFRJ
Rio de Janeiro/RJ – BRAZIL

Maria Cecília de Sousa Nóbrega, D.Sc.
Federal University of Rio de Janeiro – Technology Center – PEMM/COPPE/UFRJ
Rio de Janeiro/RJ – BRAZIL

ABSTRACT

Reaction bounded SiC were processed using 100% nanosize carbon and 100% petroleum coke as powder for carbon precursors. The materials were processed at 1550°C in vacuum for 30 min, where liquid silicon exists. The materials were examined by optical microscopy, scanning electron microscopy (SEM), Archimedes density, X-ray diffraction and Vickers microhardness.

It was found that nano carbon was less effective in producing SiC than petroleum coke. The volume fraction of residual Si (32 %) in the RBSiC processed from nano carbon was much higher then in petroleum coke (12 %). The microhardness in RBSiC made from petroleum coke was higher than in nano carbon sample.

1- INTRODUCTION

Ceramics processed by reaction bonding have been around since the 1950's. The main advantage of this process is related to the capability to produce complex shapes in an inexpensive way, good tolerance control and relatively low processing temperatures[1].

Densification by reaction bonding involves infiltrating molten silicon through the pores of a green body containing SiC and carbon. The silicon reacts with the carbon to form SiC, which bonds to others SiC grains. The excess of infiltrated molten silicon solidifies upon cooling, thereby filling the pores of the SiC body. This process is known as siliconization. The resulting product is a dense material, which contains SiC, residual free silicon and carbon. Since reaction bonding does not involve shrinkage of the green body, unlike conventional sintering, the final product has a nearly net shape[2,3,4,5].

Different from sintered SiC, the reaction-bonded SiC (RBSiC) is similar to a composite material, having silicon similar to a matrix. The mechanical properties are good and the service temperature is lower [6]. Nonetheless, the behavior is dominated by the failure of the Si matrix[7].

This paper deals with the effects of different carbon precursors to produce reaction bonded SiC. The nanosize carbon and petroleum coke were used as carbon precursors, resulting in different microstructures and amount of residual silicon; however, hardness was nearly the same.

2- MATERIALS AND METHODS

The raw materials used to process the RBSiC are listed in Table 1.

Table 1 – The raw materials used and their supplier.

Material	Formula	Supplier	Use	Purity (%)	d_{50} (mm)	Superficial area $g.m^{-2}$
Nanosize Carbon	C	Degussa	Matrix	-	-	105.72
Petroleum Coke	C	Petrobras S.A.	Matrix	-	-	5.79
Silicon	Si	Rima S.A.	Infiltration	99.9	0.42	1.44

Two different compositions were prepared. Composition 1 (C1): nanosize carbon 100 wt.%. Composition 2 (C2): coke 100 wt.%. Both were uniaxially pressed in discs of 15 mm diameter and 8 mm height under a pressure of 30MPa. The theoretical green density of C1 was around 0.56 g/cm^3 and of C2 was 0.89 g/cm^3. The processing occurred at 1550°C in a vacuum 10^{-3} torr, for 30 min, where liquid silicon exists. The infiltrated materials were characterized of Archimedes's method and the microstructures were examined by optical microscopy and scanning electron microscopy (SEM) equipped with energy-dispersive X-Rays spectrometer (EDS). The X- Rays diffraction was done with CuKα radiation (1.5418 Å - Miniflex Rigaku). Specimens for microscopy were cut from mid - height of the samples, ground flat and polished up to 1μm finish. Indentations (n=20) were performed with a Vickers tester Shimadzu Mod. HDV – 30, and load application was 500 g for 15 s. Each sample received 20 indentations.

3- RESULTS AND DISCUSSION

The microstructures of RBSiC processed in the present study are shown in Fig. 1. The microstructures of both compositions are composed Si metal (lighter gray regions) and SiC (darker gray regions). In Fig. 1(a), sample C1 (nano carbon 100 wt. %), large grains of SiC with size up to 20 μm can be observed. It can be noticed how the silicon (white) is distributed uniformly around the SiC grains (dark) and that the contact regions between SiC grains are very few and small. On the other hand, in Fig. 1(b), sample C2 (coke 100 wt. %), most of the material is composed of SiC, with isolated areas of Si metal; almost no interconnections between the Si metal. The higher volume fraction of Si metal in C1, compared to C2, is attributed to lower green density (around 37% lesser than C2) and, consequently, higher volume fraction of pores. It was also shown that nano particles were not very effective to produce high amount of SiC phase, since the excess of Si metal was much higher than observed in C2.

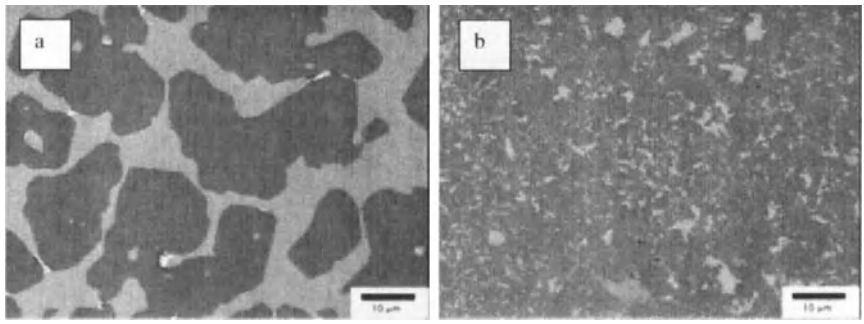

Figure 1. Optical photomicrograph (a) nanosize carbon 100 wt.% (C1) and (b) coke 100 wt.% (C2).

Figure 2 shows the SEM micrographs of C1 and C2. In Fig. 2(a), a higher porosity content is observed than in Fig. 2(b). Part of the porosity observed in both compositions might come from unreacted carbon, which detached from the material during sample preparation. Cracks were also seen to propagate from the porosity in C1, as shown in Figure 3. Such defects can be attributed to the low green body strength, which does not stand the direct contact with the silicon during infiltration. Consequently, cracks nucleate and grow. This behavior was also noted by Simmer[8], who explained the cracks as the result of a rapid melt infiltration through the green body, which is submitted to sudden heat build up from the exothermic Si + C reaction (ΔH_f β-SiC at 2000°C = - 67 kJ/mol) and a localized increase in temperature of 200-300 °C. Form processing stand point, the nano carbon material (C1) did not perform well again, since it allowed cracks to nucleate and grow during the infiltration. A different green body and a new heating cycle may overcome this problem with nano carbon material, but this need to be studied.

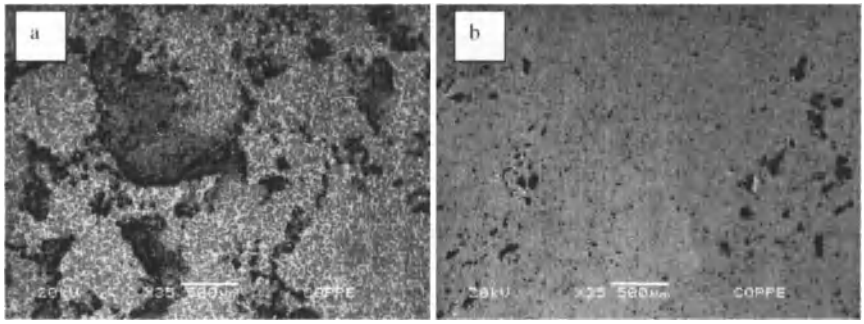

Figure 2. Sem micrograph (a) C1 and (b) C2.

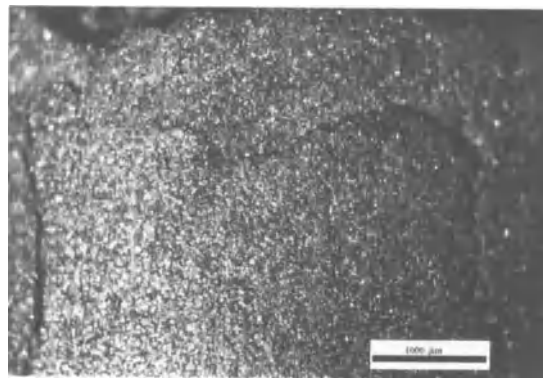

Figure 3. Stereoscopic Micrograph showing crack propagates in C1.

The X-ray diffraction patterns of Si metal and both RBSiC materials are shown in Figure 4. The presence of β-SiC and Si metal phases was observed, which confirms the reaction between carbon and liquid silicon to form β-SiC particles and, ultimately, to a dense body. The β-SiC formed because temperature (1550 ^{0}C) is lower than 1900°C. Corroborating Figure 1, the amount of Si metal in composition C1 was higher than in C2, based on peak height.

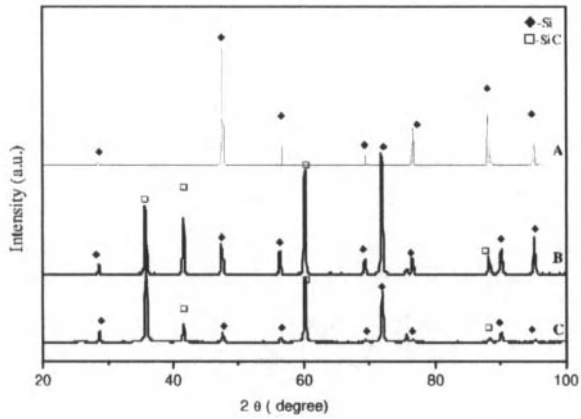

Figure 4. The XRD patterns of the Si powder (A), C1 (B), and C2 (C).

Carbon was not identified in XRD (Figure 4) because it was either nano or amorphous. However, when the samples were analyzed by SEM, carbon was present in an unreacted form, as shown in Figure 5. It is confirmed that the microstructure is composed of SiC, Si and C.

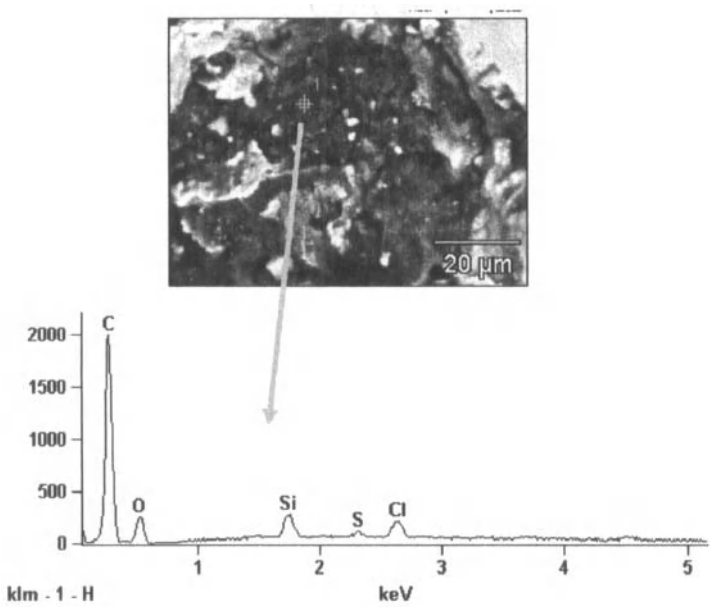

Figure 5. SEM micrograph and EDS of C1 showing the presence of reacted carbon region.

The Vickers hardness of both RBSiC (C1 and C2) samples are shown in Fig. 6. The mean value for C1 is a little bit smaller than for C2, about 7,5 %. But the dispersion in C2 was smaller than in C1. This behavior is related to the microstructure and the volume fraction of each phase present in each material. The material C1 possessed a lower density (2.782 g/cm^3) and higher amount of Si metal (32%) than C2, which had values of 2.859 g/cm^3 and 12%, respectively. It is possible to explain the lower dispersion of hardness of C2 based on the higher amount of SiC present, since the probability to indent a Si metal region (with lower hardness) would be less. Corroborating the role of microstructure and volume fraction is the fact that the maximum hardness measured in both compositions are the same, which is the upper value of SiC material.

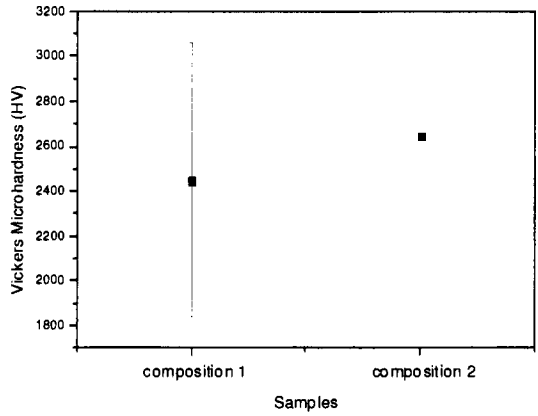

Figure 6. Vickers micro hardness of composition 1 and composition 2.

It was observed that linear shrinkages of C1 and C2 were 0.78% and 8.35%, respectively. They are low values for contraction, but they should be the closer to each other, tending to the value of C1. The higher shrinkage observed in C2 still needs to be investigated.

4- CONCLUSIONS

In this study two types of carbon precursors, nano carbon with specific surface of 105,72 $g.cm^{-3}$ and petroleum coke (5,79 $g.cm^{-3}$) were used to produce RBSiC. The influence of type of carbon on the microstructure as well as on hardness properties was investigated:

- The nano carbon particles were not very effective to produce high amount of SiC phase, since the excess of Si metal was much higher than observed when coke was used.
- Cracks were observed in nano carbon processed samples (C1) and were attributed to low green body strength.
- Both microstructures were quite homogeneous, but exhibited some differences.
- The coke processed samples had a higher mean hardness and lower dispersion, and it was attributed to the presence of more SiC and less Si metal.

ACKNOWLEDGMENTS

The authors would like to acknowledge the CNPq for the financial support and PETROBRÁS, FINEP, Deprocer and PEMM-COPPE/UFRJ for the use of the experimental facilities.

BIBLIOGRAPHY

[1] M. K. Aghajanian, B. N. Morgan, J. R. Singh, J. Mears and R. A. Wolffe, A new family of reaction bonded ceramics for armor applications, In Ceramic Armor Materials by Design, *Ceramic Transactions*, **134**, 527-539 (2002).

[2] T. M. Kenneth, P. J. Richard, Dense Carbide Composite Bodies and Method of Making Same *Carborundum Co.* **3796564** (1974), http://www.freepatentsonline.com/3796564.html, access on 01/10/2008.

[3] M. K. Aghajanian, B. N. Morgan, J. R. Singh "A New Family Of Reaction Bonded Ceramics for Armor applications" *Pac Rim 4*, November 4-8, 2001, Maui, Hawaii Paper No. PAC6-H-04-2001.

[4] Yu. P. Dyban, Structuring of multiphase compacts in the SiC-Carbon System. I. Structuring in Green Blanks, *Powder Metallurgy and Metal Ceramics*, **40**, 1-2 (2001). Ukraine.

[5] Yu. P. Dyban, Structuring of multiphase compacts in the SiC-Carbon System. II. Structuring During Sintering., *Powder Metallurgy and Metal Ceramics*, **40**, 5-6 (2001). Ukraine.

[6] U.Paik, H. C. Park, S. C. Choi, C. G. Ha, J. W. Kim, Y. G. Jung, Effect of Particle Dispersion on Microstructure and Strength of Reaction Bonded Silicon Carbide, *Materials* Science and Engineering, **334**, 267-274 (2002).

[7] F. Gutierrez-Mora, K.C. Goretta, F.M. Varela-Feria, A.R. Arellano López and J. Martínez Fernández, Indentation hardness of biomorphic SiC, *International Journal of Refractory Metals and Hard Materials*, **23**, 369-374 (2005)

[8] S. P. Simner, P. Xiao and B. Derby, Processing and Microstructural Characterization of RBSiC-$TaSi_2$ composites, *Journal of Materials Science*, **33**, 5557-5568 (1998).

Advanced Processing and Manufacturing Technologies
for Structural and Multifunctional Materials II
Edited by Tatsuki Ohji and Mrityunjay Singh

EVIDENCE OF UNIFORM MICROSTRUCTURE IN MICROWAVE SINTERED YTTRIA STABILIZED ZIRCONIA (YSZ) BY IMPEDANCE ANALYSIS

Kanchan Lata Singh[a], Ajay Kumar[a], Anirudh P Singh[a], S.S. Sekhon[c]
[a] Department of Applied Sciences and Humanities
Shaheed Bhagat Singh College of Engineering and Technology, Ferozepur - 152 004, India
[b] Department of Applied Physics, Guru Nanak Dev University, Amritsar – 143005, India.

ABSTRACT

In the present study the potentiality of microwave energy has been used in the preparation of solid solution YSZ ceramics from the precursor obtained by mechanical mixing of Y_2O_3 and ZrO_2 varying the molar concentration of $YO_{1.5}$ from 10 to14 %. This precursor behaves as reactive powder in the presence of microwave energy and is able to produce high density sintered T-YZP of different compositions. The YSZ has been prepared by conventional heating also. The various phases of the microwave and conventionally sintered samples have been characterized by XRD. The impedance and DTA/TG/DTG analysis have been done on microwave and conventionally sintered $Zr_{0.86}Y_{0.14}O_{1.93}$. The impedance analysis shows that microwave processed $Zr_{0.86}Y_{0.14}O_{1.93}$ is single phase YSZ.

INTRODUCTION

The compound zirconia is polymorphic and can have one of the three crystal structures viz. monoclinic (m), tetragonal (t) and cubic (c) at ambient temperature ZrO_2 is monoclinic (m) but transforms to tetragonal (t), and then to cubic at high temperature 1100°C and 2370°C, respectively. On cooling the transformation sequence is reversed, and the structure normally reverts back to monoclinic. It has not been possible to fabricate ceramics from pure ZrO_2 because of disruptive effect of the t-m transformation. This effect can however be suppressed by alloying ZrO_2 with other aliovalent oxides including Y_2O_3 with which it forms solid the solutions, collectively called as the stabilised zirconias[1,2]. At the stabiliser concentration of around 10% molar the solid solutions have a cubic structure at the ambient temperature similar to the high temperature cubic phase and these materials are called the fully stabilised zirconia (FSZ). Solid solutions containing 2-6 mole% of Y_2O_3, however, retain the tetragonal structure provided the grain size is sufficiently small[3]. These ceramics have exceptional high mechanical strength and toughness and they are referred to as the tetragonal zirconia polycrystals (TZP). At the intermediate level of stabiliser, the ceramics are termed partially stabilised zirconia (PSZ) consisting a matrix of c-phase containing a dispersion of t-phase and/or m-phase precipitates[4]. If a significant volume fraction of metastable t- phase is present, these precipitates give the ceramic good mechanical properties by a process known as transformation toughening. Y-TZP on prolonged aging times can produce some of the microstructural features associated with Y-PSZ ceramics. Therefore, the distinction between Y-TZP and Y-PSZ is diffuse. Principally FSZ has been used for the electrical applications, while PSZ and Y-TZP have been developed for the structural applications[5-7]. Recently, it has, however, become apparent that for moderate temperature devices, PSZ and TZP are better suited[8,9]. The major problem encountered in the preparation of dense TZP ceramics is the attainment of a homogenous distribution of yttria in the ZrO_2 grains. If ZrO_2 grains in which the yttria is not distributed homogeneously exist in TZP ceramics, local stress concentrations or micro cracks will occur around these grains due to the volume change (3%) that accompanied by the tetragonal to monoclinic martensitic transformation. It has been reported that, at the usual measuring temperature of 1400^0C, it is difficult to achieve a uniform distribution in mechanically mixed oxide powders due to the very slow diffusion of yttria in ZrO_2 at these temperatures and the large diffusion distances, equal to tens of thousands of units cells, involved in such powders[10]. Higher temperatures, however, required for the formation of uniform solid solution, result in rapid grain growth in the

material, which leads to the transformation of the larger tetragonal grains to monoclinic symmetry on cooling.

In the recent, it has been found that a wide variety of chemical reactions are accelerated by microwave irradiation of reactants[11-16]. The major advantages of microwave processing are lower reaction temperatures and shorter processing time as compared to the conventional synthetic procedures. Generally, the majority of the reactions using microwave are reported in solution phases of the reactants. High dielectric loss tangents of the polar solvents are responsible for the effective coupling to the microwave field. Relatively a few reports are available on solid state synthesis of complex oxides using microwave. In the synthesis of $BaTiO_3$, it has been observed that non-stoichiometry of TiO_2 is responsible for the enhanced coupling of microwave[12]. Also, in the synthesis of PZT, it has been reported that use of stabilized zirconia and reduced TiO_2 not only enhances the kinetics of formation of PZT but changes the mechanism also[17]. The reduction in the processing time and temperature is believed to be due to the higher diffusion rates induced by microwave field. During the formation of fully cubic calcium stabilized zirconia, higher diffusion of participating cations has been reported[18].

In the present study the potentiality of microwave energy has been used in the preparation of solid solution YSZ ceramics from the precursor obtained by mechanical mixing of Y_2O_3 and ZrO_2 varying the molar per cent of $YO_{1.5}$ from 10 to14. This concentration range of yttria stabilises tetragonal structure of zirconia at room temperature by making solid solution of $YO_{1.5}$-ZrO_2. This precursor behaves as reactive powder in the presence of microwave energy and is able to produce high density sintered partially stabilised zirconia of different compositions. The precursor has been processed by the conventional method also in order to compare the results with that of the microwave processed products. The impedance analysis of microwave processed and conventionally processed $Zr_{0.86}Y_{0.14}O_{1.93}$ has been done.

EXPERIMENTAL

The precursors were prepared by mixing yttrium oxide ($YO_{1.5}$) and monoclinic zirconia (ZrO_2) in stoichiometric ratios to form $Zr_{1-x}Y_xO_{1-x/2}$ (YSZ) of compositions x= 0.8, 0.1, 0.12, 0.14. The powders were ball milled in a polythene bottle using zirconia balls and acetone as a grinding medium for 6 hours. The precursor of each composition was mixed with 4% PVA binder and uniaxially pressed at 312 MPa in a 12.80 mm die.

The microwave system used in this study was a modified domestic microwave oven of 2.45 GHz and maximum 1.2 KW power output. The sample pellets (five in number) of precursors of composition $Zr_{1-x}Y_xO_{2-x/2}$ [x = 0.08, 0.10, 0.12 and 0.14 mol of $YO_{1.5}$ and (1-x) mol of monoclinic zirconia] prepared by mixed oxide method were taken in an alumina crucible and covered with solution of 8 mol% PVA prepared in water which acts as a microwave susceptor to pre heat the samples at a temperature where zirconia starts absorbing microwave radiation[18]. The samples were irradiated using microwave energy to heat them at a temperature of 1400°C for 20 minutes. The processing of temperature of 1400°C was chosen, since the processing temperature for zirconia system in the conventional heating has been reported to be1400°C and higher [19].

The sample pellets (five in number) of precursors with composition $Zr_{1-x}Y_xO_{2-x/2}$ [x =0.08, 0.01, 0.12 and 0.14 mol of $YO_{1.5}$ and (1-x) mol of monoclinic zirconia] prepared by mixed oxide method were taken in an alumina crucible and were processed in the conventional furnace at 1400°C for 4 hrs soaking time in order to compare the results of the products with those of the microwave processed samples.

The formation of different phases in each composition fired at 1400°C in the microwave energy for 20 minutes of soaking time and in the conventional furnace for 4 hours of soaking time were analyzed by the X-ray diffractometer (X-ray Diffractometer, Model: Bruker AXS, D-8 Advance,

Switzerland). Densities of pellets of each composition were measured by Archimedes Principle using distilled water. The electrical conductivity measurements were made on the polished sintered sample pellets coated with silver electrodes by complex impedance spectroscopy method in the frequency range 50Hz to 5 MHz using HIOKI 3532-50 LCR Hi TESTER, Japan. Thermal analysis (DTA/TG/DTG) of microwave as well as conventionally sintered samples were done in the temperature range of 25°C to 1300°C using Perkins Elmer(Pyris Diamond) DTA/TGA instrument in ambient air.

RESULTS AND DISCUSSIONS

The products were characterized by the XRD to observe the phase transformations in each system and for each composition. The crystalline phases of different polymorphs of yttrium stabilized zirconia [YSZ; $Zr_{1-x}Y_xO_{2-x/2}$ x = 0.8, 0.10, 0.12, 0.14] synthesized were determined from X-ray diffraction (XRD) patterns of the samples. Fig. 1 shows the XRD pattern of microwave processed YSZ of different compositions and the precursor, whereas fig. 2 shows the XRD patterns of conventionally processed YSZ of different compositions along with the precursor. The monoclinic phase, tetragonal phase and cubic phase of YSZ have been marked clearly in the XRD patterns of both the figures. The % age of monoclinic phase in each composition was calculated[20] from the formula and is given below.

$$\%\text{age of monoclinic phase} = \frac{I(11\bar{1})^m}{I(11\bar{1})^m + I(111)^m + I(111)^{t/c}} X100$$

The variation in the percentage change of monoclinic phase is given in the Table 1.

The XRD patterns in Fig. 1 (a, b, c) show the presence of the monoclinic, tetragonal and cubic phases for the microwave processed products YSZ of composition x = 0.08, 0.10 and 0.12. The XRD pattern in figure 1d of composition $Zr_{0.86}Y_{0.14}O_{1.93}$ does not contain any peak due to presence of monoclinic phase. Although this composition corresponds to the tetragonal phase, it is difficult to ascertain the presence of cubic phase or tetragonal phase as the splitting of peaks at higher angle side is not visible. The XRD patterns in Fig 2 (a, b, c) show the presence of the monoclinic, tetragonal and cubic phases for the conventionally processed products YSZ of composition x = 0.08, 0.10 and 0.12. The trends of disappearance of monoclinic phase in the conventionally sintered products are same as that observed in microwave processed products (Table 1). However, the percentage contribution of monoclinic phase in the conventionally sintered products is higher. The XRD pattern in figure 2d does not contain any peak due to presence of monoclinic phase. However, the XRD peaks in figure 2d are not as smooth as compared to peaks of figure 1d for the microwave processed $Zr_{0.86}Y_{0.14}O_{1.93}$,. This indicates presence of some other phase in the conventionally sintered $Zr_{0.86}Y_{0.14}O_{1.93}$t The microwave sintered as well as conventionally sintered $Zr_{1-x}Y_xO_{2-x/2}$ of composition x = 0.8,0.10,0.12 had mixture of phases and therefore their electrical properties were not measured. Since the XRD patterns of microwave processed and conventionally processed $Zr_{0.86}Y_{0.14}O_{1.93}$ were similar, their impedance analysis was done in order to asses the homogeneity. The admittance diagrams at 550°C of microwave processed $Zr_{0.86}Y_{0.14}O_{1.93}$ and conventionally processed $Zr_{0.86}Y_{0.14}O_{1.93}$ are shown in figure 3 and 4 respectively.

The relative density of microwave processed $Zr_{0.86}Y_{0.14}O_{1.93}$ was found to be 99% of theoretical density however in the conventionally processed $Zr_{0.86}Y_{0.14}O_{1.93}$ it was only 95%.

Figure 5 and figure 6 shows the temperature dependence of a.c. conductivity of the microwave processed $Zr_{0.86}Y_{0.14}O_{1.93}$ and conventionally processed $Zr_{0.86}Y_{0.14}O_{1.93}$ respectively at four fixed frequencies 100 Hz, 1 KHz, 10 KHz and 100 KHz. The a.c. conductivity of microwave processed $Zr_{0.86}Y_{0.14}O_{1.93}$ increases with the temperature more or less linearly except at 100 KHz frequency. In the figure 6, the conductivity of the conventionally processed $Zr_{0.86}Y_{0.14}O_{1.93}$ increases with the temperature and a dip is observed to be initiated in the curve at around 750°C. This may be attributed to some structural phase change in the $Zr_{0.86}Y_{0.14}O_{1.93}$ due to the diffusion of ions in the lattice. Similar phase change at 747°C in the conventionally processed $Zr_{0.86}Y_{0.14}O_{1.93}$ can also be observed in the DTA/TG/DTG result as shown in figure 7a apart from the other at 762°C. Both these changes in DTA/TG/DTG of conventionally processed $Zr_{0.86}Y_{0.14}O_{1.93}$ are exothermic in nature. Further, no such phase change is observed in the DTA/TG/DTG of microwave processed $Zr_{0.86}Y_{0.14}O_{1.93}$ as shown in figure 7b.

In polycrystalline solids, transport properties are strongly affected by the microstructure, and the impedance spectra usually contain features that can be directly related to the microstructure. Much of the work done correlating the microstructure and the electrical properties has been carried out since the pioneering work of Bauerle[21].

It has already been accepted that ionic carriers can be blocked at the internal interfaces of the solid state ionic conductors. The ion blocking can be introduced by various microstructure defects such as grain boundaries, cracks, pores and second phase inclusion. Accordingly, generic name blockers have been used to refer these defects. This phenomenon is usually observed in the impedance spectroscopy. It has been concluded by Kleitz et al[29] during the impedance spectroscopy study of ion blocking in yttria stabilised zirconia that the additional resistances that can be determined from the impedance diagram can not be correlated easily to any specific properties of the blockers. On the other hand, the blocked conductance deduced from the admittance diagrams behave with temperature, very similar to the single crystal conductance as also shown in figure 8, indicating that identical electrical carriers are responsible for these two physical parameters. According to them, the quantity of trapped electric carriers and therefore the blocked conductance are proportional to the overall volume of the blocked spaces[22-30].

The admittance diagram of microwave sintered and conventionally sintered $Zr_{0.86}Y_{0.14}O_{1.93}$ at 550°C is shown in figure 3 and figure 4 respectively. The dc conductivity $\sum_{dc}$, the bulk conductivity $\sum_{bulk}$, and blocking conductivity $\sum_{bd}$ have been marked in the figure 3. The relationship between the different conductivities is as given below:

$$\sum_{bulk} = \sum_{dc} + \sum_{bd} \qquad (1)$$

The blocking factor

$$\alpha_R = (\sum_{bulk} - \sum_{dc}) / \sum_{bulk} \qquad (2)$$

Figure 9 shows decrease in the blocking factors, α_R, with the temperature of the microwave processed $Zr_{0.86}Y_{0.14}O_{1.93}$. It is evident from the figure that α_R becomes almost constant after 550°C temperature. It has been reported that in materials with small and medium blocking magnitude, the blocking effect appears approximately temperature independent below certain transition temperature. Above this temperature it gradually decreases and disappears[28], since the conductivity of the microwave sample becomes equal to or greater than the value 10^{-3} S cm^{-1} where the blocking becomes negligible[28]. It suggests that in the microwave sintered $Zr_{0.86}Y_{0.14}O_{1.93}$ the blocking effect due to grain boundary is not effective as the bulk conductivity has increased of the order of 10^{-3} Scm^{-1} beyond 550°C. It is to be noted that the bulk conductivity of at 550°C of microwave sintered $Zr_{0.86}Y_{0.14}O_{1.93}$ is

$5x10^{-3}$ S cm^{-1} and has achieved the value of $1.5x10^{-2}$ S cm^{-1} at 700°C. The admittance diagram of conventionally sintered $Zr_{0.86}Y_{0.14}O_{1.93}$ was dispersed randomly, may be due to presence of mixed phases, and therefore could not be analysed.

CONCLUSION

1. Single phase $Zr_{0.86}Y_{0.14}O_{1.93}$ could be prepared by microwave processing at the temperature of 1400°C in 20 minutes of soaking time as compared to 4 hours of soaking time in case of conventional processing.
2. The density observed for the microwave processed $Zr_{0.86}Y_{0.14}O_{1.93}$ is higher than that of conventionally processed $Zr_{0.86}Y_{0.14}O_{1.93}$.
3. The electrical conductivity measurement along with DSC analysis show that there is no phase change in microwave processed $Zr_{0.86}Y_{0.14}O_{1.93}$ upto 900°C whereas in case of conventionally processed $Zr_{0.86}Y_{0.14}O_{1.93}$ shows phase changes at 747°C and 762°C indicating that microwave processed $Zr_{0.86}Y_{0.14}O_{1.93}$ is a single phase.
4. The electrical conductivity of microwave processed $Zr_{0.86}Y_{0.14}O_{1.93}$ is of the order of $1.5x10^{-2}Scm^{-1}$ at 700°C only whereas the conductivity of the same order is achieved at 900°Cor above in the conventionally processed YSZ as reported in literature.

ACKNOWLEDGEMENT

We wish to acknowledge the financial support provided by DST, New Delhi to carry on this research and Institute Instrumentation Centre, Indian Institute of Technology, Roorkee for characterization of material by XRD and SEM.

REFERENCES

1. E. C. Subbarao, "Zirconia—An overview". In:. *Advances in Ceramics, Vol. 3, Science and Technology of Zirconia*, ed. A.H. Heuer, L.W. Hobbs, The American Ceramic Society Columbus, OH, pp.1 (1981).
2. T. K. Gupta, J.H. Bechtold, R. C. Kuznicki, L.H. Kadoff, and B.R. Rossing, " Stabilization of Tetragonal Phase in Polycrystalline Zirconia", *J. Mat. Sci.* **12**, 2421-2426 (1977)
3. K. Kobayashi, H. Kayajima, and T. Masuki, "Phase Change and Mechanical Properties of Zirconia-Yttria Solid Electrolyte after Aging", *Solid State Ionics* 3/4 , 489-493 (1981)
4. E.C. Subbarao and H.S. Maiti, "Solid Electrolytes with Oxygen Ion Conductivity", *Solid State Ionics*, **11**, 317-338 (1984)
5. B.C.H. Steele "High Temperature Fuel Cells and Electrolytes", in *Electrode Processes in Solid State Ionics*, ed. M. Kleitz and Dupuy, Reidel Dordrecht/Boston,pp.368-384 (1976),.
6. B.C.H. Steele J. Drennan, R. K. Slotwinski, N. Bonanos, and E. P. Butler, "Factors Affecting the Performance of Oxygen Monitors", in *Advances in Ceramics, Vol.3, Science and Technology of Zirconia*, ed. A.H. Heuer and L.W. Hobbs, The American Ceramic Society, Columbus, Ohio, pp 286-309 (1981).
7. N. Bonanos, R. K. Slotwinski, B.C.H. Steele, and E.P. Butler, "Electrical Conductivity/Microstructural Relationship in Aged CaO and CaO+MgO Partially Stabilized Zirconia", *J. Mat. Sci.* **19**, 785-793 (1984)
8. B.C.H. Steele and E.P. Butler, "High Ionic Conductivity in Polycrystalline Tetragonal Y_2O_3-ZrO_2", *J. Mat. Sci. Lett.* **3**, 245-248 (1984)

9. S. Schubert, N. Claussen and M. Ruhle, in "*Advances in Ceramics, Vol. 12 - Science and Technology of Zirconia*," eds. N. Claussen, M. Ruhle and A.H. Heuer, American Ceramics Society, Columbus, Ohio, U.S.A., pp. 766-73 (1984).
11. T. T. Meek, C. E. Holcombe and N. Dykes, "Microwave Sintering of Some Oxide Materials using Sintering Aids," *Journal of Materials Science Letters*, **6**, 1060-1062 (1987)
12. D K Agrawal, "Microwave Processing of Ceramics," *Current Opinions in Solid State and Materials Science* **3,** 480-85 (1998)
13. J. P. Cheng, D. K. Agrawal, S. Komarneni, M. D. Mathis, and R. Roy, "Microwave Processing of WC_C Composites and Ferroic Titanates," *Mat.Res. Innovat.*, **1[1]**, 44-52 (1997).
14. M. D. Mathis, D. K. Agrawal, R. Roy, R.H. Plovnick, and R. Hutcheon, "Microwave Synthesis of SiAlONs," *Ceram. Trans.*, **59,** 533-537 (1995).
15. W. H. Sutton, "Microwave Processing of Ceramic Materials," *J. Am. Ceram. Soc. Bull.*, **68(2),** 376-82 (1989).
16. D. E. Clark, W. H. Sutton, D.A. Lewis, "Microwave Processing of Materials" in *Microwaves*: Theory and Application in Materials Processing IV, Ceram. Trans., 80, The American Ceramic Society, Ohio, pp. 61-96 (1997)
17. B. Vaidhyanathan, A. P. Singh, D. K. Agrawal, T. R. Shrout, and R. Roy, "Microwave Effects in Lead Zirconium Titanate Synthesis: Enhanced Kinetics and Changed Mechanisms," *J Am. Ceram. Soc.*, **84**[6], 1197-202 (2001).
18. A. P. Singh, N. Kaur, A. Kumar, K. L. Singh, "Preparation of Fully Cubic Calcium Stabilized Zirconia with 10 mol % CaO Dopant Concentration by Microwave Processing," *J. Am. Ceramic Soc.* **90 [3],** 789-96 (2007).
19. I. Abraham and G. Gritzner, "Powder Preparation, Mechanical and Electrical Properties of Cubic Zirconia Ceramics," *Journal of European Ceramic society,* 95, 71-77 (1995).
20. K. A. Khor and J. Yang, "Plasma Sprayed ZrO_2-Sm_2O_3 coatings: Lattice Parameters, Tetragonality (c/a) and Transformability of Tetragonal Zirconia Phase," *Journal of Material Science Letters*, 12 **16**, 1002-04 (1997).
21. J.E. Baurle, "Study of Solid Electrolyte Polarization by a Complex Admittance Method", *J. Phys. Chem. Solids* **30,** 2657-2670 (1969).
22. M. Kleitz, H. Bernard, E. Fernandez and E. Schouler, "Impedance Spectroscopy and Electrical Resistance Measurements on Stabilized Zirconia" in: *Advances in ceramics, Vol. 3, Science and Technology of Zirconia*, eds. A.H. Heuer and L.W. Hobbs, The Am. Ceram. Soc., Washington, D. C. , pp.310-336 (1981).
23. M. J. Verkerk, B. J. Middelhuis and A. J. Burggraaf, "Effect of Grain Boundaries on the Conductivity of High Purity ZrO_2-Y_2O_3 Ceramics," *Solid State Ionics*, 6 [2] 159-70 (1982).
24. S.P.S. Badwal, "Electrical Conductivity of Single Crystal and Polycrystalline Yttria-stabilized Zirconia," *J. Mater. Sci.* **19**, 1767–1976 (1984).
25. S.P.S. Badwal, J. Drennan, "Yttria-zirconia: Effect of Microstructure on Conductivity", *Journal of Materials Sci.* **22,** 3231 (1987)
26. S.P.S. Badwal, and J. Drennam, and A.E. Hughes, "Some Aspects of Grain Boundary Diffusion in Oxides"in : *Science of Ceramic Interfaces*, ed. J. Nowotny (Elsevier, Amsterdam); pp. 227–309(1991).
27. M. Kleitz, C. Pescher and L. Dessemond, in : *Science and Technology of Zirconia V*, eds. S.P.S. Badwal M.J. Bannister and R.H.J. Hannik (Technomic Publishing Company, Lancaser, Pa USA,) p. 593 (1993)
28. M. Kleitz, L Dessemond and M. C. Steil, "Model of Ion Blocking at Internal Interfaces in Zirconias", *Solid State Ionics*, **75**, 107-115(1995).

29. M.C. Steile, F. Thevenot, L. Dessmond and M. Kleitz, in: Third Euro Ceramics, Vol. 2, Properties of Ceramics, eds. P. Duran and J. F. Fernandez Faenza Editrice Iberica, San Vincente, Spain, 1993) p. 271.
30. L. Dessmond, R. Muccillo M. Kleitz,. "Electric Conduction-blocking Effects of Voids and Second Phases in Stabilized Zirconia", *Appl. Phys A* **57,** 57-60(1993).

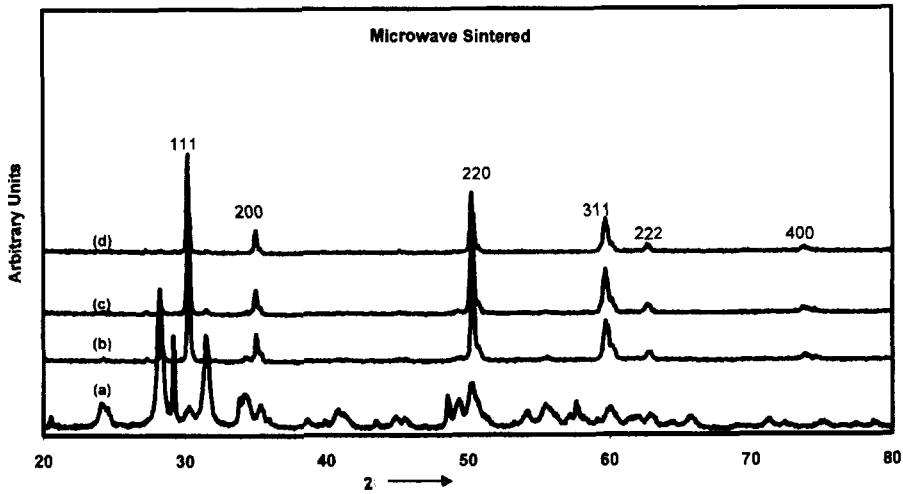

Figure 1. XRD (a) Y_2O_3-ZrO_2 precursor (b) MW Processed $Zr_{0.90}Y_{0.1}O_{1.95}$ (c) $Zr_{0.88}Y_{0.12}O_{1.94}$ (d) $Zr_{0.86}Y_{0.14}O_{1.93}$

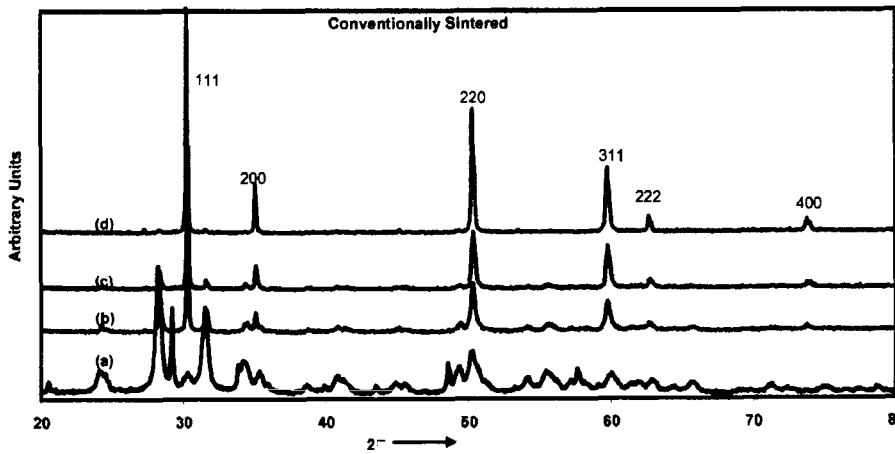

Figure 2: XRD (a) Y_2O_3-ZrO_2 precursor (b) Conventionally Processed $Zr_{0.90}Y_{0.1}O_{1.95}$ (c) $Zr_{0.88}Y_{0.12}O_{1.94}$ (d) $Zr_{0.86}Y_{0.14}O_{1.93}$

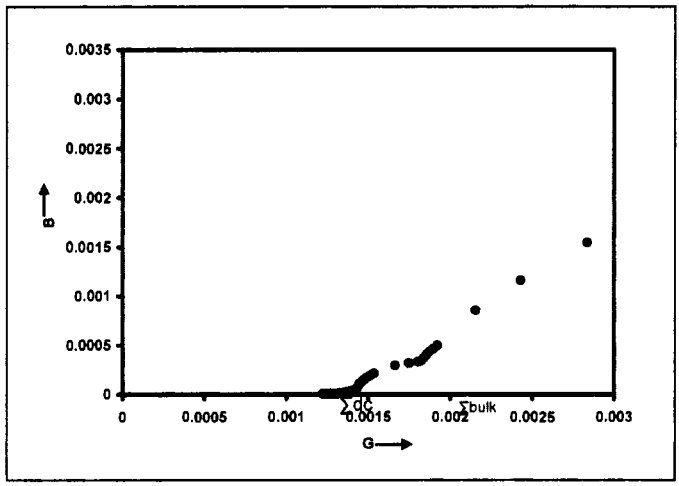

Figure 3. Impedance diagram of microwave sintered $Zr_{.86}Y_{0.14}O_{1.93}$ at 550°C

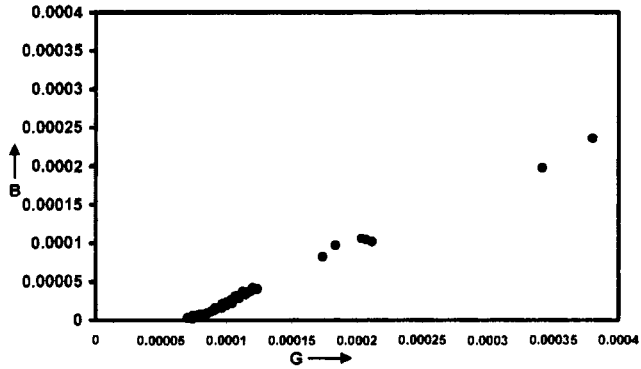

Figure 4: Impedance diagram of conventionally sintered $Zr_{.86}Y_{0.14}O_{1.93}$ at 550°C

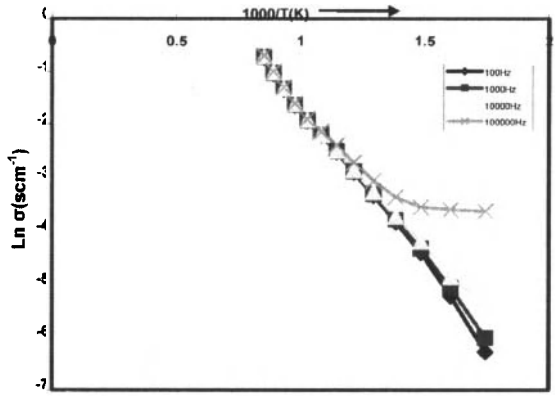

Figure 5: Variation of A.C. conductivity with temperature for microwave processed $Zr_{0.96}Y_{0.14}O_{1.93}$ at different frequencies

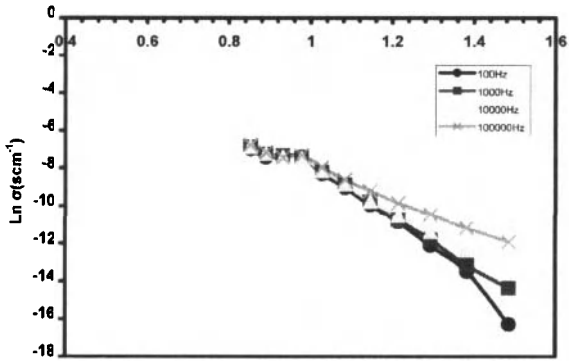

Figure 6: Variation of A.C. conductivity with temperature for conventionally processed $Zr_{0.96}Y_{0.14}O_{1.93}$ at different frequencies.

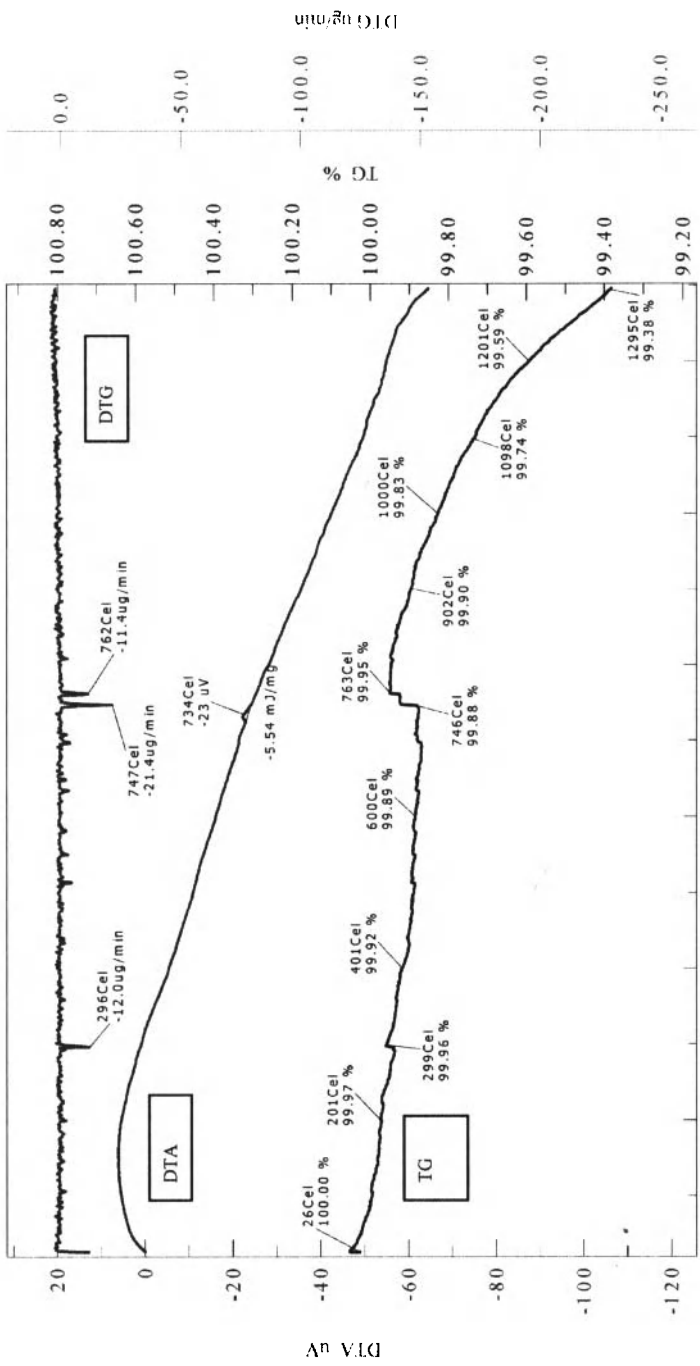

Figure 7a: DTA/TGA and DTG results of conventionally processed $Zr_{0.86}Y_{0.14}O_{1.93}$

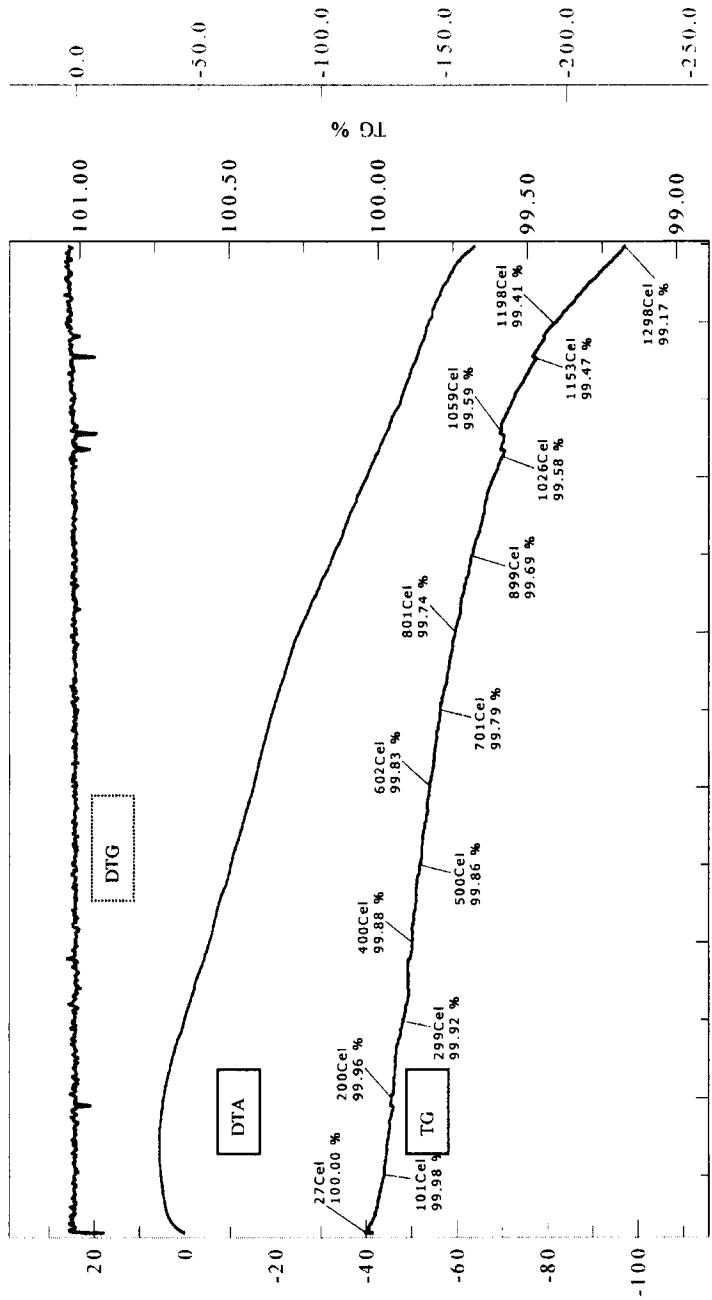

Figure 7b: DTA/TGA and DTG results of microwave processed $Zr_{0.96}Y_{0.14}O_{1.93}$

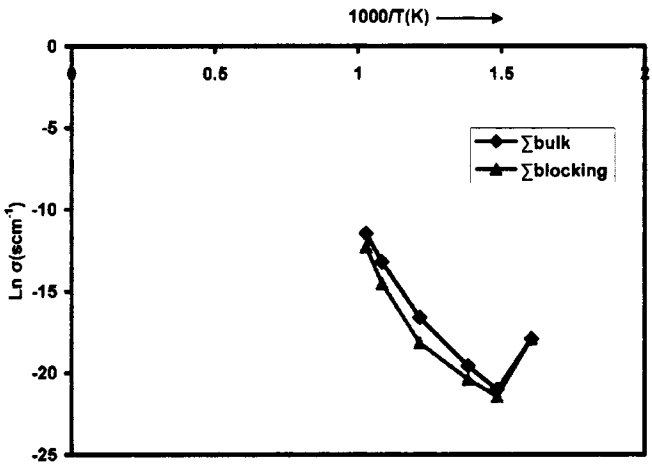

Figure 8: Variation of bulk conductivity ($\sum_{bulk}$) and blocking conductivity ($\sum_{blocking}$) with temperature for microwave processed $Zr_{0.96}Y_{0.14}O_{1.93}$

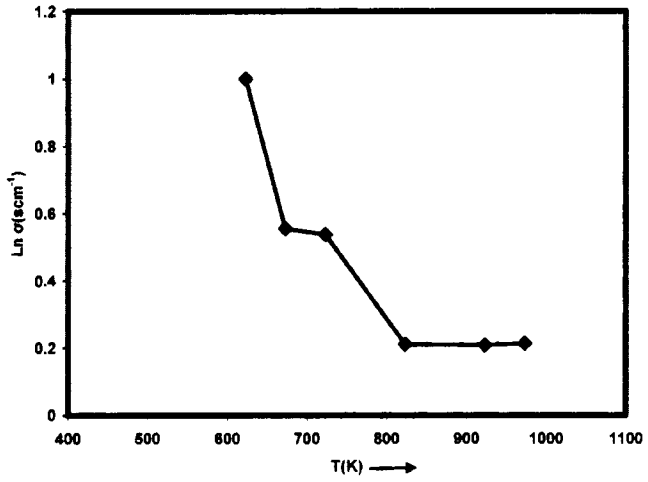

Figure 9: Variation of blocking factor α_R with temperature for microwave processed $Zr_{0.96}Y_{0.14}O_{1.93}$

Table I: Percentage variation of monoclinic phase with composition of microwave and conventionally sintered $Zr_{1-x}YxO_{1-x/2}$

Microwave Processed		Conventionally Processed	
Sample name	Per cent monoclinic phase	Sample name	Per cent monoclinic phase
$Zr_{0.90}Y_{0.01}O_{1.95}$	17.52044	$Zr_{0.90}Y_{0.01}O_{1.95}$	43.42666
$Zr_{0.88}Y_{0.12}O_{1.94}$	12.90122	$Zr_{0.88}Y_{0.12}O_{1.94}$	20.53427
$Zr_{0.86}Y_{0.14}O_{1.93}$	5.13042	$Zr_{0.86}Y_{0.14}O_{1.93}$	9.249045

Advanced Processing and Manufacturing Technologies
for Structural and Multifunctional Materials II
Edited by Tatsuki Ohji and Mrityunjay Singh

MODELING OF FIELD ASSISTED SINTERING TECHNOLOGY (FAST) AND ITS APPLICATION TO ELECTRO-CONDUCTIVE SYSTEMS

K. Vanmeensel*, S.H. Huang*, A. Laptev**, J. Vleugels*, O. Van der Biest*

*Department of Metallurgy and Materials Engineering (MTM)
Katholieke Universiteit Leuven
Kasteelpark Arenberg 44
B-3001 Heverlee (Leuven)
Belgium

**Department of Mechanical Engineering
Donbass State Engineering Academy
Shkadinova street 72
UA-84313 Kramatorsk
Ukraine

ABSTRACT

A brief overview of the general characteristics of the FAST technology will be described. Furthermore, a combined numerical-experimental technique will be presented, which allows accurate modeling of the current and temperature distribution in the punch-die-specimen set-up during FAST. The influence of the presence of contact resistances as well as of the thermal and electrical properties of the sintering powder compacts on the temperature and current distribution during FAST thermal cycling will be highlighted. A more strategic pyrometer position is proposed, allowing more accurate temperature measurements, independent of the sample properties. It will be shown how the changing electrical properties of ceramic composite powder compacts can be in-situ monitored using a double pyrometer set-up. Finally, some practical examples of different electrically conductive materials densified by FAST are presented.

INTRODUCTION

The field assisted sintering technique (FAST), also known as spark plasma sintering (SPS) or pulsed electric current sintering (PECS), belongs to a class of sintering techniques that employ a pulsed direct current (DC) to intensify sintering[1]. Some general advantages of field assisted sintering, compared to traditional hot pressing or hot isostatic pressing, are technological advantages such as short processing time, the use of high heating rates thereby minimising grain growth, which often leads to improved mechanical[2], physical[3] or optical[4] properties, and elimination of the need of sintering aids. No precise understanding of the benefit of the use of a pulsed current exists, although it is claimed that a major beneficial feature of this technique originates from the interaction of current pulses with particle contact points, potentially causing micro-sparks, which remove surface oxides on conductive powders and enhance surface grain boundary diffusion kinetics[5].

This contribution mainly focuses on the importance of a correct temperature measurement in order to be able to make the available FAST technology a fast and reliable technique to produce bulk samples that are difficult to be obtained by any other technique. A finite element model has been developed to improve our current understanding of the FAST technique. It is shown how the presence of contact resistances as well as tool geometry and material properties influence the

current and therefore the temperature distribution in the FAST tool set-up. The applicability of the model is assessed and practical examples will be shown.

DESCRIPTION OF THE FAST TECHNOLOGY

Although similar to conventional hot pressing in the sense that the powders are loaded in a graphite punch/die assembly and a uniaxial pressure is applied during sintering, the main difference between FAST and hot pressing is the way of heating. During hot pressing, the graphite punch/die assembly is heated by radiation from external heating elements installed in the processing chamber and by convection through the inert atmosphere if applicable. Radiation, conduction and/or convection are required to transfer heat from the heating element through the die surface to the specimen. The heating rate is typically low (e.g., below 80°C/min). During FAST, the graphite punches, die and/or specimen (if electrically conductive) serve as heating elements by Joule heating. Since very high electric current densities are transmitted into the punch/die assembly within seconds, the heating rate is substantially higher (e.g., up to 1000°C/min).

The FAST equipment used in this research (Figure 1-a) consists of a mechanical device capable of uniaxial pressure application and of electrical components to apply a pulsed or constant DC current. The loose powder is directly loaded into a punch and die unit. Conductive powders are mainly heated by joule heating, whereas non-conductive powders are heated by heat transfer from the die and punches that are heated through their own resistance. Temperature measurements are carried out using pyrometers and/or thermocouples. The machine is equipped with a chamber for vacuum or controlled gas environment (N_2, Argon) and a linear gauge that monitors the piston displacement during powder compaction. A schematic of a typical graphite tool set-up is presented in Figure 1-b.

The FAST HP D 25/1 machine (FCT Systeme, Rauenstein, Germany) is equipped with a 250 kN hydraulic press and a fully automated thermal and hydraulic process controller. The power supply can provide a pulsed DC current up to 10000 A at a voltage up to 10 V. The tool is made out of graphite or steel, depending on the applied temperatures and pressures. In any case, conical protection plates (Figure 1-b.) are placed between the tool punches and the water cooled steel electrodes, in order to avoid overheating and creep of the electrode surfaces. The overall resistance of the tool (die-punches-protection plates-compact) must be higher than the resistance of the current leads, hereby avoiding overheating of the power supply system. The electrode diameter was fixed to 80 mm, while the distance between the electrodes can be varied between 80 and 180 mm. Therefore, the maximum compact dimensions are estimated to be ∅ 80mm x 40 mm.

A pulsed as well as a constant direct current with on/off cycles of 0-255 ms (on-time)/0-255 ms (off-time) can be generated. Controlling the voltage difference over the electrodes through a PID controller generates a preset time-temperature profile. In this way, the current flowing through the specimen-punch-die set-up is controlled. The combination of a certain number of pulses in combination with a defined pause time between the pulses will be called 'a burst'. Different bursts can be separated as well by a burst time. All together, they form a characteristic pulse train that can be defined by four numbers, as indicated for a 10:5:0:0 pulse sequence in Figure 2, indicating that no separate bursts (and pause times between the bursts) have been defined (0:0), while a pulse time of 10 ms has been used with a pause time of 5 ms in between the 10 ms pulses (Figure 2).

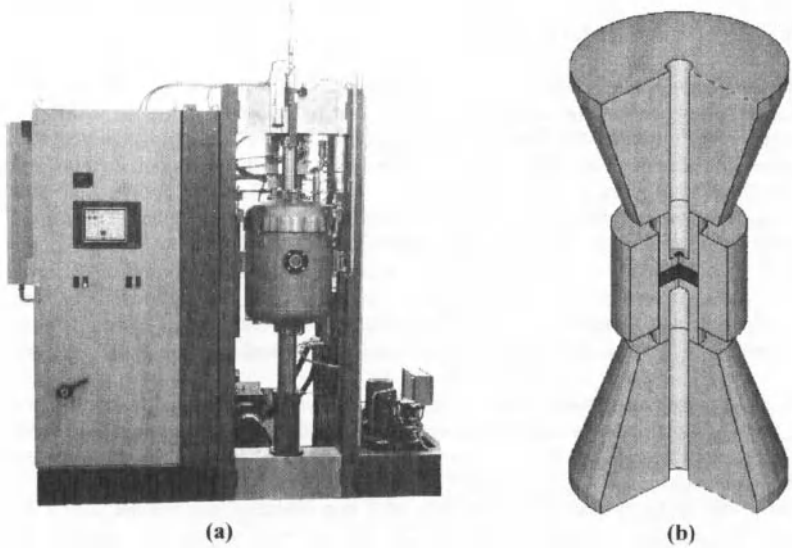

Fig. 1. HP D 25/1 FAST equipment (a) and schematic of a punch-die-sample set-up loaded inside the FAST machine.

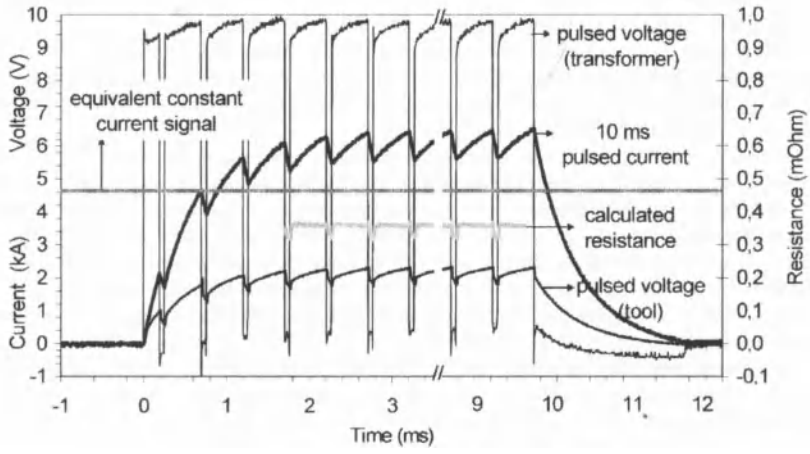

Fig.2. Visual overview of the 'ON' part of a typical 10:5:0:0 pulse generated by the FAST equipment, indicating that the pulse and pause time are set to 10 and 5 ms respectively. No special pulse train (burst) was generated, indicated by the '0' values for 'burst time' and 'time between bursts'.

DEVELOPMENT OF FINITE ELEMENT MODEL TO SIMULATE TEMPERATURE AND CURRENT DISTRIBUTIONS DURING FAST

In order to obtain a more fundamental understanding of the interaction between tool design and material properties on one hand and current and temperature distributions within the FAST tool set-up on the other hand, a finite element model, taking into account the presence of contact resistances has been developed. A general overview of the developed model, its input and output data and their interaction is shown schematically in Figure 3. After defining the tool geometry, all material properties need to be determined as function of temperature. The correct boundary conditions, describing the different heat transfer processes (Figure 4) that take place during the FAST process, need to be determined so that a temperature and current distribution inside the FAST tool set-up can be calculated. Optimisation of the finite element model was done by comparing experimentally measurable output data such as temperature and current/voltage measurements with the values that were applied/obtained throughout the finite element simulations.

During FAST, heat is generated by Joule heating and transferred by conduction between the contacting parts of the electrodes and the tool set-up. Heat is lost by radiation, which is more significant at high temperatures, and by convection since the steel electrodes are water cooled from the inside (Figure 4).

The FAST tool set-up (Figure 4) consists of a 40.7 mm diameter graphite die with a die wall thickness of 8.5 mm and a height of 60 mm. The 40 mm diameter graphite punches are separated from the die by 0.35 mm thick graphite paper (Papyex, Le Carbone Lorraine, France). To verify the correctness of the finite element model, fully dense graphite (Schunk, Germany, grade FE 879), titanium nitride (TiN) (H.C. Starck, Germany, grade C) or yttria-stabilised zirconia (3Y-ZrO_2) (Daiichi, Japan, HSY-3U) samples with a thickness of 5mm were loaded in the FAST tool set-up. The samples were separated from the graphite punches using graphite paper. Both graphite punches and conical graphite protection plates (Figure 4) contain a 10 mm diameter cylindrical borehole through which a central pyrometer (CP) measures the temperature 2.5 mm above the top of the compact that is loaded in the tool. The benefits of this pyrometer position will be proven later on.

An initial sintering cycle consisting of 6 segments was originally used: 1) a constant voltage is applied in order to increase the temperature of the tool set-up from room temperature to 450°C, which is the onset temperature of the central pyrometer, focussed on the bottom of the borehole in the upper punch; 2) heating from 450 to 1050°C at a constant heating rate of 200°C/min; 3) 1 minute dwell at 1050°C in order to increase the minimal applied pressure of 5 to 30 MPa; 4) heating from 1050 to 1500°C at a constant heating rate of 200°C/min; 5) 6 minutes dwell time at 1500°C, while the pressure is increased from 30 to 60 MPa during the first minute; 6) natural cooling after switching off the current.

All material properties as well as the thermal and electrical contact resistances have been determined in an iterative approach combining the developing finite element model with experimentally measured current, voltage and temperatures. More details can be found elsewhere[6]. The contact resistances were determined using three graphite dummies with increasing complexity as shown in Figure 5: a) the F dummy is a full graphite block with the same outer dimensions as the final FAST tool set-up; b) the SPP dummy consists of a solid central graphite part separated from the conical protection plates by horizontal graphite papers; c) the GRA dummy is the same tool used to sinter powder compacts, but containing a fully dense 5 mm thick graphite sample.

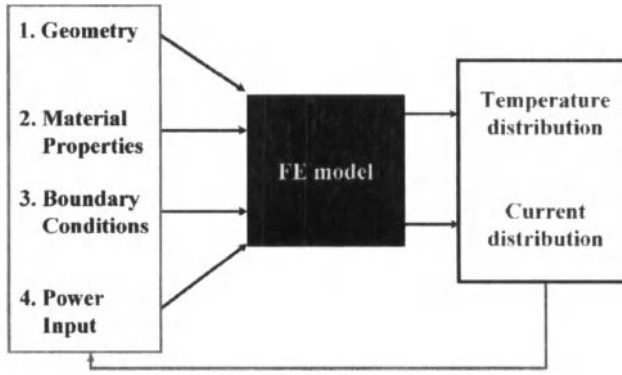

Fig.3. Schematic overview showing how the finite element model was built up and optimised.

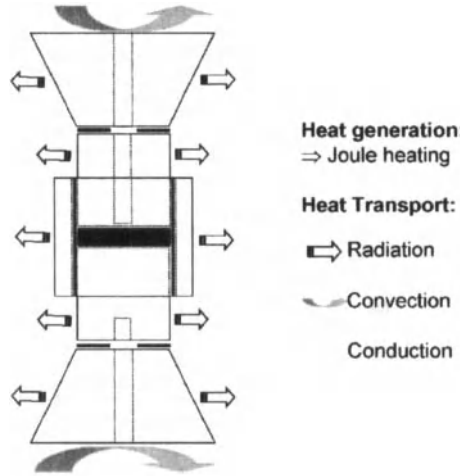

Fig. 4. Overview of the heat transfer processes that take place during FAST

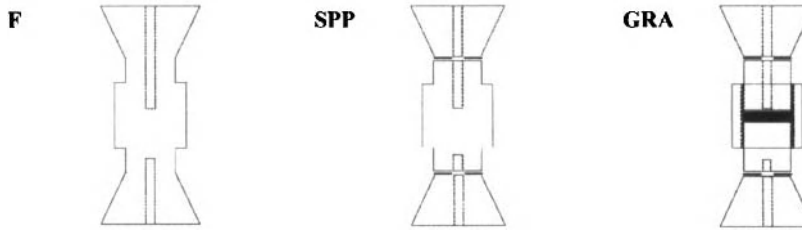

Fig. 5. Overview of the different graphite dummy geometries. Thick horizontal lines indicate the presence of horizontal graphite papers while the thick vertical lines indicate the presence of the vertical graphite paper.

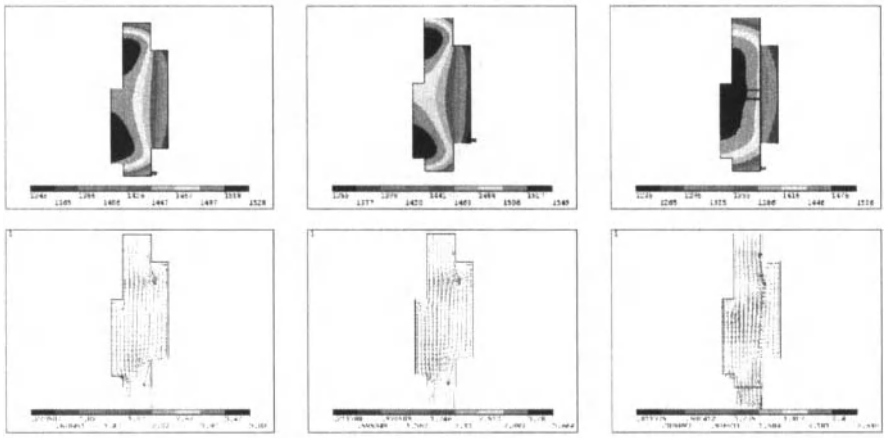

(a) F dummy **(b) SPP dummy** **(c) GRA dummy**

Fig. 6. Temperature (top) and current density (bottom) distributions inside the central parts of the different graphite dummy set-ups during the dwell period at 1500°C.

The influence of the increasing complexity of the graphite dummies on the temperature (top) and current density (bottom) distribution during the dwell segment at 1500°C are shown in Figure 6. The presence of the horizontal graphite papers, acting both as thermal and electrical contact resistances, in the SPP dummy makes the central part of the dummy to be slightly cooler compared to the F dummy, since the hottest part of the tool set-up is slightly shifted towards the contact zone between punches and protection plates. The presence of the vertical graphite paper, acting as a stronger thermal and electrical barrier compared to the horizontal paper[6], inside the GRA dummy set-up makes the graphite die to be colder than the central part of the tool. Furthermore, the hottest zone is shifted towards the central part of the tool, where the graphite sample is located, due to the two extra horizontal graphite papers separating the punches from the sample. Although the vertical graphite paper acts as a thermal barrier, a radial temperature gradient exists inside the graphite sample with the edge being about 70°C colder than the sample centre[6].

The influence of the sample properties on the temperature and current distributions inside a fully dense 3Y-ZrO_2 (a and c) and TiN (b and c) sample at 1500°C is shown in Figure 7. The electrical conductivity of graphite at 1500°C is higher than for pure 3Y-ZrO_2 and lower than for TiN. Therefore, the current density inside the 3Y-ZrO_2 sample is much lower compared to the one in the die (Figure 7-c), while it is higher inside the TiN sample (Figure 7-c). This current density distribution is also reflected in the temperature distribution inside the fully dense samples. In case of the conductor (TiN), the radiation heat losses from the die can not be completely compensated by the limited Joule heating in the graphite die, while in case of the insulator (3Y-ZrO_2), most of the current is forced to flow through the die, resulting in full compensation of the radiation heat losses. Since the relatively thin ceramic sample is surrounded by electrically conductive parts, the temperature gradient in the 3Y-ZrO_2 sample is less than 25°C. In case of TiN, however, a radial temperature gradient of about 70°C develops, similar to the one observed in the fully dense graphite sample (Figure 6-c).

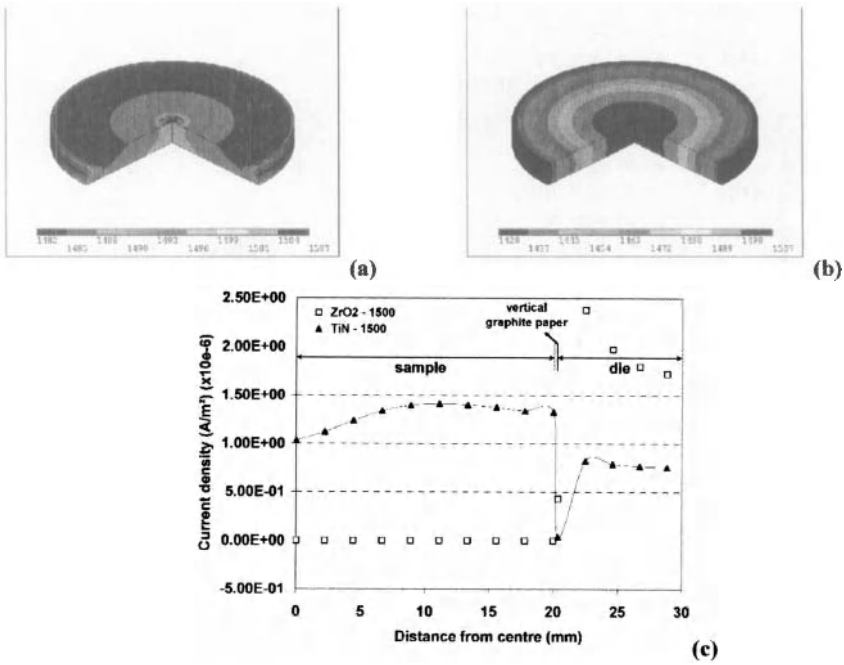

Fig. 7. Temperature (a-b) and current (c) distributions inside fully dense Y-ZrO_2 (a) and TiN (b) compacts during FAST at 1500°C, as indicated by the central pyrometer temperature, focussing on the bottom of the upper punch. as indicated in Figure 4.

Up till now, only the current and temperature distributions inside fully dense sample have been discussed. In order to fully understand the evolution of the temperature distribution during a real FAST sintering cycle, the influence of the porosity on the properties of the sintering powder compact has to be taken into account as highlighted in the following paragraph.

IN-SITU MONITORING OF PERCOLATION PHENOMENA DURING FAST DENSIFICATION OF CERAMIC COMPOSITES

A series of ceramic composite materials, combining an electrically insulating Y-ZrO_2 matrix with an electrically conductive TiN secondary phase has been developed by FAST. The TiN content inside the composite materials was varied between 35 and 90 vol %. It has been demonstrated that the electrical conductivity of this type of composite materials exhibits a percolation type of behaviour[7,8], suggesting that the volume fraction of electrically conductive particles in the composite material should be higher than 0.3 in order to have it machined by electrical discharge machining (EDM).

In order to study the temperature distribution during the sintering process, both the die wall temperature (EP-external pyrometer) and the temperature at the bottom of the borehole in the upper punch (CP – central pyrometer) were monitored simultaneously.

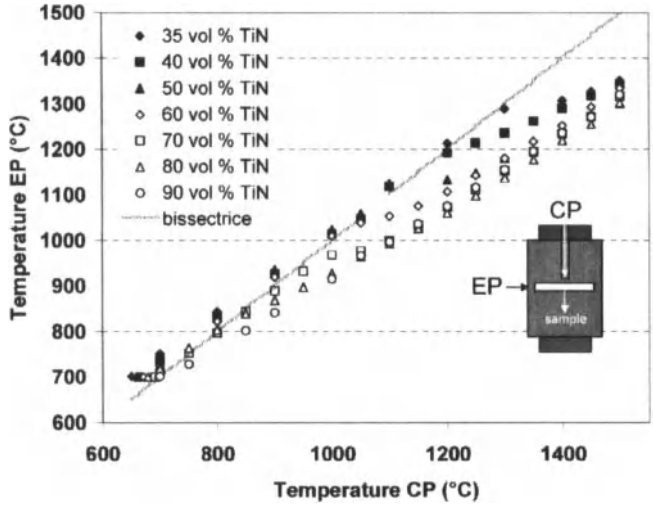

Fig. 8. Comparison of the temperature measured by an external pyrometer (EP), focussing on the die wall of a 40 mm diameter die with a die wall thickness of 8.5 mm, and a central pyrometer (CP), focussing on the bottom of a borehole in the upper punch, when ZrO_2-TiN composites with different TiN content were field assisted sintered at 1500°C.

The results shown in Figure 8 indicate that the central pyrometer temperature is similar to the external pyrometer temperature up to a certain point where they start to deviate. The deviation temperature is shown to be dependent on the volume fraction of electrically conductive particles in the sintering ZrO_2-TiN composite powder compacts, i.e., the higher the TiN content the lower the deviation temperature. In order to understand this behaviour, the electrical conductivity of the different ZrO_2-TiN composite materials were theoretically calculated (Figure 9), taking into account the volume fraction of conductive particles in the sintering powder compact as well as their densification behaviour throughout the FAST cycle described in the previous paragraph. A percolation type of mixture rule was used, assuming spherical and homogeneously dispersed secondary phase particles[9]:

$$\sigma_c = \sigma_m + (\sigma_p - \sigma_m) \frac{V_p^* \sigma_c}{\sigma_c + \frac{\sigma_p - \sigma_c}{3}} \quad (1)$$

where V_p^* is the volume fraction of secondary phase particles in a partially sintered compact containing a residual volume fraction of pores called V_{pores}. σ_c, σ_m and σ_p represent the electrical conductivities of the composite, the matrix and the secondary phase particles, respectively. Figure 9 clearly indicates that the electrical conductivity of the ZrO_2-TiN composite materials increases drastically once the percolation limit is reached. This limit is a function of the TiN volume fraction as well as of the densification behaviour and can therefore be characterised by a percolation temperature, as visualised before in case of ZrO_2-TiN (60/40) composite materials[10].

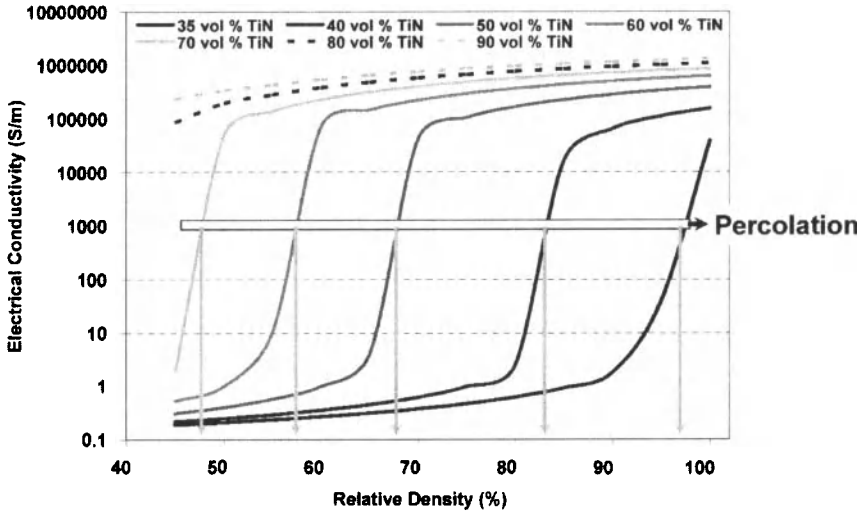

Fig.9. Electrical conductivity of ZrO_2-TiN composite powder compacts as a function of their relative density.

Before the percolation limit is reached, the sintering ZrO_2-TiN powder compact acts as an electrical insulator, so that the electrical current is forced to flow through the graphite die. During this stage, the ZrO_2-TiN sample edge is slightly overheated as compared to the sample centre (Figure 10). After percolation the current mainly flows from the upper punch into the sintering composite sample towards the lower punch, hereby generating a radial temperature gradient in the sample in the opposite direction, resulting in a colder sample edge[10]. The temperature at which percolation takes place, rather than the extent of the radial temperature gradient determines the mechanical property gradient in the ZrO_2-TiN composite samples[8]. Since the existence of thermal and mechanical property gradients should be minimised, the graphite die was surrounded by a carbon felt insulation in order to reduce the radiation heat losses and therefore the radial temperature gradient in electrically conductive samples.

MINIMISING RADIAL TEMPERATURE GRADIENTS IN ELECTRICALLY CONDUCTIVE SAMPLE MATERIALS

Figure 10 shows the simulated temperature differences between the centre and edge of a sintering ZrO_2-TiN (60/40) composite powder compact, both densified in a graphite die with (open symbols) and without (filled symbols) thermal insulation. The thermal insulation effectively reduces the thermal gradient from 140 to 35 °C during the final dwell period at 1500°C. This reduction in temperature gradient also results in a more homogeneous Vickers hardness profile that was obtained from cross-sectioned ZrO_2-TiN (20/80 vol %) discs sintered with (filled symbols) and without (open symbols) thermal insulation (Figure 11). An electrically conductive ZrO_2-TiN (20/80) composite material with an average Vickers hardness and fracture toughness of 1484 ± 7 kg/mm² and 3.3 ± 0.2 MPa.m$^{1/2}$ has been obtained.

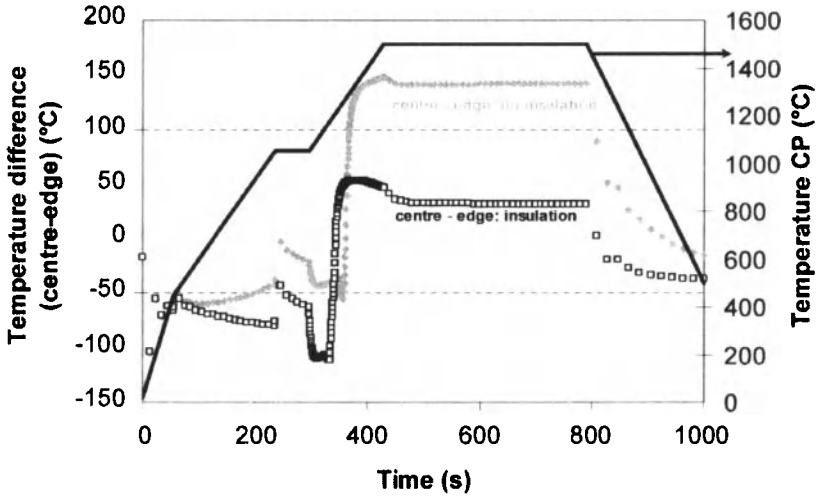

Fig. 10. Influence of thermal insulation on the radial temperature gradient (centre-edge) inside a 40 mm diameter sintering ZrO_2-TiN (60/40) (vol %) powder compact.

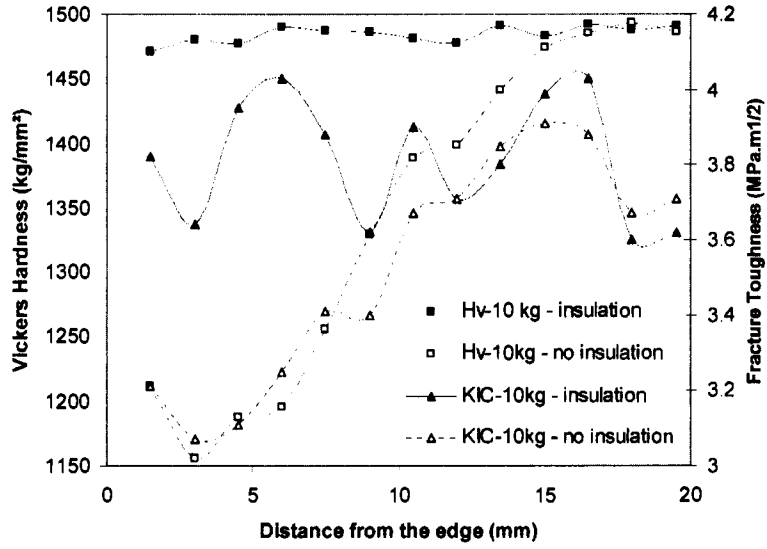

Fig. 11. Vickers hardness and fracture toughness profiles on cross-sectioned ZrO_2-TiN (20/80) discs, sintered with and without carbon felt insulation.

DEVELOPMENT OF ELECTRICALLY CONDUCTIVE CERAMICS AND HARDMETALS

Electrically Conductive Nanostructured Y-ZrO_2 based Ceramic Composites

In this paragraph it is shown how it is possible to a) maintain the intrinsic nanostructure of ceramic nanopowders throughout the FAST densification process and b) process a fully dense, electrically conductive ZrO_2-$TiC_{0.5}N_{0.5}$ (60/40) (vol %) nanocomposite material with an excellent fracture toughness.

An Y-ZrO_2 based ceramic composite material, containing 40 vol % of electrically conductive $TiC_{0.5}N_{0.5}$ nanoparticles (Hebei Sinochem, China. HTNMC grade) could be obtained after bead milling (6000 rpm, 2h, Y-TZP beads) and FAST sintering (1400°C, 2 minutes, 60 MPa, 200°C/min heating rate) of the constituent powder particles. The nanostructure could be maintained (Figure 12 a-b) by a proper selection of the sintering parameters. Furthermore, it was shown that the densification of this type of composites is enhanced by the presence of an electrical current, as indicated in Figure 13. The onset of densification is shifted towards a lower temperature as compared to traditional hot pressing (HP) and the densification rate is increased from the moment an electrical current starts to flow through the sintering composite powder compact (Figure 13).

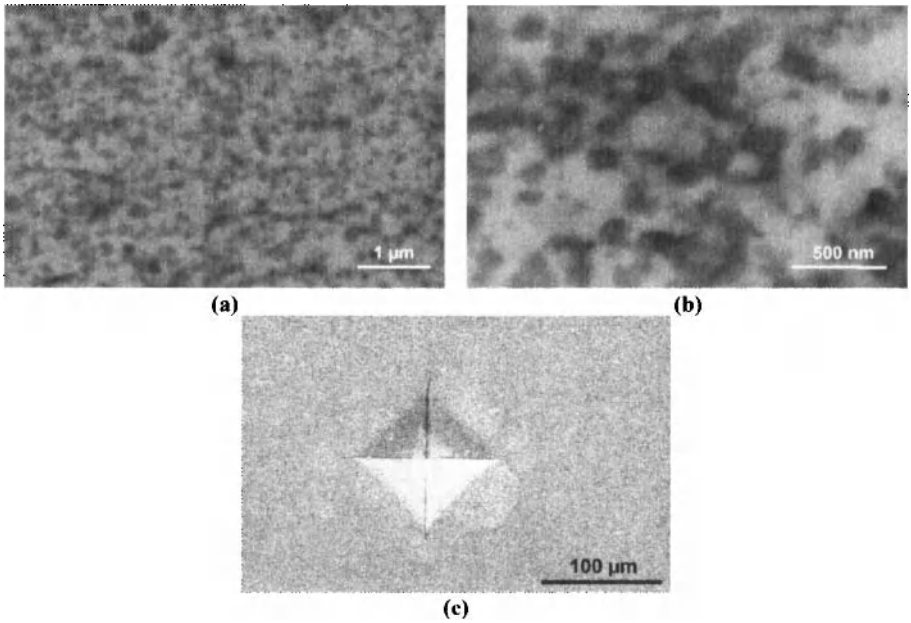

Fig. 12. Back scattered electron (BSE) micrographs of a nanostructured ZrO_2-$TiC_{0.5}N_{0.5}$ (60/40) (vol %) composite material densified by means of FAST at 1400°C for 2 minutes applying a pressure of 60 MPa (a-b). The transformed zone around a Vickers hardness indentation (10 kg) indicates that transformation toughening is the main toughening mechanism (c).

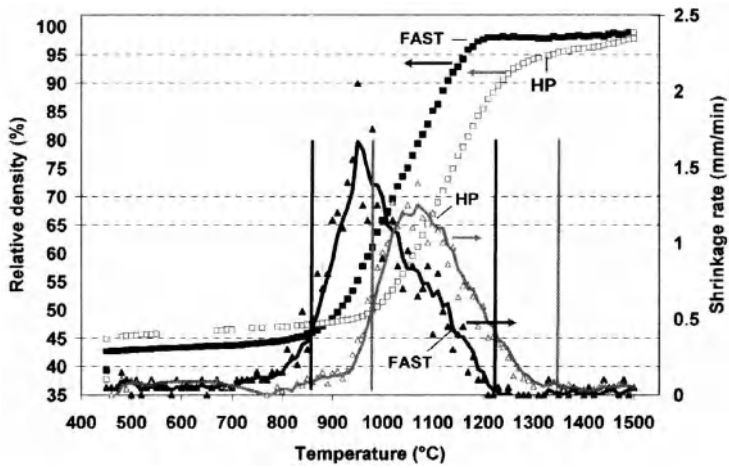

Fig. 13. Comparison of the relative density evolution of a sintering ZrO_2-$TiC_{0.5}N_{0.5}$ (60/40) composite powder compact during HP ( ) and FAST (■), following the sintering cycle shown in Figure 10. The calculated shrinkage rates, based on the experimentally determined piston travel curves are shown as well in case of HP (△) and FAST (▲). The vertical black and grey lines indicate the intermediate sintering stage during FAST and HP, respectively.

The fracture toughness of the ZrO_2-$TiC_{0.5}N_{0.5}$ (60/40) nanocomposite material was optimised by adjusting the yttria stabiliser content in the Y-ZrO_2 matrix[11]. When it was lowered from 3 to 2 mol%, the fracture toughness increased from 5.4 ± 0.3 to 9.2 ± 0.5 $MPa^{1/2}$ indicating that transformation toughening is the main toughening mechanism in this type of composites (Figure 12-c).

Binderless Tungsten Carbide (WC) based ceramics with Small VanadiumCarbide (VC) Additions

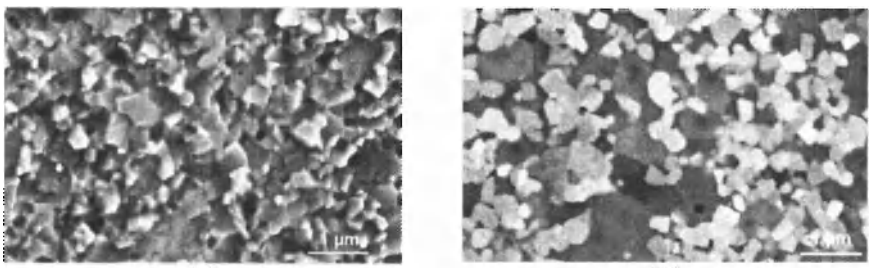

(a) (b)

Fig. 14. Fracture surface of a binderless WC material FAST sintered at 1900°C for 1.5 minutes applying a pressure of 60 MPa (a). Polished surface of a WC-12wt%VC material FAST sintered at 1800°C for 1.5 minutes. The average WC grain size was about 280 nm in both cases. The darker and larger grains that appear upon addition of VC are due to the formation of a (W,V)C phase[12].

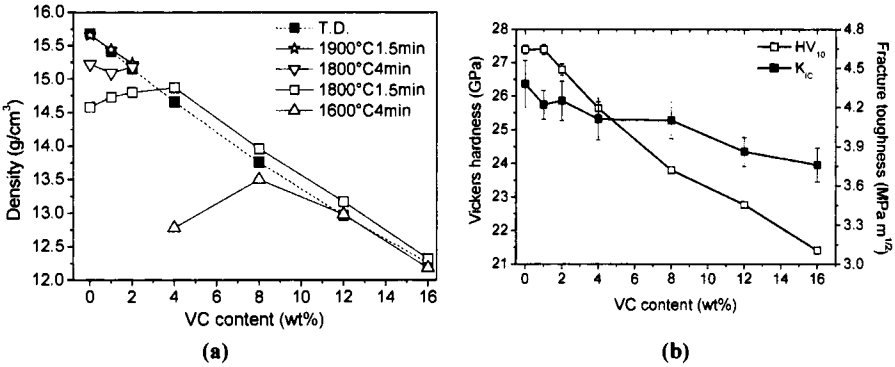

Fig. 15. Density (a) and mechanical properties of the WC-VC mixtures as function of the VC content after FAST sintering at 1600-1900°C for 1.5-4 minutes, applying a pressure of 60 MPa.

Pure WC and WC–VC powder mixtures can be fully densified by means of FAST within about 20 minutes. A dwell time of 1.5 min at 1900 °C is needed for pure and 1wt% VC doped WC material (Figure 14-a). The sintering temperature for full densification can be lowered with increasing VC addition to 1600 °C for a 16wt% VC grade (Figure 15-a). Solid state densification of the VC–WC mixtures is enhanced and accompanied by the formation of a (V,W)C solid solution (Figure 14-b). The WC grain size in all sintered material grades was about 0.28 μm and not influenced by the VC content, whereas the (V,W)C grain size increased with increasing VC content (Figure 14-b). A Vickers hardness (HV_{10}) of 27.39 ± 0.13 GPa was measured for the pure and 1wt % VC doped material grade, in combination with an indentation fracture toughness of 4.38 ± 0.18 $MPa.m^{1/2}$. Despite the lower sintering temperature (Figure 15-a), the hardness of the fully dense higher VC content grades linearly decreased down to 21.40 ± 0.20 GPa for the WC–16 wt% VC grade (Figure 15-b). The decrease in hardness is attributed to the lower intrinsic hardness and larger grain size of the (V,W)C phase. No crack deflection was established by the presence of the (V,W)C phase, resulting in a decreasing fracture toughness with increasing VC content[12].

CONCLUSIONS

A finite element model, capable of predicting the temperature and current distributions throughout the FAST process, taking into account the changing thermal and electrical properties of sintering powder compacts as well as the presence of thermal and electrical contact resistances, has been described. It was shown that both the contact resistances and the material properties influence the temperature distribution during FAST. Therefore, a more accurate temperature measurement position was chosen and its reliability was proven: independent on the material properties, the temperature in the centre of a 5 mm thick sintering compact could be accurately controlled. In case of an electrically conductive TiN sample, a large radial temperature gradient develops since the radiation heat losses from the die at high temperature can not completely be compensated by the generated Joule heat in the die.

In case ZrO_2-TiN composite materials with different TiN contents are densified by means of FAST, percolation takes places inside the sintering composite powder compact during densification. The percolation temperature depends both on the TiN content and the densification behaviour of the composite materials. The change in electrical properties of the sintering powder compacts can be monitored in-situ using a double pyrometer set-up.

Nanostructured and electrically conductive ZrO_2-TiCN (60/40) ceramic composites with an average grain size below 100 nm and with an excellent fracture toughness could be obtained after appropriate mixing and FAST densification at 1400°C for 2 minutes. It was shown that the electrical current during FAST enhances the densification of this type of composite materials by lowering the onset temperature of densification.

Finally, binderless WC and WC-VC materials with a very fine microstructure have been processed by means of FAST. The addition of VC could successfully lower the sintering temperature from 1900 to1600°C since solid state densification was enhanced by the formation of a (V,W)C solution. The coarser grain size of the (V,W)C and its incapability to deflect cracks, however, both decreased the Vickers hardness and fracture toughness of the WC-VC composite materials as compared to pure WC.

ACKNOWLEDGMENTS

K. Vanmeensel thanks the Fund for Scientific Research (FWO)-Vlaanderen for his research fellowship.A Laptev acknowledges the Research Council of K.U.Leuven for his research fellowship (F/02/096). This work was performed within the framework of the Research Fund of K.U.Leuven under project GOA/08/007 and FWO project grant number 3E060133. The authors also acknowledge the support of the Belgian Federal Science Policy Office (BELSPO) through the NACER project (contract P2/00/07).

REFERENCES

[1] Groza JR. Field assisted sintering, In: ASM handbook; Powder Metall, vol. 7; 1998. p. 583–9.

[2] Z. Shen, Z. Zhao, H. Peng and M. Nygren, Formation of tough interlocking microstructures in silicon nitride ceramics by dynamic ripening, *Nature* **417** (2002), pp. 266–269.

[3] K.A. Khor, K.H. Cheng, L.G. Yu and F. Boey, Thermal conductivity and dielectric constant of spark plasma sintered aluminium nitride, *Mater Sci Eng A* **347** (2003), pp. 300–305.

[4] X. Su, P. Wang, W. Chen, Z. Shen, M. Nygren and C. Yibing *et al.*, Effects of composition and thermal treatment on infrared transmission of Dy-α-sialon, *J Eur Ceram Soc* **24** (2004), pp. 2869–2877.

[5] T. Nagae, M. Yokota, M. Nose, S. Tomida, T. Kamiya and S. Saji, Effects of pulse current on an aluminum powder oxide layer during pulse current pressure sintering, *Mater Trans* **43** (2002) (6), pp. 1390–1397.

[6] K. Vanmeensel, A. Laptev, J. Hennicke, J. Vleugels and O. Van der Biest, Modeling of the temperature distribution during field assisted sintering, *Acta Mater.* **53** (2005), pp. 4379–4388.

[7] K. Vanmeensel, A. Laptev, J. Vleugels and O. Van der Biest, The influence of percolation during pulsed electric current sintering of ZrO_2–TiN powder compacts with varying TiN content, *Acta Mater.* **55** (2007), pp. 1801-1811.

[8] S. Salehi, O. Van der Biest and J. Vleugels, Electrically conductive ZrO_2–TiN composites, *J Eur Ceram Soc* **26** (2006) (15), pp. 3173–3179.

[9] G. Bánhegyi, Comparison of electrical mixture rules for composite, *Colloid Polymer Sci* **264** (1986), pp. 1030–1050.

[10] K. Vanmeensel, A. Laptev, O. Van der Biest and J. Vleugels, Field assisted sintering of electro-conductive ZrO_2-based ceramics, *J Eur Ceram Soc* **27** (2007) (2–3), pp. 979–985.

[11] B. Basu, J. Vleugels and O. Van der Biest, Toughness tailoring of yttria-doped zirconia ceramics, *Mater. Sci. Eng. A* **380** (2004), pp. 215–221.

[12] S.G. Huang, K. Vanmeensel, O. Van der Biest and J. Vleugels, Binderless WC and WC–VC materials obtained by pulsed electric current sintering, *International Journal of Refractory Metals and Hard Materials* **26** (2008), pp. 41-47.

Advanced Processing and Manufacturing Technologies for Structural and Multifunctional Materials II
Edited by Tatsuki Ohji and Mrityunjay Singh

POLYMETHYLSILOXANE DERIVED CERAMICS: INFLUENCE OF PYROLYSIS TEMPERATURE ON CERAMIC PHASES

Marilia Sérgio da Silva Beltrão, M.Sc.
COPPE/UFRJ
Federal University of Rio de Janeiro
P.O. Box 68505, 21945-970, Rio de Janeiro, RJ, Brazil.

Marysilvia Ferreira, D.Sc.
COPPE/UFRJ
Federal University of Rio de Janeiro
P.O. Box 68505, 21945-970, Rio de Janeiro, RJ, Brazil.

Célio A. Costa, Ph.D.
COPPE/UFRJ
Federal University of Rio de Janeiro
P.O. Box 68505, 21945-970, Rio de Janeiro, RJ, Brazil.

ABSTRACT

A new system for the pyrolysis conversion from a cross-linked polymer into a ceramic material was evaluated. Poli(dimethylsiloxane) was used as preceramic polymer and alumina and itria were used as inert fillers. Pyrolysis were carried out in a high temperature oven in air, with heating rate of $10°C.min^{-1}$, holding at 450°C for 30 minutes, heating up to temperatures that ranged from 800°C to 1400°C at $10°C.min^{-1}$, a dwell time of 1 hour and subsequent cooling. After pyrolysis, X-ray diffraction and scanning electronic microscopy were performed to identify the ceramic phases formed. Preliminary results indicate that after pyrolysis SiO_2 was the main phase formed. Oxides compounds with Al, Y and Si were found, but silica was present in the highest quantities for all temperatures.

INTRODUCTION

Porous ceramics are characterized by their low density and variety of pore size and morphology. Such microstructural features are the responsible for the variety of applications of this kind of materials, for instance: filters, permeable substrates, breather, catalysts[1,2], micro catalysts reactors[3,4], heat exchanger, turbine parts[5], molecular separations[6] and others. All these applications require a strict microstructure control regarding porosity uniformity in micro and meso scale. Furthermore, mechanical property and chemical resistance are directly dependent on the formed ceramic phases, which depend on the pyrolysis temperature. Consequently, characterization of the processed material is important to understand the transformation process

Thermal conversion (pyrolysis) of organometallic polymer into porous ceramic materials has as the major advantage to be a near net shape process and use polymer conformation technology[7,8]. The use of fillers is a well-established method in the literature[9]. Either reactive fillers or inert fillers are used. Reactive fillers react either with the precursor polymer or the pyrolysis atmosphere. These fillers expand and compensate polymer shrinkage. Filler content is around 30-50 wt% based on polymer weight and its size range from 1 to 10 μm. Silicon has been extensively studied as filler in polymer derived ceramic, and its role in the process is to react with decomposition products[10,11].

Inert fillers have been used as well. Here, fillers do not react during pyrolysis, but occupy volume on the material, which lower shrinkage. Different kinds of inert fillers can be used in the polymer thermal conversion; however, filler selection must consider final product properties. For instance, Ti[12], TiH_2[13], Si[10,11], Al[13-14], Cr[11], Fe[11], TiS_2[11,15] has been used. Porous ceramic obtained with

this method frequently present low mechanical property due to high linear shrinkage, but the use of fillers can modify this characteristic and improve the mechanical strength.

Al_2O_3 and Y_2O_3 have also been used as inert fillers in polymer pyrolysis[16,17,18], contributing to mullite formation. On the other hand, the combined use of Al_2O_3 and Y_2O_3 in euthetic composition as inert fillers has not been seen in the literature and it is presented as a new system in preceramic polymer fillers. It is expected that such system reduces shrinkage and, likewise it does in liquid phase sintering of silicon carbide[19,20], increases the mechanical strength. Then, the objective of this preliminary present study is to evaluate the ceramic phases formed after pyrolysis of polymeric precursor with alumina and yitria.

MATERIALS AND METHODS

The materials used were a commercial silicone as a polymeric precursor (Epoxitec, Brazil), Al_2O_3 (APG, Saint Gobain, Brazil, with d_{50}= 3,41μm) and Y_2O_3 (99,9%, Alfa Aesar, USA, with d_{50}=5,28μm) were fillers. They were homogenized with methylethylcetone solvent. The compositions used were: C1) 50 wt.% of silicone and 50 wt% of Al_2O_3 and Y_2O_3 in the euthetic point (60 wt% of Al_2O_3 and 40% Y_2O_3) and C2) 70 wt.% of silicone and 30 wt% of Al_2O_3 and Y_2O_3 also in the euthetic point. After solvent evaporation, a catalyst agent was added and samples were cured. The mixture polymer + filler + catalyst was transferred to a polyethylene mold. The samples were kept at room temperature for 24 hours.

The thermal conversion of the polymeric material into a ceramic body was realized in air. Several heating cycles were investigated, resulting in intermediary products. The heating cycle was composed of two parts, one for degassing and converting the polymer into ceramic, which was carried out at 450°C for one hour, at heating rate of 5°C/min, and the second one had the intention of keeping track of the crystallinity of the transformed material, which was performed with a heating rate of 10°C/min up to five different shelves temperatures (800, 1000, 1200, 1300 and 1400 °C), each one maintained for one hour, and subsequently cooled off with 10°C/min. Since each shelf temperature correspond to a single cycle, it was possible to follow the ceramic yielding during the process.

The properties analyzed were the crystalline evolution, morphology, weight loss and ceramic yield. The phase formations after pyrolysis were determined by X-ray diffraction (XDR), using CuKα radiation (1,5418 Å) in a Rigaku Miniflex equipment with 40 mA and 40 kV. The parameters used were diffraction angles from 10° to 90° and scanning rate of 5°/min. The phases were identified using JCPDS (Joint Committee on Powder diffraction Standards) Powder Data Files[21]. Fracture surfaces of the samples were observed by a scanning electronic microscopy (Jeol, model 2000 FX). Ceramic yielding and weight loss values were determined through thermogravimetric analysis (TA Instruments) until 1200°C in air. The experiments were carried out in static air, using alumina crucibles between 25 and 1200°C with a heating rate of $10°C.min^{-1}$.

RESULTS AND DISCUSSION

In Figure 1, it is shown the weight loss behavior of the silicone matrix and the both compositions used. It is clearly noted that rate of the weight loss of the matrix alone is much higher than when fillers were added; in numbers, the matrix weight loss (about 45%) is 300 % higher than with fillers (about 15%). It is also noted that beginning of the shelf temperature is a little bit higher when fillers were used, for instance, it was 450 °C for the matrix alone and 550°C and 600°C for C2 and C1, respectively. The curves have a similar format, with a fast weight loss rate in the beginning, related to the loss of volatiles, a shelf where pyrolysis take place and a decrease in the weigh loss, which is related to mass gain. For the materials with fillers, the pyrolysis temperatures ranged from 600 to 1000°C, depending on the composition. For C1, the volatiles were gone around 600°C, where pyrolysis takes place up to 1000°C, and there was a slight mass gain. For C2, the weight loss was as

fast as in C1 up to 600°C, but continued up 800°C with a slower rate. The pyrolysis was from 800 to 1000 °C and, then, a fast gain in mass was observed. The behavior observed in Figure 1 is consistent with that the reported by Greil[9], even tough he has tested in inert atmosphere. For example, the beginning of pyrolysis was 400°C[9]. while here it was 450°C. It seems that the beginning of the pyrolysis is either independent of the media used with this silicone matrix or the matrixes themselves are not exactly the same, since polymeric ramification can change the thermal behavior of the transformation reaction. Further studies will be conducted to investigate this matter. Also, this data shows that the fillers apparently has some effect on the weight loss rate and on the amount of material lost, but more refined analysis will be conducted to confirm this.

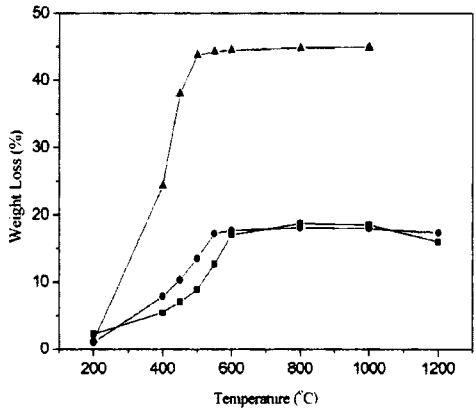

Figure 1: Weight loss of samples loaded with fillers in quantities correspondent to C1 (■) C2 (●), and cured preceramic polymer (▲) as a function of pyrolysis temperature.

The preceramic polymer without filler was processed for all heating cycles and the results were very similar, basically SiO_2 was the main ceramic phase formed for all investigated temperatures. Using the shelf temperature of 1200 °C as an example, the XRD showed the conversion to silicon oxide (SiO_2 - quartz), as shown in Figure 2. But, when the preceramic polymer alone was processed at 1400 °C, the resulting phase was cristobalite. The SiO_2 formation might be explained by the reaction of the polymeric precursor (Si based material) with the process atmosphere, which is rich in oxygen. Poli(dymethilsiloxane) monomer is constituted by Si bonded to oxygen and methyl groups, then, polymer decomposition might have been occurred readily and, due to that, generation of volatile groups, as cyclic siloxanes, HCOH, CO_2, CO, CH_3OH and HCO_2H[22]. If so, only Si and O remained bonded to each other and the high degree of freedom let both elements to rearrange themselves in a tetrahedral form. Since the crystalline structures of SiO_2 are characterized by tetrahedras of SiO_4 linked together, there are different polymorphic phases which are stable at different temperatures and conditions. The quartz phase would be expected up to 1200 °C, but cristobalite would require temperatures above 1470 °C, unless impurities were present and reduced the temperature of nucleation and growth of the cristobalite.

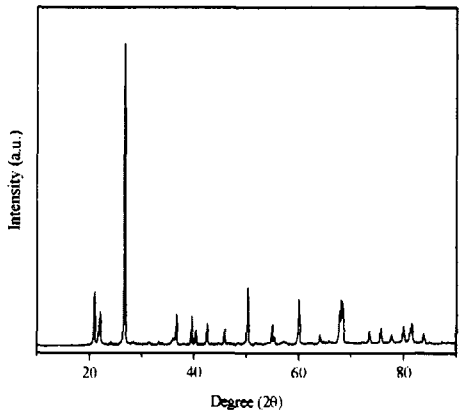

Figure 2: X-ray patterns of pyrolyzed preceramic polymer at 1200°C.

When the material with and without fillers were compared, as shown in Figure 3, the results showed the presence of peaks other than the SiO_2 observed. For the materials C1 and C2, the XRD patterns revealed the presence of Al, Y and Si oxides phases, independent of the shelf temperature. For the sample C1 at 1200 ^{0}C, shown in Figure 4, it was observed the presence of Y_2O_3 peaks and the most distinguished characteristics were: at $2\theta = 20.4°$ the intensity increased as the firing temperature increased, at 29.1° the intensity reduced for the same increase in temperature, a new peak appeared close to 30°, and around 50.1° the peaks equalized their height. The Al_2O_3 phase was also noted and all the peaks located around $2\theta = 26°$, 35°, 54°, 67° and 69° increased their intensity from 800 °C to 1300°C. For SiO_2 phase, no major change was observed. These data showed that the inert fillers did not interact to each, apparently, since no combined phase was seen until 1300 °C; however, the data in Figure 1 pointed out that filler somehow reduced the ratio of weight loss, which indicates that fillers and matrix has some form of interaction, at least until the beginning of the pyrolysis temperature.

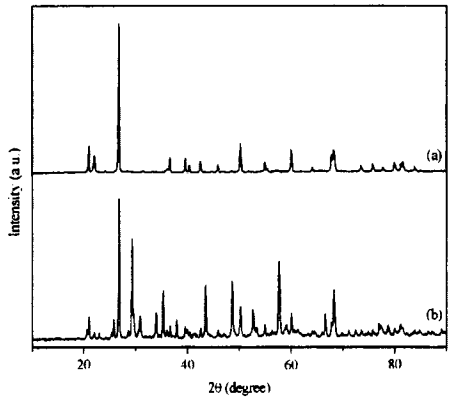

Figure 3: X-ray patterns of samples pyrolyzed at 1200°C (a) no filler and (b) C1 composition.

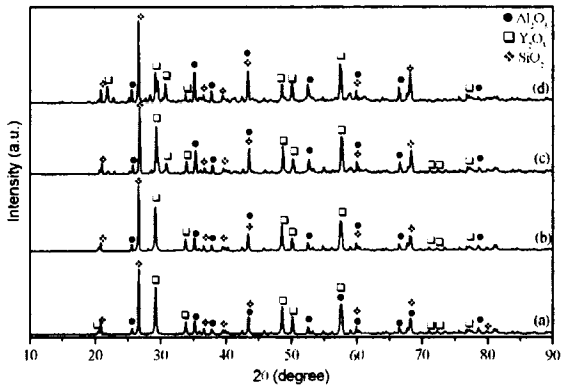

Figure 4: X-ray diffraction patterns of C1 samples pyrolyzed at temperatures (a) 800°C (b) 1000°C (c) 1200°C (d) 1300°C.

When the filled materials were heated above 1400°C, both C1 and C2 compositions formed a liquid phase which attached to the support and could not be removed yet. The Al_2O_3 and Y_2O_3 for the present compositions has an euthetic point at 1760°C[19], which could not explain the melt formed. However, the three oxides phase could have reached a composition where a liquid phase is formed[23] and so explain such observation.

The materials processed below 1300 ^{0}C were pretty much similar in morphology, which were quite porous. The appearance of the fracture surface of the sample C1 pyrolyzed at 1200 is exemplified in Figure 5. The fractography showed small porous uniformly distributed and some large ones, smaller than 100μm, also present.

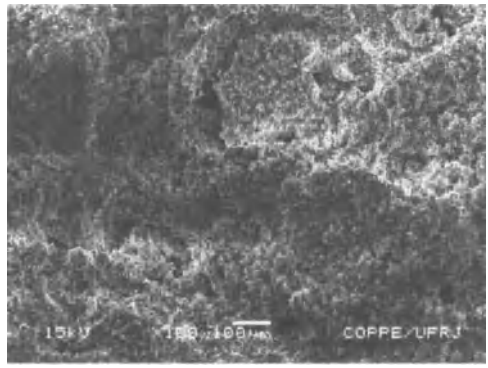

Figure 5: SEM image of the fracture surface of the sample C1 pyrolyzed at 1200°C.

Further studies will conducted on the effects of the process on the porosity control distribution, interaction of the fillers and matrix and evaluation of the mechanical properties.

CONCLUSIONS

Polymer derived ceramic based on poli(dimethylsiloxane) was prepared and the main ceramic phase formed after pyrolysis was SiO_2, quartz and cristobalite. Al_2O_3 and Y_2O_3 were used as inert fillers and did not react during the thermal conversion in temperatures up to 1300°C. Filler content did not influence the SiO_2 ceramic phase, despite of the pyrolysis temperature; however, the use of this fillers decrease the rate of weight loss. The weight loss for all investigated compositions was not superior to 18% wt, resulting in a good ceramic yield. The microstructures of specimens pyrolyzed at 1200°C were absolutely porous; however, a more in-depth investigation into morphology evaluation during pyrolysis in different temperatures and holding time is needed.

REFERENCES

[1] S. Sokolov, D. Bell, A. Stein, Preparation and Characterization of Macroporous a-Alumina, *Journal of the American Ceramic Society*, **86**, 1481-1486 (2003)

[2] K. Prabhkaran, et al., A Novel Process for Low-Density Alumina Foams, *Journal of the American Ceramic Society*, **88**, 2600-2603 (2005)

[3] J. E. Atwater, J. R. Akse, Oxygen permeation through functionalized hydrophobic tubular ceramic membranes, *Journal of Membrane Science*, **301**, 76-84 (2007)

[4] M. Scheffler, P. Greil, A. Berger, E. Pippel, J. Woltersdorf, Nickel-catalyzed in situ formation of carbon nanotubes and turbostratic carbon in polymer-derived ceramics, *Materials Chemistry and Physics*, **84**, 131–139 (2004)

[5] K. Sato, A. Tezuka, O. Funayama, T. Isoda, Y. Terada, S. Kato, M. Iwata, Fabrication and Pressure Testing of a Gas-Turbine Component Manufactured by a Preceramic-Polymer-Impregnation Method, *Composites Science and Technology*, **59**, 853-859 (1999)

[6] M. E. Davis, Ordered porous Materials for emerging applications, *Nature*, **417**, 813-821 (2002)

[7] S. Walter, D. Suttor, T. Erny, B. Hahn, and P. Greil, Injection Moulding of Polisyloxane/filler Mixtures of Oxicarbide Ceramic Composites, *Journal of the European Ceramic Society*, **16**, 387 (1996)

[8] P. Greil, Near Net Shape Manufacturing of Polymer Derived Ceramics, *Journal of the European Ceramic Society*, **19**, 1905-1914 (1998)

[9] P. Greil, Active-Filler-Controlled Pyrolysis of Preceramic Polymers, *Journal of The American Ceramic Society*, **78**, 835 (1995)

[10] J. Zeschky, T. Hofner, C. Arnold, R. Weißmann, D. Bahloul-Hourlier, M. Scheffler, P. Greil, Polysilsesquioxane derived ceramic foams with gradient porosity, *Acta Materialia*, **53**, 927–937, (2005)

[11] J. D. Torrey, R. K. Bordia, C. H. Henager Jr, Y. Blum, Y. Shin, W. D. Samuels, Composite Polymer Derived Ceramic system for Oxidizing Enviroments, *Journal of Materials Science*, **41**, 7617-4622, (2006)

[12] T. Erny, M. Seibold, O. Jarchow, P. Greil, Microstructure Development of oxicarbide composites during Active-Filler-controlled Polymer Pyrolysis, *Journal of The American Ceramic Society*, **76**, 207-213, (1993)

[13] B. Kim, D. Kim, Ti-based Ceramic Composites Derived from Polymer Pyrolysis, *Journal of the European Ceramic Society*, **27**, 837-841, (2007)

[14] J. Anggono, B. Derby, Mullite Formation from the Pyrolysis of Aluminium-loaded Polymethylsiloxanes: The Influence of Aluminium Powder Characteristics, *Journal of the European Ceramic Society*, **26**, 1107–1119, (2006)

[15] J. D. Torrey, R. K. Bordia, Mechanical Properties of Polymer-derived Ceramic Composite Coatings on Steel, *Journal of the European Ceramic Society*, **28**, 253-257, (2008)

[16] G. D. Sorarú, H. Kleebe, R. Ceccato, L. Pederiva, Development of Mullite-SiC nanocomposites by pyrolysis of filled Polymethylsiloxane Gels, *Journal of the European Ceramic Society*, **20**, 2509-2517, (2000)

[17] E. Bernardo, P. Colombo, E. Pippel and J. Woltersdorf, Novel Mullite Synthesis Based on Alumina Nanoparticles and a Preceramic Polymer, *Journal of The American Ceramic Society*, **89**, 1577-1583, (2006)

[18] D. Suttor, H. Kleebe, G. Ziegler, Formation of Mullite from Filled Siloxanes, *Journal of The American Ceramic Society*, **80**, 2541-2548, (1997)

[19] E. Gomez, J. Echeberria, I. Iturriza, F. Castro, Liquid Phase Sintering of SiC with additions of Y_2O_3, Al_2O_3 e SiO_2. *Journal of the European Ceramic Society*, **24**, 2895-2903, (2004)

[20] J. H. She, K. Ueno, "Effect of Additive Content on Liquid-Phase Sintering on Silicon Carbide Ceramics", *Materials Research Bulletin*, **34**, 1629-1636 (1999)

[21] JCPDS, X-ray Powder Data File, *International Center for Diffraction Data*, Pennsylvania, (2001)

[22] A. C. M. Kuo, Poly(dimethylsiloxane), *Polymer Data Handbook*, Oxford University Press, Inc, 1999.

[23] E.M. Levin, C.R. Robbins, H.F. McMurdie, *Phase Diagrams for Ceramists*, Supplement, edited by MK Reser, American Ceramic Society, Columbus, OH, 1969.

Advanced Processing and Manufacturing Technologies for Structural and Multifunctional Materials II
Edited by Tatsuki Ohji and Mrityunjay Singh

FREEFORM FABRICATION OF ALUMINA DENTAL-CROWN MODELS BY USING STEREOLITHOGRAPHY

Masahito Ishikawa[a)], Soshu Kirihara [a)], Yoshinari Miyamoto [a)], and Taiji Sohmura [b)]
a) Smart Processing Research Center, Joining and Welding Research Institute, Osaka University, Ibaraki, Osaka 567-0047, Japan
b) School of Dentistry, Osaka University, Suita, Osaka 565-0871, Japan

ABSTRACT

Ceramic materials have become more popular due to their desirable aesthetics and biocompatibility in the area of dental restoration. Acrylic three-dimensional dental-crown model structure with Al_2O_3 dispersion at 40 vol. % was fabricated by using stereolithography of the CAD/CAM system. After dewaxing acrylic resin at 600 °C for 2 hs in air, it was sintered at 1,500 °C for 2 hs. The linear shrinkage after sintering was approximately 25 %, and the relative density reached 98 %. The Al_2O_3 bar specimens of 1.2×4×20 mm in dimension were also fabricated by the same method. The measured average flexural strength was 64±11 MPa. To improve the mechanical property, the Al_2O_3 specimens were infiltrated with the La_2O_3-B_2O_3-Al_2O_3-SiO_2 glass used in dentistry. The infiltrated specimens were annealed at 1,100 °C for 2 hs and sandblasted. The average flexural strength could be increased to 197±24 MPa.

INTRODUCTION

In the area of dental restoration for dentures and crowns, ceramic materials have been focused in recent years. They have desirable aesthetics and biocompatibility compared with traditional metal-ceramic restorations. These dental-crowns should be formed to adjust individual shapes. A large variety of methods have been considered to produce individual ceramic structures[1-3]. Especially, cutting work is currently prevailed as the method of forming ceramic crowns. However, ceramics are difficult to cut because of their high hardness. In addition, just a single crown can be formed during one operation by this method. In contrast, rapid prototyping of layer lamination make it possible to form various arbitrarily-shaped structures at the same time. The CAD/CAM stereolithography represents one of the most common processes of rapid prototyping. But it has been limited to building models of resin materials, up to now. There are a few reports which introduce forming ceramic structures by using stereolithography[4-5]. Our group has also succeeded in fabricating millimeter-order three-dimensional ceramic structures by stereolithography[6]. In this study, we present a new technique to fabricate

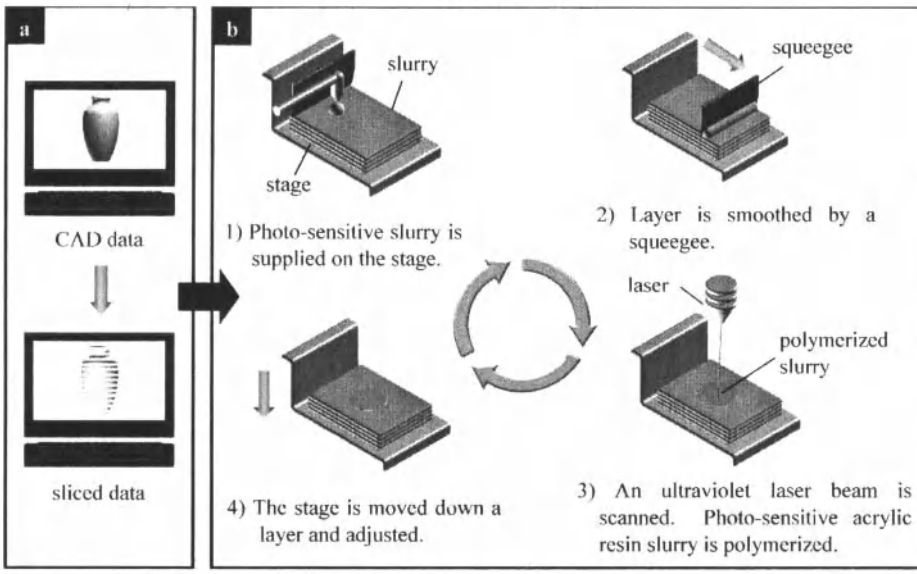

Fig. 1 (a) Computer operation of CAD data, (b) A schematic illustration of Al_2O_3-resin laminate fabrication process by stereolithography.

a dental-crown shape and their mechanical properties. A dense Al_2O_3 dental-crown model was fabricated by dewaxing and sintering of the green body composed of nanometer-sized Al_2O_3 particles dispersed in acrylic resin formed by stereolithography.

EXPERIMENTAL PROCEDURE

Figure 1(a) and (b) show a schematic illustration of the fabrication process by stereolithography. The three-dimensional CAD data of a dental-crown (an upper molar

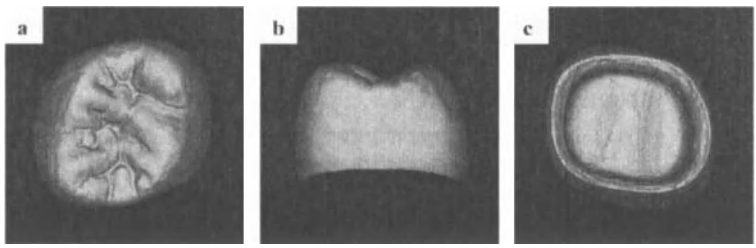

Fig. 2 Three-dimensional CAD dental-crown model of an upper molar tooth, (a) top view, (b) side view, (c) bottom view.

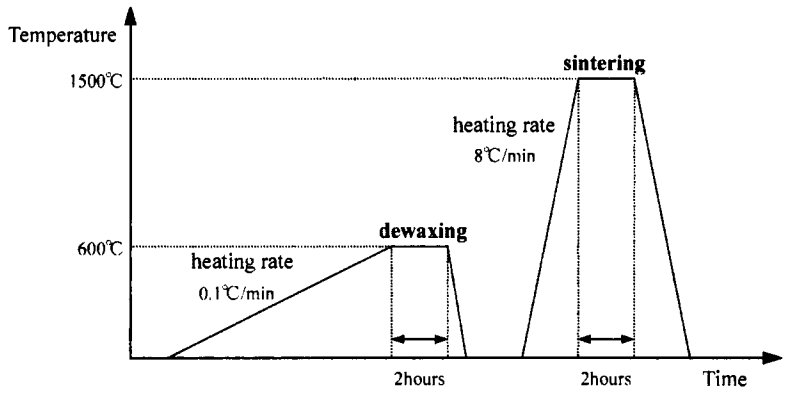

Fig. 3 Dewaxing and sintering schedule for a Al_2O_3 dental-crown model and Al_2O_3 test specimens.

tooth) was converted into a stereolithography format (STL file), and sliced into a series of two dimensional figures with uniform thickness on a computer. Figure 2(a), (b) and (c) show the CAD data along different directions. It was a real model given by a collaborator in our school of dentistry. The data was transferred to stereolithography equipment (D-MEC Co. Ltd., Japan, SCS-300P). Nanometer-sized Al_2O_3 particles of 170 nm in diameter were dispersed into photo-sensitive acrylic resin at 40 vol. %. The obtained resin slurry with ceramic particles dispersion was supplied on a stage and squeegeed. The dispersion of nanometer sized particles can give the thixotropic flow to the slurry including high ceramic content and reduce the dynamic viscosity when squeegeeing the surface layer. An ultraviolet laser beam of 355 nm in wavelength was scanned on the surface according to a computer operation. We adjusted a laser spot 100μm in beam diameter with 100mW in power. The photo-sensitive acrylic resin slurry could be polymerized with ceramic particles. Accordingly, a two dimensional composite figure was solidified. The remaining slurry could support a solid object because of its thixotropy. The stage was moved down a layer, and the slurry was supplied on the stage again. The thickness of each layer was 30μm. By repeating this layer stacking process, a three-dimensional solid object was fabricated.

The composite precursor formed by stereolithography was heated and dewaxed in air at 600°C for 2hs with the heating rate 0.1°C/min. And then, it was sintered at 1,500°C for 2hs with the heating rate 8°C/min. After sintering, it was furnace cooled. Figure 3 shows a typical dewaxing and sintering schedule. The relative density of the sintered object was measured by Archimedes method. The microstructures at the surface

of the object after dewaxing and sintering were observed by using scanning electron microscope (SEM).

Test models with the same material were fabricated by the same method for measurement of their dimensions. They were designed by simplifying the dental-crown model. The linear shrinkage ratios along the horizontal and vertical axes of the obtained test models were measured.

Twelve bulk samples with the same material were prepared by the same method in order to measure their flexural strength and Vickers hardness on the surface. Each precursor sample was 3×7×28 mm in dimension. After sintering, they were ground and polished into 1.2×4×20mm in dimension as test specimens. Six test specimens of them were heated in the La_2O_3-B_2O_3-Al_2O_3-SiO_2 glass ceramic powder (VITA Zahnfabrik Co. KG, VITA In-Ceram ALUMINA Powder) in air at 1,100°C for 2hs, and they were infiltrated by the osmotic pressure. This glass is used as a ceramic coating on a metal tooth in dentistry. The excess glass on the surface of the test specimens was eliminated by sandblasting. The flexural strength and the Vickers hardness on the surface were measured. After that, the fractured surface of test specimens were observed by SEM.

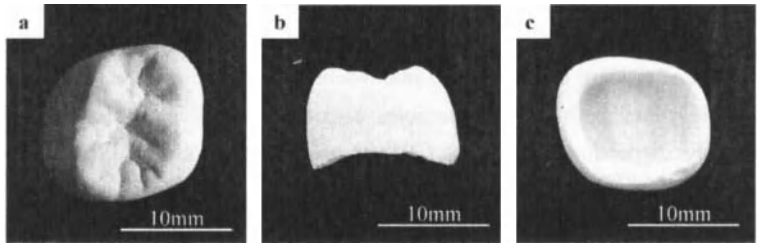

Fig. 4 Al_2O_3 dispersed resin precursor of a dental-crown model fabricated by stereolithography, (a) top view, (b) side view, (c) bottom view.

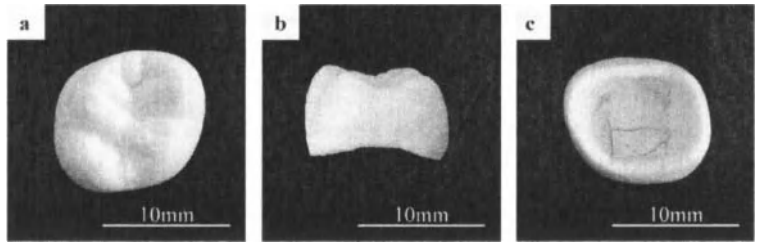

Fig. 5 Sintered Al_2O_3 body of a dental-crown model, (a) top view, (b) side view, (c) bottom view.

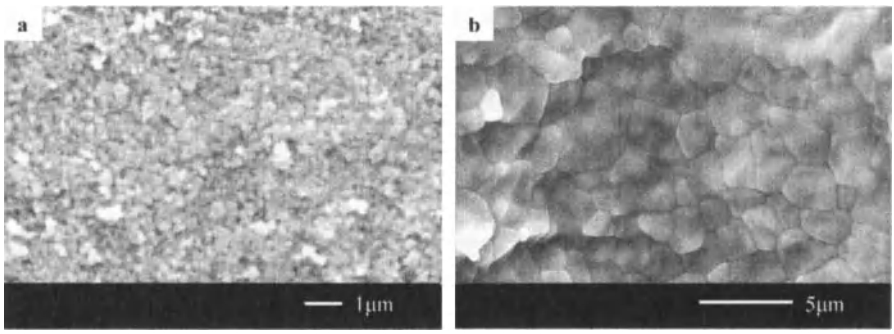

Fig. 6 Microstructure on the surface of a dental-crown model, (a) after dewaxing, (b) after sintering.

RESULTS AND DISCUSSION

Figure 4(a), (b) and (c) show the Al_2O_3 dispersed resin precursor of a dental-crown model fabricated by stereolithography along different directions. The grooves at the top surface of green body were precisely shaped, and the peripheral edge on the bottom could be sharp. No large steps by the layer lamination were found, and so the surface profile was smooth. Large delamination or staking faults of layers were not observed at the surface of the precursor. The spatial resolution was approximately 1.2%. When the layer thickness was 30μm, we could obtain a hollow structure of this dental-crown model without large faults. When it was 50μm, some stacking faults appeared. The bond strength between layers of a hollow structure may not be enough for such thick layers with small joint area. To get good bond strength of layer lamination, it would be desirable to adjust the layer thickness at 30μm or lower.

Figure 5(a), (b) and (c) show a sintered body of the dental-crown model along different directions. There was no large deformation. Its surface was smooth, and large cracks were not found at the top and the side surfaces. However, some cracks were observed at the bottom surface. The distortion in shrinkage during the heat treatment would cause the cracking. Figure 6(a) and (b) show the microstructures at the surfaces of the dewaxed and the sintered bodies, respectively. The particle size of Al_2O_3 was approximately 170nm in dewaxing and no grain growth started. Many pores were observed in the dewaxed body where the resin was pooled. In contrast, the dense structure could be observed on the sintered body. The Al_2O_3 particles grew approximately 2 to 4μm. No large grain growth occurred during sintering treatment. The relative density reached approximately 98%.

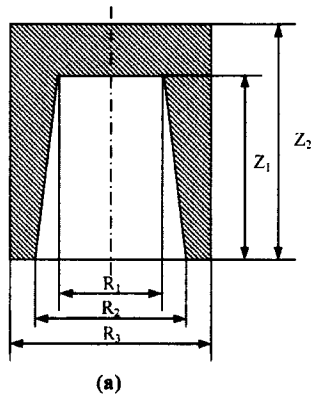

	R_1	R_2	R_3	Z_1	Z_2
Green Body Length (mm)	11.7	13.0	17.0	12.8	16.1
Sintered Body Length (mm)	8.9	9.9	12.9	9.2	11.6
Liner Shrinkage Ratio (%)	23.8	23.8	23.8	27.9	28.0

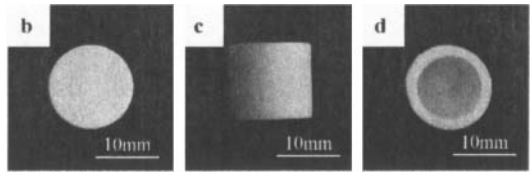

Fig. 7 (a) Diagram of a test model and the linear shrinkage ratios after sintering. (b) top view, (c) side view, (d) bottom view of a sintered Al_2O_3 test model.

It is difficult to measure precise dimension of the dental-crown model structure because of their complex shape. Therefore, test models were fabricated to measure the linear shrinkage ratio of the dental-crown model. Figure 7(a) shows a diagram of test specimens. Figure 7(b), (c) and (d) show a sintered test model along different directions. The linear shrinkage ratios of horizontal axis resulted in approximately 24%. While, that

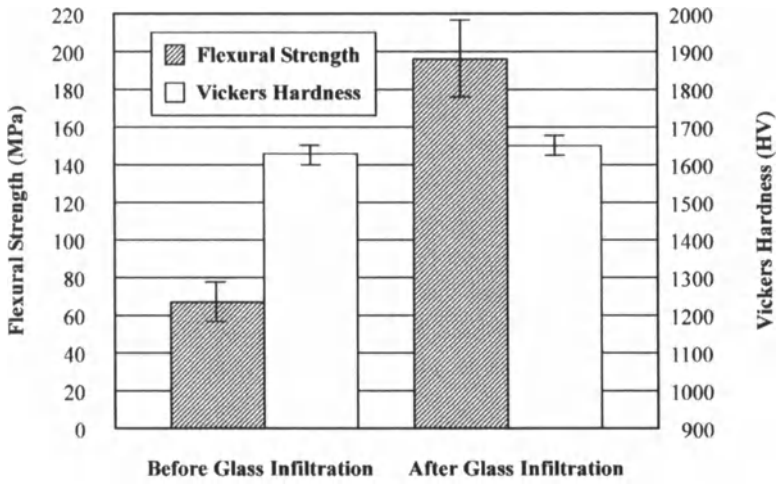

Fig. 8 Flexural strength and Vickers hardness of sintered test specimens (a) before glass infiltration, (b) after glass infiltration.

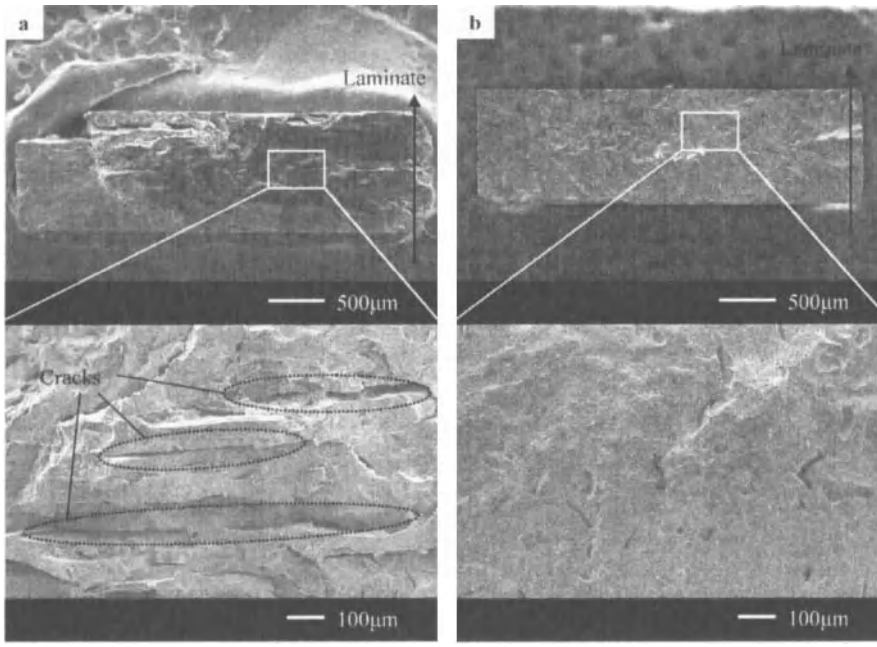

Fig. 9 SEM micrographs of the fractured surface of sintered test specimens (a) before glass infiltration, (b) after glass infiltration.

of vertical axis was approximately 28%. The larger shrinkage ratio in vertical axis could be due to the gravity effect by its own weight. It is possible to get uniform shrinkage by expanding the vertical direction in the design stage to compensate this gravity effect.

Figure 8 shows the results of flexural and hardness tests measured for the sintered bar specimens. Their average hardness resulted in approximately 1600 Hv which was close to that of conventional Al_2O_3 ceramics. It was not changed after the glass infiltration. The average flexural strength before the glass infiltration specimens was 64±11 MPa which was much lower than that of conventional Al_2O_3 ceramics. However, it could be improved to 197±24 MPa after the glass infiltration. Figure 9(a) and (b) show the fractured surface of the test specimen before and after the glass infiltration. Before the glass infiltration, many micro cracks parallel to layers were observed. These micro cracks could be produced in the freeforming stage, and expanded during the heat treatment. Some micro cracks appeared not at the joints in layers. The gasification of resin inside the specimen in the dewaxing stage seems to open the cracks. No many cracks were observed in the specimens after the glass infiltration. This result

indicates that the glass infiltration is effective to fill in cracks from the surface to the interior. To get the flexural strength required for real artificial tooth at 400~800 MPa, further improvements for uniform slurry mixing, accurate layer stacking, and moderate heat treatment are necessary.

CONCLUSION

We fabricated a three-dimensional dental-crown model composed of 40 vol. % Al_2O_3 dispersed acrylic resin by stereolithography. After dewaxing at 600°C and sintering at 1,500°C, a dense Al_2O_3 ceramic body was obtained without deformation. No large cracks were found on the surface though some micro cracks remained inside. The relative density was approximately 98%. The average Vickers hardness and flexural strength of sintered test specimens were approximately 1600Hv, 64±11 MPa, respectively. The flexural strength could be improved to 197±24 MPa by glass infiltration.

REFERENCES

[1]J. Stampfl, H. C. Liu, S. W. Nam, K. Sakamoto, H. Tsuru, S. Kang, A. G. Cooper, A. Nikel, F. B. Prinz, Rapid prototyping and manufacturing by gelcasting of metallic and ceramic slurries, *Materials Science and Engineering*, **A334**, 187-192 (2002).

[2]H. H. Tnag, F. H. Liu, Ceramic laser gelling, *Journal of the European Ceramic Society*, **25**, 627-632 (2005).

[3]R. Zauner, Micro powder injection moulding, *Microelectronic Engineering*, **83**, 1442-1444 (2006).

[4]A. Licciulli, C. E. Corcione, A. Greco, V. Amicarelli, A. Maffezzoli, Laser stereolithography of ZrO_2 toughened Al_2O_3, *Journal of the European Ceramic Society*, **25**, 1581-1589 (2005)

[5]C. Sun, X. Zhang, The influences of the material properties on ceramic micro-stereolithography, *Sensors and Actuators*, **A 101**, 364-370 (2002).

[6]S. Kirihara, Y. Miyamoto, K. Takenaga, M. Takeda, K. Kajiyama, Fabrication of electromagnetic crystals with a complete diamond structure by stereolithography, *Solid State Communication*, **121**, 435-39 (2002).

Advanced Processing and Manufacturing Technologies for Structural and Multifunctional Materials II
Edited by Tatsuki Ohji and Mrityunjay Singh

SILICON NITRIDE RAPID DECOMPOSITION FOR FORMATION OF NANOSIZED POWDERS FOR SHAPING MICRODEVICES

Dariusz Kata, Jerzy Lis;
University of Science and Technology, Faculty of Material Engineering and Ceramics, Department of Technology of Ceramics and Refractories
Al. Mickiewicza 30, 30-059, Cracow, Poland

ABSTRACT

Silicon nitride rapid decomposition at SHS conditions has been successfully used to manufacturing ceramic nanopowders in the Si-C-N and Si-O-N systems. These nanopowders are suitable for shaping ceramics microreactors. The well-mixed powdered reactants were placed in porous container, then reaction was locally ignited and combustion was propagated in self sustaining regime achieving temperatures over 2000°C. In all these experiments combustion propagated with formation of transient Si_3N_4 phase resulted in either: SiC or Si_2ON_2 nanosized grains. To elucidate role of decomposition of silicon nitride on formation of nanosized products, thermodynamic data, temperature profiles, morphology (SEM, TEM), dispersion (BET) and phase composition (XRD) of products were evaluated. It was found, that in both Si-C-N and Si-O-N systems, silicon nitride forms transiently at early stages of combustion because thermodynamic and kinetic considerations.

a) In case of Si-C-N system three steps of reaction were detected (i) nitridation of the silicon surface during initial stages, (ii) simultaneous nitridation and carbonization of the liquid silicon (iii) decomposition and carbothermal reduction of silicon nitride resulting in nanosized pure silicon carbide grains;

b) In case of Si-O-N system two steps of reaction were detected: (i) nitridation of the silicon surface during initial stages, (ii) simultaneous decompostion of silicon nitride and reaction with silica resulted in pure silicon oxynitride nano-powder;

Finally, it was demonstrated that technology of silicon carbide and silicon oxynitrde nano-powders by decomposition of Si_3N_4 is very efficient to compare other conventional techniques.

INTRODUCTION

The use of SHS may bring about a considerable and urgently needed development in ceramic technology, by enabling a manufacturing of sinterable, high-purity nanopowders. In current technologies adequate nanopowder properties have been achieved by rather very elaborate and/or time consuming processing. Therefore, the present work is aimed at efficient and convenient processing of nanopowders as an important target for future research.

In numerous systems, especially the Si-contained ones, the SHS products are formed via liquid phase by precipitation of this phase from liquid [1,2] This mechanism is believed to be responsible for the narrow grain size distribution that is usually found in the products [3]. Moreover, formation of silicon carbide or silicon oxynitride in the Si-C-N and Si-O-N systems is associated with transient formation of silicon nitride[4,5]. The transient formation can be controlled both by nitrogen gas pressure and combustion temperature [6]. At high combustion temperatures e.g. 1950-2500°C and low nitrogen pressures Si_3N_4 e.g. 1-2 MPa. silicon nitride rapidly decomposes according to $Si_3N_4=Si_{(l)}+N_2$ [7]. Lower combustion temperatures (below 1950°C) and higher nitrogen pressures (higher than 3,0 MPa) hamper decomposition of silicon nitride and lead to Si_3N_4 remains in final SHS product [8].

Utilization of silicon nitride rapid decomposition is a new approach in manufacturing of silicon carbide and silicon oxynitride nano-powders. Silicon carbide polycrystals are very perspective for

structural application. Practically, it's constant flexural strength up to 1200°C, very high Young modulus, hardness and stiffness as well as very good creep and wear resistance make silicon carbide ideal candidate for tools and parts for various kinds of machines[9]. Structural properties of silicon oxynitride are also very attractive because of it's high oxidation resistance, high fracture toughness and very good flexural strength. Thus, both materials can be used for manufacturing high temperature ceramic microreactors. However, formation methods of microreactors from SiC and Si_2ON_2 nanopowders are still at early stages.

EXPERIMENTAL PROCEDURE

The following high purity reactants were used in the SHS process: silicon, carbon and silica powders and gaseous nitrogen. Two raw mixtures were prepared with composition of solid reactants according to reaction equations: (1) $Si+C=SiC$ and (2) $Si+SiO_2+2N_2=2SiON_2$. Specific surface areas of powdered silicon, black carbon and silica were estimated to 8,2 m^2/g, 90,2 m^2/g, 200 m^2/g, respectively. Stoichiometric mixtures of solid reactants were homogeneously mixed in ethanol for 24 hours using silicon nitride grinding media.

The combustion was carried out in the high pressure reactor under the nitrogen gas pressures of 2.5 MPa; 3.0 MPa 3.5 MPa and 4.0 MPa. The reactants mixtures were placed inside high pressure chamber in form of homogeneous loose powder bed. The chamber was filled up to desired nitrogen pressure and combustion was initiated locally in one point of powdery bed having length of 40 cm, width of 8,0cm and 8,0cm in depth. The maximum temperature of the combustion was measured by thermocouples placed in the center of the bed. The input signal from thermocouple was transformed by A/C fast converter and registered by computer.

The phase composition of combustion products was determined by XRD (Philips X'Pert 2002). Products morphology was observed by SEM (JOEL) and TEM (Philips C-30) and chemical composition was analyzed by EDX. Specific surface area was measured by BET (Carlo Erba Instruments) method.

The SHS derived nanopowders were disaglomerated in ethanol for 2 hours in rotary vibration mill. Two ceramic UV curable pastes of silicon carbide and silicon oxynitride were prepared. Both included monomer BDMA (Butanediol-monoacrylate) BASF Germany and photoinitiator (Genocure TPO). Pastes were homogenized by dissolver TD100 (Pendraulik-Teja) and printed by Screen Printing. Finally, printed patterns were cured by UV lamp.

RESULTS

The Si-C-N system

The studies on the silicon carbide formation by solid combustion in the Si-C-N system were carried out to prepare the SiC nano-powder. Conventional SHS combustion in the Si-C system provides products in form of strongly agglomerated SiC coarse grains demanding long time of milling for further processing. In contrast realization of the Si+C exothermic reaction under nitrogen pressure gives much more efficient way of silicon carbide nanopowder preparation.

In Fig. 1 the X-ray diffraction patterns for SHS products obtained under 2.5 MPa; 3.0 MPa, 3.5 MPa and 4.0 MPa of N_2 pressure in the Si-C-N system are shown. Combustion reaction propagated spontaneously in self sustaining regime for all nitrogen pressures. The combustion products for 2.5 MPa; and 4.0 MPa of N_2 are consisted of β-SiC and β-Si_3N_4 phases. In case of 3.0 MPa and 3.5 MPa of nitrogen pressure pure β-SiC phase is detected only. The absence of free silicon peaks for all nitrogen pressures indicated a high reaction degree, estimated to be higher than 98%. A LECO analysis showed nitrogen content less than 0,1% in synthesized silicon carbide powder

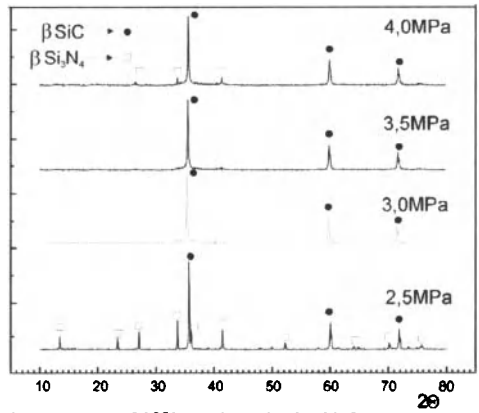

Figure 1. X-Ray diffraction patterns of SHS products in the Si-C-N system combusted under 2.5MPa; 3.0MPa, 3.5MPa, and 4.0MPa nitrogen pressure.

The specific surface area of products with associated the maximum peak temperature of combustion in the Si-C-N system are shown in Figure 2. A gradual increase of specific surface area with increasing nitrogen pressure up to 3,5MPa is observed. However, higher pressure of 4,0MPa resulted in decreasing of products dispersion. It is interesting to note that specific surface area of powders well corresponded to phase composition of products. The final pure SiC powder have the highest specific surface area of about $19m^2/g$ but products with silicon nitride content obtained under 2.5 MPa and 4.0 MPa of nitrogen pressure showed lower specific surface area of about 8-12 m^2/g. Assuming that the measured surface area is the sum of the areas of silicon nitride and silicon carbide powders, we see that synthesized SiC is much finer than Si_3N_4. The reaction maximum temperature is gradually increasing as nitrogen pressure is also increasing but high temperature of reaction does not influence the surface area of powdered products as it is commonly observed for the combustion synthesis of pure β-Si_3N_4

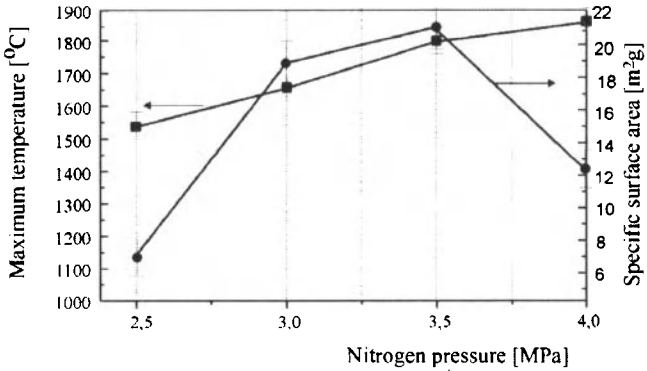

Figure 2. Specific surface area and maximum temperatures vs. nitrogen pressure of SHS combustion in the Si-C-N system. Combustion nitrogen pressure 2.5 MPa; 3.0 MPa, 3.5 MPa and 4.0 MPa

In Figure 3a and 3b the morphology products obtained under 3.0MPa and 4.0MPa are shown respectively. Based on EDS analysis and XRD measurements showed in Fig.1, it is found that nanometric particles in Fig. 3a are silicon carbide phase. Thus, we concluded that SHS reaction accomplished under 3.0MPa of nitrogen pressure resulted in silicon carbide nanopowder. A bi-modal size distribution of particles can be observed in Fig.3b. The larger particles are faceted and have sharp edges, while the smaller ones are still in nanometric size in the form of agglomerations. The presence of silicon nitride phase detected by XRD and showed in Fig 1 leads to conclusion that coarser grains are β-silicon nitride.

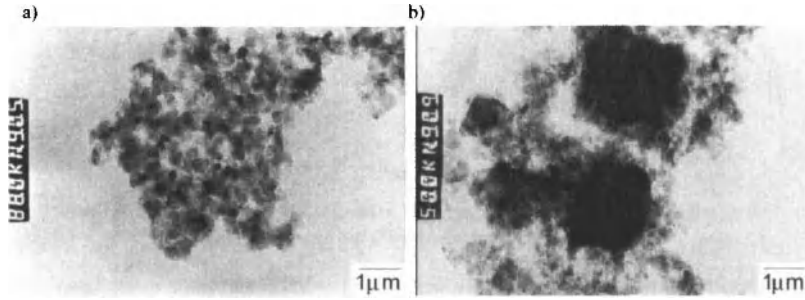

Figure 3 (a) TEM images of silicon carbide nano-powder synthesized under 3.0 MPa of nitrogen pressure; (b) silicon carbide - silicon nitride nanopowder synthesized under 4.0 MPa of nitrogen pressure;

The Si-O-N system

Existing literature indicates that silicon oxynitride can be synthesizes by several methods: reaction of silicon nitride and silica in nitrogen atmosphere [10], ammonolysis of hexachlorodisiloxane [11], hot pressing in nitrogen atmosphere of starting mixture consisted of silicon nitride and silica powders [12] and nitridation of silicon and silica powdered mixture [13]. However, preparation techniques of fine dispersed silicon oxynitride powder are very limited. Therefore the present study is aimed at preparation of silicon oxynitride nanopowder.

In Figure 4 the X-ray diffraction patterns of products combusted according to: $Si+SiO_2+2N_2=2SiON_2$ under 2.5 MPa; 3.0 MPa, 3,5 MPa and 4.0 MPa of nitrogen pressure is shown. Combustion propagated in self sustaninig regime and silicon oxynitride is detected as major phase in all products. However, remains of silicon nitride as well as unreacted free silicon are also detected in all powders as minor phases. The lower contents of Si_3N_4 and Si are found in products obtained under 3,0 MPa of nitrogen pressure. Higher pressure provided higher content of unreacted silicon and silicon nitride.

In Figure 5 the specific surface area of SHS-derived powders and the maximum temperature of combustion in the Si-O-N system are shown. The temperature of combustion is rather stable as pressure is increasing. Specific surface area of products is very high and drops down with increase of nitrogen pressure. Based on presented results we concluded that nitrogen pressure of 3.0 MPa is suitable for combustion reaction in the Si-O-N system because high specific surface area about $20m^2/g$ and almost pure silicon oxynitride are obtained.

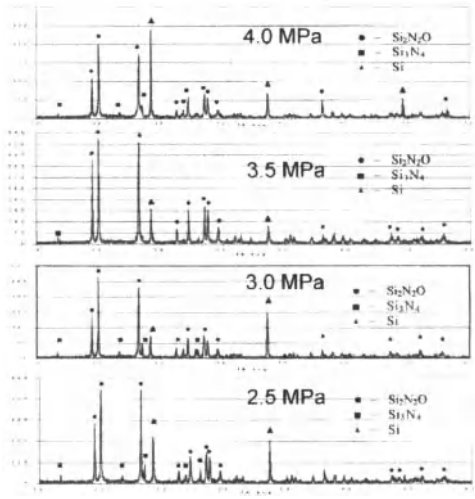

Figure 4. X-Ray diffraction patterns of SHS products in the Si-O-N system combusted under 2.5MPa; 3.0MPa, 3.5MPa, and 4.0MPa nitrogen pressure.

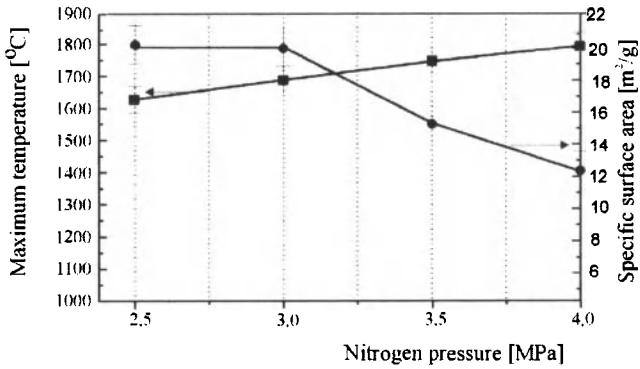

Figure 5. Specific surface area and maximum peak temperatures vs. nitrogen pressure of SHS combustion in the Si-O-N system. Combustion nitrogen pressure 2.5 MPa; 3.0 MPa, 3.5 MPa and 4.0 MPa

SUMMARY

The results of this study, and investigation of Kata at al into combustion synthesis in the Si-C-N and Si-O-N system [4] indicated the complex character of the combustion which is controlled by silicon nitride decomposition [14]. It could be illustrated by temperature profiles registered during SHS that showed in Figure 6.

a)

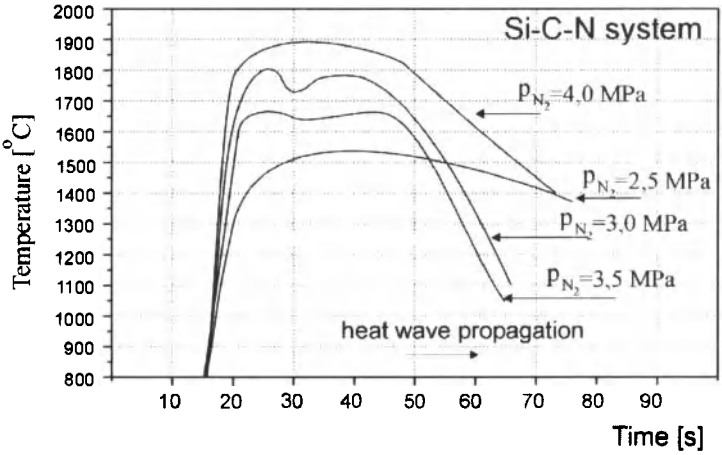

b)

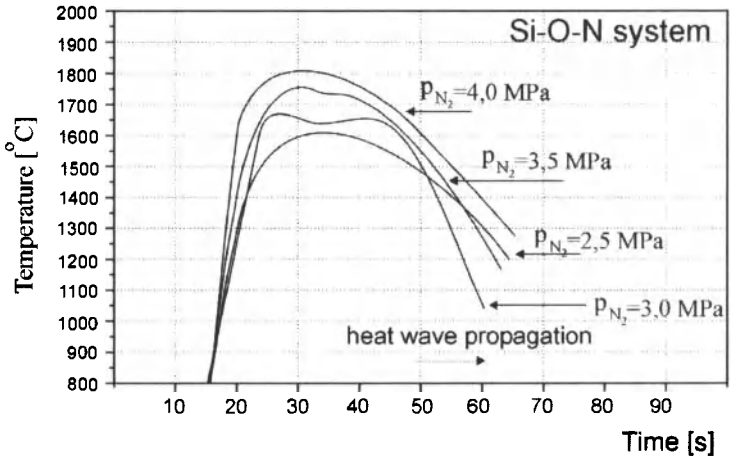

Figure 6. Temperature profiles of SHS reaction for different nitrogen pressure in the Si-C-N system (Figure 6a) and in the Si-O-N system (Figure 6b).

In the Si-C-N system temperature curves for 2,5 MPa and 4,0 MPa of nitrogen pressure have one-modal flat character with maximum temperatures reaching 1530°C and 1880°C respectively. For 3.0 MPa and 3,5 MPa of nitrogen pressure temperature profiles assumes a two-modal character with maximum temperatures reached 1650°C and 1800°C respectively (Figure 6a). This can suggest a change in the course of the combustion when bi-modal temperature curves appeared. In the Si-O-N system (see Figure 6b) two peaks of temperature are registered for mixture combusted under 3,0MPa and 3,5MPa of nitrogen pressure and for 2,5MPa and 4,0MPa the temperature curves are one-modally

shaped. Phase composition of combustion products is well correlated with combustion temperature profile. If temperature curves are bi-modally shaped the reaction products consist of pure silicon carbide or silicon oxynitride. In contrast combustion having one modally shaped temperature resulted in silicon nitride remains in products. Thus, we concluded that two-peaks of temperature are attributed to silicon nitride decomposition.

The present data and earlier published thermodynamic calculation [15] and data about the kinetics of the Si+C[1] and $Si+N_2$ [16] reactions, were used to assess the combustion mechanisms which provides the nanometric silicon carbide and silicon oxynitride powders. It can be concluded that in the SHS condition nitriding of silicon is the starting reaction which controls self sustaining regime in the Si-C-N and Si_O-N system as shown in Figure 7 - step I. When the combustion temperature reaches maximum level, the thermal decomposition of silicon nitride occurs giving free melted and/or vapour of silicon which reacts with carbon or silica providing silicon carbide or silicon oxynitride nanopowders. This mechanism is represented by Figure 7 step II and III.

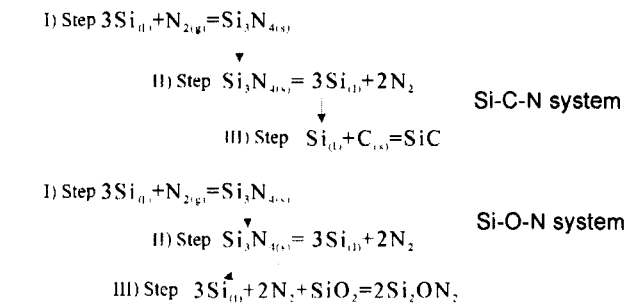

Figure 7. SHS reaction scheme in the Si-C-N and Si-O-N system

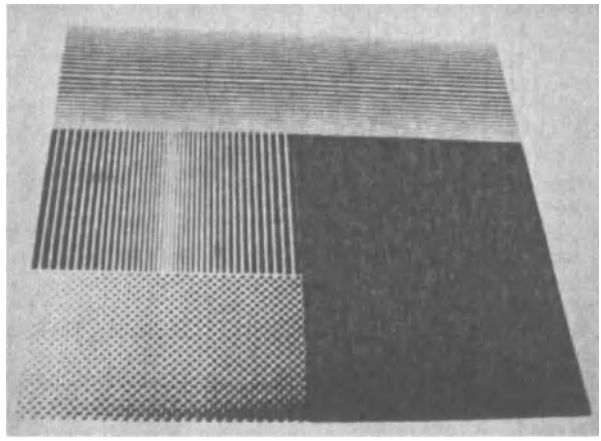

Figure 8. Screen Printed pattern of SHS derived SiC nanopowder

Obtained nanopowders are well sinterable and can be used for shaping different kind of microdevices. In Figure 8 example of screen printed pattern of silicon carbide nanopowder was shown. Cured depth of UV radiation inside SiC paste was estimated to 0,15mm. The highest silicon carbide load in ceramic paste was assessed to 45vol.%. First attempts of sintering these patterns resulted in rather low density of final polycrystals. However preparation of more dense samples are being investigated.

Acknowledgment:
We gratefully acknowledge financial support given by Polish State Committee for Scientific Research, Grant no. 3 T08D 030 29

LITERATURE

[1] R.Pampuch, J. Lis, L. Stobierski; „Mechanism of Heterogeneous Reactions under Conditions of Solid Combustion" Combustion and Plasma Synthesis of High-Temperature Materials, Z. A. Munir, J.B.Holt (eds.), pp.211-218, VCh Publ. New York-Weinheim (1990).
[2] R.Pampuch, J. Lis, L. Stobierski, "Solid Combustion Synthesis of Silicon-Containing Materials in the Presence of Liquid Silicon Alloys" Intern. J. of SHS, 1, pp.78-82, (1992).
[3] R.Pampuch, J. Lis, L. Stobierski, "Synthesis of Sinterable β-SiC Powders by a Solid Combustion Method" J.Am. Ceram.Soc. 72, pp.645-646, (1989).
[4] D.Kata, J.Lis, R.Pampuch, "Combustion Synthesis of Multiphase Powders in the Si-C-N System" Solid State Ionic 101-103, pp.65-70, (1997).
[5] D.Kata, J.Lis, R.Pampuch, L. Stobierski, E.Ermer "Preparation of Si_3N_4-SiC composite powders by combustion in the Si-C-N system" Arch. Combustionis 16, 1-2 pp.13-21, (1996).
[6] H.D. Batha and E.D. Whitney; "Kintetics and Mechanism of the Thermal Decomposition of Si_3N_4" J. Am. Ceram. Soc. 56, ,7 pp. 365-369, (1973).
[7] D. Greshovich, S. Prochazka, „Stability of Si_3N_4 and Liquid phase During Sintering" J.Amer. Ceram. Soc. 64, C-96, (1981).
[8] D. Kata, J. Lis, R. Pampuch and L. Stobierski, "Preparation of Fine Powders in the Si-C-N system using SHS" Int. J. of SHS, 7, 4, pp. 475-485, (1998);
[9] F. Lange, „Effect of Microstructure on Strength of SiC-Si_3N_4 Composite Sytem" J.Am. Ceram. Soc. 56, pp.445-50, (1973).
[10] K.H. Jack, „Review, Sialons and related nitrogen ceramics", J.Mat.Sci., 11, pp.1135-1158, (1976).
[11] C. Walter, and R.A. Lefever, „The Ammonolysis of Hexachlorodisiloxane" J.Am. Chem. Soc. 76, pp.5882-84, (1954).
[12] R. Larker, *"Reaction Sintering and Properties of Silicon Oxynitride Densified by Hot Isostatic Pressing"* J.Am.Ceram. Soc. 75 [1] p.p.62-66 (1992).
[13] M. Billy, P. Boch, C. Dumazeau, J.C. Glandus, P. Goursat, "Preparation and Properties of Silicon Oxynitride Based Ceramics" Ceramics International, 7, [1], , pp. 13-18, (1981).
[14] O. Yamada, K. Hirano, M. Koizumi, Y. Miyamoto „Combustion Synthesis of Silicon Carbide in Nitrogen Atmosphere" J. Am. Ceram. Soc. 72 pp. 1735-38, (1989).
[15] H. L. Lukas, J. Weiss, H. Krieg, E.Henig and G. Petzow, „Phase Equilibria in Si_3N_4 and SiC Ceramic" High Temperature-High Pressures 14, pp. 607-615, (1982).
[16] H. Jennings, „ Review on the Reaction Between Silicon and Nitrogen"J. Mat. Sci, 18, pp.951-967, (1983).

Advanced Processing and Manufacturing Technologies for Structural and Multifunctional Materials II
Edited by Tatsuki Ohji and Mrityunjay Singh

THE RELATION BETWEEN PEIERLS AND MOTT-HUBBARD TRANSITION IN VO_2 BY TUNNELING SPECTROSCOPY

Changman Kim[1], Tomoya Ohno[1], Takashi Tamura[1], Yasushi Oikawa[1],
Jae-Soo Shin[2] and Hajime Ozaki[1]
[1]Department of Electrical Engineering and Bioscience, Waseda University, Tokyo, Japan
[2]Department of Advanced Materials Engineering, Daejeon University, Daejeon, South Korea

ABSTRACT

Tunneling spectroscopy has been performed on W-doped VO_2 single crystal near the Metal-Insulator transition temperature. The tunneling energy gap was in good agreement with band calculations and optical measurements near the transition temperature. We have found by tunneling spectroscopy an additional density of states in the low-temperature phase. With increasing temperature, from room temperature to just below the transition temperature, an additional increase in the density of states was observed in the conduction band and it shifted downward to the bottom of conduction band. When the front of the additional density of states approaches the bottom of conduction band, edges of the tunneling energy gap becomes blurred, and the VO_2 turns into the high-temperature phase. A model for the mechanism of the Metal-Insulator transition in VO_2 is proposed.

INTRODUCTION

Vanadium oxides of magneli phase are expressed by V_nO_{2n-1} ($n=4\sqcup 8,\infty$) and several vanadium oxides of them undergo a Metal-Insulator Transition (MIT) at their transition temperatures. Among them, vanadium dioxide (VO_2) has been received most attention because of not only the dramatic reversible changes of electrical resistivity and infrared transmission, but also the transition temperature (T_t) which is close to room temperature, T_t=340K[1]. For these characteristics, VO_2 has the possibility of applications to new electronic devices such as "Thermochromic Smart Windows", "Mott-Transition Field-Effect Transistor" etc[2]. The phase transition mechanism of VO_2 has often been the topic under debate whether it is Peierls type or Mott-Hubbard type.

The early qualitative aspects of the electronic structure in the low temperature phase of VO_2 were explained by Goodenough[3]. The d states of the V atoms are split into lower lying t_{2g} state and higher lying e_g state because of O octahedral crystal field. The tetragonal crystal field further splits the multiple t_{2g} state into $d_{\parallel}$ and π^* states. In the low-temperature phase of VO_2, there are two structural components to the lattice distortion, namely a pairing and a twisting of V atoms out of the rutile axis c_r. The pairing and twisting of the V atoms result in two effects on the electronic structure. First, the π^* band is pushed higher in energy, due to the tilting of the pairs which increases the overlap of these states with O states. Second, the $d_{\parallel}$ band is split into a lower-energy bonding combination and a higher-energy anti-bonding combination. The band gap exists between the bottom of π^* band and the top of bonding $d_{\parallel}$ band. On the other hand, for such peierls-like band gap, Zylbersztejn and Mott[4], and

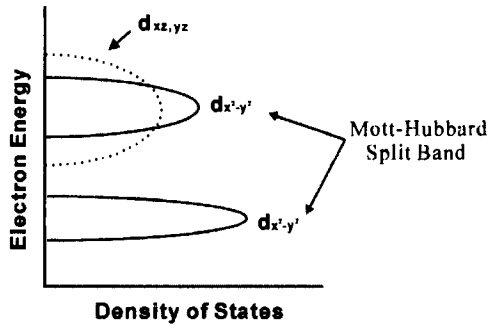

Figure 1. Schematic illustration of VO_2 in the low temperature monoclinic structure. The upper and lower d_{x2-y2} bands are Mott-Hubbard split bands. The band gap exists between the bottom of $d_{xz, yz}$ band and the top of the lower d_{x2-y2} band.

Rice et al.[5] suggested that a crystallographic distortion is not sufficient to open up an energy gap, and that the electron-correlation effects play an important role in opening the energy gap. Zylbersztejn and Mott also suggested that the role of the crystallographic distortion is only to provide an empty π^* bands. Shin et al.[6] have estimated the energy band gap as about 0.7eV from UPS + reflectance measurements.

The recent study of band calculation via local density approximation plus Hubbard U (LDA+U) has estimated the band gap as about 0.7 eV[7]. Figure 1 shows a schematic illustration for the density of states calculated within LDA+U method (The $d_{xz, yz}$ and d_{x2-y2} bands correspond with π^*, $d_{\parallel}$ bands in Goodenough's expression, respectively).

In our previous studies, we used tunneling spectroscopy in order to investigate the change in the electronic structure at the MIT in VO_2 doped with W[8-9].

In the present study, the tunneling spectroscopy results are explained for the onset of Metal-Insulator Transition in VO_2 in relation to the band diagram by the local density approximation plus Hubbard U calculation.

EXPERIMENTS

The crystal growth of VO_2 was performed using VO_2 and V_2O_5 powders and with WO_3 powder for W doping. The well mixed powders were sealed in quartz tube with 90 mm (long) ×10 mm (diameter) under 1×10^{-3} Pa. The sealed quartz tube was placed vertically in an electric furnace. The temperature of the furnace was kept at 1000°C for 5 hours and then decreased at a rate of 2.7 °C/hr to 800°C. At 800°C, the quartz tube was inverted in the furnace so as to separate the useless solution from the crystals which were grown in the melt at the bottom of the quartz tube. The crystals were annealed for 2 hours at 800 °C in the inverted tube, and then, the heater of the furnace was switched off. The typical size of the crystals obtained was $3 \times 1 \times 1$ mm^3. The crystalline c-axis of high-temperature

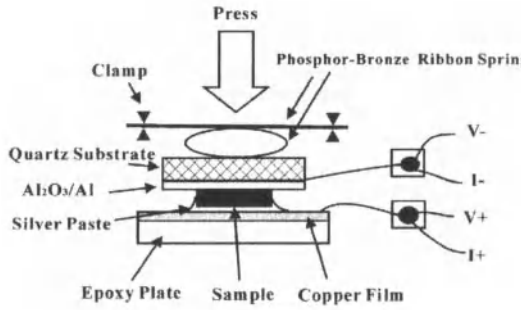

Figure 2. Schematic planar contact tunnel unit employed in this study.

rutile type lies along the length of the crystal.

The W concentration in the crystal was determined by a wavelength dispersive spectrometer electron probe microanalyser (WDS-EPMA), using JAX-8600 (JEOL). The resolution of the W content was ±0.1%.

In this study, the planar-contact structure, as shown in figure 2, was employed as the tunnel junction, instead of using an insulator evaporated on the sample surface, because in the latter case, the rigid contact and sometimes atomic diffusion between the insulator and the sample tends to suppress or modify the structural change associated with the MIT near the surface of the sample. The Al_2O_3/Al structure was fabricated as follows. Al was evaporated onto a clean quartz substrate. Then, it was heated in the evaporation chamber at about 100 °C for 1 hour in O_2 atmosphere of 1atm to oxidize the Al surface. For the back electrode, sample was bonded to copper plate using silver paste. The surface of Al_2O_3 was pressed to the sample surface using phosphor-bronze ribbon spring to form a stable contact tunnel junction. By this planar-contact method, the tunnel junction resistance can be adjusted by controlling the pressure from the top of the apparatus through a rotating shaft with fine pitch screw. To avoid the influence of the series resistance by the lead wire on the tunneling spectroscopy, a quasi four-probe method was employed in measuring the bias voltage V. The tunneling spectroscopy was performed using the ac modulation technique. The modulation bias and frequency were 1mV and 1kHz, respectively.

RESULTS AND DISCUSSION

The W composition x in $W_xV_{1-x}O_2$ was estimated by EPMA. The relationship between the starting composition and the substituted one is shown in figure 3. The substituted composition is linearly proportional to the starting composition. The segregation coefficient is 0.69.

The temperature dependences of the electrical resistivities are shown in figure 4 (a). The W composition dependence of T_t is linear with coefficient -27.8K/at.% as shown in figure 4(b), in which

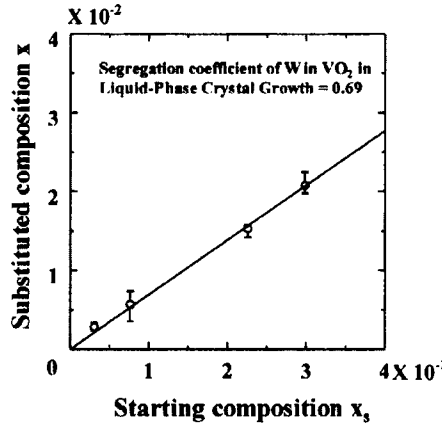

Figure 3. The relationship between starting composition x_s and substituted one x in $W_xV_{1-x}O_2$ by EPMA. The plots show the average of five measured points for each sample.

the T_t is plotted for the heating process. In table 1, the transition characteristics are listed for various W composition x. Although $W_xV_{1-x}O_2$ samples for various W composition x are in different ρ-T characteristics, we can find the similarity of ρ-T profiles between the nondoped VO_2 and $W_xV_{1-x}O_2$ except for x=0.0153. It suggests that the electronic structure was not changed basically by the W doping for x □0.01.

Figure 5(a) shows the tunneling dI/dV vs. V characteristics for $W_xV_{1-x}O_2$ with x=0.006 in the temperature region near the T_t. W was doped to reduce the electrical resistivity in the low temperature phase, for the sake of minimizing the potential drop across the bulk of VO_2, and thus, minimizing the spectroscopic error. Over the whole temperature range of measurements, the tunneling junction was unchanged. Figure 5(b) shows the curves shown in figure 5(a) shifted vertically for easy to see each curve. In figure 5, curves for 323.8 K and 327.3 K are in the high-temperature phase and those for 320.7 K and lower temperatures are in the low-temperature phase. The valence and conduction bands lie in the negative and positive bias region, respectively.

In the low-temperature phase, there appears an energy gap structure with diminished electronic density of states. The apparent residual density of states in the gap region might be due to some non-tunneling components. For temperatures above T_t, the gap structure disappears and the curves show a metallic state.

Figure 6(a) shows the temperature dependence of energy gap, estimated by the separation of biases between the maxima of $|d^2I/dV^2|$ in positive and negative biases in $|V| < 0.5V$. The tunneling energy gap at lower temperature, ~0.7eV, is in good agreement with those by optical studies[6].

In figure 5(b), a remarkable change in the density of states is seen in the conduction band

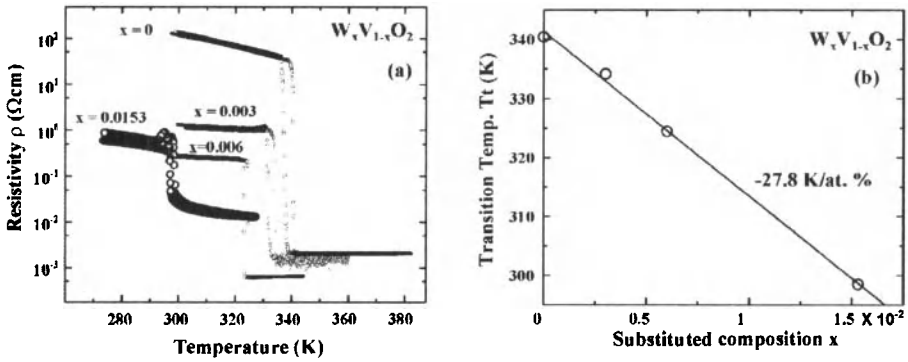

Figure 4. (a) Temperature dependences of electrical resistivities in $W_xV_{1-x}O_2$ for various W composition x. (b) MIT temperature T_t versus W composition x.

Table 1. Some characteristic parameters in the temperature dependence of electrical resistivity in tungsten doped VO_2. $T_{I\to M}$ and $T_{M\to I}$ are the midway temperatures of MIT during heating and cooling, respectively. $(\rho_I/\rho_M)_{Tt}$ is the ratio of electrical resistivities on both sides of the transition from insulator to metal. Hysteresis is the separation of temperatures between heating and cooling at the midway of transition.

Sample	W composition x	$T_{I\to M}$ (K)	$T_{M\to I}$ (K)	$(\rho_I/\rho_M)_{Tt}$	Hysteresis (K)
1	Pure	340.4	337.3	1.6×10^4	3.2
2	0.003	334.2	331.7	7.8×10^2	2.5
3	0.006	324.5	323.2	3.4×10^2	1.3
4	0.0153	298.5	297.1	1.7×10	1.4

region. At the measured lowest temperature, there appears an additional increase in the density of states above +0.8 V. With increasing the temperature, this increase in the density of states shifts toward lower bias voltage. When the front of the increase approaches the conduction band edge, the band gap structure becomes blurred, and then, the sample turns to the high-temperature phase. Figure 6(b) shows the temperature dependence of energy difference between the front of the additional increase in the density of states and the bottom of conduction band in the low-temperature phase.

Now, we would like to consider about this behavior in the change of density of states, which seems to lead to the MIT, in relation to our band diagrams in figure 7. At low temperature ($T \leq 315$K), the band gaps, shown in figure 5, might correspond to the energy separation between the $d_{xz, yz}$ and the

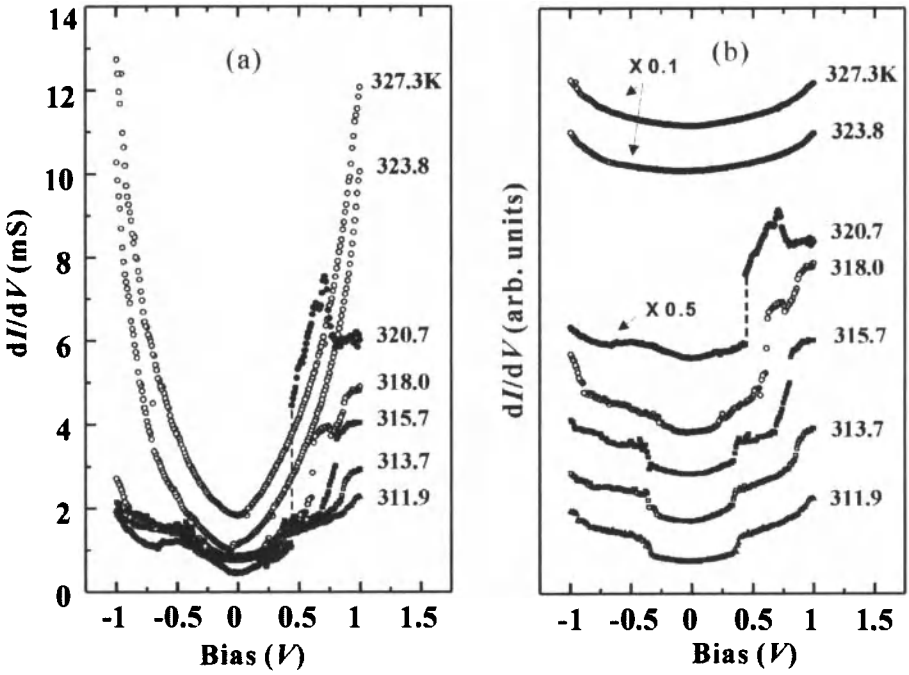

Figure 5. (a) Temperature dependence of tunneling spectroscopy for $W_xV_{1-x}O_2$ with x=0.006 in the temperature region around the T_i=323K. Measurements were carried out from high temperature to low temperature. (b) Temperature dependence of tunneling spectroscopy in (a), shifted vertically.

lower $d_{x^2-y^2}$ bands in figure 7(a), (b). Thermal carriers are excited across the band gap and the bottom of $d_{xy, yz}$ band is provided with electrons. As the upper band, where the electrons are provided, is not the Mott-Hubbard split band (upper $d_{x^2-y^2}$), the effect of the carriers in depressing the gap formation is less direct compared with the case the upper band is the Mott-Hubbard split band.

Now, we might conjecture that the increase of density of states above the bottom of upper band is the Mott-Hubbard split band (upper $d_{x^2-y^2}$). The position of the increase shifts to lower bias with increasing temperature as shown in figure 7(a), (b). When the front of the increase (bottom of upper $d_{x^2-y^2}$) approaches the bottom of the $d_{xy, yz}$ band, the electrons in the latter band transfer to the former (figure 7(c)), and thus, the carriers begin to act on depressing the Mott-Hubbard gap, leading to the metallic state (figure 7(d)). When the sample is doped with W, there more carriers exist in the $d_{xy,yz}$ band in the low temperature phase. Thus, in increasing the temperature, the M-I transition occurs earlier than the undoped case.

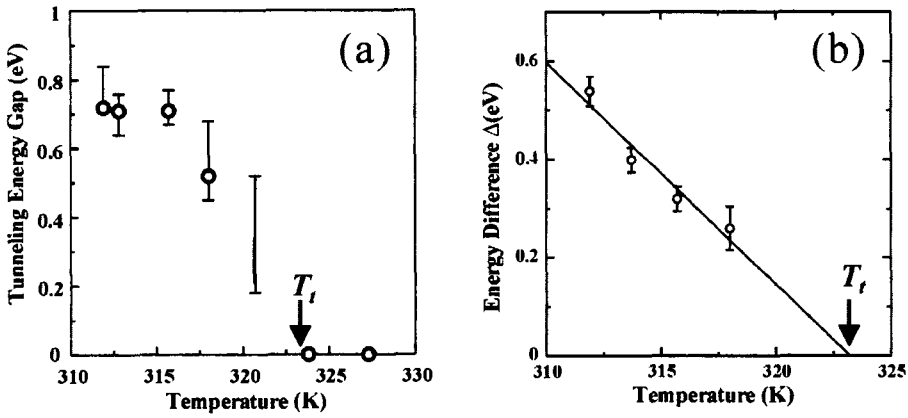

Figure 6. (a) Temperature dependence of tunneling energy gap, (b) Temperature dependence of energy difference between the bottom of the $d_{xz, yz}$ band and the bottom of the upper $d_{x^2-y^2}$ band.

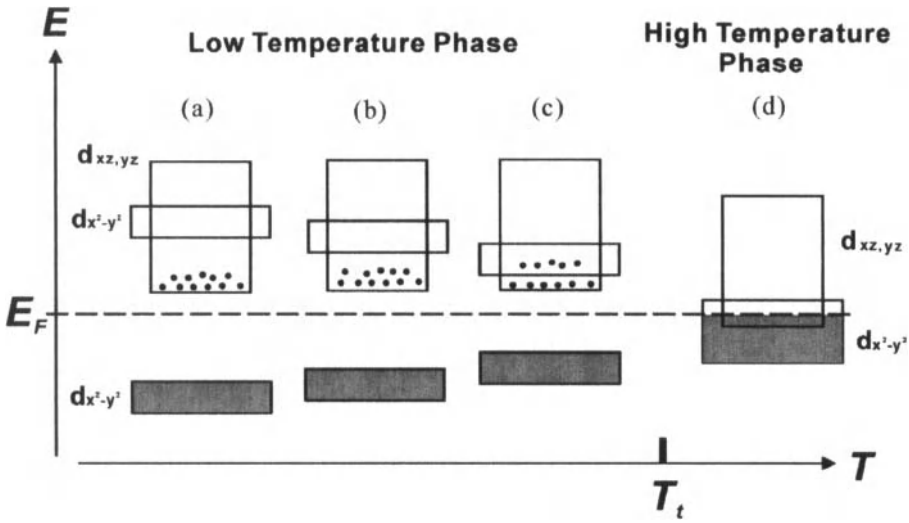

Figure 7. Schematic diagram of the change in energy bands in VO_2 with increasing temperature.

CONCLUSION

In the low-temperature phase, we observed the upper d_{x2-y2} band in the conduction band. This upper d_{x2-y2} band is one of the Mott-Hubbard split bands. We suggest that the cause of Mott-Hubbard Transition in VO_2 from insulator to metallic state is the electron transfer from the $d_{xz,yz}$ band to the Mott-Hubbard split upper d_{x2-y2} band. A crystallographic distortion by Peierls-transition-like effects brings the upper d_{x2-y2} band close to the bottom of conduction band $d_{xz,yz}$, which yield the electron transfer to the former one.

ACKNOWLEDGEMENT

This work is supported by a grant from the Marubun Research Promotion Foundation.

REFERENCES

[1]F. G. Morin, *Phys. Rev. Lett.*, **3**, 34 (1959).

[2]D. Yin, N. Xu, J. Zhang and X. Zheng, *J. Phys. D:Appl. Phys.*, **29**, 1051 (1996).

[3]J. B. Goodenough, *J. Solid State Chem.*, **3**, 490 (1971).

[4]A. Zylbersztejn and N. Mott, *Phys. Rev. B*, **11**, 4383 (1975).

[5]T. M. Rice, H. Launois and J. P. Pouget, *Phys. Rev. B*, **73**, 3042 (1994).

[6]S. Shin, S. Suga, M. Taniguchi, M. Fujisawa, H. Kanzaki, A. Fujimori, H. Daimon, Y. Ueda, K. Kosuge and S. Kachi, *Phys. Rev. B*, **41**, 4993 (1990).

[7]A. Liebsch, H. Ishida and G. Bihlmayer, *Phys. Rev. B*, **71**, 085109 (2005).

[8]C. Kim, Y. Oikawa, J. S. Shin and H. Ozaki, *J. Phys.:Condens. Matter*, **18**, 9863 (2006).

[9]C. Kim, J. S. Shin and H. Ozaki, *J. Phys.:Condens. Matter*, **19**, 096007 (2007).

Advanced Processing and Manufacturing Technologies for Structural and Multifunctional Materials II
Edited by Tatsuki Ohji and Mrityunjay Singh

Localization of Terahertz Waves in Photonic Fractal Arrays of Alumina Fabricated by Micro-Stereolithography

T. Hibino, S. Kirihara and Y. Miyamoto
Joining and Welding Research Institute, Osaka University
11-1 Mihogaoka, Ibaraki, Osaka 567-0047, Japan

ABSTRACT

A process for fabricating alumina micro photonic fractals with a Menger sponge structure using micro-stereolithography was investigated. After removing resin of the preformed sponges with alumina/ resin composite at 600°C in air for 2 h, they were sintered at 1500°C for 2 h. An array of dense alumina micro photonic fractals with stage 3 Menger sponge structure of a 810 m cube size showed a sharp localization of terahertz wave at 0.27 THz. Similarly, stage 1 and 2 samples localized terahertz waves at 0.21 and 0.24 THz, respectively. These localization frequencies were in good agreements with the TLM simulations.

INTRODUCTION

Many natural features are claimed to have the fractal geometries which are defined as the self-similar structure, like branchy trees, irregular coast lines and thunderheads.[1, 2] Their fragments have the similar patterns to the whole structures. Menger sponge structure is one of the typical three dimensional fractals. It has the fractal dimension about 2.73. Our research group has found in 2003 that a Menger sponge structure made of dielectric material can localize strongly the electromagnetic waves with specific frequencies. We named such fractal structures with the localization function as Photonic Fractal. The localization frequencies depend on the geometry and dielectric constant of the sponge structures.[3] Photonic fractal can be expected to use for efficient antennas and resonators.

Micro-stereolithography can offer a technique for the production of 3D micro structures in micrometer resolution. Recently, several research groups have developed various 3D microfabrication systems including micro-stereolithography.[4-7] We have developed a CAD/CAD micro-stereolithography system by using DMD (Digital Micromirror Device) under the collaboration with companies in 2005.[8, 9] In this research, we fabricated micrometer order photonic fractals with alumina ceramics by micro-stereolithography and successive sintering. Their terahertz wave properties were measured and compared with the simulation of the electromagnetic wave propagation.

EXPERIMENTAL PROCEDURE

Figure 1 shows model structures of Menger sponge with four different stages. Menger sponge structure is made by dividing a cube (a) into 27 smaller identical cubes and subtracting the body and face centered 7 cubes. (b) is called the stage 1 Menger sponge structure. When the same operation is

repeated to the remaining cubes, higher-stage Menger sponge structures are obtained like (c) stage 2, and (d) stage 3.

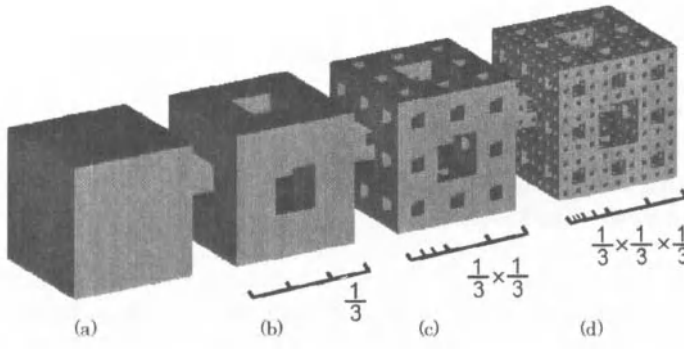

Fig. 1. Menger sponge structures; (a)stage 0, (b)stage 1, (c)stage 2, (d)stage 3

In this study, these models were designed by using 3D-CAD software (Toyota Caelum Ltd., thinkdesign ver. 5.0). The size of Menger sponge was designed to be 1080 μm in edge length. The designed CAD models were converted into STL files and sliced into a series of 2D layers with 10 μm thickness by software (Materialise Co. Ltd, Magics 9.9). These sliced data were transferred to micro-stereolithography equipment (D-MEC Co. Ltd, ACCULAS SI-C 1000) with a Digital Micromirror Device (DMD). The DMD has 1024 768 mirrors with a 14 μm square. Each mirror can be tilted independently and the 2D pattems are dynamically generated as bitmap images of the sliced data and exposed with a 2 μm space resolution.

We used the photo sensitive acrylic resin slurry including alumina particles of 170 nm in average diameter at 40 vol %. It is supplied from a syringe by a controlled air pressure and spread over the previously formed layer by moving a squeegee. According to the sliced data, the laser light is exposed on the coated layer by DMD. Then, the sliced pattem is solidified by photo polymerization. After one layer is fabricated, the elevator stage goes downward one layer thickness and a new layer is coated. This operation is repeated layer by layer, eventually forming 3D micro structures. The laser wavelength, the exposure value and the layer thickness were 405 nm, 500 mJ/mm^2 and 10 μm, respectively. The process of micro-stereolithography is schematically shown in Fig. 2.

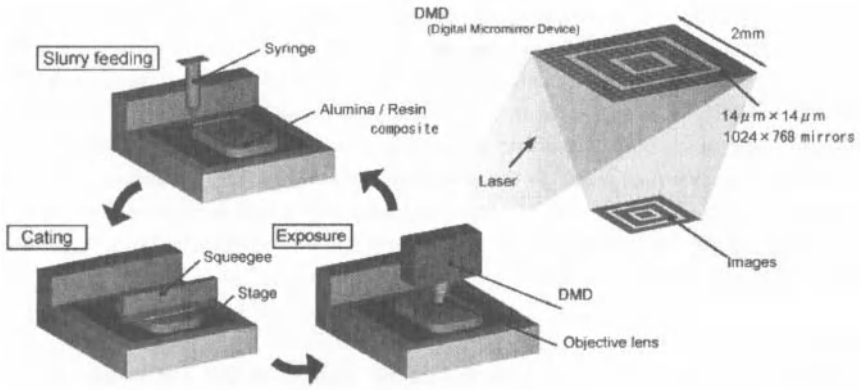

Fig. 2. A schematic illustration of micro-stereolithography using DMD

3D micro structures formed with alumina/resin composite were obtained by ultrasonic rinsing with ethanol. In order to convert the precursors of alumina/resin composite to dense alumina structures, they were dewaxed and sintered in air. Figure 3 is a temperature profile optimized in the dewaxing and sintering process. The composite precursors were dewaxed with at 600℃ with a heating rate of 1°C/min for 2 hs, and sintered at 1500°C with a heating rate of 8°C /min for 2 hs. The linear shrinkage and relative density of sintered products were measured. The microstructures were observed by using SEM. A bulk sample of sintered alumina was fabricated to measure the dielectric constant.

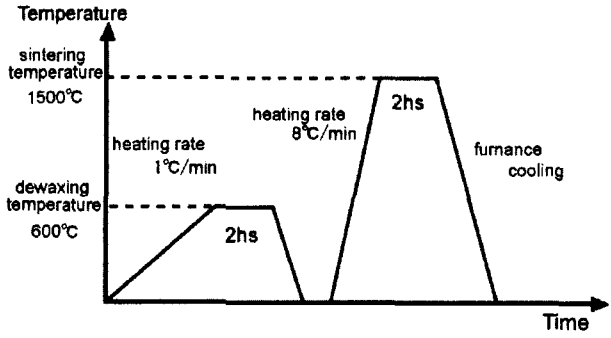

Fig. 3. A temperature profile for the dewaxing and sintering process

The terahertz wave properties of photonic fractals were measured in respect to transmittance and phase shift spectra as a function of frequency using by terahertz time-domain spectrometer (TDS, Advanced Infrared Spectroscopy Co. Ltd., J-Spec 2001 spc). In order to receive the enough signal intensity for transmission spectra, seven samples were arrayed periodically. In addition, we simulated in order to make an analysis of terahertz wave localization in photonic fractals by using TLM (Transmission Line Modeling) code.[10] In the simulation, four stage 2 fractal samples were arrayed in square lattice. The size and permittivity of the fractal structures were used as the same values as those of the sintered samples which were 810 μm in side length and 9.8, respectively. The space between samples was set to 810 μm.

RESULTS AND DISCUSSION

Figure 4 shows images of sintered samples and the fractured surface. The samples size after sintering were 810 μm in a side length. The linear shrinkage and relative density were 25 % and 97.5 %, respectively. The dielectric constant was 9.8, which is nearly constant in the measured frequency between 0.2 and 0.9 THz.

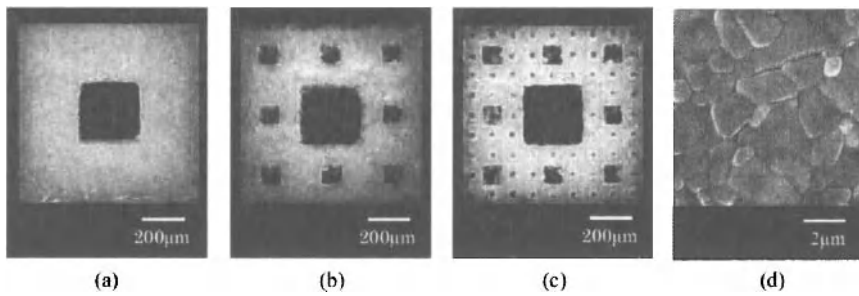

Fig. 4. Photos of sintered photonic fractal samples; (a) stage 1, (b) stage 2, (c) stage 3, (d) SEM image of microstructure

The localization of electromagnetic wave in fractal structures may occur due to the multiple resonances in the self-similar structure.[11] The wavelengths of localization modes in dielectric Menger sponge structures can be predicted using the empirical equation.[12]

$$\lambda = \frac{2^{f} a\sqrt{\varepsilon_{eff}}}{S^{2f-1}} \qquad (1)$$

where λ is the wavelength of the localized mode in air, f is the order number of the localized modes, a is the side length of the Menger sponge structure, and S is the division number of the side length. The effective dielectric constant ε_{eff} is the volume-averaged dielectric constant of the Menger sponge structure. According to this equation, the dense alumina Menger sponges with stage 1, stage 2 and

stage 3 of 810 μm in edge length can localize terahertz waves at 0.20 THz, 0.23 THz and 0.26 THz, respectively.

Figure 5 shows the transmittance and the phase shift spectra measured for alumina micro photonic fractals of stage 1, stage 2 and stage 3. The dotted lines show the localization frequencies calculated by equation (1). We could observe sharp dips and phase shift changes at frequencies close to these calculated frequencies. The measured frequencies were 0.21 THz (stage 1), 0.24 THz (stage 2) and 0.27THz (stage 3). The phase shift jump means the delay of wave propagation. Therefore, photonic fractals could be thought to localize the waves with resonance in their self-similar structures at the above frequencies. The other specific transmittance peaks, for instance 0.38 THz (stage 1), 0.49 THz (stage 2) and 0.56 THz (stage 3), could be observed. At these frequencies, the resonance may occur between each sample. This evidence will be analyzed in detail with TLM simulation hereinafter.

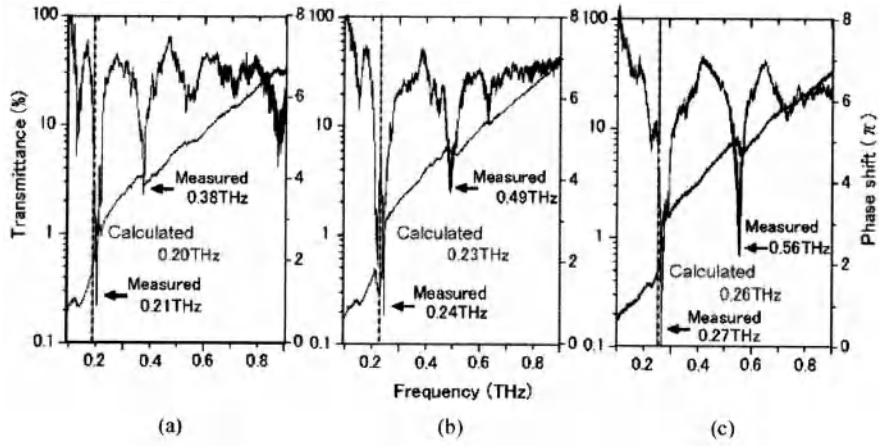

Fig. 5. Transmittance spectra as a function of frequencies for ;(a) stage1, (b) stage2, (c) stage3. The dotted line shows the localization frequencies calculated by the empirical equation.

The results in TLM simulation of transmittance spectra for the stage 1 and stage 2 samples are shown in Fig. 6. It is well seen that, similar to the measured spectra, the deep and sharp dip was observed at 0.21 THz and 0.24 THz and not so deep dips at 0.34 THz and 0.49 THz. Figure 7 presents the intensity distributions of electrical field oscillations at each dip of the stage2 transmittance spectrum; 0.24 THz and 0.49 THz. It shows the x-z plane and the propagating direction of electromagnetic waves is from left to right. When the plane wave at 0.24 THz comes, it is localized mainly in the front part of the samples, and then flew out toward the right and side directions as seen in Fig. 7 (a). Each sample localizes the wave separately. On the other hand, at 0.49 THz, electromagnetic

waves were not localized in samples but in the gap between samples. It means that the dip at this frequency in Fig. 6 (b). was produced not by the localization of photonic fractals, but by the effect of arraying.

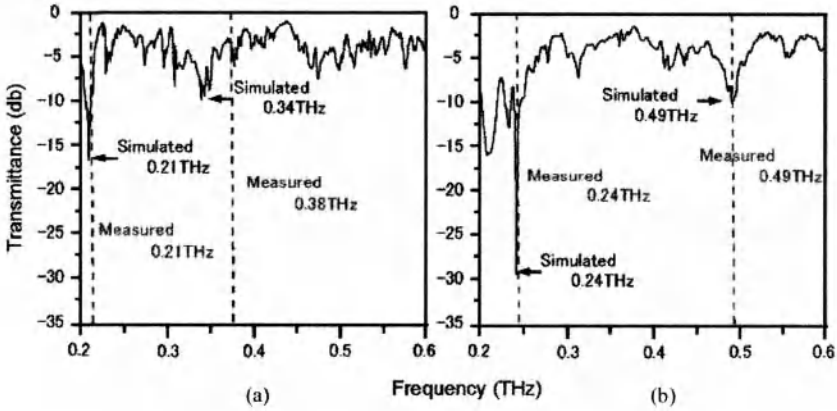

Fig. 6. TLM simulation of transmittance spectra; (a) stage 1, (b) stage 2

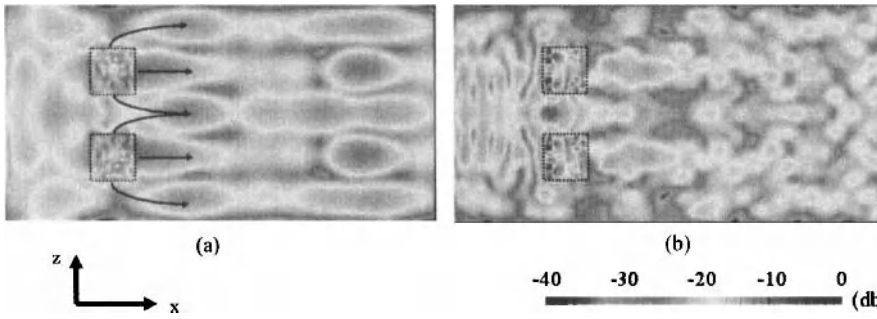

Fig. 7. Intensity distributions of electrical field oscillations of Ez component at each dip. (a) 0.24 THz, (b) 0.49 THz

CONCLUSION

We have succeeded in fabrication of micrometer order photonic fractals of dense alumina by using micro-stereolithography and sintering process. They have Menger sponge structures with 810 μm in edge length. The fractal stage is stage 1, stage 2 and stage 3. We confirmed sharp localization dips for the arrayed fractals with different stages at 0.21 THz, 0.24 THz and 0.27 THz, respectively. These localization frequencies were close to the calculated ones using the empirical equation for resonance mode of dielectric Menger sponges. Moreover, the TLM simulations of the transmission spectra for stage 1 and stage 2 arrays showed good agreements with the measured spectra. These evidences suggest that the dielectric Menger sponges can localize terahertz waves by resonances in the fractal structures.

REFERENCE

1. B. B. Mandelbrot, The Fractal Geometry of Nature. Freeman, San Francisco, 1982.
2. J. Feder, Fractals. Plenum, New York, 1988.
3. S. Kirihara, M. Takeda, K. Sakoda, K. Honda, Y. Miyamoto, Strong localization of microwave in photonic fractals with Menger-sponge structure, J. Euro. Ceram. Soc., 26, 1861-1864, 2006.
4. J. W. Lee, I. H. Lee, D. W. Cho, Development of micro-stereolithography technology using metal powder, Microelectronic Engineering, 83, 1253-1256, 2006.
5. X. Zhang, X. N. Jiang, C. Sun, Micro-stereolithography of polymeric and ceramic microstructures, Sensors and Actuators, 77, 149-156, 1999.
6. C. Sun, X. Zhang, The influences of the material properties ceramic micro-stereolithography, Sensors and Actuators A, 101, 364-370, 2002.
7. S. Maruo, K. Ikuta, Submicron stereolithography for the production of freely movable mechanisms by using single-photon polymerization, Sensors and Actuators A, 100, 70-76, 2002.
8. http://www.d-mec.co.jp
9. W. Cheng, S. Kirihara, Y. Miyamoto, Fabrication of three-dimensional micro photonic crystals of resin-incorporating TiO_2 particles and their terahertz wave properties, J. Am. Ceram. Soc., 90, 92-96, 2007.
10. J. A. Morente, G. J. Molina-Cuberos, J. A. Porti, K. Schwingenschuh, B. P. Besser, A study of the propagation of electromagnetic waves in Titan's atmosphere with the TLM numerical method, Icarus, 162, 374-384, 2003
11. E. Semouchkina, Y. Miyamoto, S. Kirihara, G. Semouchkin, M. Lanagan, Analysis of electromagnetic response of 3-D dielectric fractals of Menger sponge type, IEEE Transactions on Microwave Theory and Techniques,55, 1305-1313, 2007.
12. M. Yoshinari, S. Kirihara, M. Takeda, M. W. Localization of electromagnetic wave in 3D periodic and fractal structures, Chemistry letter, 35, 342-347, 2006.

Advanced Processing and Manufacturing Technologies for Structural and Multifunctional Materials II
Edited by Tatsuki Ohji and Mrityunjay Singh

ANISOTROPIC VARISTOR VIA MAGNETIC TEXTURING

Yoshiaki Kinemuchi, Kumi Okanoue, Hisashi Kaga, Juan P. Wiff, Satoshi Tanaka*, Keizo Uematsu*, and Koji Watari
National Institute of Advanced Industrial Science and Technology, (AIST)
Nagoya, Aichi, Japan
*) Nagaoka University of Technology
Nagaoka, Niigata, Japan

ABSTRACT

We report anisotropy of varistor property in Pr-ZnO textured by magnetic alignment. High magnetic field, flux density of 10 T, generated by super conducting magnet was applied to the particles dispersed in water, in order to align those crystallographic orientations. Subsequent sintering effectively enhanced the degree of orientation, leading to *c*-axis texturing. Because of the larger ionic radius of Pr than that of Zn, Pr segregated at grain boundary, which gave rise to non-ohmic current-voltage curves, and the amount of Pr primary affected the resistivity at pre-breakdown region. In accordance with orientation direction, pronounced difference in the resistivity was observed in textured Pr-ZnO, while isotropic property was found in randomly oriented one. This anisotropic varistor property demonstrates that the segregation amount varied with orientation direction, indicating potential usage of magnetic texturing for the control of grain boundary segregation.

INTRODUCTION

A varistor is an electrical element to shunt a current created by instant high voltage, which is utilized to protect electric devices from electric spikes. The non-ohmic current-voltage characteristics of ZnO ceramics are widely applied to this purpose, and it is recognized that the electrical property is strongly dependent upon grain boundary properties [1, 2]. Additives, such cations as Bi or Pr having larger ionic radius than that of Zn, are known to enhance the varistor property due to their segregation at the grain boundary. The non-ohmic property of ZnO is usually explained in terms of double Schottky barriers that are assumed to originate from charged grain boundary phase and the compensating space charge in the vicinity [3, 4]. Hence, the control of segregation is crucial for the design of varistor property.

Because the segregation is driven by the difference in interfacial energy, the structure of grain boundary is the key to understand the varistor property. Comprehensive study on this issue was done by Sato *et al.* who simulate the grain boundary by using bicrystal of ZnO [5, 6]. They clarified that the amount of segregation strongly depended on the mis-orientation between crystals: coherent and incoherent boundary structures resulted in the low and high amount of segregation, respectively.

Magnetic alignment enables to align grains based on the difference in magnetic susceptibility of

each crystal axis. Thus the grain boundary as a result of the magnetic alignment is supposed to have different interfacial energy corresponding to crystal plane and configuration of adjacent planes, which may lead anisotropic segregation in ceramics. It is an objective to elucidate the influence of texturing on grain boundary segregation in Pr-ZnO ceramics in the present report.

EXPERIMENTAL PROCEDURE

The magnetically aligned Pr_6O_{11} added ZnO (Pr-ZnO) ceramics was prepared by the rotating high magnetic field and gelcasting techniques. A water-based gelcasting system described in Ref. 9 was used in this study. Acrylamide (Wako Pure Chem. Ind., Japan) as a monomer and methylenebisacrylamide (Wako Pure Chem. Ind., Japan) as a cross-linker were dissolved in distilled water to form a premix. ZnO (99.8%, Hakusui Tech, Japan) powders added with Pr_6O_{11} (99.9%, Japan Pure Chem. Ind., Japan) were prepared as starting materials. The powders with 0.5 mass% dispersant (poly ammonium acrylate A-6114, Toagosei, Japan) were added in the premix for 2 h to prepare the slurry. The slurry was then degassed in a vacuum desiccator. Before casting into a Teflon mold at room temperature, the initiator (ammonium persulfate solution, Wako Pure Chem. Ind., Japan) and catalyst (tetramethylethylenediamine, Wako Pure Chem. Ind., Japan) were added into the slurry, and the mold was placed in a 10T magnetic field (TM-10VH10, Toshiba, Japan). Gelation in the high magnetic field initiated within 10 min by adjusting the amount of catalyst after casting. The mold was rotated at 30 rpm in the horizontal magnetic field during the gelation. The sample was then dried in a controlled-humidity chamber at room temperature to avoid nonuniform shrinkage due to rapid drying. The relative humidity was kept at 95%. The dry green bodies were then placed in a furnace for removing organic substances. The green bodies were heated at 575°C for 1 h in air with a heating rate of 0.25°C/min. The dewaxed green bodies were sintered at 1100°C for 1 h with a heating rate of 5°C/min and then it was cooled down to room temperature. Randomly oriented ceramics was also prepared in the same procedure as mentioned above without applying the magnetic field as a reference.

Crystalline phases were determined by X-ray diffraction (XRD, Model RINT-TTR, Rigaku, Japan) analysis with CuKα radiation. The scan was carried out in the range of 20 - 80° in 2θ at a scan rate of 4°/min. For each pattern, the peaks were indexed using the card file patterns (JCPDF) of possible reaction products in comparison with the obtained patterns. The degree of orientation was evaluated by means of the Lotgering factor, using the equations described elsewhere [7]. Pole figures were measured in reflection geometry on an X-ray diffractometer (RINT2550, Rigaku, Japan) equipped with a pole figure goniometer. Measurements were performed on polished surfaces of both magnetically processed and randomly oriented specimens for (002) peak. The measurements were carried out in the range of azimuthal angle of $0°<\beta<360°$(2.5steps) and polar angle of $0°<\alpha<75°$ (2.5°steps). The normal direction of the specimen was set to be parallel to the rotational axis of magnetic texturing during XRD analysis.

For the magnetically aligned specimens, the current-voltage (I-V) characteristics were

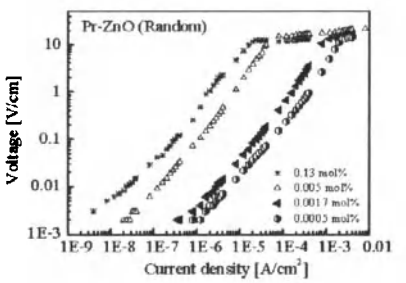

Fig. 1 The dependence of Pr amount on *I-V* characteristics of randomly oriented specimens.

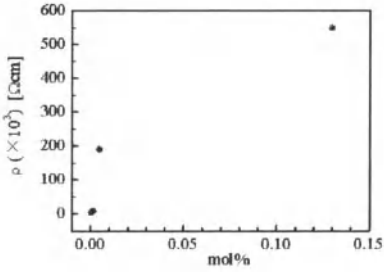

Fig. 2 The dependence of Pr amount on the resistivity at pre-breakdown region.

examined on rectangular bars parallel (denoted as //*B*) and perpendicular (denoted as ⊥*B*) to the horizontal magnetic field with Ag electrodes at room temperature.

RESULTS AND DISCUSSION

Figure 1 indicates the dependence of Pr amount on *I-V* characteristics of randomly oriented specimens. Here, the segregation of Pr is expected to be isotropic due to the random distribution of crystallographic orientation. With increase in voltage, current monotonously increased up to breakdown voltage. At this region, *I-V* followed linear relation. When the voltage reached the breakdown value, current rapidly increased, showing non-ohmic characteristic. The influence of the amount of Pr was found in the resistivity at pre-breakdown region: larger amount of Pr resulted in higher resistivity at the region. The dependence of the amount on the resistivity is shown in Fig. 2. Because Pr hardly dissolves

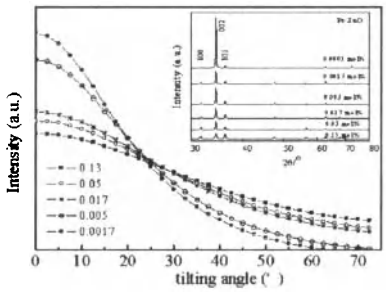

Fig. 3 XRD results of magnetically aligned specimens. Main figure and inset show (002) pole figure and 2θ-θ pattern, respectively.

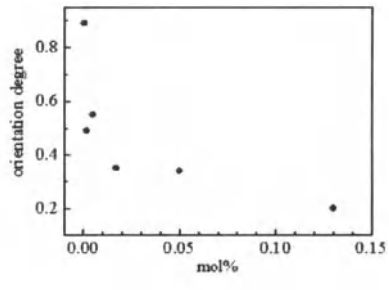

Fig. 4 The degree of orientation as a function of Pr amount.

into ZnO due to its larger ionic radius than that of Zn, larger amount of Pr results in larger amount of segregation at grain boundary, which leads to increase in the resistivity. This relation will be used to evaluate the segregation amount in the magnetically aligned specimens.

The (002) pole figures for magnetically aligned specimens with various Pr amount are shown in Fig. 3. Inset of this figure shows 2θ-θ scan of these specimens. It was found that *c*-axis orientation emerged by magnetic alignment. It was also noticed that the orientation of *c*-axis corresponded to the direction perpendicular to the magnetic field ($\perp B$). Thus the direction parallel to the magnetic field ($//B$) corresponded to *ab*-plane. Although procedure of magnetic alignment was identical, the gradual degradation in orientation degree was observed with increase in the amount of Pr, which can be confirmed either by the broadening of peak in (002) pole figures or by the reducing of (00*l*) intensities in 2θ-θ diffraction patterns. This tendency is summarized in Fig. 4, showing a sharp increase in orientation degree below 0.01 at%.

Typical *I-V* characteristics of magnetically aligned specimens are shown in Fig. 5. The characteristics can be classified into three categories in terms of additive amount. At high Pr amount (See Fig. 5a), there was no large difference between $//B$ and $\perp B$, and the resistivity at pre-breakdown showed a value corresponding to that of randomly oriented specimen. At low Pr amount (See Fig. 5c), the characteristic also showed similar behavior between $//B$ and $\perp B$, although the resistivity at

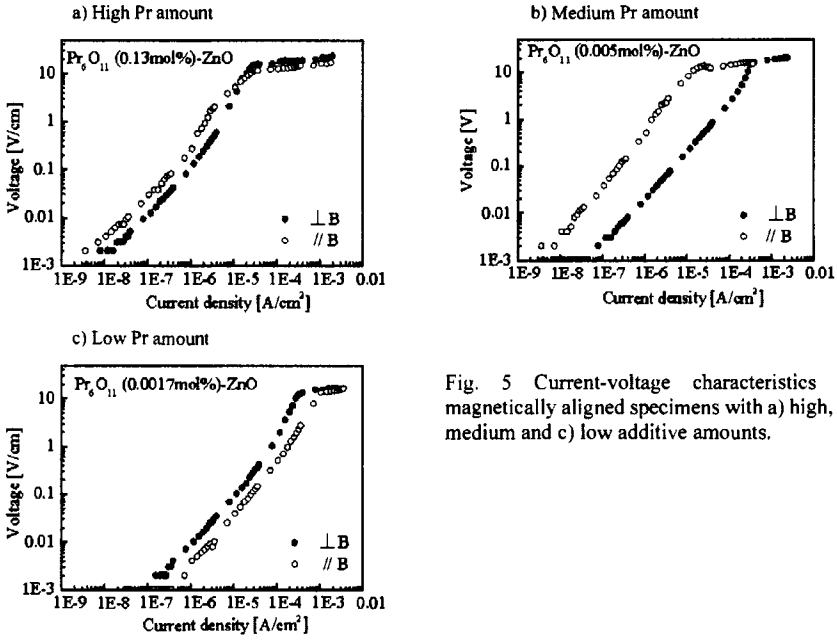

Fig. 5 Current-voltage characteristics of magnetically aligned specimens with a) high, b) medium and c) low additive amounts.

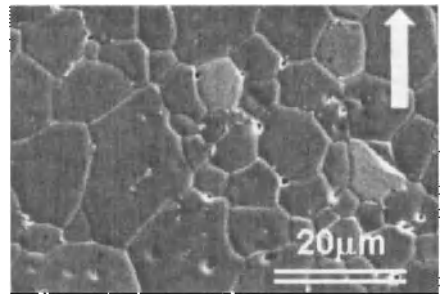

Fig. 6 Grain morphology of magnetically aligned ZnO with 0.005 at% Pr. Arrow indicates ⊥B direction.

pre-breakdown region was quite lower than that of highly added specimens. In the middle of them (See Fig. 5b), large difference in the resistivity at pre-breakdown region was observed between *//B* and *⊥B*. The resistivity of *⊥B*, namely resistivity along *c*-axis of ZnO ceramics, was higher than that of *//B*, i.e. *ab*-plane.

Although the influence of Pr amount on *I-V* characteristics is not straight forward, the emergence of anisotropic behavior in the middle range of addition is a unique result of magnetic alignment. This anisotropic property may originate in the difference in either segregation amount or number of grain boundary. Figure 6 shows the grain morphology of specimen with 0.005 at%. The arrow in this figure corresponds to *⊥B*. The shape of grain is almost isotropic, indicating that the number of grain boundary is not responsible for the anisotropic *I-V* characteristic.

Isotropic *I-V* characteristic at high Pr amount can be understood from its low degree of orientation: the characteristic should be close to that of randomly oriented specimen. However, uncertainty remains at low Pr amount, which is hardly explained by the orientation degree. Detailed analysis of segregation state of Pr is required to elucidate this issue, which will be performed in the future.

SUMMARY

Non-ohmic characteristics of Pr-ZnO have been focused on in order to clarify the impact of magnetic alignment on segregation. By applying rotational magnetic field to the slurry, *c*-axis oriented specimens were prepared. It was found that the addition of Pr deteriorated the orientation degree, and the *I-V* characteristic became identical with that of randomly oriented specimen at high amount of Pr. When the adequate amount of Pr was added, remarkable anisotropic *I-V* characteristic emerged, which is responsible for the difference in segregation amount between *//B* and *⊥B* directions. These results indicate potential application of magnetic alignment for the segregation control in ceramics.

REFERENCES

[1] M. Matsuoka, Jpn. J. Appl. Phys., 10 (1971) 736.

[2] T. K. Gupta, J. Am. Ceram. Soc., 73 (1990) 1817.

[3] F. Greuter and B. Blatter, Semicond.Sci. Technol., 5 (1990) 111.

[4] D. R. Clarke, J. Am. Ceram. Soc., 82 (1999) 485.

[5] Y. Sato, F. Oba, M. Yodogawa, T. Yamamoto, and Y. Ikuhara, J. Appl. Phys., 95 (2004) 1258.

[6] Y. Sato, M. Yodogawa, T. Yamamoto, N. Shibata, and Y. Ikuhara, Appl. Phys. Lett., 86 (2005) 152112.

[7] F. K. Lotgering, J. Inorg. Nucl. Chem., 9 (1959) 113.

Advanced Processing and Manufacturing Technologies for Structural and Multifunctional Materials II
Edited by Tatsuki Ohji and Mrityunjay Singh

FARADAYIC PROCESS FOR ELECTROPHORETIC DEPOSITION OF THERMAL BARRIER COATINGS

Joseph Kell, Heather McCrabb
Faraday Technology, Inc.
Clayton, Ohio, USA

Binod Kumar
University of Dayton Research Institute
Dayton, Ohio, USA

ABSTRACT

Faraday is pursuing the development of an electrically mediated process for electrophoretic deposition (EPD) of thermal barrier coatings (TBCs), termed the *Faradayic* EPD Process. This process will be capable of depositing coating materials that enable higher temperatures in natural gas and synthesis gas environments while maintaining the necessary durability and reliability required to sustain the engine life expectancy. This process will alleviate issues associated with other deposition methods, such as DC EPD, which can have poor throwing power due to non-uniform current distributions, poor utilization of powder and increased cost. This electrically mediated process utilizes an asymmetric electric field to control the uniformity, deposition rate and material properties of a ceramic coating.

Prior work used the *Faradayic* EPD process to apply thermal barrier coatings onto Inconel 718 substrates. Experimental studies showed that the *Faradayic* EPD process could a) uniformly deposit YSZ thermal barrier materials and b) increase deposition rates of thermal barrier materials compared with more conventional processes. In current work, Faraday is optimizing and validating the *Faradayic* EPD process for thermal barrier coatings to prevent coating failure during standard and accelerated turbine engine operation. This includes the development and validation of deposition related parameters to ensure a suitable coating, post deposition thermal treatments to preserve the necessary microstructure to maintain coating durability and reliability during operation, and the selection of appropriate tests of merit to qualify the coating durability and reliability.

INTRODUCTION

The design and manufacturing of gas turbine engines is a challenging prospect from both an engineering and material science standpoint due to extreme operating environments. The engine's high rotational speeds and operating temperatures lead to component failure caused by corrosion due to hot gases contaminated with chloride and sulfate, oxidation in an enriched oxygen environment, mechanical wear, and erosion[1]. In addition, the components are exposed to extreme temperatures, constant thermal cycling, and thermal shock. Turbine blades and other hot section components are especially susceptible to damage, requiring routine maintenance to repair, refurbish, or replace worn and failed parts. One of the most effective ways to protect the components of a gas turbine is with the addition of thermal barrier coatings (TBCs) and bond coats. The bond coat is critical, as it protects the substrate from oxidation and helps alleviate thermal expansion mismatches between the substrate and the TBC[2,3]. The TBC extends the life of the turbine components by providing thermal, oxidation, and mechanical protection, reducing thermal gradients, and lowering the temperature of the metal substrate surface. In order to do so, the TBC must meet several material requirements, including possessing a high melting point, low thermal conductivity, have a thermal expansion coefficients similar to metals, have a low sintering rate of the microstructure, and be chemically inert[4].

The primary material for TBC applications is yttrium-stabilized zirconia (YSZ) and is the most widely studied and used TBC material. Largely chemically inert, YSZ prevents corrosion, performs

well during thermal cycling and thermal shock, possesses a relatively high thermal expansion coefficient and melting point, and has a low thermal conductivity[5]. Traditionally, air plasma spray (APS)[6,7] and electron beam assisted physical vapor deposition (EB-PVD)[6,8,9] have been used to deposit YSZ-based TBCs. However, both of these processes have their shortcomings. While APS films have low thermal conductance and are produced quickly and economically, they tend to have thickness variations and spallation problems[10,11]. Alternatively, EB-PVD films exhibit good wear and spallation resistance, but the thermal conductance is higher relative to the APS counterparts and EB-PVD is a slow and expensive to process[7,8,11]. This leaves much to be desired, as neither process seems to address the problems of the other without negating some of the key benefits. One solution to this is to deposit the coatings using electrophoretic deposition (EPD).

EPD uses an applied voltage across two electrodes within an electrophoresis cell that contains a stable suspension of the particles to be deposited. The particles, which are charged using a chemical agent, are then transported by the electric field, with any non-uniformity in the electric field distribution resulting in a non-uniformity of the deposited coating thickness.[12] In addition, the EPD process is largely a non-line of sight process, as the electric field will readily wrap around the electrodes. EPD also has several other attractive properties such as, fast deposition rates, ability to uniformly coat complex shapes, reduction of waste due when compared to spraying or vapor processes, low levels of contamination, and simple deposition equipment. These thickness non-uniformities, as well as other potentially electrochemically related problems, can be solved using an electrically mediated form of EPD termed the *Faradayic* EPD process[13]. Faraday has shown that electrically mediated waveforms can substantially impact the structural characteristics of electrodeposited coatings[14] and in anodically surface finished surfaces[15]. As this improvement is primarily due to better control of the electric field, similar benefits are expected for the *Faradayic* EPD process.

EXPERIMENTAL

Two suspensions of YSZ particles (8 mol% Y_2O_3, submicron powder, Sigma Aldrich) in ethanol (EtOH) were investigated. One suspension contained polyvinyl alcohol (% hydrolyzed) (PVA) as the binder and poly(diallyldimethylammonium chloride) (PDDA) as the charging agent. The other suspension contained PVA and poly(vinyl butyral-co-vinyl alcohol-co-vinyl acetate) (PVB) as binders and PDDA as the charging agent. The powder, EtOH, and charging agent were added to the bath, mixed, and ultrasonicated. The binders were added after the charging agents to prevent competitive adsorption between the binding and charging agents. After the binders were added, the solution was again mixed and ultrasonicated, before allowing the suspension to age overnight.

EPD was performed in a glass electrophoresis cell. The electrodes consisted of an iridium oxide coated titanium anode and the nickel superalloy substrate as the cathode. The substrate holder was made in house. EPD was performed with the cathode and anode in the vertical plane and the particles were deposited upon the face of the substrate. The solutions were freshly agitated to ensure uniform particle deposition. The substrates consisted of Haynes 230 alloy (for preliminary studies) and a bond coated IN939 for more advanced studies to approximate end use conditions. Deposition conditions are outlined in Table I. Deposition times varied from 30 s to 30 min. Voltages for the PVA only baths was kept to 50 V as 100 V depositions tended to slide off the substrate and showed large amounts of hydrolysis. Samples were dried in an oven for a few hours at ~95°C following the EPD experiments, cooled in a desiccator, and then immediately weighed.

Green samples were analyzed for roughness and thickness with a Mitutoyo SJ-400 surface profilometer before binder burnout tests and sintering experiments. Roughness measurements were taken both parallel and perpendicular to erosion channels that were created on the substrate when removed from the solution. Select samples were submitted for differential scanning calorimetry (DSC) and thermogravimetric analysis (TGA). This data was used to establish temperatures of interest for

binder burnout tests to examine how ramp rates affected the removal of the binders and the structural integrity of the film. Ramp rates tested were 0.1 °C/min, 0.5 °C/min, and 1.0 °C/min.

Table I: Deposition conditions for Haynes 230 and bond coated IN939

Substrate	Haynes 230		Bond coated IN939
Alloy	Haynes 230		IN939
Electrode Distance	1 cm		1 cm
Bond Coat	None		Yes
Dimensions	~ 5 cm x 5 cm x 0.16 cm		~2.54 cm dia. x 0.35 cm
Binder	PVA/PVB	PVA	PVA
Electric Field	25 – 200 V cm^{-1}	50 V cm^{-1}	50 V cm^{-1}
Current Density	1.5 – 15.5 mA cm^{-2}	2.0 mA cm^{-2}	2.7 mA cm^{-2}
Max. Deposit. Time @ 50V	180 s	45 s	1800+ s
R_a (Uncoated)	0.74 ± 0.09 μm	0.74 ± 0.09 μm	10.85 ± 0.91 μm
R_q (Uncoated)	0.98 ± 0.15 μm	0.98 ± 0.15 μm	13.37 ± 1.05 μm
$R_{a\perp}$ (Coated)	N/A	1.21 ± 0.30 μm @ 45 s	12.36 ± 3.13 μm @ 1 min
$R_{q\perp}$ (Coated)	N/A	1.54 ± 0.39 μm @ 45 s	15.69 ± 3.42 μm @ 1 min
Deposition Rate @ 50 V	N/A	19.1 ± 7.8 mg cm^{-2} min^{-1}	28.7 ± 3.7 mg cm^{-2} min^{-1}
Survive Binder Burnout?	No	Yes	Yes
Survive Thermal Sintering?	-	No	Yes

Samples were selected for furnace and laser sintering experiments. Furnace sintering studies were performed to determine the affect of heating and cooling rates, maximum temperature, atmosphere, and the presence of a bond coat upon the densification and mechanical integrity of the film. Furnace sintering was performed in a Barnstead-Thermolyne F48000 series muffle furnace for the samples for air and nitrogen atmosphere experiments, and a tube furnace was used for the sample thermally treated in an argon atmosphere. The furnace sintering experimental parameters are shown in Table II. Laser sintering experiments were performed using one coated Haynes 230 sample and one bond coated IN939 sample. Further tests were performed on the Haynes 230 sample to check for further compatibility of IR laser sintering, including EDS to check for carbon content and the generation of an IR absorbance spectrum to determine which wavelengths of IR were absorbed by the YSZ coating. The laser used for the IR laser sintering study was a CO_2 laser with a wavelength of 10.6 μm. Multiple power levels and scan rates were investigated. The IR absorbance spectrum was scanned over a range of ~2.5 μm to 25 μm.

Table II: Sintering experiments performed using Haynes 230 and bond coated IN939

Test	A	B	C	D	E	F
Sample	Haynes	Haynes	Haynes	Haynes	Haynes	Bond Coated IN939
Initial Temp (°C)	25	25	25	25	25	25
Maximum Temp (°C)	1000	1000	700	600	700	1000
Ramp Rate (°C/min)	10	1	1	1	1	1
Cooling Rate (°C/min)	Ambient	Ambient	1	Ambient	Ambient	Ambient
Atmosphere	Air	Nitrogen	Air	Air	Argon	Air
Spallation	Yes	Yes	Yes	No	Yes	No
Corrosion	Yes	Yes (less)	Yes (less)	Minimal	Minimal	Minimal

RESULTS AND DISCUSSION

PVA/PVB Binder Combination

Figure 1 shows the difference between coatings prepared from a mixture of PVA and PVB (Fig. 1, left) for the binder and those that only used the PVA binder (Fig. 1, right). Small pinholes were evident in all samples deposited from the PVA/PVB solution, using voltages ranging from 25V to 200V. While the films deposited from the PVA/PVB seemed to have stronger adhesion to the surface of the Haynes 230, the pinholes from enhanced hydrolysis are likely to be detrimental to the mechanical integrity of the films during turbine operation. The increased hydrolysis is likely due to the enhanced conductivity of the PVA/PVB suspension, which is approximately 1.6 times more conductive than the PVA only suspension. As expected, the current density of the PVA/PVB suspension was ~1.6 time larger. The maximum deposition time for particles deposited from the PVA/PVB suspension was considerably higher than the deposition time for particles deposited from the PVA only suspension (240 s vs. 45 s), but a longer deposition time and a higher voltage were necessary to deposit a coating of the same thickness (29 μm in 60 s at 100 V for PVA/PVB vs. 29 μm in 45 s at 50 V for PVA only).

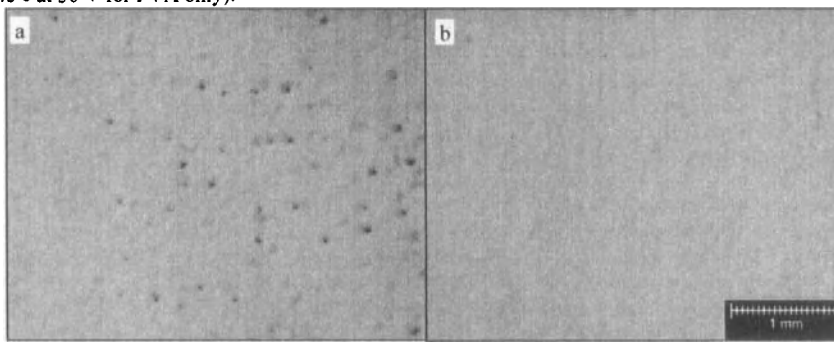

Figure 1: A comparison of (a) PVA/PVB and (b) PVA deposited onto Haynes 230 substrates. Notice the hydrolysis damage in (a) and the lack of such damage in (b).

PVA Binder

The deposition of TBCs from the PVA bath resulted in much more uniform films. Pinholes, at least small ones as seen in PVA/PVB films, are not observed. Hydrolysis was not observed for shorter deposition times, however, two longer depositions (30 minutes) w run within a few days of each other showed an increase in hydrolysis and a corresponding drop in deposition mass (~20%). A pH drop of the solution from ~8 to ~4 was also observed for deposition times of 30 minutes.

The deposition mass versus time follows a linear trend at all deposition times investigated, as shown in figure 2. This trend is expected according to the equation:

$$\frac{m}{a} = CtEu_e \qquad (1)$$

where C is the particle concentration, t is the deposition time, E is the electric field and u_e is the electrophoretic mobility[16].

Overall, the deposition rate stayed fairly constant for all depositions, with an average of 29.21 ± 2.60 μm/cm^2/min.

The surface roughness of the films also increases with time and appears to be related to the deposition time. As can be seen in figure 3, the roughness increases for both regions perpendicular and parallel to erosion channels that form on the sample upon removal from the suspension. It is also interesting to note that the roughness is generally related to the original roughness of the substrate, as the roughness (R_a) of Haynes 230 increases from 0.74 μm to 1.21 μm in 45 s of deposition and the roughness (R_a) of the bondcoated samples increases from 10.85 μm to 12.36 μm in 60 s of deposition.

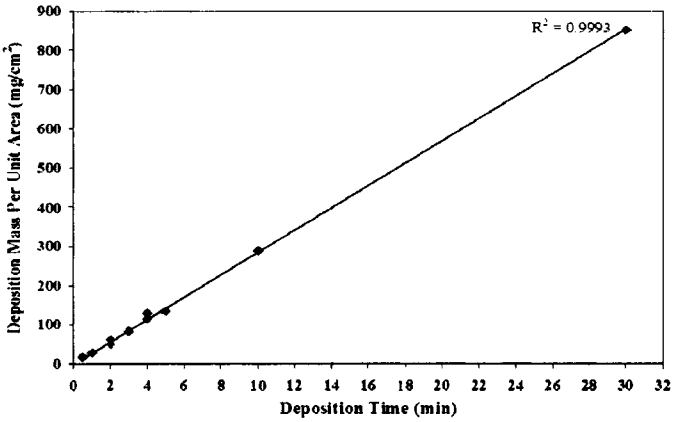

Figure 2: Deposition mass per unit are vs. time for PVA series films. Data has a very high coefficient of determination of 0.9993.

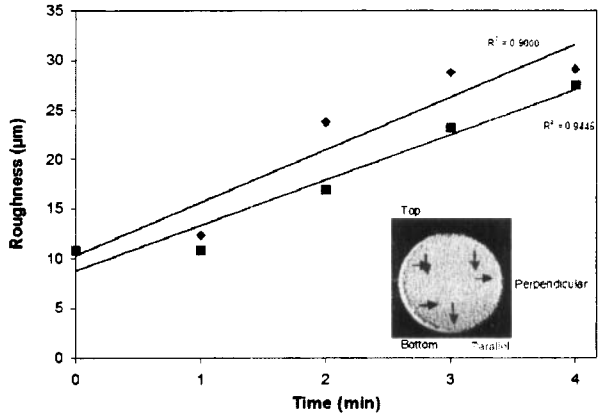

Figure 3: Average Roughness vs. deposition time for PVA binder suspension. In general, the roughness increases with time. Further depositions shows that the roughness continues to increase with increasing deposition time. The diamonds correspond to the scans that are perpendicular to the erosion lines and the squares correspond to the scans that are parallel to the erosion lines.

Binder Burnout

Haynes 230 substrates containing YSZ coatings deposited from PVA suspensions and PVA/PVB suspensions were submitted for TGA and DSC analysis to determine the temperatures required to burn out the binders incorporate into the green films during EPD. TGA and DSC curves are shown in figure 4. These curves show that the zones of primary interest for the binder burnout steps ranges from ~100 °C to 600 °C.

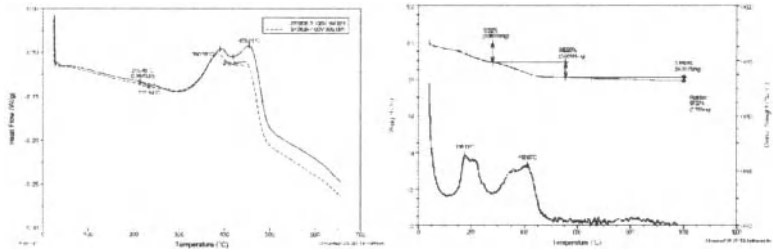

Figure 4: DSC (left) and TGA (right) of YSZ films containing PVA binder. Both the DSC and TGA correspond to each other and literature[17].

An experimental process was developed to determine the necessary ramp rate for the binder burnout regime. Literature stated[18,19,20] that binder burnout ramp rates may be as low as 0.1 °C/min. This ramp rate served as a baseline for the initial tests. In an effort to minimize the time required for binder burn out, other ramp rates were also investigated. Green film deposition results are presented in figure 5. The PVA/PVB binder films showed cracks running through the pinholes in the films. The PVA films showed no observable damage throughout all burnout ramp rates tested, showing a high tolerance for surviving the binder burnout process. The behavior of the bond coated IN939 substrates is similar to the Haynes 230 coated substrates when using the PVA binder.

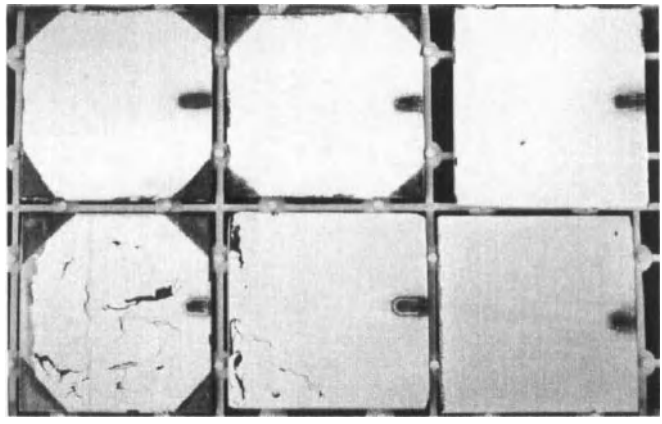

Figure 5: Top row is the films that were deposited with PVA binder. Bottom row is the films deposited with PVA/PVB binder. Heating ramp rate increases as you go from left to right. Haynes 230 substrates are shown.

Furnace Sintering

Table II shows the test parameters and results for the furnace sintering experiments that were conducted to determine the temperature tolerance of the substrates and film. The Haynes 230 substrates, which did not contain a bond coat, consistently resulted in a YSZ film that flaked and spalled off the substrate. It was theorized that either the spallation was a result of an oxide film forming on the substrate during sintering resulting in spallation or the coefficient of thermal expansion mismatch between the nickel superalloy substrate and the ceramic TBC caused the spallation. Sintering experiments in the inert argon atmosphere also resulted in spalling of the YSZ films, therefore, sintering experiments were conducted on substrates that contained YSZ deposited onto a bond coated substrate. Furnace sintering experiments for YSZ films on IN939 substrates that contained a bond coat did not suffer from spallation. It was determined that the bond coat plays a critical role in film adhesion to the surface of the substrate and is performing in the role of compensating for the difference between the coefficient of thermal expansion between the Ni-based superalloy and the YSZ.

Figure 6: Example of how Haynes 230 samples behaved when exposed to temperatures over 600 °C. For each case, this behavior was typical and is believed to be due to the lack of a bond coat, which helps alleviate the coefficient of thermal expansion mismatch.

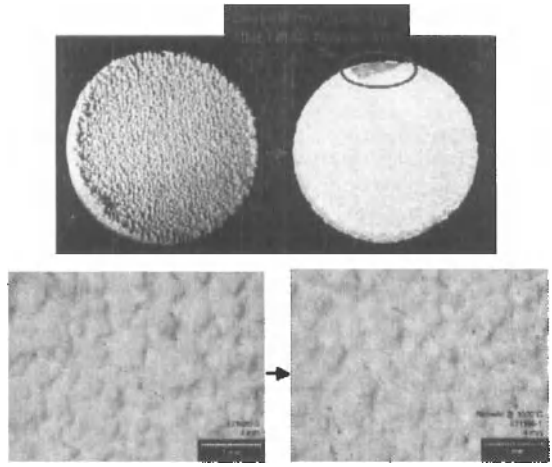

Figure 7: Behavior of the bond coated IN939 samples. Sintering changed the color of the coating from a matte white to a light yellow. Micrographs are shown on the bottom. Cracks can be seen in the green and sintered samples.

The bond coated IN939 samples showed a characteristic color of YSZ after sintering, namely a light yellow. In addition, both the green coating and sintered samples showed that the coating contained small cracks. These cracks may actually be beneficial in this case, as they may provide strain tolerance to the TBC, which can prolong life of the coating when subjected to the thermal and mechanical stresses seen in end use. Further testing of additional temperatures beyond 1000 °C, sintering times beyond 1 hour, and of ramp rates beyond 1 °C/min will be undertaken to determine the optimal sintering parameters required for the film.

Laser Sintering

Laser sintering experiments were performed on YSZ coated Haynes 230 and bond coated IN939 substrates. Figure 8 shows how a binder burnout step affects the laser sintering. In the absence of the binder burnout step, film spallation is observed over the entire exposed area. This is likely due to the combustion by-products of the organic binders. When it became apparent that the film was not undergoing significant sintering under fairly large laser power loads, a section of the film was removed to generate an infrared (IR) absorption spectrum to determine the IR wavelength absorbed by the YSZ.

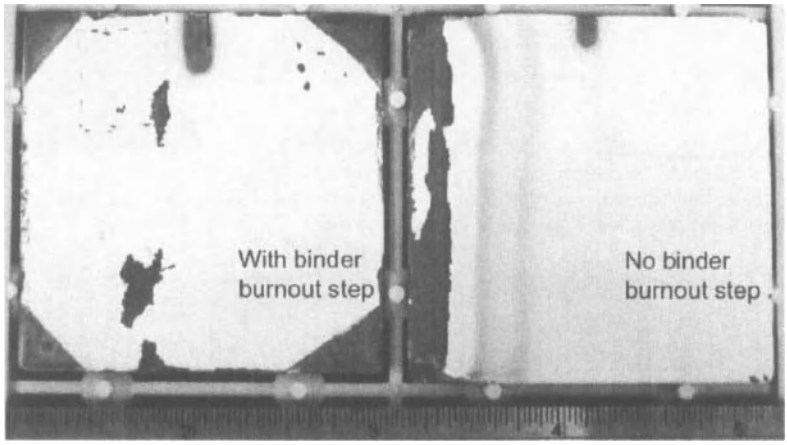

Figure 8: Laser sintering on Haynes 230 substrates. The one on the left underwent a binder burnout step and the one on the right did not. Notice discoloration due to partially burnt binder and large missing section of coating on left hand side of the substrate that did not experience binder burnout step. Red box on the sample that underwent the binder burnout step is one area that was exposed to the infrared (IR) laser. Some film was removed on the left sample for IR analysis.

The IR absorption spectrum is shown in figure 9. Three areas of high absorbency are apparent in the figure. The first region, at ~3 μm, is likely due to H_2O that may be absorbed by the film. The second region, the peak at 9-10 μm is an artifact peak that occurs from the salt plate used to mount the sample for IR analysis. The third region, from 14-25+ μm, is likely the only region where the film readily absorbs IR light. Unfortunately, this narrows the choices of IR lasers to either an HF laser (emission ~3 μm) or to a quantum cascade laser (QCL, emission from 1-70+ μm). Neither laser is of much use for this study as HF lasers are expensive and dangerous to operate and QCL lasers do not have the necessary power required to sinter the film at the wavelengths of interest.

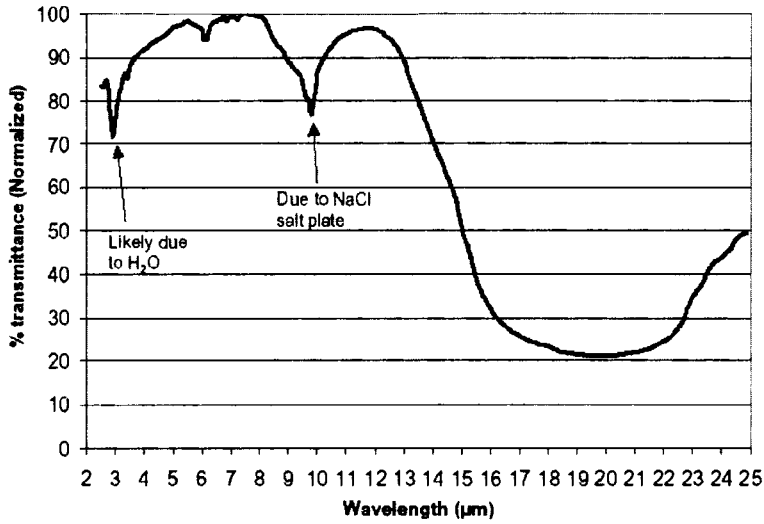

Figure 9: IR absorption spectrum for the YSZ coating. Three major areas of absorbency are shown.

CONCLUSIONS

Throughout this work, several important milestones were achieved, stable suspensions were made, films were deposited, binder was successfully removed, and the films were sintered to 1000 °C. It was also learned, that if we wish to perform laser sintering of the substrates, we will need to investigate lasers within the visible (likely blue to violet) or UV wavelengths. In addition, further work will focus on additional ways to sinter the films, including higher temperature furnace sintering and other ways to preferentially heat the film. Further work will also include optimizing bath chemistry and the binder burnout steps.

ACKNOWLEDGEMENTS

This material is based upon work supported by the Department of Energy under Grant No DE-FG02-05ER84202. Any opinions, findings, and conclusions or recommendations expressed in this material are those of the authors and do not necessarily reflect the views of the Department of Energy.

Faraday gratefully acknowledges both Haynes International, Inc and Siemens Power Generation for supplying substrates for deposition experiments.

REFERENCES

[1]D. Wolfe, J. Singh, Functionally gradient ceramic/metallic coatings for gas turbine components by high-energy beams for high-temperature applications, *J. Mater. Sci.*, **33**, 14, 3677-92 (1998).
[2]D.R. Mumm, A.G. Evans, Failure of a Thermal Barrier System Due to a Cyclic Displacement Instability in the Thermally Grown Oxide, Mat. Res. Soc. Symp. Proc., **645E**, M2.6.1-6 (2001).

[3]C. Leyens, U. Schultz, M. Bartsch, M. Peters, R&D Status and Needs for Improved EB-PVD Thermal Barrier Coating Performance, Mat. Res. Soc. Symp. Proc., **645E**, M10.1.1-12 (2001).
[4]X.Q. Cao, R. Vassen, and D. Stoever, Ceramic materials for thermal barrier coatings, *J. Eur. Ceram. Soc.*, **24**, 1, 1-10 (2004).
[5]T. Narita, S. Hayashi, L. Fengqun, K.Z. Thosin, The Role of Bond Coat in Advanced Thermal Barrier Coating, *Mat. Sc. Forum*, **502**, 99-104 (2005).
[6]J.D. Vyas, K.L. Choy, Structural characterisation of thermal barrier coatings deposited using electrostatic spray assisted vapour deposition method, *Mat. Sc. Eng.*, **A277**, 1-2, 206-212 (2000).
[7]H. Wang, R.B. Dinwiddie, Characterization of Thermal Barrier Coatings Using Thermal Methods, *Advanced Engineering Materials*, **3**, 7, 465-468 (2001).
[8]D.D. Hass, P.A. Parrish, H.N.G. Wadley, Electron Beam Directed Vapor Deposition of Thermal Barrier Coatings, *J. Vac. Sci. Technol.*, **16**, 6, 3396-401 (1998).
[9]P. Hancock, M. Malik, *Materials for Advanced Power Engineer, Part I*, edited by D. Coutsouradis *et al.*, Kluwer Academic, Dordrecht, The Netherlands, 685-704 (1994).
[10]W. Beele, G. Marijnissen, A. van Lieshout, The Evolution of Thermal Barrier Coatings-Status and Upcoming Solutions for Today's Key Issues, *Surf. & Coatings Tech.*, **120-121**, 61-7 (1999).
[11] E. Tzimas, H. Mullejans, S.D. Peteves, J. Bressers, W. Stamm, Failure of Thermal Barrier Coating Systems Under Cyclic Thermomechanical Loading, *Acta Materialia*, **48**, 18-19, 4699-4707 (2000).
[12]T. Ishihara, K. Sato, Y. Takita, Electrophoretic Deposition of Y_2O_3-Stabilized ZrO_2 Electrolyte Films in Solid Oxide Fuel Cells, *J. Am. Ceram. Soc.*, **79**, 4, 913-9 (1996).
[13]H. McCrabb, M. Inman, E. Taylor, Faradayic Electrophoretic Deposition of Thermal Barrier Coatings, Poster Presented at *31st International Conference & Exposition on Advanced Ceramics and Composites*, Daytona Beach, Fl, USA, The American Ceramics Society, ICACC-S2-054-2007 (2007).
[14]E.J. Taylor, *et al.*, Electrically Mediated Plating of Semiconductor Substrates, Chip Scale Packages & High-density Interconnect PWBs, *Plating and Surf. Fin.*, **89**, 88 (May 2002).
[15]J. J. Sun, *et al.*, Electrically Mediated Edge & Surface Finishing for Automotive, Aerospace & Medical Applications, *Plating and Surf. Fin.*, **89**, 94 (May 2002).
[16]H.C. Hamaker, Formation of deposit by electrophoresis, *Trans. Faraday Soc.* **35**, 279-87 (1940).
[17]J.W. Gilman, D.L. VanderHart, T. Kashiwagi, Thermal Decomposition Chemistry of Poly(vinyl alcohol): Char Characterization and Reactions with Bismaleimides, in *Fire and Polymers II: Materials and Tests for Hazard Prevention*, Chapter 11, American Chemical Society, ACS Symposium Series 599, Washington, D.C., USA, August 21-26, 1994.
[18]R.V. Shende, S.J. Lombardo, Determination of Binder Decomposition Kinetics for Specifying Heating Parameters in Binder Burnout Cycles, *J. Am. Ceram. Soc.*, **85**, 4, 780-6 (2002).
[19]M.B. Kakade, S. Ramanathan, P.K. De, Combustion synthesis, powder treatment, dispersion and tape casting of lanthanum strontium manganite, *British Ceram. Trans.*, **102**, 5, 211-5 (2003).
[20]Y. Kinemuchi, T. Tsugoshi, K. Watari, H. Ishiguro, Binder Burnout from Layers of Alumina Ceramics Under Centrifugal Force, *J. Am. Ceram. Soc.*, **89**, 3, 805-9 (2006).

Advanced Processing and Manufacturing Technologies for Structural and Multifunctional Materials II
Edited by Tatsuki Ohji and Mrityunjay Singh

INDIUM TIN OXIDE CERAMIC ROTARY SPUTTERING TARGETS FOR TRANSPARENT CONDUCTIVE FILM PREPARATION

Eugene Medvedovski,* Christopher J. Szepesi, and Olga Yankov
Umicore Indium Products
Providence, RI, USA

Maryam K. Olsson
Umicore Materials AG
Balzers, Liechtenstein

ABSTRACT

Indium tin oxide (ITO) thin films are widely used in optoelectronic devices, such as flat panel displays, solar cell windows and others, due to their high transparency and electrical conductivity. One of the most reliable methods of these films preparation is DC magnetron sputtering technique using high quality ITO sputtering targets. Planar sputtering targets are successfully used for the sputtering process; however, in order to improve film quality, to significantly increase utilization of expensive sputtering targets and to reduce process downtime, sputtering machines with rotary sputtering targets have to be employed. ITO ceramic rotary sputtering targets consisted of hollow ceramic cylinders bonded to a metallic backing tube, for the first time, have been successfully manufactured and tested for the TCO film processing. These ITO ceramic components have been manufactured using innovative ceramic technology consisting of ITO slip preparation and forming of the required hollow cylindrical shapes with subsequent firing, machining and bonding. Despite the challenges of forming and firing of rather large ITO components from sub-micron starting materials, these components with density greater than 99% of TD have been successfully manufactured, assembled to the targets with a height greater than 1 m and tested producing thin high-quality ITO films.

INTRODUCTION

Highly transparent and electrically conductive oxide (TCO) thin films are widely used as electrode layers in optoelectronic devices, such as flat panel displays (FPD), e.g. liquid crystal displays (LCD), organic light-emitting diodes (OLED), plasma-display panels (PDP), touch panels, solar cells, electrochromic devices, as well as antistatic conductive films and low-emission coatings [1-4]. The films are commonly produced by conventional DC magnetron sputtering onto glass or polymer substrates, requiring a fine-tuned deposition process and high quality sputtering targets; ceramic sputtering targets are used as a cathode for magnetron sputtering equipment. Indium tin oxide (ITO) is the most reliable material, among different ceramic materials, which may be used for this purpose, because it provides highly homogeneous nanostructured transparent (greater than 90% of transmittance in optical range) and electrically conductive thin films with a thickness of 100-250 nm [1-4]. Due to continual growth of consumption and related manufacturing of display products, necessity of the use alternative (to oil and gas) sources of energy and use of "clean" energy, the demand of ITO products (ceramics and films) is continuously increasing with higher requirements for film quality and process efficiency. Currently, planar sputtering targets are used in thin film processing, and these targets consist of one or several tiles bonded onto a metallic backing plate. Conventional planar sputtering targets (PST) are eroded during sputtering resulting in a specific racetrack (localized plasma zone), and the utilization of such targets is 20-40%. Moreover, the risk of formation of particulates on the surface of the targets that disrupts the film processing is relatively high; thus, the need for system maintenance reducing the film processing efficiency is inevitable using a planar cathode configuration.

In order to increase the utilization of expensive ITO ceramic sputtering targets and efficiency of the sputtering process, rotary sputtering cathodes equipped with tubular ceramic targets may be employed. Such rotary sputtering targets (RST) may be considered as a new generation of sputtering targets used for TCO thin film preparation. Opposed to PST, the entire surface of RST becomes a working surface that results in a significant increase of target utilization (70-90%, i.e. several times greater than planar). Due to a tubular configuration of the cathode, a much higher power per unit area may be applied in comparison with PST that increases not only the efficiency of the sputtering process and film formation rate, but also reduces undesired particle re-deposition of the surface of the targets. Utilization of expensive ITO ceramics from the RST is 80% or greater, i.e. about 3 times higher than in the case of planar targets. Hence, a sufficient reduction of the thin film production cost and a longer service cycle may be achieved. A general description of RST is performed by W. De Bosscher et al. [5], and the schematic design of RST vs. PST is shown in the Fig. 1.

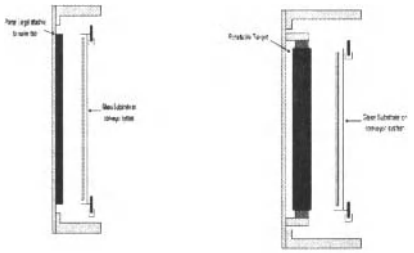

Fig. 1. Schematics of sputtering targets
a) planar sputtering targets; b) rotary sputtering targets

Although ceramic sputtering targets are considered to provide higher performance compared to metallic targets, ceramic RST have not been widely implemented and used in the FPD industry. One of the recently implemented designs of RST consists of the cylindrical metal substrates coated with ceramic powders used for TCO thin film preparation (e.g. ITO) employing high temperature processing [6-9]. This design and related technology (e.g. the arc spray coating or plasma spray method described in [7]) allow the manufacturing of ITO layers with a thickness of up to 3 mm and densities of up to 90-95% of TD. The methods of forming a target by hot isostatic pressing (HIP) on the outer surface of cylindrical metallic substrates (e.g. in accordance with [8, 9]) may provide higher density and thicker ceramic layers, but these layers are not thick enough for stable continual film processing. The targets formed by this method, as well as by other methods in which the ceramic is directly attached to the metallic substrate, cannot be easily separated, and therefore, the targets and, especially, the ceramic segment, may be very difficult to recycle. The difficulties in recycling of the ceramics from targets make all these methods less economical, especially if expensive ITO ceramic is used in sputtering targets.

Generally, PST have a thickness of 5-9 mm that is required in many applications of FPD industry. Moreover, the target surface should be very smooth; an appropriate low roughness is achieved by a dedicated surface grinding process. Hence, prior to the machining step, the thickness of

the ceramics are made larger than the desired final thickness. The same thickness and surface quality requirements are valid for RST.

Another type of the RST design and related technology approach utilizes the "ceramic" processing technology to manufacture the ITO components of the target. However, before recent time, "ceramic" processing (including ITO ceramic) was not very successful for RST. For this application, the RST should consist of high-density hollow ceramic cylinders assembled and bonded to an interior metallic backing tube. The total industrial target length is usually large (from 1 to 2.7 m), and, for that reason, the ceramic part of the RST has to be assembled from several sections with a substantial length. The diameter of the hollow ceramic parts is selected and prepared for several industrial dimensions denoted as small, medium and large with a substantial wall thickness mentioned above (i.e. the technology has to provide a dimensional flexibility). As an additional benefit of the use of the "ceramic" technology approach, the homogeneity in the cross-section (wall) of ceramic cylindrical bodies may be high, and the outside diameter of the ceramic cylinders (i.e. the sputtering surface) may be machined to high surface quality.

The challenges related to ceramic sputtering targets manufacturing, particularly ITO ceramics, using "ceramic" technology include obtaining high density sintered bodies (fired density has to be greater than 99% of TD) with a hollow cylindrical shape and relatively large dimensions without deformation in accordance with industry needs. Thus, the ceramic slurry composition, slurry preparation process, shaping and firing conditions have to be optimized, and the shaping process has to provide a high particle packing efficiency while remaining practical and economically beneficial. In general, the larger the ceramic body, especially with the above described shape, the more challenges are faced to obtain a body without cracks and deformation from sub-micron particles, as required for high density ceramic manufacturing.

Advanced ITO RST made from relatively large hollow cylinders of 99+% of TD applying an innovative "ceramic" technology using pressureless sintering have been developed and manufactured, for the first time, at Umicore Indium Products (UIP). The technology provides flexibility in different dimensions (diameters and wall thickness) and the opportunity to produce "ultra"-high density components. The assembled sputtering targets have been successfully tested using a conventional rotary sputtering system, producing high-quality ITO thin films with properties in accordance with the optoelectronic industry requirements.

EXPERIMENTAL

High-purity commercially produced In_2O_3 and SnO_2 powders were used as the main starting materials for production of ITO ceramics. The In_2O_3 powders are manufactured at UIP using a proprietary process from pure indium via its dissolution with subsequent neutralization and precipitation of $In(OH)_3$ and subsequent calcination at an appropriate temperature. Each lot of starting In, prepared $In(OH)_3$ and In_2O_3 powders are qualified by chemical analyses and powder characterization. In the present work, ITO 90/10 ceramic composition (10 wt.-% of SnO_2), as the most reliable and commonly used in the FPD industry, was employed. ITO composition is prepared through the wet processing providing a high level of homogeneity of the In_2O_3/SnO_2 distribution. The features of ITO ceramic slip formulation and wet milling process were utilized in accordance with earlier developed and implemented state-of-the-art process for the manufacturing of large ITO tiles used for PST [4]. The developed shaping process provided hollow cylindrical bodies, made by "ceramic" technology, which then were dried and machined in the green state with subsequent firing. Firing was conducted in electric furnaces at relatively low temperature (below 1600°C) without assistance of pressure for sintering. It should be noted that a multi-step process control during powder preparation

and ceramic manufacturing is maintained providing a high purity of ceramic components. Fired ceramic bodies (Fig. 2a) were inspected and then machined with diamond tooling to obtain a high surface quality and precise dimensions. The finished ITO ceramic hollow cylinders were bonded to a metallic (Ti) backing tube using indium as a bonding material. The assembled sputtering targets had a total length of the ceramic part of min. 1200 mm (Fig. 2b). Hollow ceramic bodies with a wall thickness of 6 mm after post-firing machining and the assembled target after bonding, have been inspected using ultrasonic testing equipment.

Phase composition and microstructure of the fired ceramics and sputtered films were studied using X-ray diffraction (XRD) and Scanning Electron Microscopy (SEM) under different magnifications using "as-received" or etched samples. Density of ceramic components was determined by the water immersion method based on Archimedes law. Specific electrical resistivity of ceramics was measured using a four-point probe unit for the tile witness samples. Film thickness was optically determined using a reflectometer analyzer (J.Y. Horiba). Specific electrical resistivity of the films also was measured using a Jandel four-point probe measuring unit. The transmittance in the visible range from 400 to 800 nm wavelength was measured using an optical analyzer (Perkin Elmer).

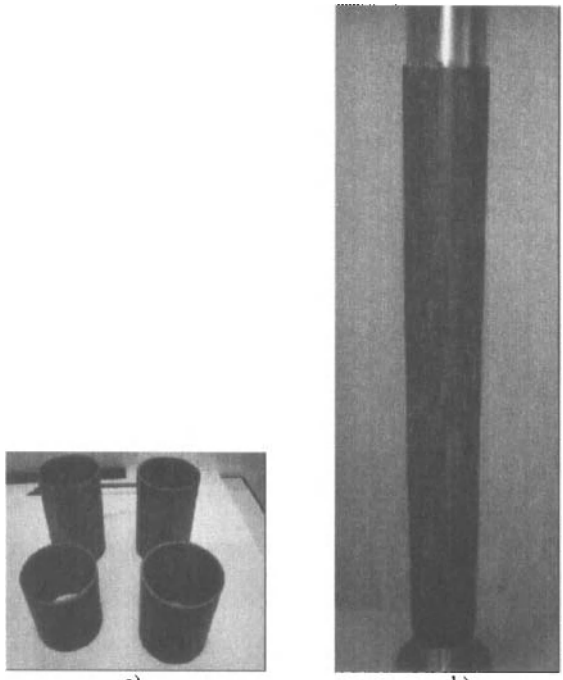

Fig. 2. Rotary ITO Ceramic Sputtering Target
a) Ceramic sections
b) Bonded and assembled target (a total length of greater than 1200 mm)

Sputtering was conducted in collaboration with a distinguished sputtering system manufacturer using a conventional DC magnetron sputtering system providing rotation of the target. Sputtering behavior (e.g. plasma behavior, cycling performance, film uniformity) was evaluated.

RESULTS AND DISCUSSION

Density of the fired hollow cylindrical bodies is achieved as 7.10-7.13 g/cm^3, i.e. up to 99.5% of TD, as a result of the developed manufacturing process. The required high densification is achieved by through optimization of the ceramic composition, material preparation process and firing conditions without assistance of pressure. The latter has to be outlined because, in general, ITO ceramics have low sinterability dealt with partial decomposition of In_2O_3 and SnO_2 at elevated temperatures and evaporation of the decomposition products. The technology allows to produce ceramic cylinders with dimensional flexibility (e.g. diameter of 100-200 mm, wall thickness of 4-7 mm, and length of 200 mm or greater). Due to optimized firing conditions and furnace loading, deformation of the hollow cylindrical bodies is minimized reducing possible stress formation in the cylinders during densification. Ultrasonic testing of the hollow ceramic cylinders indicated no detectable defects in the scan images. Specific electrical resistivity of ceramics was in the range of (1.3 -1.7)x10^{-4} Ohm.cm.

Microstructure of the ITO ceramics is dense, rather uniform, and consists of the grains with sizes varying from 5 to 10 μm, mostly with a cubic shape (Fig. 3). The grains are composed of crystallites with sizes of 25-45 nm as determined via XRD analysis using the Scherrer formula for calculation. In accordance with XRD analysis, the ITO ceramics consist of In_2O_3 (bixbyite) as a major crystalline phase with an absence of free SnO_2 phase. Intragranular cleavage of the grains can be seen on the SEM image that may indicate a high level of densification of the sintered ceramic material.

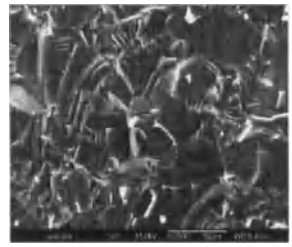

Fig. 3. Microstructure of ITO 90/10 ceramics

Sputtering tests of the UIP RST consisting of the ITO hollow cylinders with medium ID and a thickness of 6 mm bonded to the titanium backing tube with a total length of the ceramic part of 1200 mm. These tests demonstrated acceptable results, including a high level of the film properties, e.g. electrical resistivity and transparency, which satisfy industrial requirements. The films with thicknesses in the range of 70-100 nm had electrical resistivity of around 500 μOhm.cm and transmittance greater than 86% in as-deposited stage, and these properties may be upgraded to around 200 μOhm.cm and greater than 90%, respectively, after annealing. These results are comparable with those obtained in the case of deposition from planar ITO sputtering targets under standard conditions. The films also had a high uniformity (deviation less than 10%) comparable with uniformity of films prepared using metallic rotary targets. A stable behavior during the cycling process tested when the plasma was exposed to off and on states for several hundreds time in order to test real manufacturing

conditions was noted. With a designed sputtering procedure, the following achievements may be outlined:

- no abnormalities with plasma ignition at a high power level
- uniform and steady plasma behavior
- stable cycling performance (e.g. stable sputtering voltage over a long period of time and low arcing)
- sputtered nanostructured film with a high uniformity
- excellent film properties (electrical resistivity and transmittance) well comparable with film properties, which are achieved using planar sputtering targets
- reduced re-deposition on the target

The use of a rotary cathode allowed to apply a higher sputtering power and therefore, to increase a deposition rate, and as a result, provided a higher efficiency of film deposition.

CONCLUSIONS

The proposed ITO ceramic RST with a total length of greater than 1 m consisting of hollow cylinders with a wall thickness of 6 mm (or greater) bonded to a backing tube have been developed and manufactured, for the first time, using innovative "ceramic" technology. The RST was successfully tested in a conventional sputtering system under obtained stable plasma conditions producing high quality ITO thin films, which satisfy industrial requirements. The ITO ceramic components have densities up to 99+% of TD. The designed rotary cathode allows to apply a higher sputtering power, increasing film deposition rate with uniform plasma behavior. The use of sputtering targets with ceramic cylinders provides a significant increase in the ITO thin film production efficiency and overall reduction of film processing cost. ITO RST are an excellent replacement of ITO PST in LCD technology and other optoelectronic applications, particularly because of their significantly higher utilization of the expensive ITO ceramics (about 70-90% depending on the sputtering system and sputtering conditions) and reduced re-deposition.

REFERENCES:

[1]J.L. Vossen, "Transparent Conducting Films", *Phys. Thin Films*, Ed. By G. Haas, M.H. Francombe, and R.W. Hoffman (Academic, New York) **9**, 1-71 (1977)
[2]D.S. Ginley, C. Bright, "Transparent Conducting Oxides", *MRS Bulletin*, **8**, 15-18 (2000)
[3]I. Hamberg, C.G. Granquist, "Evaporated Sn-Doped In_2O_3 Films: Basic Optical Properties and Applications to Energy-Efficient Windows"; *J. Appl. Phys.*, **60**, R123-160 (1986)
[4]E. Medvedovski, N.A. Alvarez, O. Yankov, M.K. Olsson, "Advanced Indium-Tin Oxide Ceramics for Sputtering Targets"; *Ceramics International,* (2007), *in press*
[5]W. De Bosscher, K. Dellaert, S. Luys, et al., "ITO Coating of Glass for LCDs", *Information Display*, 21, N. 5, 12-15 (2005)
[6]W. De Bosscher, H. Delrue, J. Van Holsbeke, et al., "Rotating cylindrical ITO targets for large area coating", *J. of Society of Vacuum Coaters*, 48, 111-115 (2005)
[7]JP-A-10-068072
[8]JP-A-05-156431
[9]US Patent 5,354,446

Advanced Processing and Manufacturing Technologies
for Structural and Multifunctional Materials II
Edited by Tatsuki Ohji and Mrityunjay Singh

THE EFFECT OF DOPING WITH TITANIA AND CALCIUM TITANATE ON THE MICROSTRUCTURE AND ELECTRICAL PROPERTIES OF THE GIANT DIELECTRIC CONSTANT CERAMIC $CaCu_3Ti_4O_{12}$

Barry A. Bender, Ed Gorzkowski, and Ming-Jen Pan
Naval Research Lab
Code 6351
Washington, DC 20375

ABSTRACT

Small amounts (1-5 mole%) of TiO_2 and $CaTiO_3$ were added to the giant dielectric constant ceramic $CaCu_3Ti_4O_{12}$ (CCTO) in the attempt to lower dielectric loss without sacrificing high permittivity. The undoped and doped ceramics had similar microstructures consisting of primarily large grains in the range of 35 to 40 microns. Doping CCTO with TiO_2 lead to an increase in the dissipation factor of $CaCu_3Ti_4O_{12}$ from 0.049 to a high of 0.078, while its permittivity increased from 43949 to 77585. Doping with $CaTiO_3$ followed a similar trend as the tan δ increased to a high of 0.303 and the dielectric constant at 1 kHz increased to a high of 75687. Doping at these levels also led to a 50% drop in electrical breakdown voltage.

INTRODUCTION

In its development of the all-electric ship the US Navy has made significant outlays in the technology of power electronics. Passive components, especially filter capacitors, remain a limiting factor in power converter design. This is due to their low volumetric efficiency which causes them to be responsible for occupying 50 to 60% of the volume associated with today's state-of-the-art power converter. The ideal ceramic filter capacitor would consist of a high dielectric ceramic with good stability over a range of temperatures and frequencies. Commercial dielectric oxides such as $BaTiO_3$ typically sacrifice high permittivity for temperature stability. Recently, a new dielectric oxide, $CaCu_3Ti_4O_{12}$, has been uncovered with the potential to have high permittivity (single crystal dielectric constant is 80,000) that is stable over a wide range of temperatures and frequencies.[1,2] Also the material can be engineered into an internal barrier layer capacitive-like (IBLC) dielectric via one-step processing in air[3] at modest sintering temperatures of 1050 to 1100°C and it is environmentally-friendly since CCTO is a lead-free dielectric.

However, the dielectric loss properties of $CaCu_3Ti_4O_{12}$ have to be improved if this material is going to be used commercially. Dissipation factors as low as 0.05 to 0.06 (20°C, 10 kHz) have been reported for undoped $CaCu_3Ti_4O_{12}$ but are very sensitive to temperature.[4,5] At temperatures as low as 40°C dielectric loss values begin to climb leading to losses that exceed 0.10 before 60°C is reached.[4,6-8] To improve CCTO's dielectric loss properties the nature of the giant permittivity of $CaCu_3Ti_4O_{12}$ has to be fully comprehended. The consensus of most researchers is that the high permittivity of $CaCu_3Ti_4O_{12}$ is extrinsic in nature and is the result of the formation of insulating layers around semiconducting grains. This creates an electrically inhomogeneous material that is similar to internal barrier layer capacitors (IBLCs).[3] However, the exact nature of the insulating boundaries and semiconducting grains is still under scientific debate. Electrical measurements show that the insulating boundaries are electrostatic potential barriers that can be best described using a double Schottky barrier (DSB) model.[9,10] The electrical properties of electroceramics that contain these type of DSB barriers can be very sensitive to the presence of dopants and oxygen.[11-13] Electrical measurements show that the grains are n-semiconductors,[14] but why the grains are semiconducting is unclear. Li *et al.*[15] believe that cation nonstoichiometry occurs during processing resulting in the replacement of Ti ions on Cu ion sites. They believe that small increases in Ti ion concentration as low as 0.0001 can account for

the measured semiconductivity in CCTO grains. Researchers have added TiO_2 and $CaTiO_3$ in amounts of 10% or higher and have shown that it leads to dramatic reductions in dielectric loss.[16-18] However, it also results in substantial 75% decreases in permittivity too. At the moment, no research has been reported on the addition of small additions of TiO_2 or $CaTiO_3$ which according to Li's model[15] may have significant impact on the dielectric and electrical properties of CCTO. This paper reports on the attempt to decrease the loss of CCTO ceramics by doping them with small amounts of TiO_2 and $CaTiO_3$. The effects of doping on the resultant microstructure, dielectric properties, and electrical breakdown of $CaCu_3Ti_4O_{12}$ are reported.

EXPERIMENTAL PROCEDURE

$CaCu_3Ti_4O_{12}$ was prepared using ceramic solid state reaction processing techniques. Stoichiometric amounts of $CaCO_3$ (99.98%), CuO (99.5%) and TiO_2 (99.5%) were mixed by blending the precursor powders into a purified water solution containing a dispersant (Tamol 901) and a surfactant (Triton CF-10). The resultant slurries were then attrition-milled for 1 h and dried at 90°C. The standard processed powder, STD, was calcined at 900°C for 4 h and then 945°C for 4 h. After the final calcination the STD powders were attrition-milled for 1 h to produce finer powders. The titania-doped powders, T, were fabricated by mixing various amounts of titania with the calcined STD powder (0.95 mole% (95T), 1.9 mole% (190T) and 2.8 mole% (280T)). The $CaTiO_3$-doped powders, C, were made by mixing various amounts of $CaTiO_3$ with the calcined STD powder (0.95 mole% (95C), 1.35 mole% (135C), 2.7 mole% (270C), and 5.4 mole% (540C)). A 2% PVA binder solution was mixed with the powders and they were sieved to eliminate large agglomerates. The dried powder was uniaxially pressed into discs typically 13 mm in diameter and 1 mm in thickness. The discs were then placed on platinum foil and sintered in air for three hours at 1100°C.

Material characterization was done on the discs and powders after each processing step. XRD was used to monitor phase evolution for the various mixed powders and resultant discs. Microstructural characterization was done on the fracture surfaces using scanning electron microscopy (SEM). To measure the dielectric properties, sintered pellets were ground and polished to achieve flat and parallel surfaces onto which palladium-gold electrodes were sputtered. The capacitance and dielectric loss of each sample were measured as a function of temperature (-50 to 100 °C) and frequency (100 Hz to 100 KHz) using an integrated, computer-controlled system in combination with a Hewlett-Packard 4284A LCR meter. Electrical breakdown was measured on samples typically 1 mm in thickness with gold electrodes at an applied rate of voltage of 500 volts per second.

RESULTS and DISCUSION

Effect of Ti-Doping on the Microstructure and Dielectric Properties of $CaCu_3Ti_4O_{12}$

Ti-doping had a mixed effect on the microstructure of CCTO. The microstructure of undoped CCTO was bimodal consisting of pockets of small grains distributed randomly throughout a matrix of coarser grains (see Fig. 1a). The average grain size of the large grain was 37 microns (see Table I) while the smaller grains were typically 2 to 4 microns in size and occupied less than 5 vol%. Fractographs indicated that the fracture was basically transgranular and showed evidence of a possible very thin submicron grain boundary phase (see Fig. 1b). The only overt evidence of a second phase observed to be present was a Cu-rich phase whose presence was always detected in the mix of the smaller grains (see Fig. 1c). Ti-doping did not lead to the presence of any other overt second phases either as detected by XRD or SEM. However, higher resolution techniques like TEM need to be used to clarify the nature of the grain boundaries and the presence and nature of second phases. Ti-doping did lead to mixed results in microstructure and transgranular fracture (see Fig. 1). The average grain size of 190T and 280T had similar values (Table I) but at the 99% confidence level the 95T CCTO had

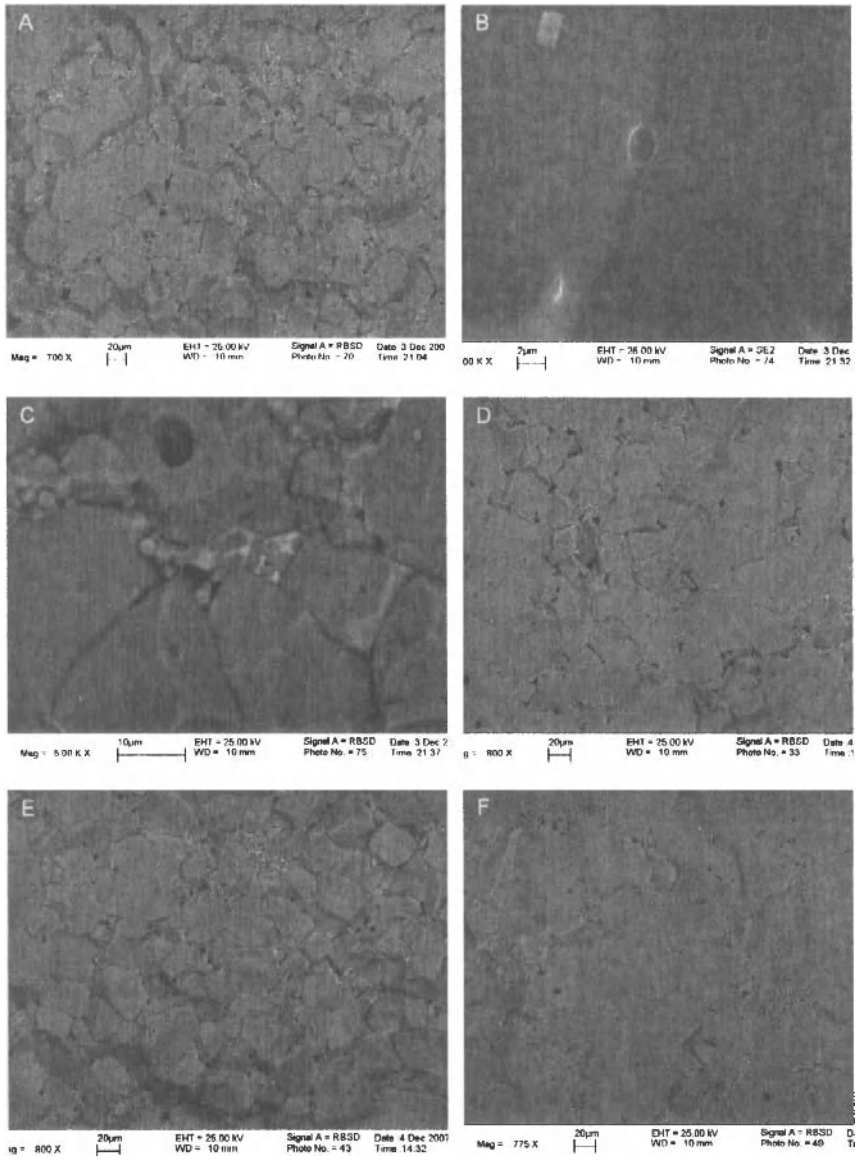

Fig. 1 SEM fractographs of undoped CCTO (a-c) and CCTO doped with TiO_2- (d) 95T, (e) 190 (f) 280T. Fig. (a) and (c-f) are back-scattered SEM micrographs.

a grain size that was 15% smaller. It is unclear how doping with titania at this level could reduce the grain size but not at the higher dopants levels. The only other major difference between all the samples was that the 280T sample fractured in a very flat, highly transgranular mode which is often indicative of a stronger grain boundary (see Fig. 1f).

Table I. Effect of Doping on Grain Size, Dielectric, and Electrical Properties of $CaCu_3Ti_4O_{12}$

Sample	Grain Size (μm)	Permittivity (1 kHz)	Dissipation Factor	Breakdown Voltage (V/mm)
STD	37 (9)	43939	0.049	1100
95T	31 (10)	49100	0.060	750
190T	39 (11)	48249	0.049	740
280T	40 (10)	77585	0.078	520
95C	32 (8)	65000	0.193	415
135C	35 (9)	70683	0.303	400
270C	40 (10)	75687	0.231	450
540C	38 (9)	67420	0.287	950

(xx) is the standard deviation of the measured grain size

However, doping CCTO with titania did have an effect on the dielectric properties. Though the trends were mixed, adding titania to CCTO increased its dielectric constant (20°C- 1 kHz) from 43939 to 77585 for the 280T sample (see Table I and Fig. 2). It also led to an increase in the dissipation factor as it increased from 0.049 for the undoped sample to 0.078 for the 280T sample. The 190T sample was an anomaly in regards to dielectric properties as the permittivity and dielectric loss both decreased in value as compared to the 95T. However, this result provided clues to what the effect of doping with small amounts of titania has on the $CaCu_3Ti_4O_{12}$ system. The dielectric constant in an IBLC or material with a Schottky barrier layer can be represented as[10]

$$\varepsilon' = \varepsilon_B (d/t_B) \quad (1)$$

where ε_B is the permittivity of the boundary or barrier layer, d can be approximated by the grain size, and t_B is the thickness of the boundary or barrier layer. Since the dielectric loss is very similar for the STD and 190T sample, at both 20 and 80°C, they should have similar values of ε_B. Grain sizes are similar for the two samples so that means that the effective barrier or boundary thickness for the Ti-doped system must have decreased. This would also explain the increase in permittivity for the other two samples (95T and 280T). The dielectric data also provides other clues to the effect of Ti-doping. In an IBLC the approximation for the loss tangent is[19]

$$\tan \delta = 1/(\omega R_{gb} C) + \omega R_g C \quad (2)$$

where ω is the angular frequency, R_{gb} is the resistance of the boundary layer, R_g is the resistance of the semiconducting grains, and C is the capacitance. This means that the low frequency loss is dominated by R_{gb} while higher frequency loss is dominated by R_g. Looking at Fig. 2 it can be determined for 95T and 280T that the change in loss from the STD ceramic at 100 Hz is 3 to 4 fold while at 100 kHz the change in loss is only 1.1 to 1.5. This implies that Ti-doping effects R_{gb} causing the grain boundaries to be more conductive resulting in higher dielectric losses. How the presence of extra Ti ions affects the nature of the boundary or barrier layer is unknown. It is well known that Ti segregates to the grain boundaries in $BaTiO_3$ and $SrTiO_3$ ceramics.[20] Also Ti has been measured by STEM analysis to segregate to the grain boundaries in CCTO ceramics.[21] Electrical measurements by Zang *et al.*[10] have shown that Schottky barriers exist in CCTO. They and Marques *et al.*[22] postulate that the barrier layer

consists of adsorbed oxygen atoms. Since Ti is a known oxygen getter it is possible that the presence of extra Ti segregating to the boundary changes the chemistry of the barrier layer and leads to less adsorbed oxygen. This would lead to a thinner boundary or barrier layer and a lower barrier height. From I-V measurements on $SrTiO_3$ and impedance spectroscopy (IS) on Ti-doped CCTO, barrier heights and R_{gb} has been directly linked with changes in permittivity and dielectric loss so that lower barrier heights lead to a decrease in R_{gb} which leads to higher permittivity and higher loss which is what we observe in the Ti-doped CCTO samples.[23,16]

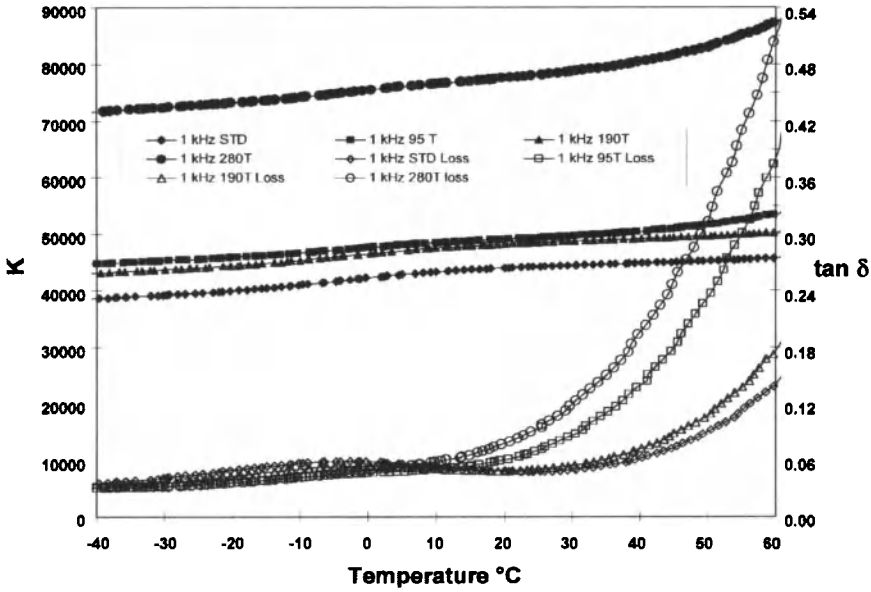

Fig. 2 Temperature dependence at 1 kHz of the dielectric constant and dissipation factor of undoped CCTO (STD) and TiO_2-doped CCTO (95T, 190T, and 280T).

Effect of $CaTiO_3$-Doping on the Microstructure and Dielectric Properties of $CaCu_3Ti_4O_{12}$

$CaTiO_3$-doping led to results that were very similar in nature to the effects that titania-doping had on the microstructure of CCTO. Again the sample with the least amount of $CaTiO_3$, 95C, showed a 15% reduction in grain size (see Table 1) while the other $CaTiO_3$-doped samples had grain sizes similar to that of the STD sample (see Fig. 3). Also the $CaTiO_3$-doped samples tended to fracture in a more transgranular fracture as compared to the undoped sample with the 270C sample showing the flattest fracture (Fig 3- c vs. d). XRD and SEM picked up no evidence of any second phases but their presence can not be ruled out until higher resolution TEM analysis is done on these ceramics too.

Doping with $CaTiO_3$ led to mixed results in its effect on the dielectric properties of $CaCu_3Ti_4O_{12}$. All the doped samples had significantly higher dielectric constants (see Table I and Fig. 4) as the permittivity increased by 75% from 43939 to 75687 when doped with 2.7 mole% $CaTiO_3$. All the samples showed significant increases in dielectric loss as the tan δ increased 6 fold going from 0.049 to 0.303 when doped with 1.35 mole% $CaTiO_3$. Again there were anomalies present in the data. The 270C data showed a significant drop in dissipation factor (see Table I) which was counter to the

trend of the rest of the data, while the 540C showed a drop in dielectric constant which was counter to the trend of increasing permittivity with increasing doping amounts of $CaTiO_3$. These results indicate that there may be possible different mechanisms or effects that small amounts of $CaTiO_3$ have on the defect chemistry of the semiconducting grains and insulating boundaries in CCTO dielectrics.

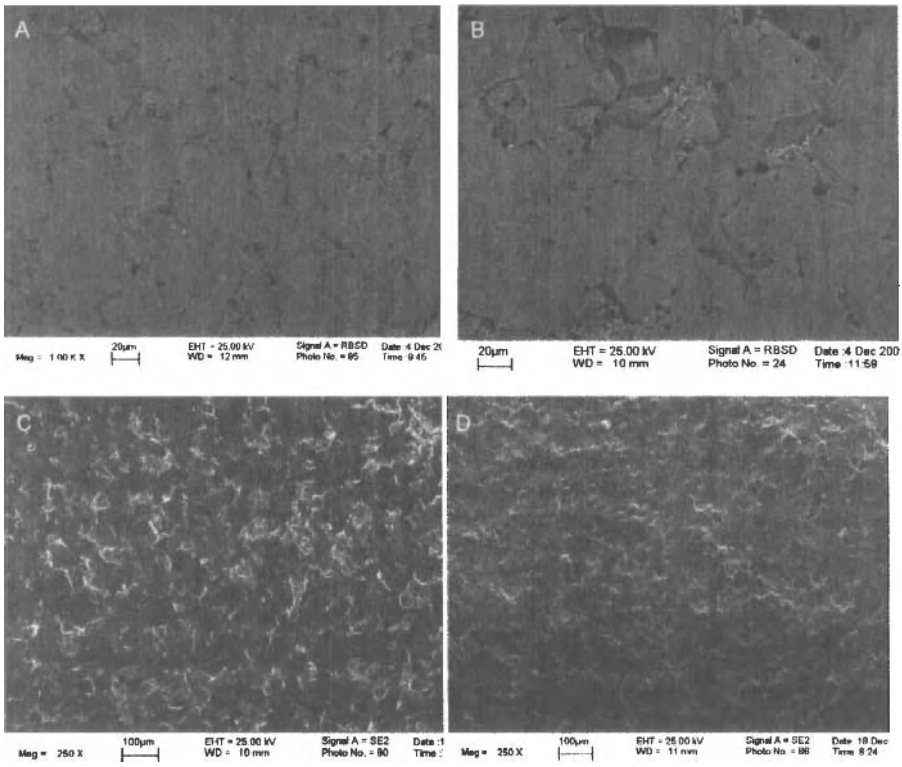

Fig. 3 SEM fractographs of undoped CCTO doped with $CaTiO_3$- (a) 95C, (b) 135C, (c) 270C, (d) 540C. Fig. (a) and (b) are back-scattered SEM micrographs.

In CCTO ceramics doped with large amounts of $CaTiO_3$ ($x > 0.1$, $Ca_xCu_3Ti_{4+x}O_y$), the addition of $CaTiO_3$ led to 75% drops in permittivity and an order of magnitude drop in tan δ.[17,18] The researchers attributed the drop in dielectric constant due to the formation of $CaTiO_3$ in CCTO. Since $CaTiO_3$ is a low loss (tan $\delta = 0.001$) dielectric of 180 that is used to lower dielectric loss and the temperature dependence of loss in titanates it is not unexpected a composite containing $CaTiO_3$ would have lower permittivity and dielectric loss.[24,25] However, as shown from the data in Table I this is not the case for when small amounts of $CaTiO_3$ were added to CCTO, which resulted in the opposite general trend of higher permittivity and higher losses as compared to the undoped material. Similar to Ti-doped CCTO, detailed examination of the dielectric spectra (Fig. 4) reveals that the changes in loss as compared to the undoped sample versus the doped sample are greater at 100 Hz then at 100k Hz

(i.e. for 135C- 33 fold (100 Hz) vs. 2.5 fold at (100 kHz)). This shows that the addition of small amounts of $CaTiO_3$ is lowering R_{gb}. This is in contrast to Yan *et al.*[17] who showed using IS that large $CaTiO_3$ additions increased the resistance of the boundary layers. It is postulated that with low amounts of added $CaTiO_3$, that $CaTiO_3$ is segregating to the boundary layer. This is quite feasible as Ti, Ca, and $CaTiO_3$ have been reported to segregate to the grain boundaries.[21,26,27] There it can react with the boundary layer changing its chemistry and defect nature to make the effective boundary layer thinner and less insulative which leads to a higher dielectric constant and higher losses as seen for 95C and 135C. In the case of 540C it is possible that the segregation has reached its saturation limit and $CaTiO_3$ is now forming as a second phase. Since the dielectric constant of $CaTiO_3$ is much lower than CCTO (43939 vs. 180)[24] and the permittivity is much lower too (0.0490 vs. 0.001)[24] it is expected by the rules of mixture that the resultant doped-CCTO would start to see a decrease in its permittivity and tan δ as compared to 135C.

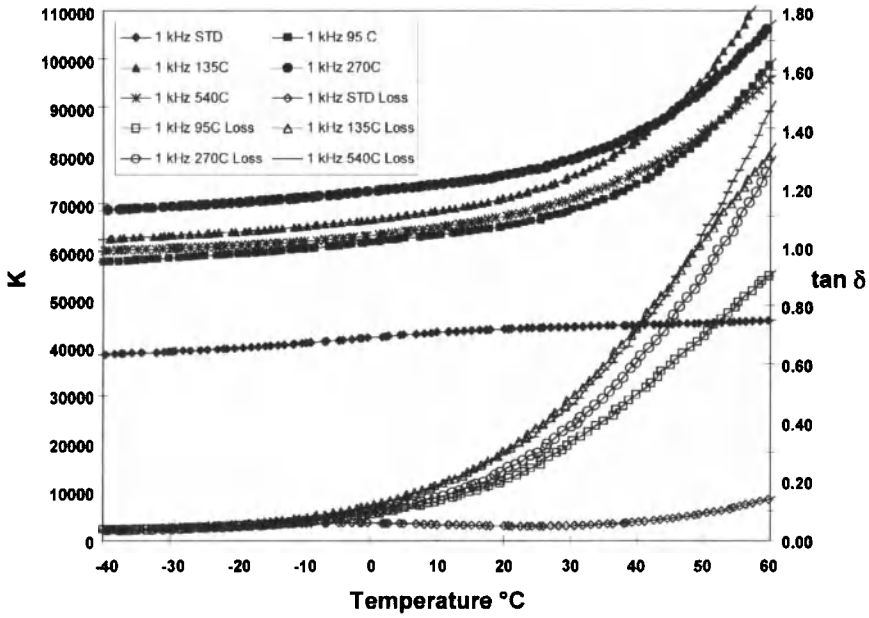

Fig. 4 Temperature dependence at 1 kHz of the dielectric constant and dissipation factor of undoped CCTO (STD) and $CaTiO_3$-doped CCTO (95C, 135C, 270C, and 540C).

Effect of Doping on the Electrical Breakdown Voltage of $CaCu_3Ti_4O_{12}$

High breakdown voltage (E_b) is a desirable characteristic for a capacitive material. Commercial ferroelectric $BaTiO_3$-based capacitor materials have high breakdown voltages in the range of 30 kV/cm.[28] However, varistors and IBLCs have a much lower E_b due to the presence of Schottky barriers. Typical values for varistors range from 400 for TiO_2-based varistors to 1300 V/cm for ZnO and SnO_2-based varistors.[29-31] For a $SrTiO_3$-based IBLC E_b has been measured to range from 200 to 400 V/cm.[32] For CCTO materials there has been no thorough study on its breakdown voltage but there

is scattered data available in the literature. Breakdown voltages for undoped CCTO have been reported to be 400, 600, 1300, and 1300 v/cm.[33-35,14] However, E_b is sensitive to processing as the breakdown voltage drops from 1300 to 300 V/cm due to a 10-fold increase in grain size and E_b increases from 400 to 570 V/cm when heat-treated in flowing oxygen.[14,33] Table I data indicates that the breakdown voltage for CCTO is sensitive to doping. In the samples doped with TiO_2 E_b drops from 1100 V/cm for the undoped dielectric to as low as 520 V/cm for the 280T sample. As discussed earlier it was postulated that Ti doping leads to effectively a thinner boundary layer which leads to a lower boundary energy and a less insulative boundary layer. This should result in a lower E_b because Chung *et al.*[36] have done IS research on Sc-doped CCTO and have shown a direct correlation between changes in R_{gb} and E_b.

Doping with $CaTiO_3$ also lowered the breakdown voltage for CCTO. However, the data trend was mixed in a similar fashion as the dielectric data was (see Table I). The E_b dropped from 1100 for the STD sample to a low of 400 for the 135C sample and started to increase with further doping to a value of 950 for 540C. As postulated for the dielectric data it is believed that the doping CCTO at the lower amounts of $CaTiO_3$ led to a decrease in R_{gb} and as discussed above this would lead to lower electrical breakdown voltages as observed for 95C and 135C. However, when doped with 5.4 mole% $CaTiO_3$ it was believed that $CaTiO_3$ started to develop as a second phase at the grain boundaries. This could lead to the observed increase in E_b for 540T because a 1 part $CaCu_3Ti_4O_{12}$:2 part $CaTiO_3$ composite saw a dramatic increase in E_b to 6500 V/cm due to the large amounts of $CaTiO_3$ present in the composite.[26]

CONCLUSIONS

Unlike the results of reduced loss and permittivity reported for doping CCTO with large amounts of TiO_2 and $CaTiO_3$, addition of small amounts of these dopants led to higher dissipation factors and higher dielectric constants. Instead of 10-fold reduction of tan δ the dissipation factors were increased from about 0.05 to a high of 0.08 for the Ti-doped material and 0.3 for the $CaTiO_3$-doped material. This increase in tan δ was accompanied by a 75% increase in permittivity as the dielectric constant increased from about 44000 to 77000 for both doped-materials. Analysis of the dielectric spectra indicated that doping led to a decrease in the resistivity of the insulative boundary layers. It also indicated that the effective thickness of the layers was narrower. These results can also account for the 50% drop in electrical voltage breakdown from doping CCTO dielectrics with TiO_2 or $CaTiO_3$. Impedance spectroscopy and TEM analysis are needed to shed further insight on the complex role of these dopants at low levels. With this information the nature of the boundary layers should be clearer which will allow for material engineering CCTO in order to obtain low-loss CCTO dielectrics without sacrificing the giant permittivity of $CaCu_3Ti_4O_{12}$.

REFERENCES

[1]C. C. Homes, T. Vogt, S. M. Shapiro, S. Wakitomo, A. P. Ramirez, "Optical Response of High-Dielectric-Constant Perovskite-Related Oxide," *Science*, **293**, 673-76 (2001).

[2]M. A. Subramanian, D. Li, N. Duan, B. A. Reisner, and A. W. Sleight, "High Dielectric Constant in $ACu_3Ti_4O_{12}$ and $ACu_3Fe_3O_{12}$ Phases," *J. of Solid State Chem.*, **151**, 323-25 (2000).

[3]T. B. Adams, D. C. Sinclair, and A. R. West, "Giant Barrier Layer Capacitance Effects in $CaCu_3Ti_4O_{12}$ Ceramics," *Adv. Mater.*, **14**, 1321-23 (2002).

[4]B.A. Bender and M.-J. Pan, "The Effect of Processing on the Giant Dielectric Properties of $CaCu_3Ti_4O_{12}$," *Mat. Sci. Eng. B.*, **117**, 339-47 (2005).

[5]E.A. Patterson, S. Kwon, C.-C. Huagn, and D.P. Cann, "Effects of ZrO_2 Additions on the Dielectric Properties of $CaCu_3Ti_4O_{12}$," *Appl. Phys. Lett.*, **87**, 182911-1-3 (2005).

[6]T.-T. Fang, L.-T. Mei, H.-F. Ho, "Effects of Cu Stoichiometry on the Microstructures, Barrier-Layer Structures, Electrical Conduction, Dielectric Responses, and Stability of $CaCu_3Ti_4O_{12}$," *Acta Mat.*, **54,** 2867-75 (2006).
[7]R.K. Grubbs, E.L. Venturini, P.G. Clem, J.J. Richardson, B.A. Tuttle, and G.A. Samara, "Dielectric and Magnetic Properties of Fe- and Nb-doped $CaCu_3Ti_4O_{12}$," *Phys. Rev. B*, **72,** 104111-1-11 (2005).
[8]T.-T. Fang and H.K. Shiau, "Mechanism for Developing the Boundary Barrier Layers of $CaCu_3Ti_4O_{12}$," *J. Am. Ceram. Soc.*, **87,** 2072-79 (2004).
[9]T.B.Adams, D.C. Sinclair, A.R.West, "Characterization of Grain Boundary Impedances in Fine- and Coarse-Grained $CaCu_3Ti_4O_{12}$ Ceramics", *Phys. Rev. B*, **73**, 094124-1-9 (2006).
[10]G. Zang, J. Zhang, P. Zheng, J. Wang, and C. Wang, "Grain Boundary Effect on the Dielectric Properties of $CaCu_3Ti_4O_{12}$ Ceramics," *J. Phys. D. Appl. Phys.*, **38**, 1824-27 (2005).
[11]D.R. Clarke, "Varistor Ceramics," *J. Am. Ceram. Soc.*, **82**, 485-502 (1999).
[12]R.C. Buchanan, *Ceramic Materials for Electronics*, Marcel Dekker, New York, pp. 377-431 (2004).
[13]G.V. Lewis, C.R. Catlow, and R.E. Casselton, "PTCR Effect in $BaTiO_3$," *J. Am. Ceram. Soc.*, **68**, 555-58 (1985).
[14]S.Y. Chung, I.-D. Kim, and S.J.L. Kang, "Strong Nonlinear Current-Voltage Behaviour in Perovskite-Derivative Calcium Copper Titanate," *Nature Materials*, **3**, 774-78 (2004).
[15]J. Li, M.A. Subramanian, H.D. Rosenfeld, C.Y. Jones, B.H. Toby, and A.W. Sleight, "Clues to the Giant Dielectric Constant of $CaCu_3Ti_4O_{12}$ in the Defect Structure of $SrCu_3Ti_4O_{12}$," *Chem. Mater.*, **16**, 5223-25 (2004).
[16]Y.-H. Lin, J. Cai, M. Li, C.-W. Nan, and J. He, "High Dielectric and Nonlinear Electrical Behaviors in TiO_2-Rich $CaCu_3Ti_4O_{12}$ Ceramics," *Appl. Phys. Lett.*, **88**, 172902-1-3 (2006).
[17]Y. Yan, L. Jin, L. Feng, and G. Cao, "Decrease of Dielectric Loss in Giant Dielectric Constant $CaCu_3Ti_4O_{12}$ Ceramics by Adding $CaTiO_3$," *Mat. Sci. Eng. B*, **130**, 146-50 (2006).
[18]W. Kobayashi and I. Terasaki, "$CaCu_3Ti_4O_{12}/CaTiO_3$ Composite Dielectrics: Ba/Pb-free Dielectric Ceramics with High Dielectric Constants," *Appl. Phys. Lett.*, **87**, 032902-1-3 (2005).
[19]Y. Yan, L. Jin, L. Feng, and G. Cao, "Decrease of Dielectric Loss in Giant Dielectric Constant $CaCu_3Ti_4O_{12}$ Ceramics by Adding $CaTiO_3$," *Mat. Sci. Eng. B*, **130**, 146-50 (2006).
[20]Y.-M. Chiang and T. Takagi, "Grain-Boundary Chemistry of Barium Titanate & Strontium Titanate: I, High-Temperature Equilibrium Space Charge," *J. Am. Ceram. Soc.*, **73** [1], 3278-85 (1990).
[21]C. Wang, H. J. Zhang, P.M. He, and G.H. CaO, "Ti-rich and Cu-Poor Grain-Boundary Layers of $CaCu_3Ti_4O_{12}$ Detected by X-ray Photoelectron Spectroscopy," *Appl Phys. Lett.*, **91**, 052910 (2007).
[22]V.P.B Marques, A. Ries, A.Z. Simoes, M.A. Ramirez, J.A. Varela, and E. Longo, "Evolution of $CaCu_3Ti_4O_{12}$ Varistor Properties During Heat Treatment in Vacuum," *Ceram. Intl.*, **33**, 1187-90 (2007).
[23]P. Prabhumirashi, V. P. Dravid, A.R. Lupini, M.F. Chisholm, and S.J. Pennycook, "Atomic-Scale Manipulation of Potential Barriers at $SrTiO_3$ Grain Boundaries, *Appl. Phys. Lett.*, **87**, 121917-1-3 (2005).
[24]W. Qin, W. Wu, J. Cheng, and Z. Meng, "Calcium-Doping for Enhanced Temperature Stability of $(Ba_{0.6}Sr_{0.4})_{1-x}Ca_xTiO_3$ Thin Film Dielectric Properties," *Mat. Lett.*, **61**, 5161-63 (2007).
25R.K. Dwivdi, D. Kumar, and O. Parkash, "Valence Compensated Perovskite Oxide System $Ca_{1-x}La_xTi_{1-x}Cr_xO_3$," *J. Mat. Sci.*, **36**, 3641-48 (2001).
[26]M.A. Ramirez, P.R. Bueno, J.A. Varela, and E. Longo, "Non-Ohmic and Dielectric Properties of a $Ca_2Cu_2Ti_4O_{12}$ Polycrystalline System," *Appl. Phys. Lett.*, **89**, 212202-1-3 (2006).
[27] S.F. Shao, J.L. Zhang, P. Zheng, C.L. Wang, J.C. Li, and M.L. Zhao, "High Permittivity and Low Dielectric Loss in Ceramics with the Nominal Compositions of $CaCu_{3-x}La_{2x/3}Ti_4O_{12}$," *Appl. Phys. Lett.*, **91**, 042905-1-3 (2007).
[28]B.-C. Shin, S.-C. Kim, C.-W. Nahm, and S.-J. Jang, "Nondestructive Testing of Ceramic Capacitors by Partial Discharge Method," *Mat. Lett.*, **50**, 82-86 (2001).

[29]A.B. Gaikwad, S.C. Navale, and V. Ravi, "TiO_2 Ceramic Varistor Modified with Tantalum and Barium," *Mat. Sci. Eng. B*, **123**, 50-52 (2005).
[30]C.-W. Nahm, "Microstructure and Electrical Properties of Tb-Doped Zinc Oxide-Based Ceramics," *J. Non-Crystl.* Sol., **353**, 2954-57 (2007).
[31]S.R.D. Hage, V. Choube, and V. Ravi, "Nonlinear I-V Characteristics of Doped SnO2," *Mat. Sci. Eng. B*, **110**, 168-71 (2004).
[32]S.-M. Wang and S.-J. L. Kang, "Acceptor Segregation and Nonlinear Current-Voltage Characteristics in H2-Sintered SrTiO3, "*Appl. Phys. Lett.*, **89**, 041910-1-3 (2006).
[33]V.P.B Marques, P.R. Bueno, A.Z. Simoes, M.Cilense, J.A. Varela, E. Longo, and E.R. Leite, "Nature of Potential Barrier in $CaCu_3Ti_4O_{12}$ Polycrystalline Perovskite," *Sol. State Comm.*, **138**, 1-4 (2006).
[34]S.-Y. Chung, S.-Y. Choi, T. Yamamoto, Y. Ikuhara, and S.-J. L. Kang, "*Site-Selectivity of 3d Metal Cation Dopants and Dielectric Response in Calcium Copper Titanate*," *Appl. Phys. Lett.*, **88**. 091917-1-3 (2006).
[35]M. Guo, T. Wu, T. Liu, S.-X. Wang, and X.-Z. Zhao, "Characterization of $CaCu_3Ti_4O_{12}$ Varistor-Capacitor Ceramics by Impedance Spectroscopy," *J. Appl. Phys.*, **99**, 124113-1-3 (2006).
[36]S.-Y. Chung, S.-I. Lee, J.-H. Choi, S.-Y. Choi, "Initial Cation Stoichiometry and Current-Voltage Behavior in Sc-Doped Calcium Copper Titanate," *Appl. Phys. Lett.*, **89**, 191907-1-3 (2006).

Advanced Processing and Manufacturing Technologies for Structural and Multifunctional Materials II
Edited by Tatsuki Ohji and Mrityunjay Singh

SYNTHESIS AND CHARACTERIZATION OF ELECTRODEPOSITED NICKEL NANOWIRES

Valeska da Rocha Caffarena[1], Alberto Passos Guimarães[2], Magali Silveira Pinho[3], Elizandra Martins Silva[4], Jefferson Leixas Capitaneo[5], Marilia Sergio da Silva Beltrão[4]

[1] Petróleo Brasileiro S. A – Gas&Power - Av. Almirante Barroso, 81 – 31° andar – Centro, ZIP CODE 20031-004, Rio de Janeiro, Brazil, valeskac@petrobras.com.br
[2] Centro Brasileiro de Pesquisas Físicas (CBPF), Rua Dr. Xavier Sigaud, 150, ZIP CODE 22290-180, Urca, RJ, Brazil, apguima@cbpf.br
[3] Brazilian Navy Research Institute (IPqM) - Rua Ipiru 2, Praia da Bica, Ilha do Governador, Rio de Janeiro, RJ, Brazil, Zip Code 21931-090, magalipinho@yahoo.com.br
[4] Dep. of Metallurgical and Materials Engineering, COPPE-PEMM/UFRJ, PO Box 68505, Zip Code 21941-972, Rio de Janeiro, RJ, Brazil, elizams@metalmat.ufrj.br, marilias@metalmat.ufrj.br
[5] Centro Universitário Estadual da Zona Oeste (UEZO)/ Instituto de Macromoléculas, IMA/UFRJ, jeff@ima.ufrj.br

ABSTRACT

One-dimensional nanostructures have attracted considerable attention due to their potential applications in a new generation of nanodevices. The template synthesis method has played an important role in the fabrication of many kinds of nanowires and nanotubes, for their interesting and useful features.

Nanowires are expected to play an important role in future electronic and in electromechanical systems. When the nanowire diameter is of the same order as the charge carrier wavelength, quantum confinement effects shift energy states and the properties of nanowires strongly depend on size, shape and structure.

We have studied the Ni nanowire electrodeposited in nanoporous anodic alumina membrane from a sulfate electrolyte containing 270 g/l $NiSO_4.7H_2O$, 40 g/l $NiCl_2.H_2O$ and 40 g/l H_3BO_3. The particle size was determined by AFM and SEM and the samples were characterized using XRD and EDX.

INTRODUCTION

Nanostructured materials (nanoparticles, nanobelts, nanotubes and nanowires) have unique electrical, optical and magnetic properties compared with bulk materials [1-5].

A nanowire is a wire having a diameter in the range of about one nanometer (nm) to about 500 nm and length usually larger than 500 nm [1].

In the nanometer-size range of dimensions, the physical size of the samples may have a critical effect on their magnetic properties and some of the electronic and optical properties of the nanomaterials will be different than the ones of larger sizes materials, due to the quantum confinement phenomena [6].

The nanowires can be prepared using a variety of methods including template synthesis within pores of polycarbonate or anodic alumina membranes, solution phase reduction, physical vapor deposition (PVD) onto carbon nanotubes and electron beam lithography [5-8].

Recently, the template synthesis method has attracted great interest, because of its ability to control both the diameter and aspect ratio (ratio between length and diameter) of nanowire. This is an effective method to prepare uniform sized nanomaterials, whose morphology can be controlled by the distribution and size of the template pores.

In this work, we focus on nickel nanowires fabricated by filling a porous anodic alumina membrane (AAM) template using electrodeposition, which is a simple and low-cost method. The nickel nanowires were fabricated by anodization of pure Al to obtain the porous template and sequential nickel AC electroplating.

EXPERIMENTAL

A 99.997% pure Al sheet (Vetec) was pretreated in a 5% NaOH solution at 60°C for 60 seconds to remove the grease that existed on the surface, neutralized in 1:1 HNO_3 for 30 seconds, washed in Milli-Q water and etched in HNO_3.

The electrochemically polished Al sheet was anodized at 40 V for 5-10 minutes, using 0.3 mol L^{-1} H_3PO_4 as electrolyte. The aluminum oxide was slightly soluble in this acid electrolyte and the reaction product at the polished Al sheet anode was aluminum oxide (Equation 1):

$$2\,Al(s) + 3\,H_2O \rightarrow Al_2O_3\,(s) + 6H^+\,(aq) + 6\,e^- \qquad (1)$$

The formed alumina oxide was dissolved in 1% H_3PO_4 at 60°C for 20 minutes.

The Al sheet was then anodized for 12 hours to create long-range ordering. The oxide film was removed again and the Al sheet anodized again for 30 minutes more.

After anodization, the Al sheet was cleaned ultrasonically in water. The pores were opened in 1% H_3PO_4 for 6 minutes and the anodic alumina membrane (AAM) was obtained.

The nickel electrodeposition was carried out on the anodized aluminum sheets at room temperature by AC electroplating (50 Hz, 28V/ 10 seconds). The electrolyte was a water solution with 270 g/l $NiSO_4.7H_2O$, 40 g/l $NiCl_2.H_2O$ and 40 g/l H_3BO_3. The pH of the electrolyte solution was controlled between 4.0 – 4.5 by addition of NaOH (0.1 mol L^{-1}).

SEM and AFM observations, EDX analyses and X-ray diffraction confirmed the existence of Ni nanowires.

The removal of Ni nanowires from anodic alumina membrane was done by dissolving the template in 1.25 mol L^{-1} NaOH at 25°C for 120 min.

A portion of the partially dissolved AAM sample (dissolved in NaOH solution during only 10 minutes) was observed using a LEO 940A Scanning Electron Microscope operated at 20 kV.

After completely dissolution, a drop was put on a silicon substrate and the nanowire size and the shape measurements were performed by AFM topography examinations in a non-contact mode with a Topometrix II® Atomic Force Microscope, and by SEM using a Jeol Noran scanning electron microscope. EDX analysis was also carried out using this equipment.

The crystallographic structure of the electrodeposited nanowire was investigated by X-ray diffraction analysis (XRD) using a Miniflex diffractometer, with a dwell time of 1°/min, in the θ-2θ Bragg-Brentano geometry.

RESULTS AND DISCUSSION

After dissolving the AAM template in 1.25 mol L^{-1} NaOH for 10 minutes, the nickel nanowire could be seen partly from the template as shown in Figure 1.

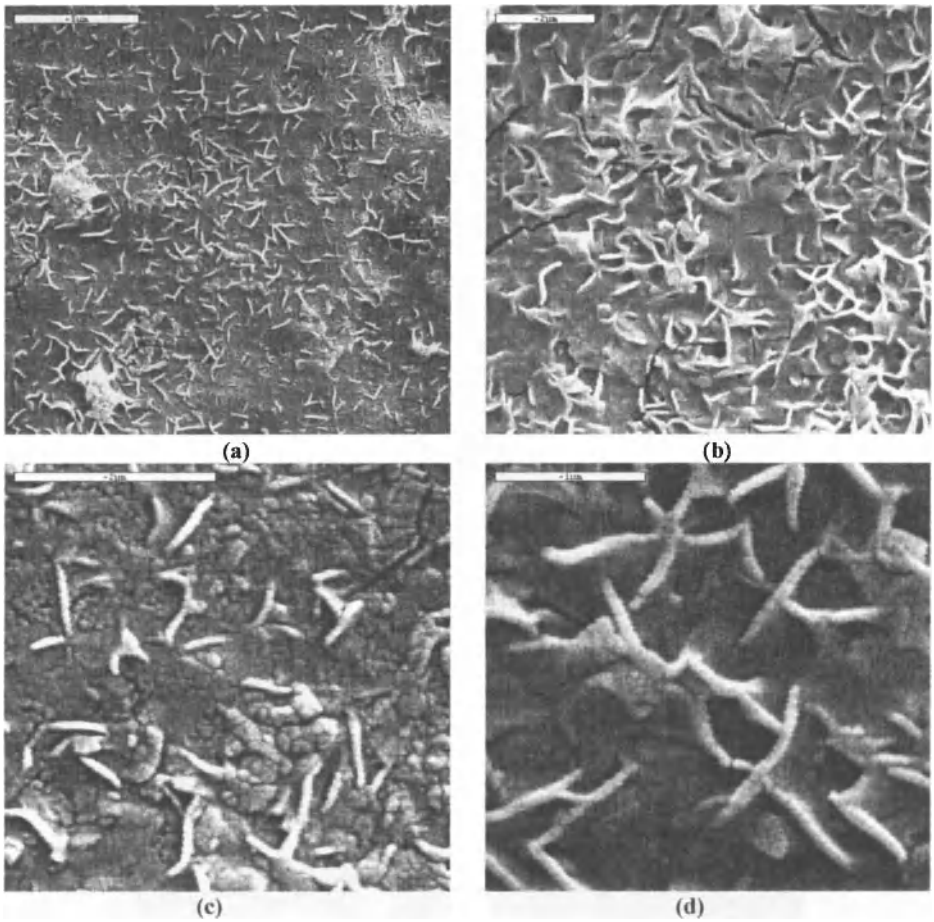

Figure 1: SEM micrograph of Ni nanowires in partially dissolved alumina membrane (1.25 M NaOH/10 minutes) at different magnifications of: (a) 5000 X, (b) 10000 X, (c) 20000 X and (d) 30000 X.

When the dissolving process is complete (after 120 minutes in NaOH), the visible length of the nanowires becomes longer, as can see in Figure 2.

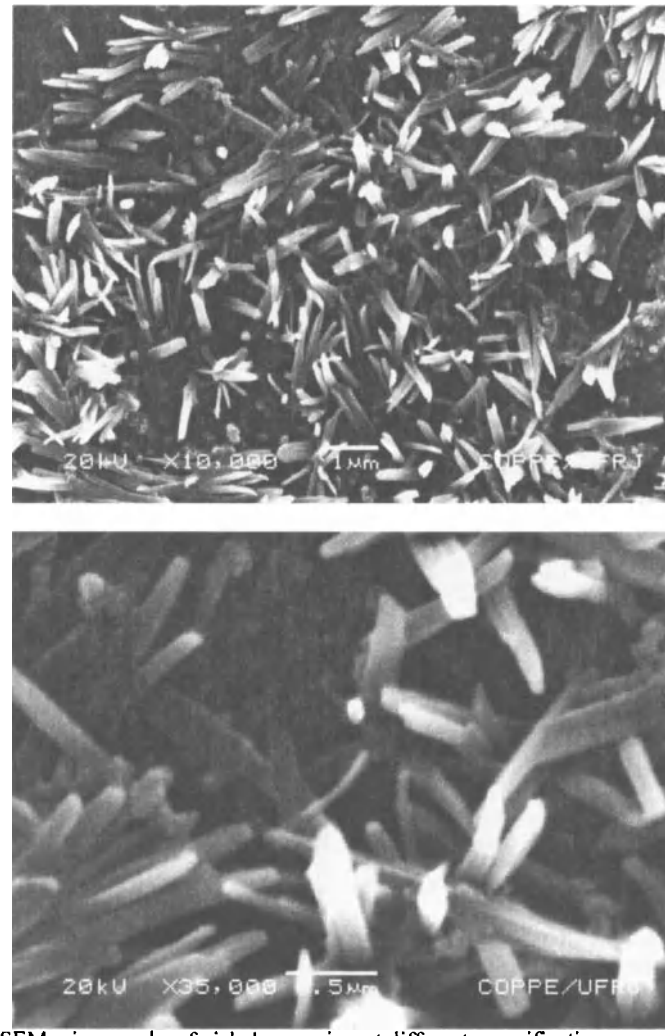

Figure 2: SEM micrographs of nickel nanowires at different magnifications.

The nickel nanowires average diameter and length are, respectively, 125 nm and about 2.5 μm as confirmed by AFM (Figure 3).

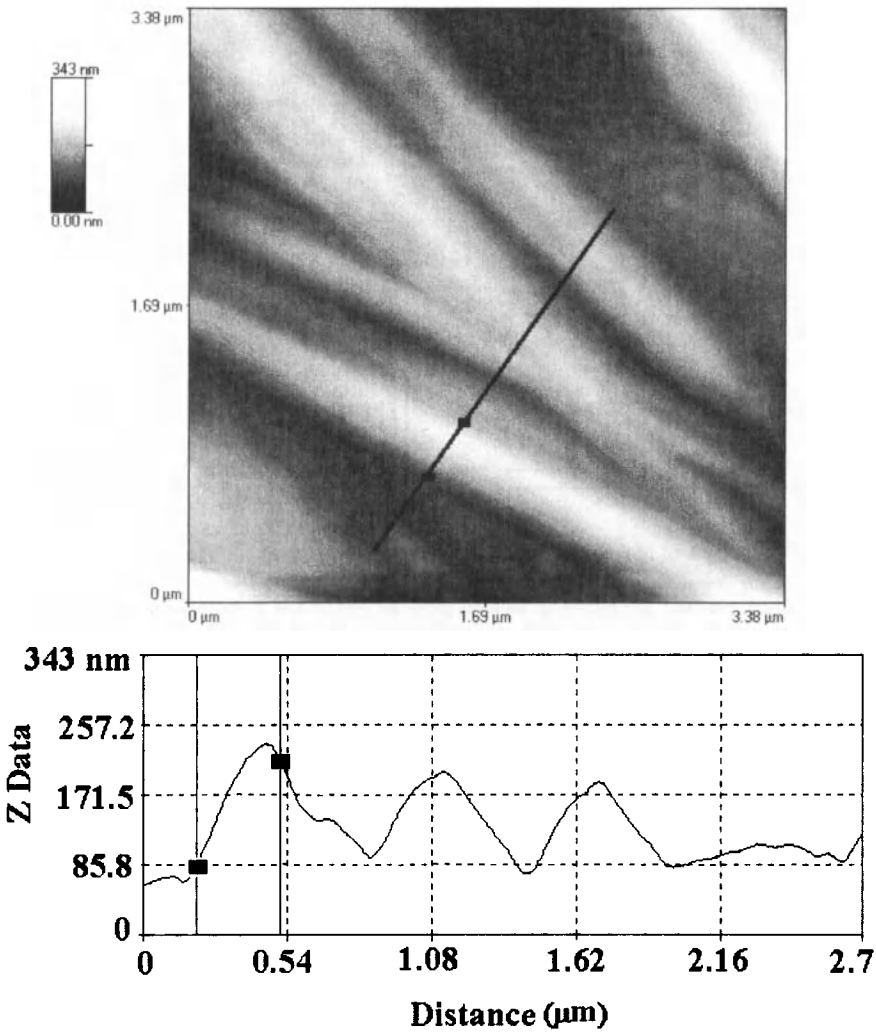

Figure 3: AFM micrograph of nickel nanowires.

It is seen from the EDX spectrum, as shown in Figure 4, that the nanowires contain only nickel and oxygen. The Al peaks are due to the support and the Au peaks to the gold film sputtered on the surface of the sample.

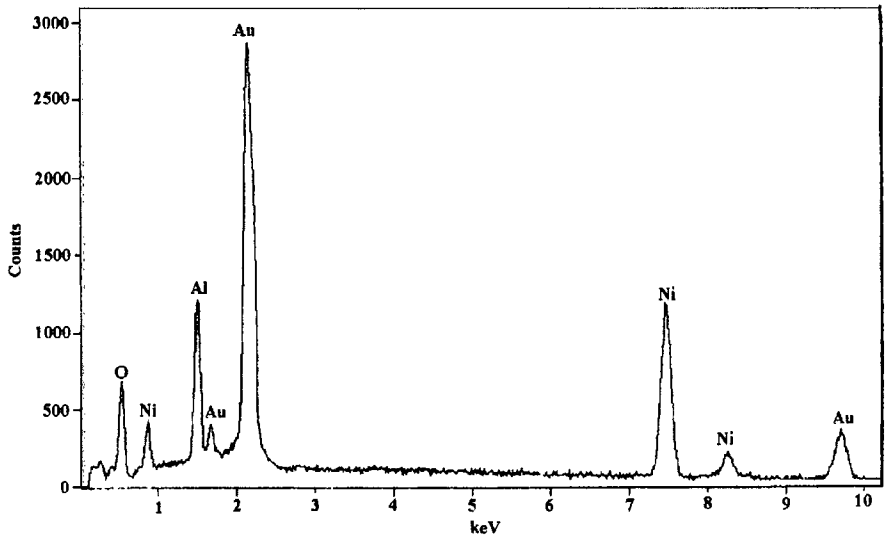

Figure 4: EDX spectrum of nickel nanowires on an aluminum support.

The structural and geometrical factors play an important role in determining the various attributes of nanowires, such as their electrical, optical and magnetic properties.

The XRD pattern for the Ni nanowires obtained in the pores of AAM is shown in Figure 5.

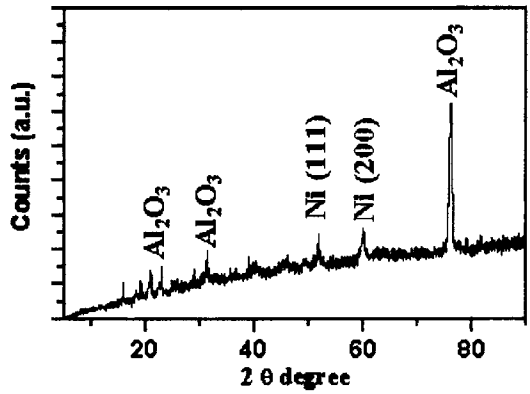

Figure 5: XRD pattern of Ni nanowire obtained in AAM template.

The growth orientation of Ni nanowires in different directions can be adjusted by the electrodeposition conditions.

Figure 5 indicates that the obtained nanowires grow preferentially along the (1 1 1) and (2 0 0) crystal directions of nickel. It can be attributed to the confined growth of the nanowires within the porous AAM template. The surface energy of Ni crystals decreases in sequence for (1 1 0), (1 0 0) and (1 1 1) faces. Therefore, the preferred growth of Ni

nanowires along the (1 1 1) direction was associated to the low-surface-energy face that much easily appears during the electrodeposition process [9].

CONCLUSIONS

In this work, we report a successful procedure to obtain nickel nanowires with 125 nm x 2.5 μm in the pores of an anodic alumina template. The XRD, AFM, SEM and EDX analysis are used to characterize them. Morphologic observations by AFM and SEM confirm that this method is suitable to produce nanowires simply and cheaply. These structures can be useful both for the investigation of fundamental physics and chemistry and for the construction of new nanodevices.

ACKNOWLEDGEMENTS

The authors gratefully acknowledge the financial support and other forms of aid provided by PETROBRAS, FAPERJ, PEMM/COPPE, CBPF, IF/UFRJ and IPqM, which were crucial for the success of this research.

REFERENCES

[1] Walter, E. C., Murray, B. J., Favier, F., Kaltenpoth, G., Grunze, M., Penner, R. M., *J. Phys. Chem. B*, v. 106 (44), pp. 11407-11411, 2002.
[2] Whitney, T. M., Jiang, J. S., Searson, P. C., Chien, C. L., *Science*, v. 261, pp. 1316-1320, 1993.
[3] Vázquez, M., *Physics B*, v. 299, pp. 302-313, 2001.
[4] Foss, C. A., Tierney, M. J., Martin, C. R. J., *J. Phys. Chem.*, v. 96, pp. 9001-9006, 1992.
[5] Chiriac, J., Moga, A. E., Urse, M., Óvári, T. A., *Sensors and Actuators*, 2004, in press.
[6] Zhang, R. Q., Chu, T. S., Cheung, H. F., Wang, N., Lee, S. T., *Mat. Sci.Eng.*, v. C 16, pp. 31-35, 2001.
[7] Ross, C. A. et al., *J Magn. Mag. Mat.*, v. 249, pp. 200-207, 2002.
[8] Zhang, L. D., Meng, G. W., Phillipp, F., *Mat. Sci. Eng.*, v. A286, pp. 34-38, 2000.
[9] Yu, C.Y. et al., *Materials Letters*, v. 61, pp. 1859–1862, 2007.

Advanced Processing and Manufacturing Technologies for Structural and Multifunctional Materials II
Edited by Tatsuki Ohji and Mrityunjay Singh

CRYSTALLIZATION OF TITANIA FILMS IN AQUEOUS SOLUTIONS AND THEIR DYE ADSORPTION PROPERTIES

Yoshitake Masuda, Tatsuo Kimura, Xiulan Hu, Xiangju Meng, Kazumi Kato and Tatsuki Ohji
National Institute of Advanced Industrial Science and Technology (AIST)
2266-98 Anagahora, Shimoshidami, Moriyama-ku,
Nagoya 463-8560, Japan

ABSTRACT

TiO_2 was crystallized to form thin films on transparent conductive films in aqueous solutions. The films had assembly of acicular TiO_2 nanocrystals on the surface. The crystals grew along c-axis to form acicular particles. Growth direction, i.e., c-axis was perpendicular to the substrates. Amount of dye adsorption increased with film thickness. The intensity of the photoluminescence originated from the dye adsorbed on the nano-structured films showed 3 times higher than that of thicker particulate films constructed of TiO_2 nanoparticles (P25). Assembly of acicular crystals on the surface increased surface area and amount of dye adsorption.

INTRODUCTION

TiO_2 film has been fabricated using various techniques such as TiO_2 nanoparticle sintering (P-25), sol-gel[1], magnetron sputtering[2], chemical vapor deposition[3], liquid phase deposition of amorphous TiO_2[4-7], etc. Deki et al.[4-7] reported preparation of amorphous TiO_2 thin films[7] on glass substrates. The TiO_2 thin films were transparent because of the polycrystalline particles with diameters smaller than the wavelength of visible light. More recently, anatase TiO_2 thin films have been successfully prepared at 50°C using liquid phase deposition (crystallization)[8]. The nucleation and growth processes of anatase TiO_2 on several kinds of self-assembled monolayers (SAMs) in an aqueous solution have been evaluated using a quartz crystal microbalance[8]. Homogeneously nucleated TiO_2 particles and amino groups of SAM showed negative and positive zeta potential in the solution, respectively. The adhesion of TiO_2 particles onto the surface of amino group by attractive electrostatic interaction would cause rapid growth of TiO_2 thin films in the supersaturated solution at pH 2.8. On the other hand, TiO_2 was deposited on SAMs without the adhesion of TiO_2 particles regardless of the type of SAM in the solution at pH 1.5 whose supersaturation degree was low due to high concentration of H^+. The growth via attachment of particles is usually associated with high growth rate, but also high roughness and reduced crystallographic orientation. However, the method described above avoided this compromise, resulting in a high growth rate as well as partial crystallographic orientation and smooth surfaces. In addition, liquid phase patterning (LPP) of anatase TiO_2 was realized using SAMs[9-11]. It was proposed based on scientific knowledge obtained from investigation of interactions and chemical reactions between functional groups of SAMs and ions, clusters and homogeneously nucleated particles in solutions. Mechanisms and site-selectivities for LPP were also discussed in details. These studies showed high performance and high potential of solution chemistry for inorganic materials.

In this study we prepared porous anatase TiO_2 film on SnO_2: F (FTO) substrates using liquid phase deposition (LPD). Morphology of TiO_2 particles and particulate films was controlled to have high specific surface area. Dye adsorption properties were investigated as a function of deposition time. It increased with the increase of film thickness. The 760-nm-thick film achieved dye adsorption that was 3 times larger than that of 1000-nm-thick particulate film constructed of TiO_2 nanoparticles (P25).

EXPERIMENTAL

Ammonium hexafluorotitanate ($[NH_4]_2TiF_6$) (Morita Chemical Industries Co., Ltd., FW: 197.95, purity 96.0%) and boric acid (H_3BO_3) (Kishida Chemical Co., Ltd., FW: 61.83, purity 99.5%) were used as received. Silicon wafers or a glass substrate coated with F doped SnO_2 transparent conductive film (FTO, SnO_2: F, Asahi Glass Co., Ltd., 9.3-9.7 Ω/□, 26 by 50 by 1.1 mm) were used after surface cleaning. Both ends (26 × 14 mm) of the glass substrates were covered by scotch tape (CM-18, 3M) to prevent deposition. Morphology of TiO_2 films was observed by a field emission scanning electron microscope (FE-SEM; JSM-6335F, JEOL Ltd.) and a transmission electron microscope (TEM; JEM4010, 400 kV, point-to-point resolution 0.15 nm, JEOL Co., Ltd.). The crystal phase was evaluated by an X-ray diffractometer (XRD; RINT-2100V, Rigaku) with CuKα radiation (40 kV, 30 mA). The diffraction patterns were evaluated using ICSD (Inorganic Crystal Structure Database) data (FIZ Karlsruhe, Germany and NIST, USA).

Ammonium hexafluorotitanate (2.0096 g) and boric acid (1.86422 g) were separately dissolved in deionized water (100 mL) at 50°C. An appropriate amount of HCl was added to the boric acid solution to control pH. Boric acid solution was added to ammonium hexafluorotitanate solution. The concentrations of boric acid solution and ammonium hexafluorotitanate were 0.15 M and 0.05 M, respectively. Solutions (200 ml) with 0, 0.2 or 1.2 ml of HCl showed pH 3.8, 2.8 or 1.5, respectively. Supersaturation of solution can be changed by pH value. Silicon wafers or FTO substrates were immersed vertically in the middle of the solution[8]. The solution was kept at 50°C for 48 h. It became cloudy 10 min after the mixing of the solutions. The particles were homogeneously nucleated in the solution and made the solution white. They were then gradually precipitated and covered the bottom of the vessel over a period of several hours. The substrates were removed from the solution in 2, 5, 25 and 48 h.

RESULTS AND DISCUSSION

Deposition of Anatase TiO_2

Deposition of anatase TiO_2 proceeds by the following mechanisms[8]:

$$TiF_6^{2-} + 2H_2O \rightleftharpoons TiO_2 + 4H^+ + 6F^- \quad ...(1)$$
$$BO_3^{3-} + 4F^- + 6H^+ \longrightarrow BF_4^- + 3H_2O \quad ...(2)$$

Equation (1) is described in detail by the following two equations:

$$TiF_6^{2-} \xrightarrow{nOH^-} TiF_{6-n}(OH)_n^{2-} + nF^- \xrightarrow{(6-n)OH^-} Ti(OH)_6^{2-} + 6F^- \quad ...(3)$$

$$Ti(OH)_6^{2-} \longrightarrow TiO_2 + 2H_2O + 2OH^- \quad \ldots(4)$$

Fluorinated titanium complex ions gradually change into titanium hydroxide complex ions in the aqueous solution as shown in Eq. (3). Increase of F^- concentration displaces the Eq. (1) and (3) to the left, however, produced F^- can be scavenged by H_3BO_3 (BO_3^{3-}) as shown in Eq. (2) to displace the Eq. (1) and (3) to the right. Anatase TiO_2 was formed from titanium hydroxide complex ions ($Ti(OH)_6^{2-}$) in Eq. (4), and thus the supersaturation degree and the deposition rate of TiO_2 depend on the concentration of titanium hydroxide complex ions. The high concentration of H^+ displaces the equilibrium to the left in Eq. (1), and the low concentration of OH^-, which is replaced with F^- ions, suppresses ligand exchange in Eq. (3) and decreases the concentration of titanium hydroxide complex ions at low pH such as pH 1.5. The solution actually remained clear at pH 1.5, showing its low degree of supersaturation. On the other hand, the solution at high pH such as pH 2.8 or 3.8 became turbid because of homogeneously-nucleated anatase TiO_2 particles caused by a high degree of supersaturation. Anatase TiO_2 thin film was formed by heterogeneous nucleation in the solution at pH 1.5, while the film was formed by heterogeneous nucleation and deposition of homogeneously nucleated particles at pH 2.8 or 3.8.

Crystal Phase of As-Deposited Films[12]

After having been immersed in the solution at pH 3.8, the substrates with films were dried in air. The films were colored to slight white. This indicated that the films were deposited with no colored by-product. The films showed the same whiteness over the whole area, which supported the high uniformity of film thickness and chemical composition. Whiteness gradually increased as a function of deposition time due to increase of film thickness. The films did not peel off during ultrasonic oscillation treatment in acetone for 30 min as they showed high adhesion strength.

Strong X-ray diffractions were observed for films deposited on FTO substrates and assigned to SnO_2 of FTO films. Glass substrates with no FTO coating were immersed in the solution for comparison. Weak X-ray diffraction peaks were observed at 2θ = 25.3, 37.7, 48.0, 53.9, 55.1 and 62.7° for films deposited on glass substrates and assigned to 101, 004, 200, 105, 211 and 204 diffraction peaks of anatase TiO_2 (ICSD No. 9852), respectively. (Fig. 1). A broad diffraction peak from the glass substrate was also observed at about 2θ = 25°. The 004 diffraction peak of anatase TiO_2 was not distinguished clearly for film on FTO substrates because both of the weak 004 diffraction peak of TiO_2 and the strong diffraction peak of FTO were observed at the same angle. Crystallite size perpendicular to (004) planes was estimated from the full-width half-maximum of the 004 peak to be 17 nm.

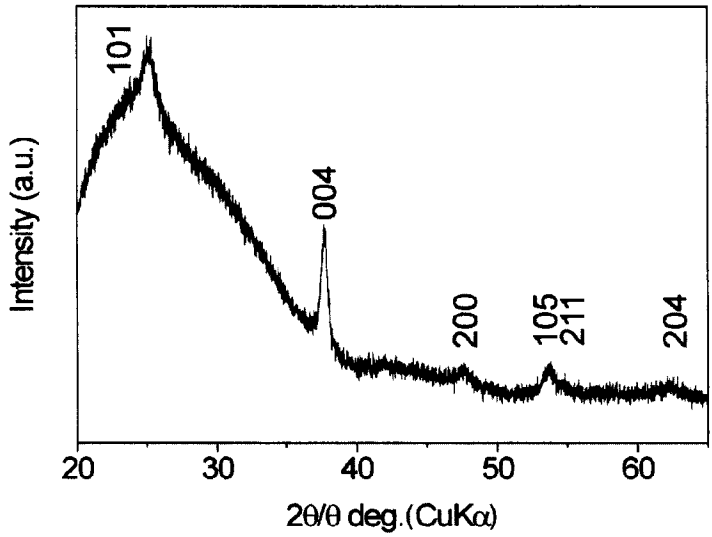

Figure 1. XRD diffraction pattern of anatase TiO_2 film on glass substrate.

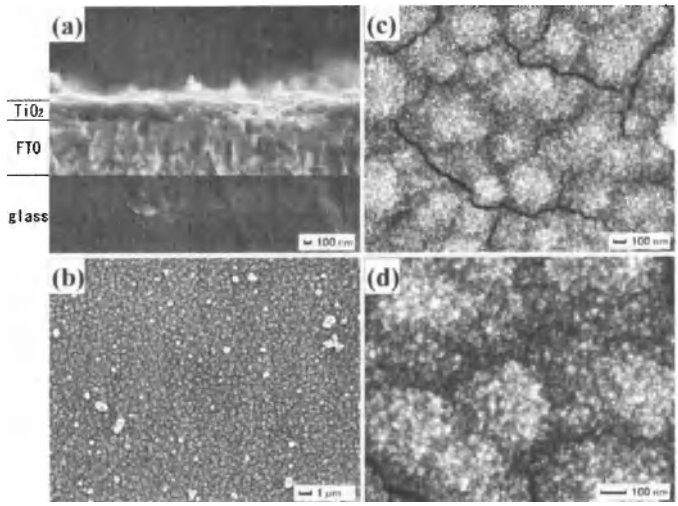

Figure 2. SEM micrographs of anatase TiO_2 films deposited on SnO_2: F substrates for 2 h. (a) cross-section (b) top view (c-d) magnified top view.

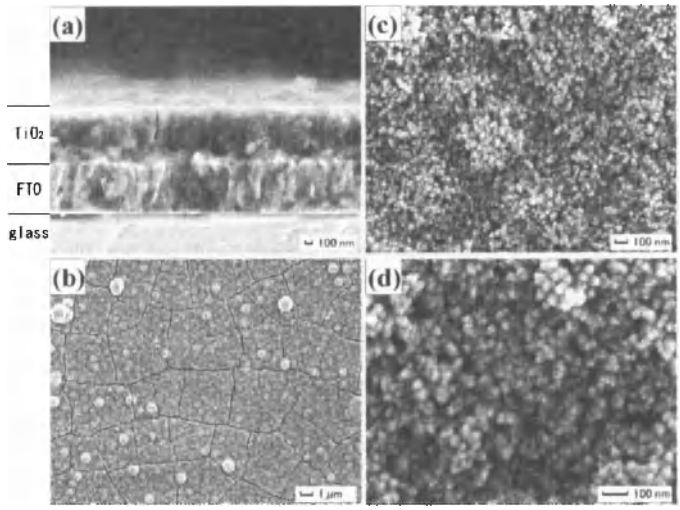

Figure 3. SEM micrographs of anatase TiO_2 films deposited on SnO_2: F substrates for 48 h. (a) cross-section (b) top view (c-d) magnified top view.

Morphology and Film Thickness Change of TiO_2 Films[12]

Thickness of film increased to 260 nm by the immersion for 2 h at pH 3.8. The TiO_2 films were constructed of particles and had a relief structure on the surface (Fig. 2). The diameter of the particles was estimated to be 100–600 nm and cracks were observed at the boundaries of particles, which would have been generated during the drying process due to shrinkage of the films. The particles had many projections on the surface, and so probably had a multi-needle shape (Fig. 2). Thus, the films had a large relief structure due to the assembly of particles and a small relief structure due to needles on the particle surface. The films grew to 360 nm, 600 nm and 760 nm in thickness for 5, 25 and 48 h, respectively. The surface of the films gradually became smoother as a function of deposition time (Fig. 3 for 48 h).

Black and white contrast caused from surface relief in the micrographs decreased gradually. On the other hand, the size of cracks increased with deposition time. Thick films would suppress the generation of small cracks to form long cracks because of stress accumulation due to the high mechanical strength of the films. Boundaries of particles were modified and became more difficult to determine as deposition time increased because of film growth. Particle size was roughly estimated to be 300–600, 450–600 and 550–670 nm for 5, 25, and 48 h, respectively. On the other hand, small needles on the surface of films changed and became visibly clearer as deposition time increased (Fig. 3 for 48 h). Small needles of anatase crystals increased in size. Rapid growth occurred at the initial stage and the growth rate gradually decreased with deposition time.

Dye adsorption characteristics of TiO_2 film

Polyvinyl chloride tape (PVC, CH_2-$CHCl)_n$, 26×22 mm, 100-μm thickness) was perforated with 9 (3 holes × 3 rows) holes 25 mm in diameter using a flatbed cutting plotter (CG-60ST; Mimaki Engineering Co., Ltd.). The TiO_2 film was covered with PVC tape (Fig. 4-(7)).

ssDNA-Cy5 (cy5-DP53-t: Cy5-GCGGCATGAACCTGAGGCCCATCCT, dye labeling DNA) or ssDNA (lambda-gt10: TTGAGCAAGTTCAGCCTGGTTAAG) was dissolved in water. ssDNA-Cy5 solution (1 μM), ssDNA-Cy5 solution (100 nM) and ssDNA solution (1 μM) were dropped onto the 3 holes in the upper, middle and bottom row, respectively, in the PVC tape (Fig. 4-(7))[13]. The film was dried at 95°C for 10 min in air. The film was then rinsed 3 times in sodium dodecyl sulfate (SDS, $NaC_{12}H_{25}SO_4$) for 15 min each time and rinsed 3 times in ultrapure water. It was then boiled in water for 2 min, immersed in dehydrated ethanol at 4°C for 1 min and dried by strong air flow.

Photoluminescence image and intensity were evaluated by Typhoon Trio scanner (GE Healthcare UK Ltd.) using excitation light of 633 nm (He/Ne laser) (Fig. 4-(8)).

Particulate film 1000 nm thick was formed using TiO_2 nanoparticles (TiO_2 P25, Degussa) and was sintered at 500°C for 30 min in air. Photoluminescence intensity of the particulate film and bare FTO substrate was evaluated after adsorption of 100 nM ssDNA-Cy5 for comparison.

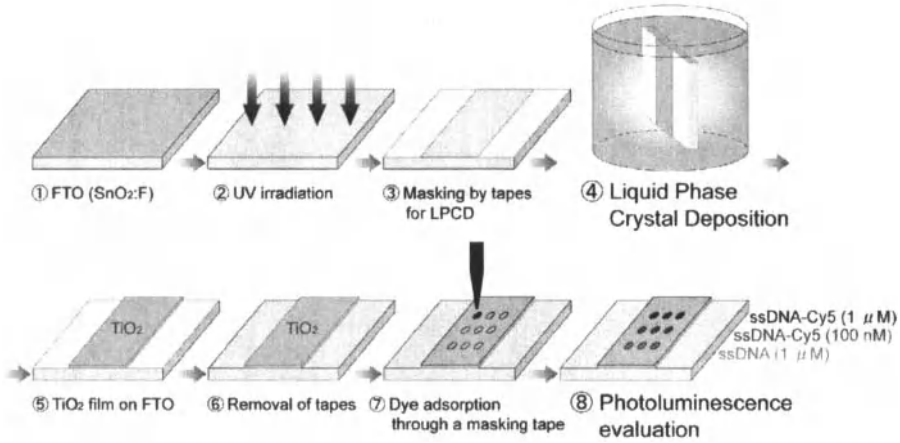

Figure. 4 Conceptual process for fabrication of anatase TiO_2 thin film and evaluation of dye adsorption characteristics.

Strong visible luminescence from ssDNA-Cy5 was observed at holes in the upper and middle rows (Fig. 5). Photoluminescence was not observed at holes in the bottom row because ssDNA has no luminescence properties. Holes in the upper row showed stronger luminescence than that from holes in the middle row. High concentration of ssDNA-Cy5 solution would result in a large adsorption amount of ssDNA-Cy5 to show strong luminescence. Luminescence from the holes in both the upper and middle rows increased in brightness with increased film thickness. Increase of photoluminescence indicates that the adsorption amount of ssDNA-Cy5 increased with film thickness. This would be related to surface morphology and film thickness.

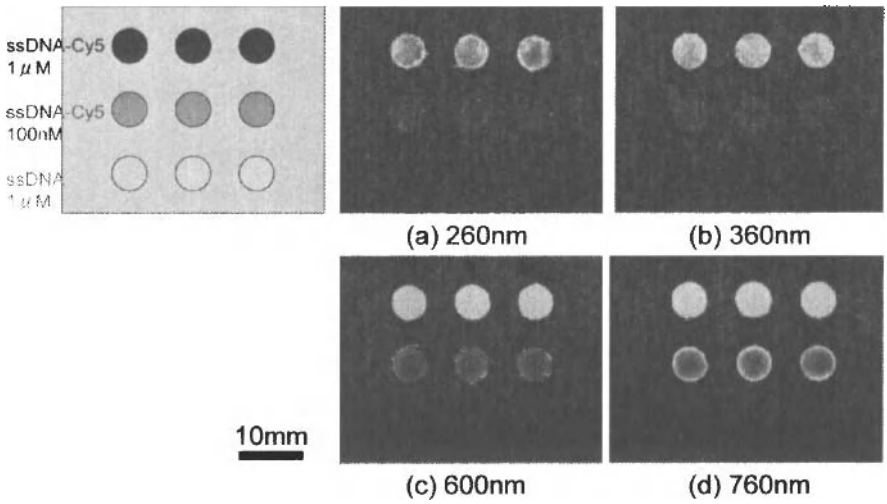

Figure 5 Photoluminescence images of anatase TiO_2 film with varying thickness, covered with ssDNA-Cy5 solution of 1 μM (upper side), ssDNA-Cy5 solution of 100 nM (middle side), or ssDNA solution of 1 μM (bottom side). Thickness of anatase TiO_2 film: (a) 260 nm, (b) 360 nm, (c) 600 nm, and (d) 760 nm.

Photoluminescence at the upper-row holes of 600- and 760-nm-thick film was too strong to evaluate the difference in intensity. Therefore, photoluminescence intensity at middle-row holes was evaluated in detail. Photoluminescence intensity from ssDNA-Cy5 on TiO_2 film increased with film thickness and was much higher than that of FTO substrate (Fig. 6). It is particularly worth noting that photoluminescence intensity from the 760-nm-thick TiO_2 film was 3 times larger than that from the 1000-nm-thick particulate film constructed of nano TiO_2 particles (P25). Assembly of acicular TiO_2 crystals would increase the surface area and effectively adsorb ssDNA-Cy5 due to its nano/micro relief structure.

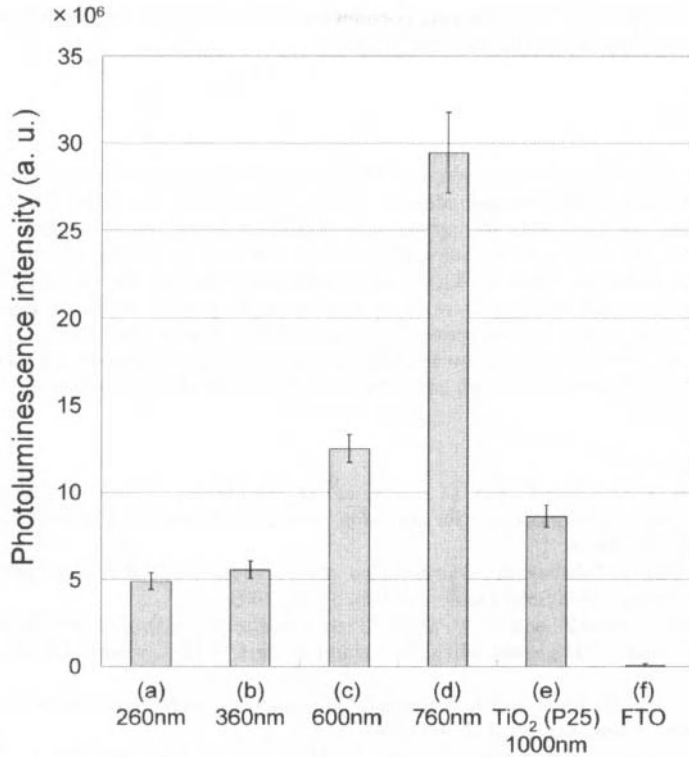

Figure 6 Photoluminescence intensity of anatase TiO_2 film with varying thickness deposited by LPCD ((a)-(d)), 1000-nm-thick particulate film constructed of TiO_2 nanoparticles (e) and bare FTO substrate (f). All substrates were covered with ssDNA-Cy5 solution of 100 nM.

It is also important to remember that luminescence intensity from the 760-nm film is much higher than that from the 600-nm film, although the difference in film thickness is small compared to the 260- and 360-nm film. This would be strongly related to the film surface morphology. The film deposited for 25 h was constructed of a dense layer and assembly of acicular crystals. Dense polycrystalline film would be formed at the initial stage of immersion for roughly 10–15 h. Acicular TiO_2 was then crystallized to form an assembly on the film surface after roughly 10–15 h. The film deposited for 25 h was thus constructed of two layers. Dense polycrystalline film had low surface area and flat surfaces. Only a small amount of ssDNA-Cy5 was adsorbed on dense film deposited for 2 or 5 h. The film deposited for 25 h had an assembly of acicular TiO_2 that adsorbed a larger amount of ssDNA-Cy5 compared to the film deposited for 2 or 5 h. Acicular crystals would continue to grow on the surface of the film to increase film thickness. The film deposited for 48 h thus has an assembly of acicular crystals that grew well in the solution. The film would have a high surface area and nano/micro relief structure suitable for

adsorption of ssDNA-Cy5. Consequently, photoluminescence intensity improved dramatically from film deposited for 25 h to film deposited for 48 h.

CONCLUSION

Anatase TiO_2 films were prepared on FTO substrates in aqueous solutions. The particles were homogeneously nucleated and adhered to the substrates at the initial stage to form particulate films. The films were then grown with deposition period. Small needles of anatase TiO_2 crystals on the surface of the films increased in size and so became visibly clearer as deposition time increased. Thus, the films had a large relief structure due to the assembly of particles and a nano-scale relief structure due to needles on the particle surface. The assemblies of acicular crystals on the surface showed high potential to adsorb dye. Photoluminescence intensity from ssDNA-Cy5 adsorbed on the film increased with film thickness, and successfully realized high intensity that was 3 times larger than that from particulate film constructed of nano TiO_2 particles (P25).

REFERENCES

[1] G. X. Shen, Y. C. Chen, L. Lin, C. J. Lin, and D. Scantlebury, "Study on a hydrophobic nano-TiO2 coating and its properties for corrosion protection of metals," Electrochimica Acta, 50(25-26), 5083-89 (2005).
[2] P. Zeman and S. Takabayashi, "Nano-scaled photocatalytic TiO2 thin films prepared by magnetron sputtering," Thin Solid Films, 433(1-2), 57-62 (2003).
[3] P. Evans, M. E. Pemble, and D. W. Sheel, "Precursor-directed control of crystalline type in atmospheric pressure CVD growth of TiO2 on stainless steel," Chem. Mater., 18(24), 5750-55 (2006).
[4] S. Deki, Y. Aoi, O. Hiroi, and A. Kajinami, "Titanium(IV) oxide thin films prepared from aqueous solution," Chem. Lett., 6, 433-34 (1996).
[5] S. Deki, Y. Aoi, H. Yanagimoto, K. Ishii, K. Akamatsu, M. Mizuhata, and A. Kajinami, "Preparation and characterization of Au-dispersed TiO2 thin films by a liquid-phase deposition method," J. Mater. Chem., 6(12), 1879-82 (1996).
[6] S. Deki, Y. Aoi, Y. Asaoka, A. Kajinami, and M. Mizuhata, "Monitoring the growth of titanium oxide thin films by the liquid-phase deposition method with a quartz crystal microbalance," J. Mater. Chem., 7(5), 733-36 (1997).
[7] H. Kishimoto, K. Takahama, N. Hashimoto, Y. Aoi, and S. Deki, "Photocatalytic activity of titanium oxide prepared by liquid phase deposition (LPD)," J. Mater. Chem., 8(9), 2019-24 (1998).
[8] Y. Masuda, T. Sugiyama, W. S. Seo, and K. Koumoto, "Deposition Mechanism of Anatase TiO2 on Self-Assembled Monolayers from an Aqueous Solution," Chem. Mater., 15(12), 2469-76 (2003).
[9] Y. Masuda, S. Ieda, and K. Koumoto, "Site-Selective Deposition of Anatase TiO2 in an Aqueous Solution Using a Seed Layer," Langmuir, 19(10), 4415-19 (2003).
[10] Y. Masuda, T. Sugiyama, and K. Koumoto, "Micropattening of anatase TiO2 thin films from an aqueous solution by site-selective immersion method," J. Mater. Chem., 12(9), 2643-47 (2002).

[11] Y. Masuda, N. Saito, R. Hoffmann, M. R. De Guire, and K. Koumoto, "Nano/micro-patterning of anatase TiO2 thin film from an aqueous solution by site-selective elimination method," Sci. Tech. Adv. Mater., 4, 461-67 (2003).
[12] Y. Masuda and K. Kato, "Rapid Growth of Thick Particulate Film of Crystalline ZnO in an Aqueous Solution," Thin Solid Films, in press.
[13] H. Tokudome, Y. Yamada, S. Sonezaki, H. Ishikawa, M. Bekki, K. Kanehira, and M. Miyauchi, "Photoelectrochemical deoxyribonucleic acid sensing on a nanostructured TiO2 electrode," Appl. Phys. Lett., 87(21), 213901 (2005).

Advanced Processing and Manufacturing Technologies for Structural and Multifunctional Materials II
Edited by Tatsuki Ohji and Mrityunjay Singh

MICRO SCALE MEASUREMENT OF THERMAL EFFUSIVITY/CONDUCTIVITY OF SiC BY THERMAL MICROSCOPE

Ikuko Yamada[1], Shoichi Kume[1], Koji Watari[1], Kimihito Hatori[2], Genzo Matsui[2]
[1]Advanced Manufacturing Research Institute, National Institute of Advanced Industrial Science and Technology (AIST)
Nagoya, Japan
[2]Hudson Laboratory, Bethel Co. Ltd.
Ishioka, Ibaraki, Japan

ABSTRACT

Thermal properties of SiCs at the micrometer-scale were quantitatively measured with a thermal microscope using thermo-reflectance and periodic heating techniques. This equipment measures the phase lag, which is the delay between the signal of periodic heating laser and the reflectance signal of detecting laser, to calculate thermal effusivity using the calibration curve obtained from standard materials, such as SiC, Si and Ge. Thermal conductivity is calculated from thermal effusivity, density and specific heat. In this study, a SiC single crystal and a sintered SiC polycrystal were investigated. The average value of 366±8 $Wm^{-1}K^{-1}$ for the single crystal was obtained. The small values of standard deviation suggested that the single crystal had homogeneous thermal conductivity. The average value of 257 $Wm^{-1}K^{-1}$, which was obtained from the polycrystal, was in good agreement with the value, 270 $Wm^{-1}K^{-1}$, obtained by the laser flash technique. However, the thermal conductivity of the polycrystal was heterogeneous at the micrometer-scale. The values of the polycrystal were ranged from 300 to 220 $Wm^{-1}K^{-1}$ from the regions of the polycrystal.

INTRODUCTION

Silicon carbide (SiC) possesses high thermal conductivity, excellent corrosion resistance and resistance to high temperatures. However, SiC is very hard to sinter due to its covalent bonding character. The effect of pressure and sintering additives were investigated to obtain dense SiC ceramics. As a result of which highly dense SiC ceramics having a high thermal conductivity was obtained[1,2]. There is much interest in the SiC ceramics as engineering components. On the other hand, quantitative thermal property characterization of SiC at the micrometer-scale has been in increasing demand for its application in the electric component industry, recently. Porosities, random orientation of grains, existence of secondary phases at grain boundaries, lattice impurities and structural defects within the grains strongly affect the thermal conductivity of sintered SiC polycrystal at the micro-scale[3-5]. In the past, the relationship between the microstructure of sintered SiC and the thermal conductivity at the micro-scale was hard to reveal. Though there are few reports, quantitatively thermal property measurement at the micrometer-scale is now possible by using a thermal microscope. Hence, the objective of this study is to correlate the thermal conductivity distributions of sintered SiC polycrystal at the micrometer-scale to its microstructure. Thermal conductivity of the sintered SiC polycrystal is also compared with that of the SiC single crystal.

MEASURMENT SYSTEM OF THERMAL MICROSCOPE

Fig. 1 illustrates a schematic diagram of thermal microscope (Bethel, Ibaraki, Japan)[6,7]. The specimen's surface that is polished to a mirror finish and coated with a molybdenum film of 100±5 nm thickness is irradiated by a heating laser which intensity changes into periodically. As a result, the periodic temperature change at the surface occurs. The temperature change is detected as a reflectance signal by a detecting laser, which is coaxially aligned with the heating laser. Therefore, the phase lag, which is the delay between the signals of periodic heating and the reflectance signal, is measured. The

measured phase lag is used in estimating the thermal effusivity of the sample using calibration curves obtained from standard materials like SiC, Si and Ge[7-9]. Phase lags of Si and Ge are corrected based on the volume specific thermal capacity of SiC. Since the phase lag depends on the thermal effusivity of specimen, high thermal effusivity of ones have small phase lags.

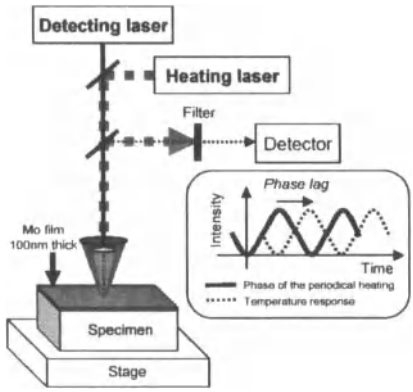

Figure 1. Schematic diagram of thermal microscope.

EXPERIMENTS

Table I lists the specifications of the SiC-6H single crystal used in this study. Thermal properties of SiC-6H doped with nitrogen (wafer of thickness about 250 μm, Cree, Inc., Durham, NC, USA) were measured from the *c*-plane. The sintered SiC polycrystal specimen was prepared by mixing a commercially available α-SiC powder with 2 wt% BeO powder, as sintering aid, followed by hot pressing at 2313K for 1 h at 20 MPa[1]. Specimen surface was coated with a molybdenum film of thickness 100±5 nm in an Ar gas atmosphere with a gas pressure of 6 Pa at room temperature (MSP-30, Vacuum device Inc., Ibaraki, Japan). The thermal microscope and the chamber were kept at room temperature. The heating laser was oval shaped with a major axis of 28 μm and a minor axis of 25 μm, a wavelength of 808 nm and a modulation frequency of 1 MHz. The detecting laser had a diameter of 3 μm, a wavelength of 658 nm and a output power of 35 mW. Based on the calibration curve established using the data of calibrants, such as SiC, Si and Ge, the thermal effusivity was estimated from phase lag. Then, the thermal conductivity was calculated using the following expression[7],

$$b = \sqrt{\kappa \rho C} \tag{1}$$

where b, κ, ρ and C are thermal effusivity, thermal conductivity, density and specific heat capacity, respectively. The densities of SiC single crystal and that of sintered SiC polycrystal are taken as 3.21×10^3 $kg\cdot m^{-3}$ [10] and 3.21×10^3 $kg\cdot m^{-3}$ [4], respectively. The specific heat capacity of both specimens is taken as 673.6 $J\cdot kg^{-1}K^{-1}$ [10].

The first measurements by the thermal microscope were taken from individual points to confirm the reproducibility. Randomly chosen 10 points were repeatedly analyzed up to 5 times. It should be noted that each measurement was an average of one hundred data points that were recorded in every one second. The distribution of thermal conductivity was obtained by line and area scanning. Both specimens were analyzed along the line of 50 μm in length at regular intervals of 2 μm. Areal distribution of thermal

conductivity from a SiC-6H single crystal was measured within an area of 40 μm square at regular intervals of 2 μm. On the other hand, areal scanning of sintered SiC polycrystal was done within an area of 100μm × 100 μm at regular intervals of 2 μm. The surface of sintered SiC polycrystal from the same area analyzed by the thermal microscope was observed by a reflecting microscope simultaneously.

Table I. Specifications of SiC single crystal (SiC-6H)

Specimen	Manufacturer	Type	Dopant	Surface orientation	Measurement surface	Micropipe density
SiC Single crystal	CREE, USA	n	Nitrogen	on axis	*c*	N/A

RESULTS AND DISCUSSION

SiC single crystal (SiC-6H)

The results obtained from individual points by the thermal microscope are shown in Fig. 2. The average value of thermal conductivity was 368±15 $Wm^{-1}K^{-1}$. The standard deviations calculated from 5 repeated measurements at each point were 12 to 26 $Wm^{-1}K^{-1}$ (4 to 7 %). The smallness of standard deviation of thermal conductivity values at each point confirmed the high reproducibility in measurements.

Figs. 3 and 4 show the results of line (50 μm) and area (40 μm × 40 μm) scans from which average values of thermal conductivity were calculated as 391±17 and 366±8 $Wm^{-1}K^{-1}$, respectively. The standard deviation of thermal conductivity values within the measured area were less than 10 %, indicating that SiC single crystal has highly homogeneous thermal property. As shown in Table II, the average value of 366±8 $Wm^{-1}K^{-1}$ obtained from the scanned area falls within the 5 % of the literature value, which is 380 $Wm^{-1}K^{-1}$ [11].

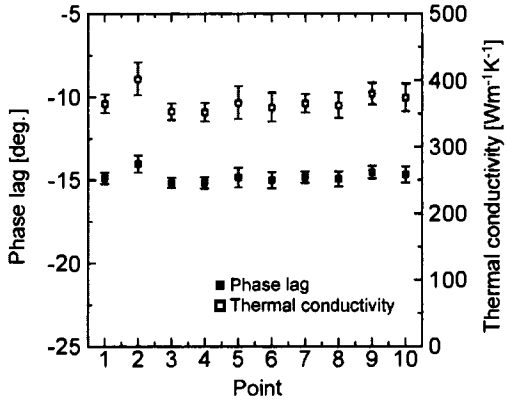

Figure 2. Reproducibility of phase lags for SiC single crystal.

SiC Polycrystal

From the results of point measurements, the average value of thermal conductivity was calculated as 227 $Wm^{-1}K^{-1}$. The standard deviation values from 5 repeated measurements at each point were estimated to be between 6 and 23 $Wm^{-1}K^{-1}$ (2 to 9 %). The reproducibility in measurements was high because of the small scatter in the thermal conductivity values at each point. The result of line scan is shown in Fig. 5. The average, maximum and minimum values of thermal conductivities were calculated as 264, 319 and 218 $Wm^{-1}K^{-1}$, respectively. The standard deviation values at each point were between 7 and 26 $Wm^{-1}K^{-1}$. Variations in the thermal conductivity values were more than the standard deviation values at each point, indicating that the thermal conductivity of the polycrystal was not only significantly different than that of single crystal but also inhomogeneous.

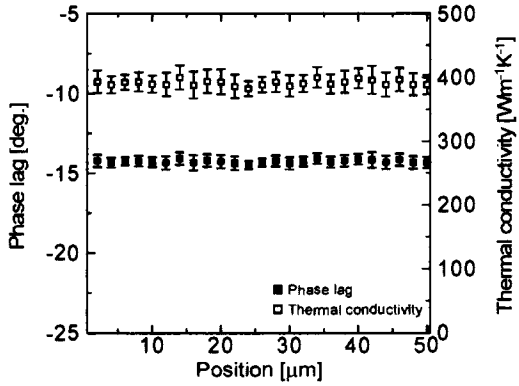

Figure 3. The results of phase lag and thermal conductivity along a 50 μm line for SiC single crystal.

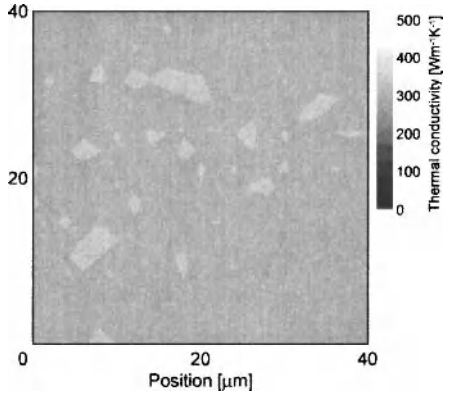

Figure 4. Thermal conductivity distribution map for SiC single crystal.

Table II. Comparison of measured thermal conductivity values with the literature ones of SiC single crystal (SiC-6H) and sintered SiC polycrystal

Specimens	Thermal conductivity [$Wm^{-1}K^{-1}$]	
	This study	Literature data
SiC single crystal (SiC-6H)	366 ± 8	380 [11]
Sintered SiC polycrystal	257	270 [4]

The reflecting microscope image from the area (100 μm × 100 μm) analyzed by the thermal microscope is shown in Fig. 6a. The thermal conductivity distribution map of the same area scans is shown in Fig. 6b. The average value of 257 $Wm^{-1}K^{-1}$ was obtained from the area scanning. This value is in good agreement with the value obtained by the laser flash technique, which is 270 $Wm^{-1}K^{-1}$ [4](Table II). On the other hand, from the look of the map in Fig. 6b, it is clear that the thermal conductivity distribution of a sintered SiC polycrystal is heterogeneous and very low conductivity regions exist as well. Black regions, less than 100 $Wm^{-1}K^{-1}$, in Fig. 6b were found to correspond to pores present in the microstructure in Fig.6a (arrows show pores). The presence of light and dark contrast regions excepting pore portions in Fig. 6b indicated a heterogeneous thermal conductivity distribution. The highest and lowest values of thermal conductivity from the regions of the polycrystal were about 300 and 220 $Wm^{-1}K^{-1}$, respectively. Thermal conductivity variations up to 80 $Wm^{-1}K^{-1}$ within the same sintered SiC polycrystal were not uncommon. The thermal conductivity variations must be affected by microstructural defects[4].

It was revealed that though the thermal conductivities of average value at micro-scale areal scanning and that of macro-scale measurement gave similar results, a variation of 80 $Wm^{-1}K^{-1}$ in terms of microscopic analysis existed between points in a sintered SiC polycrystal.

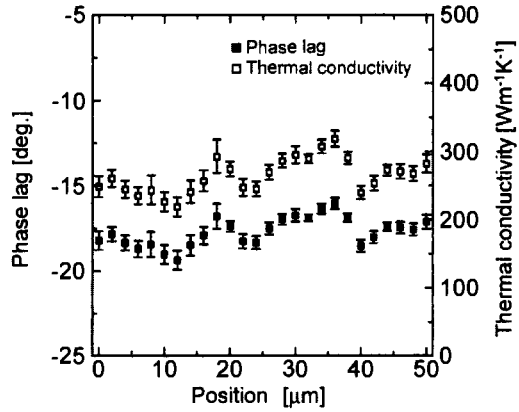

Figure 5. The results of phase lag and thermal conductivity along a 50 μm line for sintered SiC polycrystal.

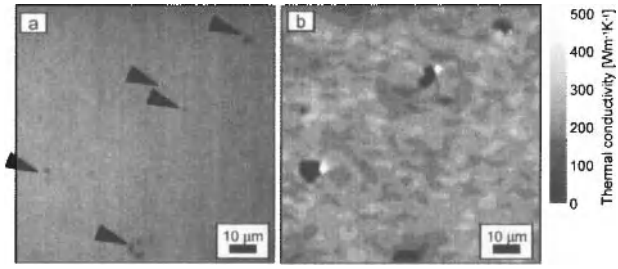

Figure 6. Reflecting photo image (a) and distribution map of thermal conductivity by thermal microscope (b) of the sintered SiC polycrystal. Arrows show pores in the figure (a).

SUMMARY

The thermal conductivities of SiC single crystal (SiC-6H) and polycrystal at the micrometer-scale were measured. It was revealed that the thermal characteristic of the single crystal was homogeneous and that of the polycrystal was heterogeneous. The average thermal conductivity obtained from an area at the micrometer-scale from the polycrystal was consistent with the result obtained by the laser flash technique. However, the thermal conductivity variation from 300 to 220 $Wm^{-1}K^{-1}$ was found from the microscopic areal measurement in the polycrystal.

ACKNOWLEDGEMENT

The authors are greatly indebted to Dr. H. Nakano (Ryukoku University, Japan) and Dr. H. Yilmaz (AIST, Japan) for the instructive discussions.

REFERENCE

[1] Y. Takeda, K. Nakamura, K. Maeda and M. Ura, "Effects of Elemental Additives on Densification, Microstructure, Strength and Thermal Conductivity of Silicon Carbide Ceramics." *Advanced Ceram. Mater.*, **1**, 162-65 (1986).

[2] K. Watari, "High Thermal Conductivity Non-oxide Ceramics," *J. Cera. Soc. Japan*, **109**, S7-S16 (2001).

[3] T. Kinoshita and S. Munekawa, "Effect of Grain Boundary Segregation on Thermal Conductivity of Hot-pressed Silicon Carbide," *Acta Mater.*, **45**, 2001-12 (1997).

[4] K. Watari, H. Nakano, K. Sato, K. Urabe, K. Ishizaki, S. Cao and K. Mori, "Effect of Grain Boundaries on Thermal Conductivity of Silicon Carbide Ceramics at 5 to 1300K," *J.Am.Ceram.Soc.*, **86**, 1812-14 (2003).

[5] H. Nakano, K. Watari, Y. Kinemuchi, K. Ishizaki and K. Urabe, "Microstructural Characterization of High-thermal-conductivity SiC Ceramics," *J. Eur. Ceram. Soc.*, **24**, 3685-90 (2004).

[6] K. Hatori and H.Ohta, "Thermophysical Property Measurment of Micro- and Nano-Structure-Progress of a Thermoreflectance Method" *Materia Japan*, **43**, 129-35 (2004). (In Japanese)

[7] K.Hatori, N.Taketoshi, T.Baba and H.Ohta, "Thermoreflectance technique to measure thermal effusivity distribution with high spatial resolution," *Rev. Sci. Instrum.*, **76** 114901, 1-7 (2005).

[8] I. Yamada, S. Kume, K. Watari, K. Hatori and G. Matsui, "Thermal Conductivity and Effusivity Measurement of High Thermal Conductive SiC Single Crystal Using Thermal Microscope" *J. Soc. Mat. Sci. Japan.* (in press) (in Japanese)

[9] K. Hatori, G. Matsui, I. Yamada, S. Kume, K. Watari, H. Ohta, "Thermal Effusivity Measurement Technique of SiC Using a Thermal Microscope," *28th Jpn. Symp. Thermophys. Prop. Sapporo,* 169-71 (2007).

[10] Japan Thermophys. Prop. Soc. "Thermophysical properties Handbook," (Yokendo LTD., Tokyo) 260 (1990).

[11] C.H.Carter,Jr., V.F.Tsvetkov, R.C.Glass, D.Henshall, M.Brady, St.G.Müller, O.Kordina, K.Irvine, J.A.Edmond, H.-S.Kong, R.Singh, S.T.Allen, J.W.Palmour, "Progress in SiC: from Material Growth to Commercial Device Development," *Mater. Sci. Eng. B.*, **61-62,** 1-8 (1999).

Advanced Processing and Manufacturing Technologies for Structural and Multifunctional Materials II
Edited by Tatsuki Ohji and Mrityunjay Singh

Author Index

Asthana, R., 15

Bender, B. A., 185

Costa, C. A., 87, 123

da Rocha Caffarena, V., 195
da Silva Beltrão, M. S., 123, 195
de Sousa Nóbrega, M. C., 87

Ferreira, M., 123

Gorzkowski, E., 185

Halbig, M. C., 3
Hatori, K., 215
Hibino, T., 155
Homa, J., 73
Hu, X., 203
Huang, S. H., 109

Ishikawa, M., 131

Kaga, H., 163
Kata, D., 139
Kato, K., 203
Kell, J., 169
Kim, C., 147
Kimura, T., 203
Kinemuchi, Y., 163
Kirihara, S., 131, 155
Knoll, M., 63
Kotani, M., 27
Kumar, A., 95
Kumar, B., 169
Kume, S., 215

Laptev, A., 109
Leixas Capitaneo, J., 195
Liersch, A., 73
Lin, S., 54
Lis, J., 139

Martins Silva, E., 195
Masuda, Y., 203
Matsui, G., 215
Matsuzaki, S., 27
McCrabb, H., 169
Medvedovski, E., 179
Meng, X., 203
Miyamoto, Y., 131, 155

Neukam, M., 43
Nishiyabu, K., 27

Ohji, T., 203
Ohno, T., 147
Oikawa, Y., 147
Okanoue, K., 163
Olsson, M. K., 179

Ozaki, H., 147

Pan, M.-J. 185
Passos Guimarães, A., 195

Ribeiro da Silva, C. E., 87

Sekhon, S. S., 95
Selig, J., 54
Shin, J.-S., 147
Silveira Pinho, M., 195
Singh, A. P., 95
Singh, K. L., 95
Singh, M., 3, 15
Singh, S., 33
Sohmura, T., 131
Srivastava, V. K., 33
Stampfl, J., 73
Szepesi, C. J., 179

Tamura, T., 147
Tanaka, S., 163

Uematsu, K., 163

Van der Biest, O., 109
Vanmeensel, K., 109
Vleugels, J., 109

Watari, K., 163, 215
Wiff, J. P., 163
Willert-Porada, M., 43, 63

Yamada, I., 215
Yankov, O., 179

Zellhofer, S., 73
Zimmer, A., 27